Electro-Mechanical Modelling of Tidal Arrays

Marios Charilaos Sousounis

THE UNIVERSITY
of EDINBURGH

Doctor of Philosophy – The University of Edinburgh – 2018

To my wife Esthir

and my son Dimitris,

Without whom none of my success

would be possible

Acknowledgements

I would like to thank my supervisor Dr. Jonathan Shek for his close supervision, informative discussions, understanding of the problems I faced and advice throughout my PhD research.

Also, I would like to thank my second supervisor, Markus Mueller, for the opportunity and the support to study and carry out research at the University of Edinburgh. His guidance and support at the initial, and at the same time difficult, stages of the PhD were crucial for the progress of the research.

In addition, I would like to thank Andritz Hydro Hammerfest for the financial support as well as the information, data and advice received regarding my research. My research was also financially supported by the Institute for Energy Systems of the University of Edinburgh.

Finally, I would like to thank all my friends and colleagues for the discussions we had, the different perspectives they gave me to approach problems and most importantly by making my everyday life during the last four years enjoyable.

Abstract

The aim of this study is to present, compare and improve the options of power transmission for tidal current arrays. The potential to generate low or zero carbon power from the world's tides is increasing as technology moves forward. The technically available tidal current energy resource, the resource that can be captured using existing technology, in the United Kingdom can supply a significant amount of the UK electricity demand. Even though tidal current devices have similarities to offshore wind turbines in many aspects, a number of characteristics differentiate the approach needed regarding power transmission and drive-train design. Some of these characteristics are: predictable direction and speed of the tidal current, predetermined available area in a tidal channel, less swept area due higher density of water, continuous underwater operation and smaller distances to shore.

This thesis is based on the hypothesis that tidal current energy can be harnessed using today's technology in an efficient manner. Technology progression never stops and as new materials and methods become available the cost of utilising tidal current energy will drop in the years to come. However, the research question that has to be asked is whether using today's technology tidal arrays can be an alternative source of electrical power.

In order to respond to this research question electromechanical models of tidal current devices have been developed in detail, from resource to the grid connection, using mathematical linear and non-linear programming in MATLAB/Simulink. The tidal models developed include the tidal resource, the tidal turbine with pitch control, geared induction and synchronous generators, the power electronics with the generator controller, the grid side controller, the cables for power transmission, the filters and the grid connection. All the modelling aspects of this study are presented in Chapter 3. Single tidal current devices were compared using different generator technologies, squirrel cage induction generator or permanent magnet synchronous generator, and different location of the power converters, in the nacelle near the generator or many kilometres apart from the generator. Regarding the generator technology, results showed that even though differences are minor, the permanent magnet synchronous generators are more efficient. Regarding the location of the power converters results showed that positioning the power converters in the nacelle always yields fewer electrical losses but component accessibility is minimised due to the underwater operation of the tidal current device.

A key focus aspect of the study is the power transmission option with onshore converters which is presented in detail. Using this concept it is possible to generate electricity from tidal current devices but at the same time keep the highest possible system reliability despite the continuous underwater operation. This concept has been used in the first demonstration tidal current arrays developed by Andritz Hydro Hammerfest. What is more, data provided by Andritz Hydro Hammerfest were utilised in order to validate the simulation models. In this study a step forward is taken regarding the concept of keeping the converter dry and controlling the tidal current generator from afar. An algorithm is developed to design power harmonic filters for systems that use long distance controls. Power harmonic filters allow the long distance control system to operate reliably under all conditions but generate significant electrical losses. The power harmonic filter design algorithm presented in this thesis estimates the exact filter parameters so that the filter ensures maximum system reliability and generate minimum possible losses. In addition tidal array topologies using this concept are developed.

The final part of this thesis compares a number of different tidal array topologies based on resource to grid efficiency and component accessibility for maintenance. Results showed that when tidal current devices are clustered per four turbines on offshore platforms it is efficient to use as many clusters as possible connected to a single cable whose both ends are connected to the grid. Locating the power converters in the nacelle yields fewer electrical losses compared to locating the power converters on the offshore platform. However, the difference is minimised because the distance between the tidal current device and the offshore platform is the least possible. Having the power converters on an offshore platform is beneficial in terms of accessibility for maintenance and operation because they are not underwater. The results and the methodology from this thesis can be extended to other offshore renewable energy systems such as the wind and wave. In addition, this study can be used as a stepping stone for decision making by tidal current developers.

Lay summary

The aim of this study is to present, compare and improve the options of power transmission for tidal current arrays. Tidal current devices convert the incoming tidal current to useful electricity. This process takes place underwater, usually on the sea bed where the tidal current device is mounted. Transmitting the useful electricity from the underwater tidal current device to the electrical network can produce a significant amount of losses. This thesis is based on the hypothesis that tidal current energy can be harnessed using today's technology in an efficient manner. Technology progression never stops and as new materials and methods become available the cost of utilising tidal current energy will drop in the years to come. However, the research question that has to be asked is whether using today's technology tidal arrays can be an alternative source of electrical power. The potential to generate low or zero carbon power from the world's tides is increasing as technology moves forward. The tidal current resource that can be converted to electricity with today's technology in the United Kingdom can supply a significant amount of the UK electricity demand.

With the aim of responding to this research question a number of ways of transmitting the useful electricity to the electrical network are presented. The ways of transmitting electricity are compared in this study based on the generation of the least possible electrical losses and the highest possible accessibility of components for maintenance. Conclusions are drawn regarding the preferred generator technology, location of components that control the generator and tidal array architecture for power transmission. Detailed research is undertaken in tidal current systems where the converter and the generator are many kilometres apart. The operation of the generator is controlled by the power converter through long cables. This enables us to install the converter on land or on an offshore platform and therefore keep it easily accessible for maintenance. A method is developed to design power harmonic filters for these systems to ensure maximum system reliability and minimum possible losses. In order to perform the above mentioned study, computer models that represent tidal current devices were developed using the software MATLAB/Simulink. These tidal current device models were based on a reference model which was validated by actual data provided by Andritz Hydro Hammerfest.

Declaration

I declare that this thesis was composed by myself, that the work contained herein is my own except where explicitly stated otherwise in the text, and that this work has not been submitted for any other degree or professional qualification except as specified.

Significant parts of the work outlined in this thesis have been published:

- Chapter 3 is based on three publications: “Sousounis, Marios Charilaos; Shek, Jonathan K.H.; Mueller, Markus A.: 'Modelling, control and frequency domain analysis of a tidal current conversion system with onshore converters', IET Renewable Power Generation, 2016, 10, (2), p. 158-165.”, “M. C. Sousounis, J. K. H. Shek and M. A. Mueller, "Modelling and control of tidal energy conversion systems with long distance converters," 7th IET International Conference on Power Electronics, Machines and Drives (PEMD 2014), Manchester, 2014, pp. 1-6.” and “M. C. Sousounis, J. K. H. Shek, R. C. Crozier and M. A. Mueller, "Comparison of permanent magnet synchronous and induction generator for a tidal current conversion system with onshore converters," 2015 IEEE International Conference on Industrial Technology (ICIT), Seville, 2015, pp. 2481-2486.”.
- Chapter 4 is based on two publications: “Sousounis, Marios Charilaos; Shek, Jonathan K.H.; Mueller, Markus A.: 'Modelling, control and frequency domain analysis of a tidal current conversion system with onshore converters', IET Renewable Power Generation, 2016, 10, (2), p. 158-165.” and “M. C. Sousounis, J. K. H. Shek and M. A. Mueller, "Filter Design for Cable Overvoltage and Power Loss Minimization in a Tidal Energy System With Onshore Converters," in IEEE Transactions on Sustainable Energy, vol. 7, no. 1, pp. 400-408, Jan. 2016.”.

The full list of publications is presented in Appendix D.

Marios Charilaos Sousounis

Table of Contents

List of Figures

List of Tables

Nomenclature

β	Blade pitch angle [deg]
Γ_{Gen}	Voltage reflection coefficient of the generator
Γ_{n}	Voltage reflection coefficient
Γ_{VSC}	Voltage reflection coefficient of the voltage-sourced converter
ΔV_{max}	Maximum allowable overvoltage
ζ	Damping ratio
η	Generator efficiency [%]
θ_{g}	grid voltage angle [rad]
θ_{r}	Generator rotor angular position [rad]
θ_{s}	Angle between stator voltage and current [rad]
θ_{T}	Torque angle [rad]
λ	Tip speed ratio
N_{π}	Number of π-sections
N_{π}`	Number of π-sections chosen
ρ_{water}	Sea water density [kg/m^3]
σ	Total leakage factor
$\vec{\varphi}_s, \vec{\varphi}_r$	Stator and rotor flux-linkage vectors [Wb]
φ_r	Flux amplitude induced by rotor magnets [Wb]
ω	Rotating speed of the arbitrary reference frame [rad/s]
ω_{error}	Rotational speed error [rad/s]
ω_{g}	angular frequency of the grid [rad/s]
ω_m	Generator rotor mechanical speed [rad/s]
ω_{opt}	Optimum generator speed for maximum power point tracking [rad/s]
$\omega_{opt}{}'$	Optimum rate limited generator speed for maximum power point tracking [rad/s]
$\omega_{opt}{}^{up}$	Supervisory controller generator rotational speed upper limit [rad/s]

${\omega_{opt}}^{low}$	Supervisory controller generator rotational speed lower limit [rad/s]
ω_R	Turbine rotor rotational speed [rad/s]
ω_r	Generator shaft rotational speed [rad/s]
ω_{rated}	Generator shaft rated rotational speed [rad/s]
A	Turbine sweep area [m^2]
C_p	Hydrodynamic coefficient of the tidal turbine
C_{RC}	*RC* filter capacitance [F]
C_C	Cable Capacitance [µF/km]
C_{RLC}	*RLC* capacitance [F]
C_{dc}	DC link capacitance [µF]
C_{filter}	Filter capacitance [F]
F	Rotor and load viscous friction coefficient [N]
f_{max}`	Maximum accurately represented frequency [Hz]
f_{mt}	Step-down transformer nominal frequency [Hz]
f_{sw}	Generator controller switching frequency [Hz]
f_{tuned}	Filter tuned frequency [Hz]
f_{tuned}^{RLC}	*RLC* filter tuned frequency [Hz]
f_{gt}	Grid side transformer nominal frequency [Hz]
$\vec{\imath}_s, \vec{\imath}_r$	Stator and rotor current vectors [A]
i_{ds}, i_{qs}	*dq-axis* stator currents [A]
J	Moment of inertia of the rotor [kgm^2]
${K_I}^I$	Integral gain of the current loop of the VOC controller
${K_I}^{SC}$	Integral gain of the speed controller
${K_I}^V$	Integral gain of the voltage loop of the VOC controller
${K_P}^I$	Proportional gain of the current loop of the VOC controller
${K_P}^{SC}$	Proportional gain of the speed controller

$K_P{}^V$	Proportional gain of the voltage loop of the VOC controller
k	Maximum power point curve coefficient
L_{ls}, L_{lr}	Stator and rotor leakage inductances [H]
L_s, L_r	Stator and rotor self-inductances [H]
L_m	Magnetising inductance [H]
L_d, L_q	dq-axis inductances [H]
L_C	Cable inductance [mH/km]
L_{RLC}	*RLC* inductance [H]
L_{mt}^{wye}	Step-down transformer wye inductance [pu]
L_{mt}^{delta}	Step-down transformer delta inductance [pu]
L_{mt}^{mag}	Step-down transformer magnetisation inductance [pu]
L_{gt}^{wye}	Grid side transformer wye inductance [pu]
L_{gt}^{delta}	Grid side transformer delta inductance [pu]
L_{gt}^{mag}	Grid side transformer magnetisation inductance [pu]
L_{filter}	Filter inductance [H]
$L_{part}{}^i$	Percentage power losses of part *i* (%)
l_C	Cable length [km]
N_m	Generator rotor mechanical speed [rpm]
N_{opt}	Optimum generator speed for maximum power point tracking [rpm]
N_{opt}'	Optimum rate limited generator speed for maximum power point tracking [rpm]
n_R	Turbine rotor rotational speed [rpm]
n_r	Generator shaft rotational speed [rpm]
P_{tide}	Power potential of tidal currents [W]
P_{mec}	Mechanical output power of the turbine [W]
P_{gen}	Generator active power output [W]
$P_{input}{}^i$	Active power input to *part i* coming from the generator [W]
$P_{output}{}^i$	Active power after *part i* [W]

P_{el}	Electrical active power of the generator [W]
p	Number of pole pairs
Q^{RLC}	*RLC* filter quality factor
Q_g*	Reactive power flow from the grid side [var]
R_R	Rotor radius [m]
R_s, R_r	Stator and rotor winding resistances [Ω]
R_C	Cable resistance [Ω/km]
R_{RC}	*RC* filter damping resistance [Ω]
R_{RLC}	*RLC* filter damping resistance [Ω]
R_{mt}^{wye}	Step-down transformer wye resistance [pu]
R_{mt}^{delta}	Step-down transformer delta resistance [pu]
R_{mt}^{mag}	Step-down transformer magnetisation resistance [pu]
$R_{dc}^{discharging}$	DC link capacitor discharging resistance [Ω]
R_{dc}^{ESR}	DC link capacitor ESR [Ω]
R_{gt}^{wye}	Grid side transformer wye resistance [pu]
R_{mt}^{delta}	Grid side transformer delta resistance [pu]
R_{gt}^{mag}	Grid side transformer magnetisation resistance [pu]
R_{filter}	Filter resistance [Ω]
S_{mt}	Step-down transformer apparent power range [VA]
S_{gt}	Grid side transformer apparent power range [VA]
T_{mec}^{TT}	Mechanical torque output from the tidal turbine [Nm]
T_{mec}^{G}	Mechanical torque input to the generator [Nm]
T_m	Mechanical torque from the generator shaft [Nm]
T_e	Electromagnetic torque [Nm]
T_e*	Reference electromagnetic torque [Nm]
T_{opt}	Optimum torque [Nm]
T_e^{up}	Speed controller electromagnetic torque upper limit [Nm]
T_e^{low}	Speed controller electromagnetic torque lower limit [Nm]
T	Sampling interval

t_r	Pulse rise time [s]
t_t	Pulse travelling time [s]
V_{GAIN}	Voltage gain magnitude
V_{mt}^{wye}	Step-down transformer wye connection voltage [V]
V_{mt}^{delta}	Step-down transformer delta connection voltage [V]
V_{gt}^{wye}	Grid side transformer wye connection voltage [V]
V_{gt}^{delta}	Grid side transformer delta connection voltage [V]
V_{dc}	DC link voltage [V]
v_{ds}, v_{qs}	*dq-axis* stator voltages [V]
$v_{current}$	Tidal current speed [m/s]
$\bar{v}$	Mean tidal current speed [m/s]
v_{rms}	RMS tidal current speed [m/s]
v_{swell}	Swell effect of tidal current speed [m/s]
$\vec{v}_s, \vec{v}_r$	Stator and rotor voltage vectors [V]
$\vec{x}_s$	Stator vector
$\vec{x}_r$	Rotor vector
x_T	Torque comparator control signal
x_φ	Flux comparator control signal
Z_n	Impedance at node *n* [Ω]
Z_C	Cable characteristic impedance at specified frequency *ω* [Ω]
Z_{filter}	Filter impedance [Ω]

Abbreviations

ADCP	Acoustic Doppler Current Profiler
AHH	ANDRITZ HYDRO Hammerfest
AIM	Active interface module
ALM	Active line module
ARL	Atlantis Resources Limited
BTB	Back-to-back
DD	Direct drive
DFIG	Doubly-fed induction generator
DIVAST	Depth Integrated Velocities and Solute Transport
DTC	Direct torque control
EMEC	European Marine Energy Centre
EPR	Ethylene propylene rubber
ESR	Equivalent series resistance
FEM	Finite element model
FOC	Field oriented control
FTC	Fault tolerant control
FTCS	Filter-Transformer-Cable system
GE	General Electric
HOSM	Higher order sliding mode
ICAD	Individual channel analysis and design
IGBT	Insulated-gate bipolar transistor
LCC	Line commutated converter
LCOE	Levelised cost of energy
LCR	Second-order low-pass filter
LDC	Long distance controls
LV	Low voltage
MPPC	Maximum power point curve
MPPT	Maximum power point tracking
MSF	Multivariable structure functions
MTPA	Maximum torque per ampere

MV	Medium voltage
O&M	Operation & maintenance
OPT	Optimised Power Transmission
PMSG	Permanent magnet synchronous generator
PWM	Pulse-width modulation
RC	First-order damped high-pass filter
RLC	Second-order series resonant band-pass filter
ROMS	Regional ocean modelling system
SCIG	Squirrel cage induction generator
SG	Synchronous generators
SME	Sustainable Marine Energy
SSE	Summed square of residuals
SSR	Sum of squares of the regression
SST	Total sum of squares
SVM	Space vector modulation
T.I.	Turbulence intensity
TCCS	Tidal current conversion system
TCS	Transformer-Cable system
THD	Total harmonic distortion
TSR	Tip speed ratio
VOC	Voltage oriented control
VSC	Voltage-source converter
VTHD	Voltage total harmonic distortion
ZDC	Zero d-axis current control

Chapter 1

Introduction

1.1 Motivation

The potential to generate carbon free energy from the world's tides is becoming more and more evident as tidal energy developers move from single demonstration devices to tidal arrays. However, tidal energy developers have not yet decided on a preferred design for a tidal system and that is the reason a significant number of different designs are tested. In the tidal energy sector tidal current technologies are the ones that have made enormous progress towards commercialisation. The technically available tidal current energy resource in the United Kingdom can supply up to 11.3% of the UK electricity demand based on 2016 statistics [1], [2]. The technically available tidal current resource is defined as the resource that can be captured using the existing technology. In order to optimise the power output from a tidal current conversion system (TCCS), the operation, transmission, maintenance and power generation aspects have to be considered.

All the above mentioned aspects are universal for all the different designs which are being tested at present by tidal energy developers. Power generation is a crucial part of a TCCS and the electrical generator has to be chosen and designed for the specific application. In addition, the TCCS requires continuous underwater operation if they are to become cost competitive. This means that the downtime of components must be reduced to a minimum and also that components must be made available for repairs despite the harsh offshore environment that the TCCS operates. Finally, power must reach the end user with the least losses in order to increase the profitability of the systems and ensure their economic sustainability.

This thesis progresses the knowledge of efficient and reliable power transmission from tidal arrays taking into account the electrical efficiency from the generator to grid connection and also the mechanical aspects of a TCCS such as the turbine and also reliability of components in an onshore and offshore environment. Even though all the models of electrical architectures developed are based on the horizontal-axis tidal current turbines the knowledge described in this thesis can be applied to any tidal system that requires electrical power transmission.

1.2 The tidal current conversion systems

In this section a brief introduction to tidal energy and how this form of energy can be exploited is given. The TCCS converts kinetic energy from the flow of water due to tidal currents into electrical energy suitable for grid connection. At this point it should be noted that the focus of this work relates to tidal current energy conversion which differs from converting energy from a tidal barrage. Tidal current technologies are installed into a tidal channel and there is no need to build a wall to obstruct the free flow of the tidal current which is the case in tidal barrage technologies. Most of the TCCSs have a lot of similarities to wind turbines, especially the offshore wind turbines. However a number of characteristics differentiate the approach regarding resource and power transmission. Some of these characteristics are the predictable direction and speed of the tidal current, the pre-determined available area in the tidal channel, smaller distances to shore and continuous underwater operation [3].

1.2.1 The tidal current resource

Tidal currents are created by the changing gravitational pull of the Moon and the Sun on the Earth’s oceans. Depending on the location on Earth, tides are characterised as Diurnal, occur every 24 hours and 50 minutes, semidiurnal, occur every 12 hours and 25 minutes, and mixed tides. In addition, the total gravitational pull can be strong or weak depending on the alignment of the Earth, Moon and Sun. A strong gravitational pull occurs when gravitational forces from the Sun and Moon are added; the opposite is true when the gravitational forces from the Moon and the Sun work at different directions. Hence, spring and neap tides are created respectively. Figure 1.1 describes the effect of gravitational pull on the Earth’s oceans.

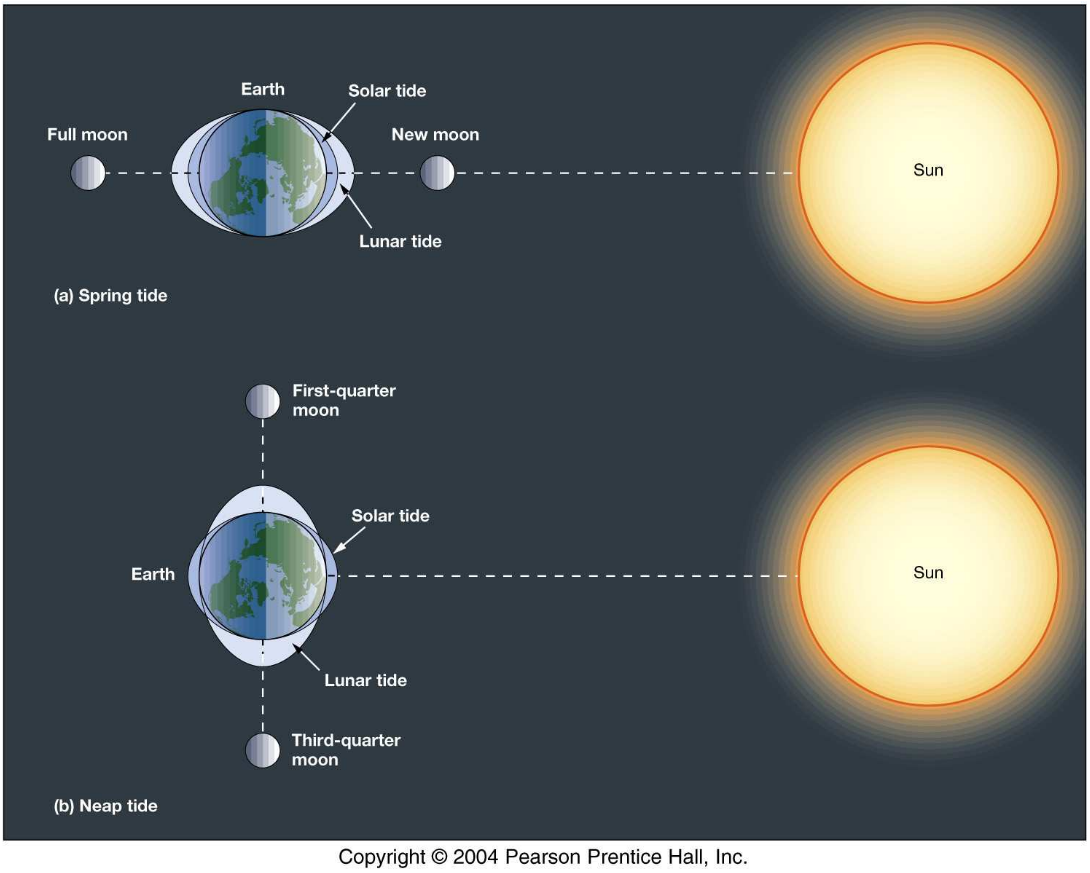

Copyright © 2004 Pearson Prentice Hall, Inc.

Figure 1.1 The formation of tides [4].

The UK predominantly experiences two high and two low tides every day which is a semidiurnal type of tide.

For a TCCS to generate accountable amounts of power a significant tidal current resource is required. For UK waters, the *Atlas of UK Marine Renewable Energy Resources* was published [5] which includes tidal current speeds for neap and spring tides as well as mean tidal speeds arounds the UK. In Figure 1.2 an example of the tidal data that can be accessed is presented.

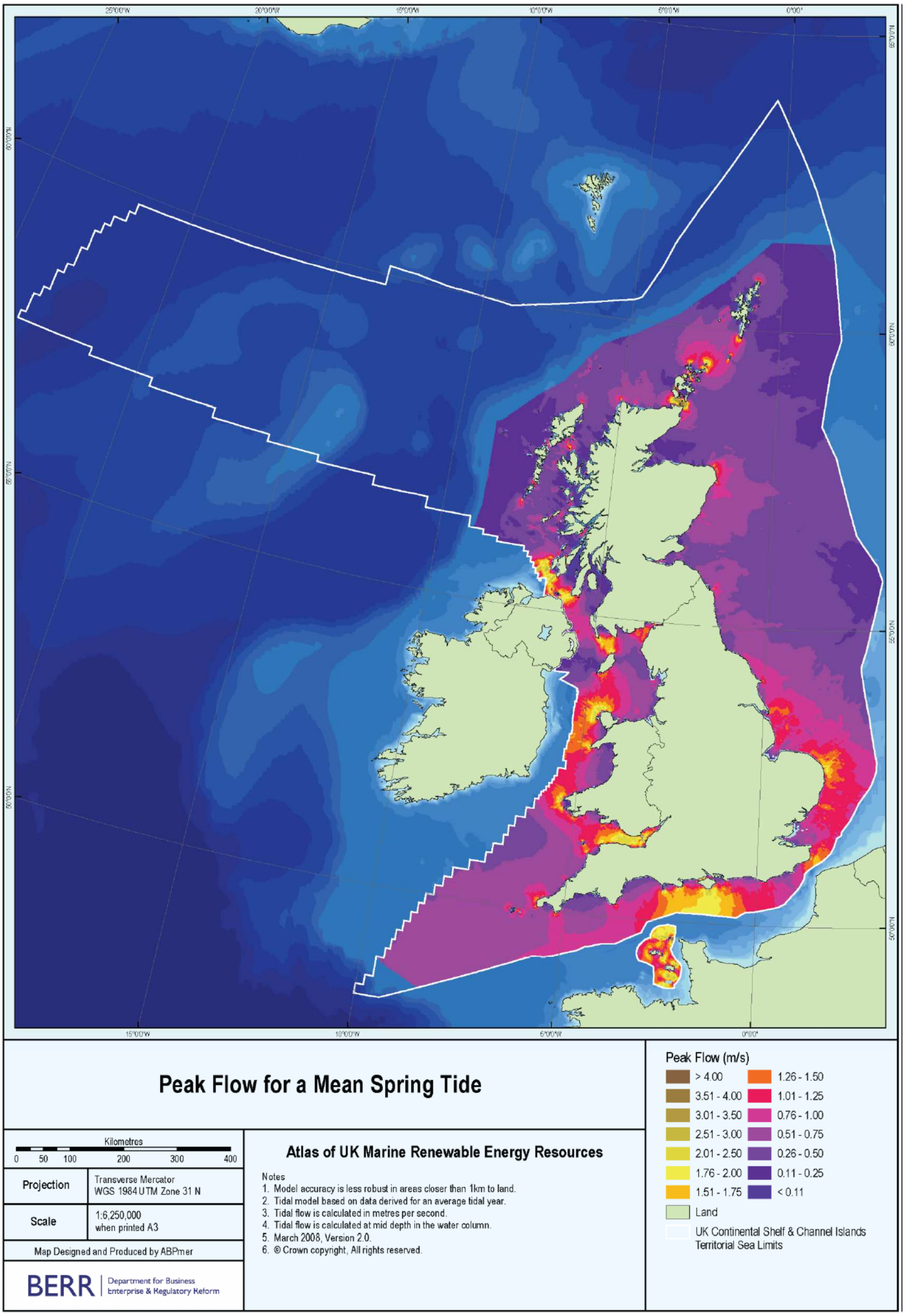

Peak Flow for a Mean Spring Tide

Atlas of UK Marine Renewable Energy Resources

Projection: Transverse Mercator, WGS 1984 UTM Zone 31 N

Scale: 1:6,250,000 when printed A3

Map Designed and Produced by ABPmer

Notes
1. Model accuracy is less robust in areas closer than 1km to land.
2. Tidal model based on data derived for an average tidal year.
3. Tidal flow is calculated in metres per second.
4. Tidal flow is calculated at mid depth in the water column.
5. March 2008, Version 2.0.
6. © Crown copyright, All rights reserved.

Figure 1.2 Peak tidal currents speeds for a spring tide [5]. ***Reproduced from http://www.renewables-atlas.info/ © Crown Copyright.***

As it can be seen in Figure 1.2 significant tidal current speeds appear in channels between islands, between islands and the mainland and in narrow inlets and straits. In addition, tidal current speeds are site dependant and therefore a detailed resource analysis is required before the planning and positioning of a TCCS array. Another observation that can be made is that all the tidal energy resource is close to shore, either close to an island or close to UK mainland. This unique feature of the tidal resource can change the approach of power transmission from the turbines to the grid compared to other renewables such as the wind energy.

In 2005 and 2011 reports were published by Black & Veatch Ltd. [2], [6] regarding the tidal energy resource. In their conclusions they estimated the technically available tidal current resource in the UK waters at 18TWh/y which was re-estimated in 2011 to 29TWh/y for the base scenario. In addition, the cost of energy for tidal current energy developers was estimated in the base scenario at around 19.7p/kWh. If practical constraints are also included in the technically available tidal current resource the energy from the TCCS is reduced to 20.6TWh/y and 21p/kWh for the base scenario.

Tidal current energy developers utilise the above mentioned tidal current resource data in order to identify suitable locations in which to develop and test their TCCS and optimise their performance.

1.2.2 Tidal current energy developers’ status

The idea of utilising the free flow of the moving water has been exploited throughout history by using water and tidal mills to convert the kinetic energy of the tidal current to useful mechanical energy. Today’s challenge is to use the same process in order to generate electricity suitable for grid connection. There are a lot of different designs of tidal current devices. The European Marine Energy Centre (EMEC) classifies the tidal current devices as [7]:

- *Horizontal-axis turbines* where the tidal current forces the rotor to rotate around the horizontal axis in order to generate power (Figure 1.3a).
- *Vertical-axis turbines* where the tidal current forces the turbine to rotate around a vertical axis in order to generate power (Figure 1.3b).

- *Oscillating hydrofoil* where a hydrofoil is attached to an oscillating arm. The tidal current forces the hydrofoil to oscillate in order to generate power (Figure 1.3c).
- *Venturi* effect devices where a duct is used to concentrate the tidal current through a turbine that generates electricity. (Figure 1.3d)
- *Archimedes screw* devices where the corkscrew-shaped device generates power as the tidal current moves through the turning turbines (Figure 1.3e)
- *Tidal kite* devices where the device flies into the tidal current in a figure in order to increase the water flowing into the turbine which is installed under the kite (Figure 1.3f).

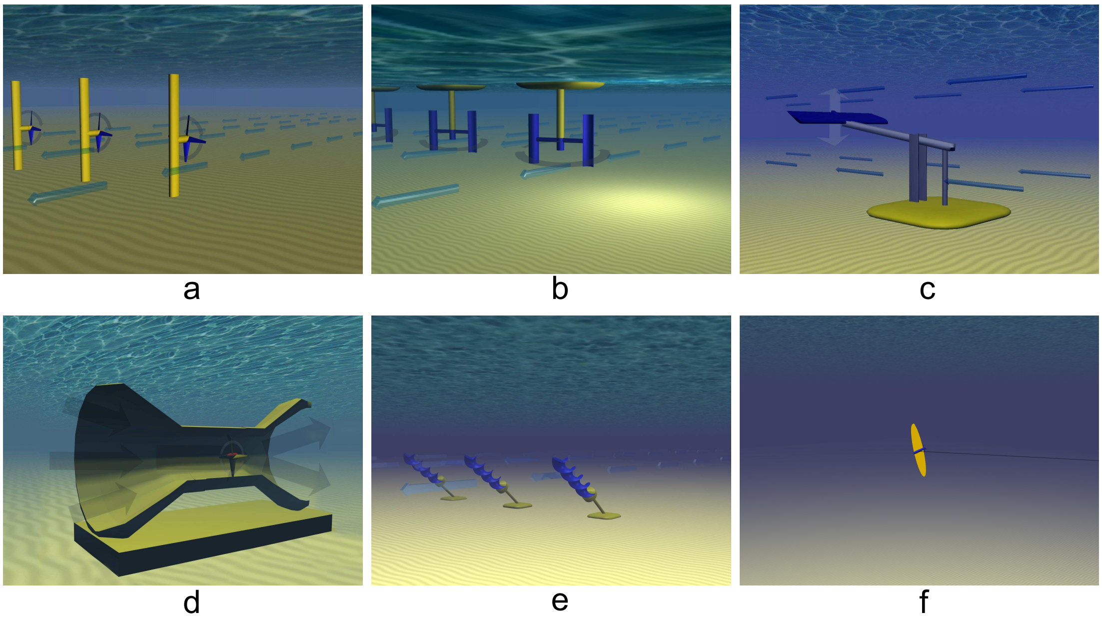

Figure 1.3 (a) Horizontal-axis turbine. (b) Vertical-axis turbine. (c) Oscillating hydrofoil. (d) Venturi device. (e) Archimedes screw. (f) Tidal kite [8].

In addition, EMEC has tried to gather and categorise all the available concepts that utilise tidal currents in order to produce electricity [7]. This list numbers 120 different concepts from 19 different countries around the world. This massive list of developers around the world shows the increasing importance of tidal current energy in a future energy mix. From the 120 different tidal current devices 47 of them are horizontal-axis turbines, 15 vertical-axis turbines, 3 of them use oscillating hydrofoils, 4 utilise the venture effect, 2 use the Archimedes screw concept, 2 devices use the tidal kite concept and 47 devices have an unspecified concept. It is evident that most of the developers prefer the horizontal-axis turbines due to the similarity of the concept with the wind turbines which extract energy from the moving air instead of the moving water.

A frontrunner tidal current energy developer in design and installation of tidal current turbines is *ANDRITZ HYDRO Hammerfest* (AHH). AHH was the first developer in the world to successfully generate electricity from tidal currents and connect their TCCS to the grid. At the moment AHH is involved in two projects around Scotland.

- The first project AHH is involved is a demonstration array of ten 1MW HS1000 devices (Figure 1.4a) at the Sound of Islay.
- The second project AHH is involved is the Phase 1 of the MeyGen project and will provide three 1.5MW HS1000 Mk1 devices (Figure 1.4b) to create and array at the Inner Sound of the Pentland Firth. The long-term plan for the MeyGen project is to install 269 tidal current turbines in order to achieve installed capacity of 398MW.

Figure 1.4 (a) 1MW HS1000. (b) 1.5MW HS1000 Mk1 [9].

Moreover, the total generated energy of AHH tidal current turbines at EMEC have exceeded 3GWh. The HS1000 only, has generated over 1GWh to the grid in a 6 month period. The HS1000 concept is based on a modular seabed design for the mooring system in order to reduce installation time and enable fast and efficient maintenance. The nacelle is attached to the mooring system underwater and can be easily lifted for maintenance. The tidal turbine is based on the standard three-bladed horizontal-axis rotor with pitching blades and yawing capabilities. The generator used is a conventional squirrel cage induction generator (SCIG) with a gearbox. In order to achieve maximum efficiency fully rated back-to-back converters are installed that enable the SCIG to operate at variable speed. The system can start to generate power from 1m/s tidal current speeds and can be installed to water depths up to 100m. Finally, a distinct advantage of AHH is that the system is completely submerged and therefore there is no obstruction to shipping and no negative visual effect from the presence of the turbines.

Another tidal current turbine developer who is involved in the MeyGen project is *Atlantis Resources Limited* (ARL) [10]. The tidal turbine which is planned to be installed at the Inner Sound of the Pentland Firth is called AR1500 and is a 1.5MW horizontal-axis three-bladed turbine with pitching and yawing capabilities (Figure 1.5a). ARL also develops ducted (venturi) systems (Figure 1.5b) as well as turbines that can utilise the flow of rivers to generate electricity (Figure 1.5c).

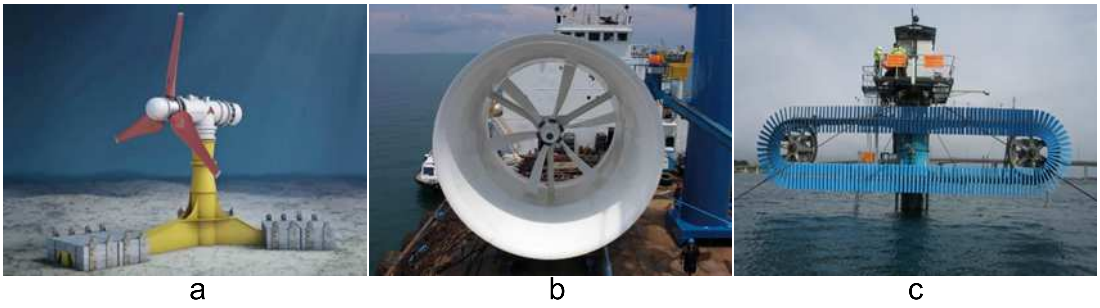

Figure 1.5 (a) Artist impression of the AR1500. (b) Venturi device AS series of ARL. (c) Aquafoils™ turbine AN series for rivers [10].

The tidal current energy developer that boasts to have the biggest tidal turbine is *Scotrenewables Tidal Power* [11]. Their device is called SR2000 and it will be tested at EMEC for a period of 4 years in order to demonstrate the reliability and easy maintenance concept of the system. The SR2000 has two 1MW horizontal-axis tidal current turbines that operate at variable speed but with fixed pitch blades. The power take-off system is attached to a transportation vessel which is 6m long (Figure 1.6a). In addition, for power generation mode the SR2000 requires a single point mooring system (Figure 1.6b).

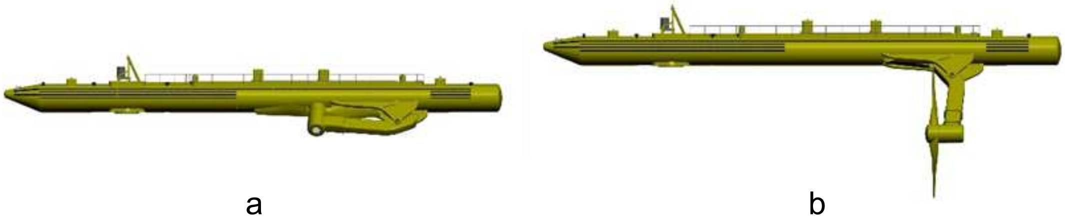

Figure 1.6 (a) Artist impression of the SR2000 at transportation/survivability mode. (b) Artist impression of the SR2000 during power generation mode [11]**.**

General Electric (GE) have a tidal stream solution called Oceade (formerly owned by Alstom Ocean Energy) [12]. The GE tidal current turbine is based on a horizontal-axis three-bladed tidal turbine with pitch and yaw mechanisms. The 1MW concept has already been tested at EMEC and has exported more than 1.2GWh to the grid. Apart from the unique mooring system of Oceade (Figure 1.7a) the developer is designing a subsea hub for connection and transmission of energy from tidal arrays (Figure 1.7b). The development of such a hub will enable lower installation and maintenance costs as well as easier connection of the future tidal arrays to the grid. In the beginning of 2017 it was reported that GE suspended the development of Oceade tidal turbine [13].

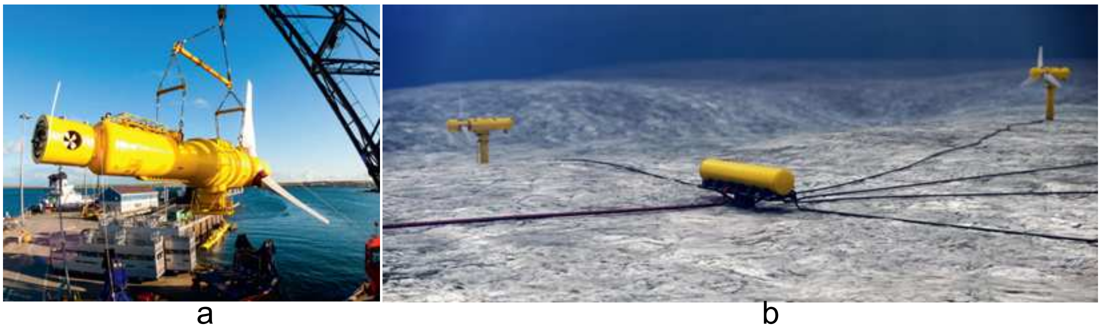

Figure 1.7 (a) GE 1MW tidal stream turbine. (b) Artist impression of the GE tidal array electrical hub [12].

The spinout company of the year 2015 at the New Energy & Cleantech awards was a tidal current developer from the University of Strathclyde called *Nautricity*. *Nautricity* has developed a second generation tidal current device, called CoRMaT, based on horizontal-axis contra-rotating turbine, two rotors rotating in opposite directions (Figure 1.8a) [14]. The first 500kW CoRMaT tidal current turbine will be evaluated at

EMEC in 2016 while at the same time the company has already taken full consent to build its first demonstration array at Mull of Kintyre.

A notable tidal current developer that aims at a completely different mooring system is *Sustainable Marine Energy* (SME). SME has developed a buoyant platform called PLAT-O that is moored using an anchor (Figure 1.8b). The main selling point of this platform is the fact that PLAT-O can change the operating water depth so that the tidal turbines are placed at the optimum area, the area where maximum power can be extracted from the tidal currents [15]. SME is currently planning to install a 200kW PLAT-O at EMEC for testing and grid connection.

Figure 1.8 (a) 500kW CoRMaT device [14]. (b) SME PLAT-O device [15].

As it was stated at the beginning of this section the list of tidal current developers is extensive and is increasing every year. The tidal developers mentioned above have proceeded to commercialisation and array planning or have demonstrated notable innovations for future tidal current turbines. What all the above mentioned developers need, with either fully submerged devices or floating ones, is a way to transmit the tidal energy produced to the grid with the least possible losses and the highest possible reliability. The electrical architecture of a TCCS becomes even more complex when commercial arrays are developed and economics play a major role in the system design.

1.2.3 Electrical architecture options for tidal current conversion systems

An overview of the electrical architecture options for TCCS is given in [16]–[18]. As specified in [16] an electrical architecture can be separated into three distinct systems:

- Collection: This part of the TCCS includes the cables that collect the power from the generator to the hub or the shore depending on the electrical architecture. The collection process also includes the rectifier (generator side power converter).
- Aggregation: This part of the TCCS is where the power from a number of devices is gathered. To achieve this the devices have to be electrically connected using same voltage and fixed frequency in AC systems or a common DC link.
- Transmission: At this part of the TCCS the voltage from all or part of the devices that form the tidal array is stepped up for grid connection.

The general topology of an electrical architecture can be categorized to three different options:

- *Direct connection to shore* for each individual device. In this option, each tidal current device is connected to the grid using separate cables (Figure 1.9).
- *Radial architecture*. Radial networks have been preferred in the wind energy industry due to the redundancy options they offer and cost minimisation of cable installations. In this architecture a number of devices can be connected to a single cable which is connected to shore or an offshore hub. Redundancy can be achieved if both ends of the single cable terminate at the shore or the offshore hub creating a ring network (Figure 1.10).
- *Star cluster architecture*. In this architecture a number of tidal current devices are connected to an offshore hub with separate cables. The offshore hub collects and aggregates power from the tidal current devices. In addition, voltage is stepped-up for transmission and grid connection (Figure 1.11).

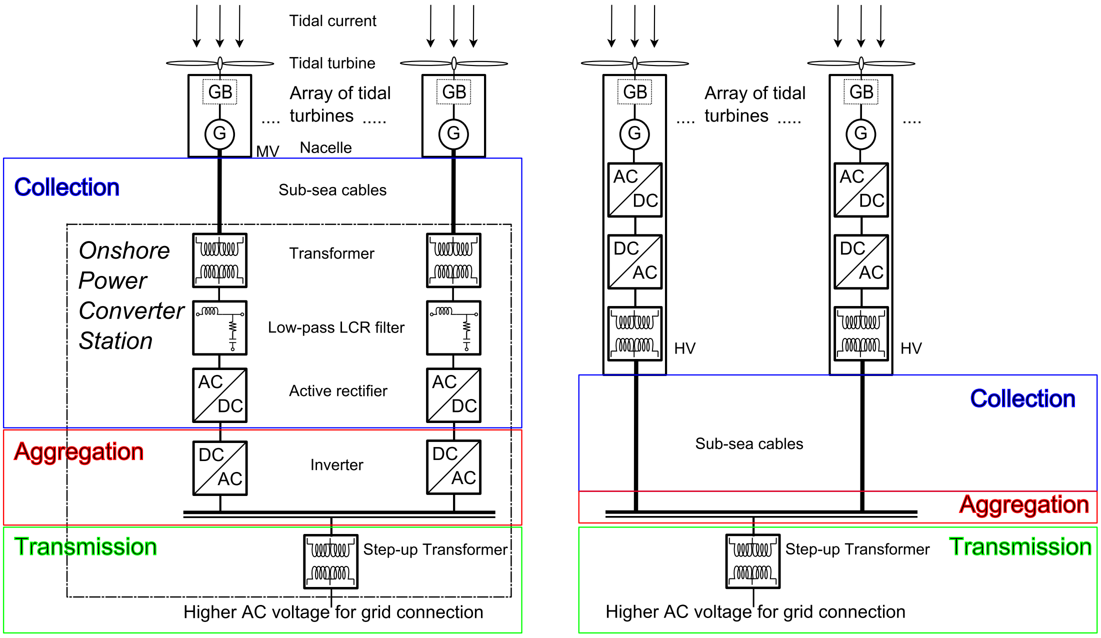

Figure 1.9 Direct connection to shore for each individual device. Two cases are presented depending on the location of power electronics: Tidal array with onshore power electronics (left). Tidal array with power electronics in the nacelle (right).

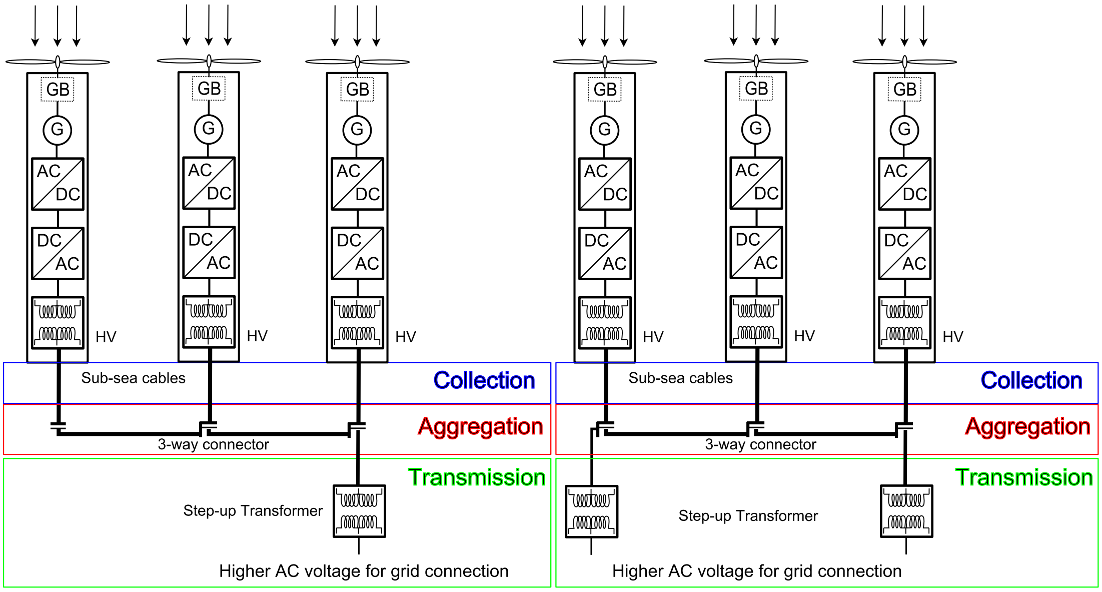

Figure 1.10 Radial architecture. Single cable radial architecture (left). Ring radial architecture with two cables to shore for grid connection (right).

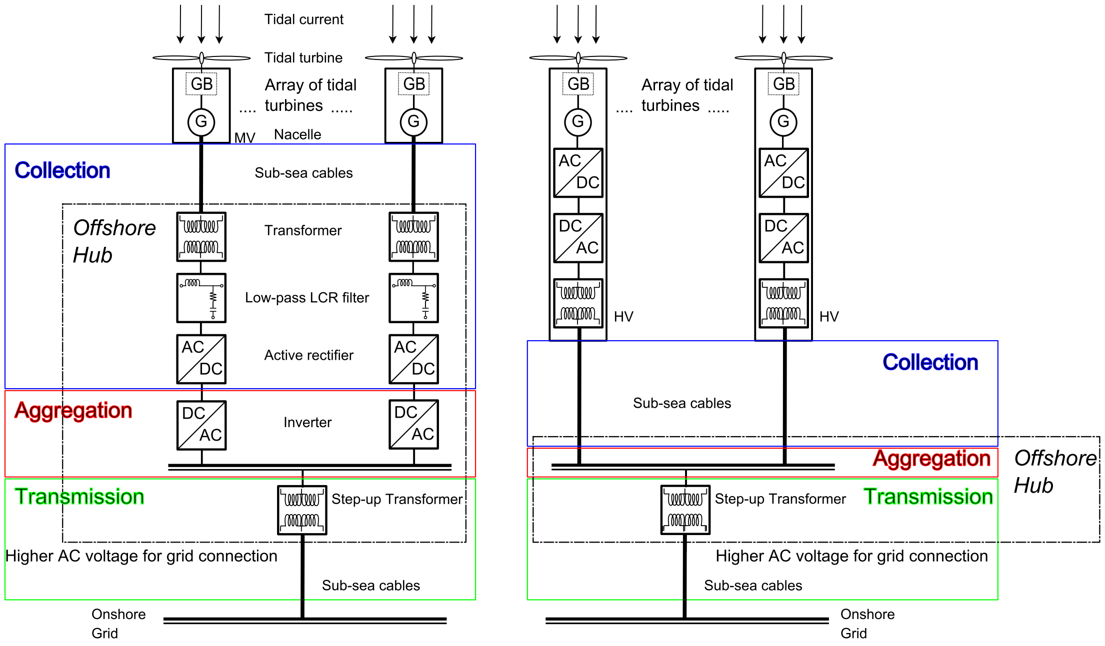

Figure 1.11 Star cluster architecture. Power electronics are placed on the offshore hub (left). Power electronics are in the nacelle (right).

Apart from the general electrical architecture a TCCS can be categorised based on the location of the power converters. A TCCS must have fully rated back-to-back (BTB) power converters in order to be able to connect to the grid. Only exemption is when a doubly-fed induction generator is used in which case power electronics are rated at 25%. The power converters can be placed in three different locations in the system. Depending on the location of the power converters the part of the system that operates at fixed frequency and variable frequency changes:

- *On land*. Placing the power converter on land improves accessibility for maintenance and therefore a TCCS with power converters on land will have reduced operation & maintenance (O&M) costs. However this is only possible in the direct connection to shore architecture and, as it will become evident later on, only for short distances to shore.
- *On an offshore hub*. At the moment offshore hubs can be placed on surface piercing platforms. However, as technology progresses offshore hubs will be available as floating devices and submerged devices with buoyant capabilities.

- *In the nacelle*. Based on the experience from the wind energy industry, power converters are mostly installed in the nacelle. However, the underwater operation of the tidal current devices makes the use of underwater power converters difficult to maintain.

The final categorisation of a TCCS is based on the generator technology. Not all the generator types can be used in all the cases. Depending on the architecture and the location of the power converters certain types of generators such as the doubly-fed induction generator (DFIG), may be restricted. A list of generator options is given below:

- Squirrel cage induction generator (SCIG).
- Doubly-fed induction generators (DFIG).
- Synchronous generators (SG).
- Permanent magnet synchronous generators (PMSG).

Based on all the above mentioned categorisations a diagram can be created with all the possible electrical architectures including the general topology, the location of the power converters and the type of generator that can be used. A TCCS can either have AC collection points or DC collection points. However, DC collection points in the tidal energy industry are not currently being used therefore only AC options will be considered in this thesis. In addition, the suggestions of the three major electrical companies will be discussed in detail in Chapter 4 where the majority of the options are in AC. The diagram with all the possible electrical architectures is shown in Figure 1.12.

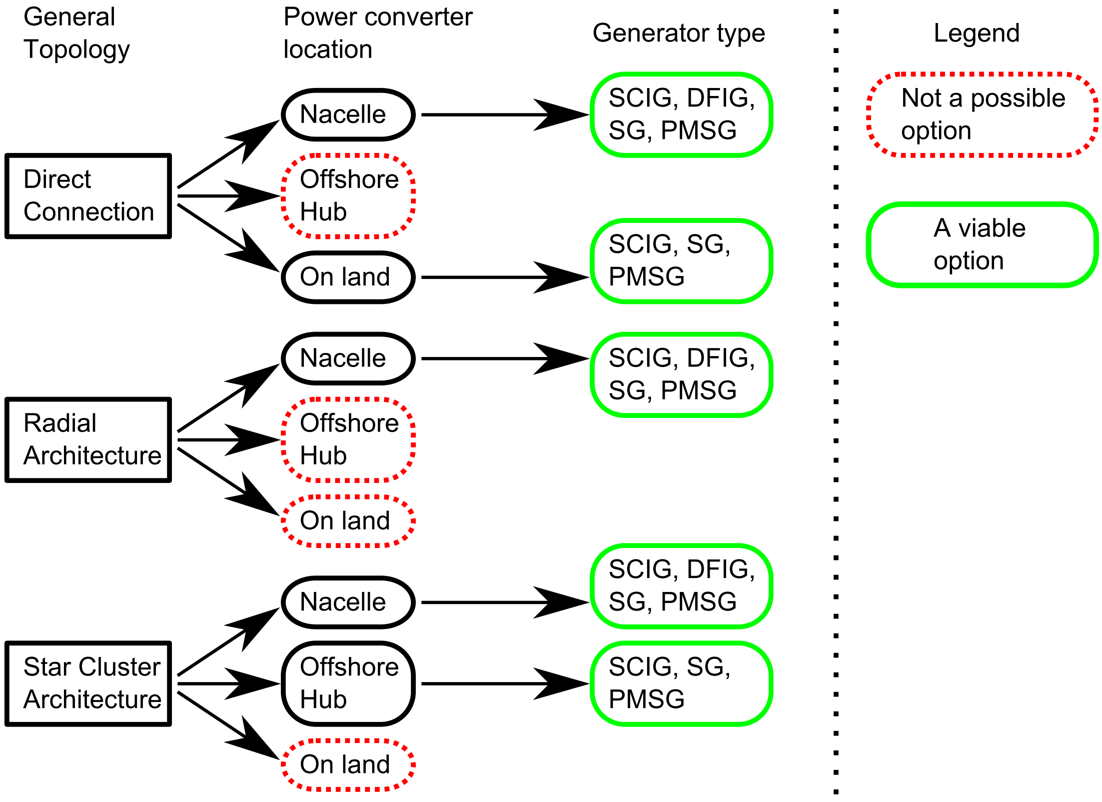

Figure 1.12 Block diagram of all the possible AC options of an electrical architecture for tidal arrays.

Using direct connection to shore the power electronics can only be placed in the nacelle or on land. Placing the power electronics on land requires long cables operating in variable frequency making the use of a DFIG impossible. In this thesis the electrical topology of direct connection to shore with power electronics in the nacelle or on land will be presented with SCIG and PMSG.

The radial architecture is usually implemented in a ring topology. Each turbine has fully rated BTB power converters and a step-up transformer in the nacelle or enclosed in a separate subsea structure next to the turbine. A high voltage cable, 33kV in AC or ±7.5kV in DC, connects a number of turbines based on the rated power. Both ends of the cable end onshore or on a surface piercing platform if the shore is further away. In this thesis the radial architecture is implemented for a system of up to 16 tidal turbines with a 33kV cable.

In the star cluster architecture power electronics can be placed either in the nacelle or on the offshore hub that collects the power. Placing the power electronics in the offshore hub makes them more accessible, easier to operate and maintain. The DFIG generator is not a possibility when power electronics are on the offshore hub. In addition, the star cluster architecture can be implemented with a ring topology by connecting all the offshore hubs of the array in a single cable similar to the radial topology. In this thesis, star clusters of tidal current turbines will be implemented and compared with the other two electrical topologies.

1.3 Problem definition and research questions

At the moment tidal current developers face the barrier of reduced TCCS efficiency and at the same time increased installation and maintenance costs due to the offshore nature of the tidal energy. There is no supply chain for the components of the TCCS to reduce the levelised cost of tidal current energy and the components required by the renewable energy industry are with high specifications and high cost [19]. The challenge the tidal energy industry faces is to manage to decrease the cost and risk for investors by using existing technology, currently used in other related industries such as onshore and offshore wind as well as the offshore oil and gas industry.

Therefore, the main problem that has to be addressed is whether existing technologies and electrical architecture options can provide alternatives for TCCS to become more efficient and more accessible for maintenance. In addition, as stated in [20] control systems for tidal systems have to be improved, power take-off systems have to be re-evaluated, preferred options in power transmission have to be re-considered and accessibility to offshore tidal energy systems for maintenance has to be increased.

1.4 Aims and objectives

The interest in tidal current technology is increasing and tidal current energy developers are planning to proceed to commercialisation phase. Numerous tidal turbines are planned to be installed in the next 20 years and the cost of the TCCS is the main barrier. Increasing the efficiency and maintainability of a TCCS can reduce the risk of investment and the levelised cost of energy for developers.

In this chapter it became evident that based on the location of the tidal currents and the requirements of the industry, new approaches in power transmission can be found.

These approaches can use already existing technology to increase the efficiency of the TCCS based on the specific requirements of each location. Technological advances in new components and materials will enable further improvements in power transmission and increased efficiency of the TCCS.

The main aim of this thesis is to explore and evaluate the alternative ways of connecting a tidal current turbine to the grid. The purpose of exploring and evaluating the electrical architecture options is to reduce losses to a minimum but at the same time keep the system components as accessible as possible for maintenance. In order to achieve the above mentioned aim a number of transmission topologies are modelled in detail using MATLAB/Simulink. MATLAB/Simulink is chosen due to the flexibility it provides to work on both time and frequency domain as well as parameterise the models which allows an analytical way to improve model performance. The models are optimised to have minimum losses to grid and finally they are compared based on their overall efficiency.

1.5 Thesis outline

The following chapter of this thesis presents the literature review regarding power transmission from tidal arrays, power conversion in a TCCS, tidal turbine variations and their effect on power conversion. Tidal resource modelling is also explored.

In Chapter 3, the modelling of a single TCCS is presented in detail. All the models are based on MATLAB/SIMULINK and the different model variations used in this thesis are presented. This includes modelling of SCIG and PMSG together with their controllers. At the final part of this chapter the model of the TCCS developed is validated using data provided by AHH.

Chapter 4, presents the option to transmit power from a TCCS using long distance controls. All the aspects of transmitting power with long distance controls are explored, system is analysed in the time and frequency domain, challenges risen with this specific design are discussed and solutions for the problems associated are presented. A novel algorithm to design filters required for this particular electrical topology is presented.

Chapter 5, presents an analytical comparison between SCIG and PMSG for single TCCS with long distance controls and converters in the nacelle. Options are compared based on power losses from the generator to the grid and the accessibility of the components for maintenance. Based on the results from this chapter the conclusions are drawn regarding favourable electrical topologies for single TCCS.

Chapter 6, expands from the results of Chapter 5 to apply the favourable electrical topologies to tidal current arrays. The radial and star cluster electrical topologies are explored in addition to the hybrid solution of radial cluster electrical topology.

Finally, in Chapter 7 conclusions are drawn, contributions to knowledge are made specific and suggestions for future research are given.

Chapter 2

State of the art on electrical infrastructure for tidal systems

As described in Chapter 1 the electrical architecture of a TCCS is affected by a number of parameters including distance to shore, resource availability, type of generator used together with the associated controllers and location of power electronics. The literature regarding electrical infrastructure in TCCS is limited especially if it is compared to research in onshore and offshore wind. However, all the above aspects and many more are addressed by universities and research institutes from all around the world and in addition, from the three major electrical companies ABB, General Electric and Siemens. In the sections to follow, a brief introduction to the research that affects the electrical architecture in TCCS is presented. Special reference is given to research that looks into power conversion, power transmission alternatives, long distance controls (LDC) and the industrial reports published by the three major electrical companies.

2.1 Resource assessment and power potential

The first step when designing a TCCS is to perform a resource assessment and estimate the power potential from the specific resource. In [21], *Bryden et al.* uses published tidal speed data and applies the flux approach in order to model and estimate the power potential from a tidal channel in *Pentland Firth*. Authors conclude that it is not only the power potential that has to be considered but also other factors such as environmental, economic, dependant on the geography of the channel and the seabed.

They also state that extracting tidal energy from mid water layers, and not the seabed as most developers are planning to do, will still affect the morphology of the sea bed and the environmental impact has to be taken into account during the design process.

A different modelling approach was used in [22] to estimate the mechanical energy flux in a tidal channel in Washington state, USA. Authors based the model on *Stanford University's SUNTANS* code [23] that creates a three-dimensional (3D) flow of the waters, predicts height variation, and creates 3D currents, temperature and salinity. This model managed to estimate with relative accuracy most sections of the *Puget Sound* channel; however its sensitivity to boundary conditions and most importantly to bathymetry data led to inaccurate data being generated for one section of the channel. Authors plan to develop the model further using higher accuracy bathymetry data. Three-dimensional modelling was also used by *Lewis et al.* [24] to estimate the kinetic energy potential in the Irish waters. Authors used the software called *ROMS* (regional ocean modelling system) and separated their study based on the generation of tidal devices. Estimating which resource can be used from each generation of tidal current device, they derived a map with the resource of the Irish Sea that can be exploited from each generation of tidal current device. A similar resource assessment but with different focus was performed in [25] using *Delft3D-FLOW* [26] in the 2D depth-integrated mode. The resource assessment was carried out for the *Ria de Ortigueira* which is composed of four lobes with complex morphology. Using the model the authors firstly determined the areas of the channel where it is best to install a tidal array. The focus of the research was to determine the rated power and swept area of the devices in order to extract as much power as possible without at the same time over-estimating the devices and the costs. This was done by calculating the capacity factor of the devices at each step of the research.

Many more research studies have been carried out that estimate the power potential of the tidal current resource. In this section, these four studies have been analysed in order to show the extent of the resource assessment, the approaches that can be taken in order to calculate the kinetic flux energy of the tidal currents and that the research is carried out at an international level.

2.2 Tidal array planning

Optimised array planning can significantly increase power production in a tidal current array. Tidal array planning research is growing and three notable references are given in this section. In [27] authors create a blade element momentum – computational fluid dynamics model to evaluate single, double and triple tidal current turbine arrangements. They concluded that, even with spacing of 40 diameters in the longitudinal axis between two devices, the downstream turbine will have a significant decrease in power production. On the other hand, spacing the first row of turbines with three diameters or greater lateral spacing the downstream turbine is not affected at all. In addition, the authors managed to run a 14-turbine simulation and compared two different array arrangements. The first arrangement was with standard spacing of 3 diameters lateral and 10 diameters longitudinal spacing and the second arrangement was optimised based on their observations. The research concluded that a 10% increase in array power output can be achieved with optimised planning. In a similar context authors in [28] used the velocity deficit superposition to estimate combined wake width and velocity reduction in a tidal array. Their study included small arrays with a maximum of three rows and showed that 90% of array efficiency can be achieved using an optimisation method for tidal array planning. Finally, authors in [29] are using an open source software called DIVAST (Depth Integrated Velocities and Solute Transport) to simulate the impact of a tidal current array to the coastal environment. The environmental study concluded that a tidal array does not pose a flood threat to the local community but showed that sediment levels and aquatic life is increased at the sides of the array and significantly decreased within the array.

The optimised location of the tidal current devices is important and comes before assessing the ideal electrical architecture for power transmission. The economic considerations of the power transmission options described in Section 1.2.3 can be altered depending on the estimated array efficiency.

2.3 Power conversion in a tidal current system

Tidal current resource assessment, estimating power potential and tidal array planning are important aspects in the development of a tidal array project as they try to optimise the array based on the maximum kinetic energy of the tidal currents. However, power conversion is the part of the system where the kinetic energy is converted to electrical energy useful to the consumers. In the following sections the research regarding power conversion is discussed and evaluated. The aspects that affect power conversion are the controller, the type of the generator and the problems associated with underwater operation. Apart from these aspects of the research literature some comparative studies regarding tidal current turbines are presented and the idea of using energy storage in tidal systems is also introduced.

2.3.1 Control of tidal current turbines

Electrical generators used in TCCS are listed in Section 1.2.3 and are of the same type as those used in wind energy industry. Different types of generators are controlled using different types of controllers. The controllers' aim is to make the generator extract as much as possible energy from the tidal currents by achieving higher power coefficient. An overview of marine energy systems, including tidal current systems, has been given in [30]. The focus of the research is on monitoring by collecting data during operation and on the control of the system in order to achieve maximum power extraction from the marine resource. Even though the research is not specifically focused on TCCSs, the outputs of the research can be applied to such systems. Figure 2.1 and Figure 2.2 show the block diagrams of a monitoring and control structure in a marine energy system [30].

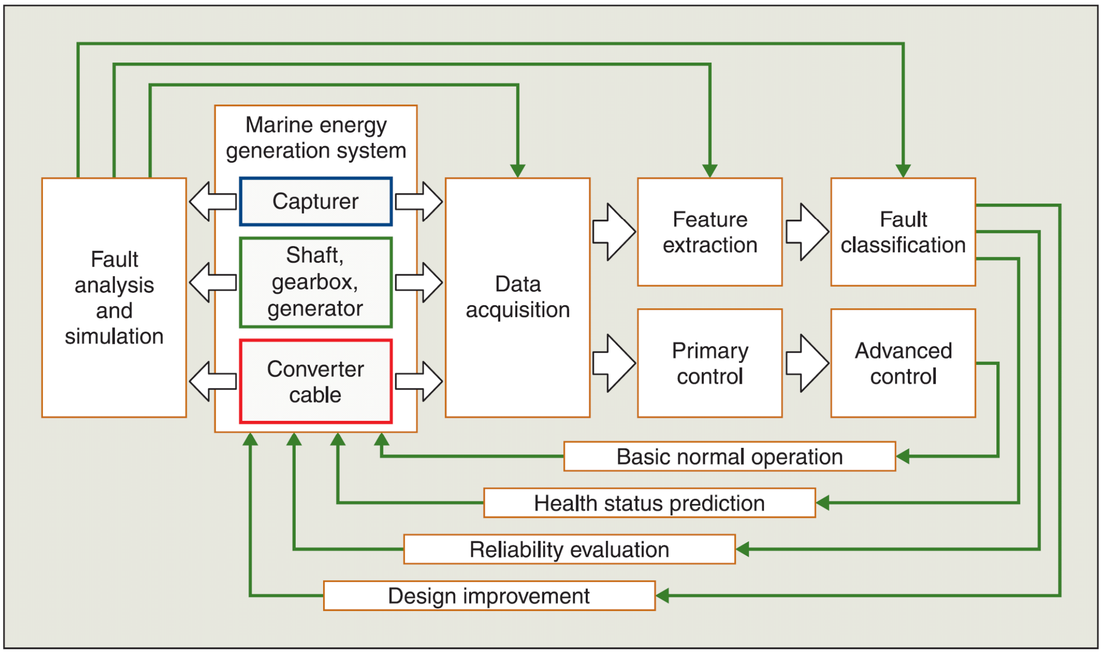

Figure 2.1 Generic monitoring structure in a marine energy system [30]**.**

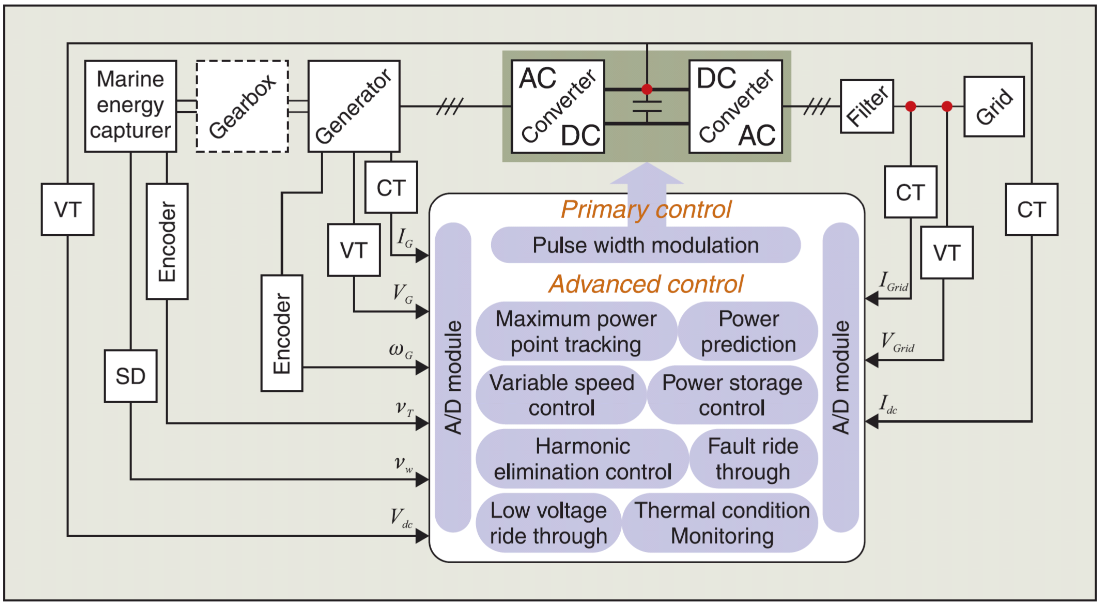

Figure 2.2 Generic control structure in a marine energy system [30]**.**

An important part of the control system in a tidal current turbine is the power limitation mechanism that operates when the power output is higher than the rated power of the turbine. A comparison between pitch and stall regulated tidal current turbines is performed in [31]. The research carried out in [31] was based on horizontal-axis turbines during variable speed operation. The pitch regulated turbines have variable pitch blades that can feather if the speed of the turbine is above rated speed. On the other hand, stall regulated turbines have fixed pitch blades and use the inherent blade design to limit the speed of the turbine at rated levels. Even though in the research both types of speed regulation have satisfactory results when assessed based on their aim, the stall regulated turbines generate a lot higher loads on the blades and require more complicated control system design. Similar research [32] focused on the passive pitch control of a 2-bladed tidal current turbine and the potential benefits in increasing power generation and improving load and structural performance. The researchers compared turbine loads, structural and lifetime performance for three cases: pitch to stall, pitch to feather and a reference blade design. They concluded that the reference blade design has reduced loadings, which can be beneficial to blade lifetime, but reduced power generation as well. In [33] the blades of a horizontal-axis tidal current turbine are designed to achieve feathering by over-speeding, optimise efficiency and take into account phenomena such as the cavitation. In addition, authors in [33] describe the potential disadvantages in using the over-speeding method in tidal current turbines:

- Operating at high rotational speeds increases the voltage generated by the machine.
- Cavitation effect has to be considered.
- Depending on the design, operating at increased rotational speed can increase thrust forces on the turbine.
- Increased centrifugal forces that can cause blade failure.

Based on the literature reviewed it can be concluded that stall regulated turbines in TCCS have a number of disadvantages compared to pitch regulated turbines. These include unstable dynamics, increased out-of-plane bending moments, increased thrust forces and reduced energy yield assuming both systems have 100% availability. In this thesis, pitching to feather technique was implemented for a horizontal-axis three-blade tidal turbine. This is due to the advantages pitching to feather regulation has compared to stall regulation but as well as due to the fact that the TCCS modelled in this thesis is based on the AHH device described in Section 1.2.2.

The majority of research papers regarding control design in tidal current turbines deal with the use of novel control strategies in generators used in tidal current systems. In

[34] the researchers use a vector type controller to control a 3-level neutral point clamped (3L-NPC) converter in order to increase the efficiency of the TCCS (Figure 2.3). In their proposed study the generator used is an SCIG and the focus of the research is to increase the efficiency of the system at fast changing tidal current speeds. As stated by the research, even though the controller manages to increase system efficiency in fast changing tidal current speeds, use of the controller is limited due to the torque loads imposed on the turbine and the high currents drawn.

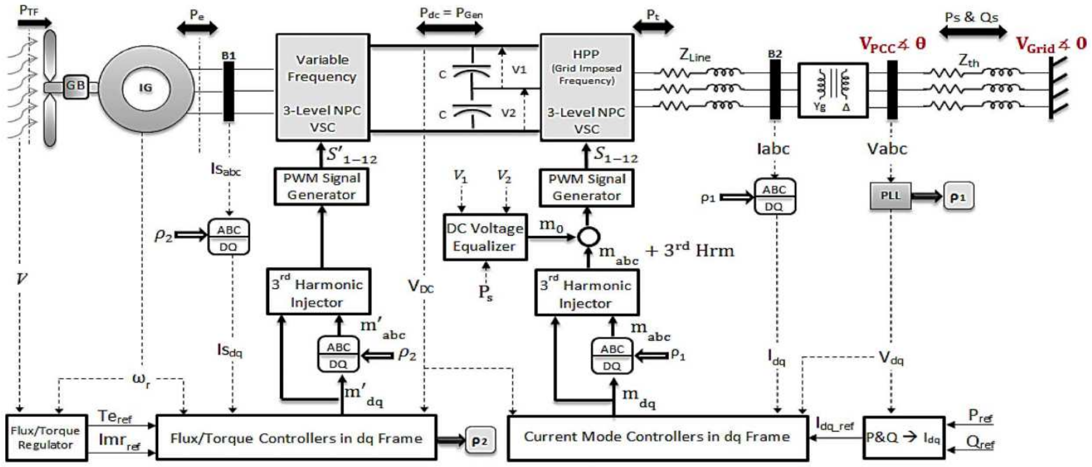

Figure 2.3 Schematic diagram of the grid connected SCIG with the novel control strategy presented in [34]**.**

Other research that uses SCIG in tidal current turbines is presented in [35], [36]. Researchers in [35] use long sub-sea cables between the SCIG and the voltage-source converter (VSC) in order to transmit power to the grid. This type of power transmission is a direct connection to shore as discussed in Section 1.2.3 in Figure 1.9. In order to achieve this they use a direct torque controller (DTC) with space vector modulation (SVM) and design filters specifically for this application. In addition, the researchers suggest an expansion of this application to a star cluster architecture. The control of generators through long cables is a vast subject and will be discussed in detail in Section 2.8.

Control of DFIG is discussed in papers [37], [38]. Researchers in [37] model a resource to grid tidal current turbine and compare the results with data measured from Raz de Sein, Brittany, France. A lot of detail is given to the correct modelling of the tidal current resource by adding turbulence and the swell effect to the averaged tidal current speed. In addition, they study a vector type of controller for DFIG which is directly connected to the grid (Figure 2.4). However, in the study no discussion is made as to how power can be transmitted from the DFIG to the shore. In [38] the same system as depicted in Figure 2.4 is used but the controller proposed is a 2nd order higher order sliding mode (HOSM) controller. Researchers conclude that the HOSM controller can be used for speed tracking and power regulation and that if the resource is unknown then these type of controllers can be good candidates to replace classical vector controllers. However, HOSM controllers appear to have high frequency oscillations around the sliding mode creating a possible problem for the operation of the generator.

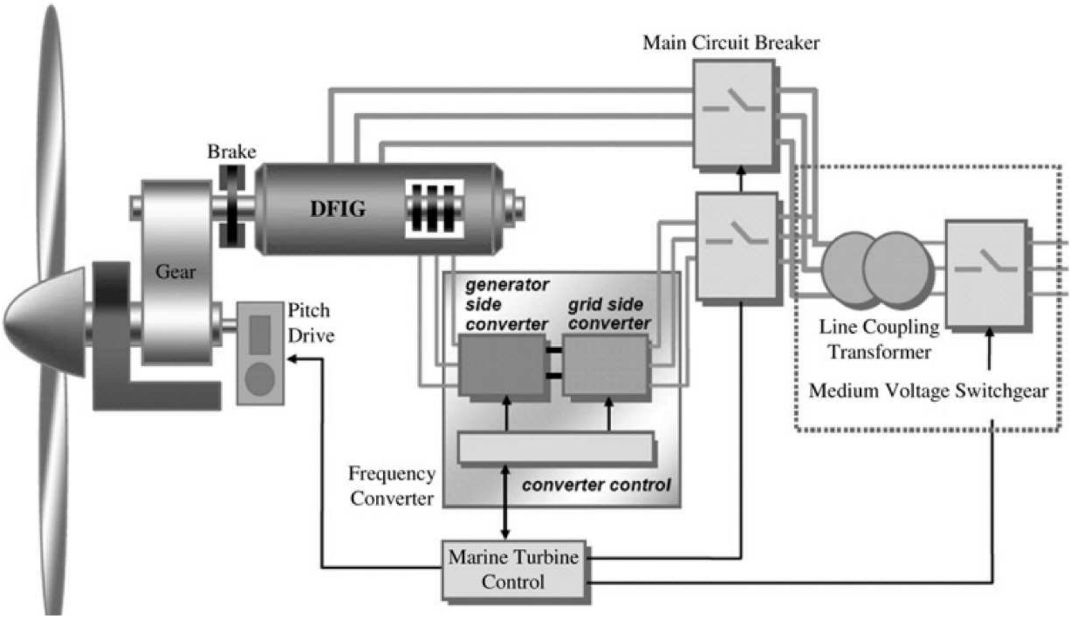

Figure 2.4 Schematic diagram of the grid connected DFIG as presented in [37]**.**

The same controller designed in [38] is also used in [39] to control a PMSG. The PMSG is first modelled in MATLAB/Simulink and then validated with experimental results. The aim of the researchers is to create a tool that experimentally validates tidal current systems with data from Raz de Sein. The block diagram of the PMSG is shown in Figure 2.5.

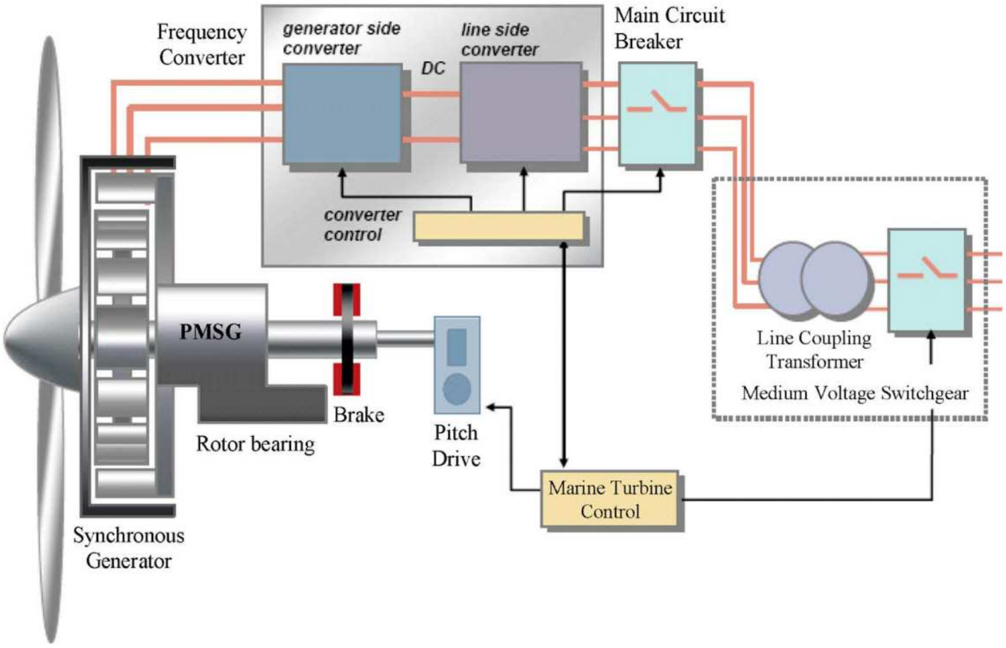

Figure 2.5 Schematic diagram of the PMSG tidal current system [39]**.**

Other variations in controlling a PMSG are presented in [40] using passive rectifiers and in [41] using a fixed pitch blade tidal current turbine. Researchers in [42] perform dynamic stability analysis to a grid connected tidal current turbine with PMSG. In [40] authors suggest that more than one PMSG can be connected on the same shaft and use passive rectifiers to connect to the DC link. The extraction of maximum power from the tidal currents is achieved by knowing the exact tidal currents experienced by the system and designing the generators accordingly. This system is proposed to have similar efficiency as a conventional one but less complicated system with lower power converter losses. However, the main disadvantage of this design is the previous knowledge of the resource that is required which is not always possible to acquire and may not be accurate. In [41] authors are trying to regulate the power of a non-pitchable tidal current turbine. In order to achieve power regulation they use a flux-weakening control strategy which is presented in Figure 2.6.

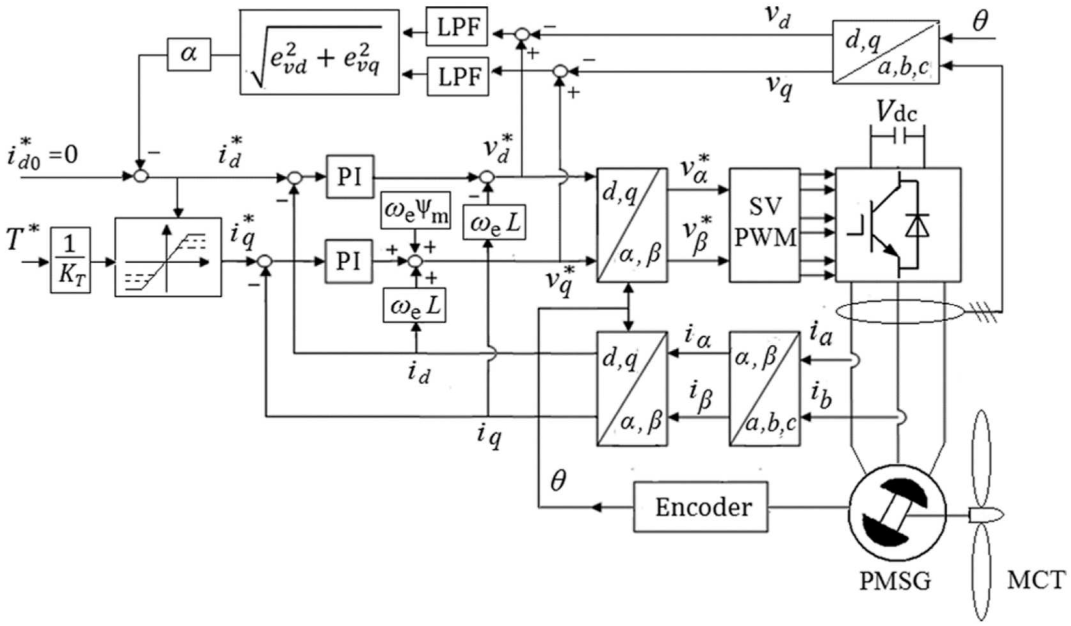

Figure 2.6 Flux-weakening control strategy for PMSG as proposed in [41]**.**

The flux weakening control strategy can be controlled in two different modes. The first mode is to limit the power output to a constant value by over-speeding and reducing the power coefficient. By doing so authors concluded that power is limited effectively and the power losses are low. On the other hand, the second mode of the flux-weakening control strategy is to produce above rated power. This will cause additional copper losses and can possibly reduce the lifetime of the generator. Researchers in [43] use a frequency domain analysis framework of control systems, named individual channel analysis and design (ICAD), on a tidal current turbine with PMSG. ICAD investigates the limitations for control design of multivariable systems. ICAD produces multivariable structure functions (MSFs) which give an evaluation of the internal coupling and the dynamic structure of the tidal current system. Using the MSFs and the MATLAB 2x2 ICAD toolbox [44] the decoupling loops of the conventional vector controller can be replaced by a diagonal controller. The ICAD produced diagonal controller is simpler, has similar response to the conventional vector controller and is not affected by uncertainties of the PMSG parameters. The ICAD technique can also be implemented to control SCIG [45].

2.3.2 Permanent magnet synchronous generators in tidal current systems

Research literature regarding the design of PMSG in tidal current systems is quite extensive compared to other types of generators. Novel generator designs have been proposed for tidal current turbines by a number of researchers. A generator design for tidal current turbines, which also led to start-up company *Nautricity*, is analysed in [41]. This design refers to two sets of contra-rotating blades which are driven by a PMSG directly (Figure 2.7a). A scaled prototype was tested in the Sound of Islay (Figure 2.7b) and a full-scale turbine was tested at EMEC in order to proceed to commercialisation phase. Authors in [46] also consider all the different options they can connect the contra-rotating turbine, the types of generators and converter topologies, but they concluded that the use of a PMSG with active PWM vector control is the most efficient and reliable option.

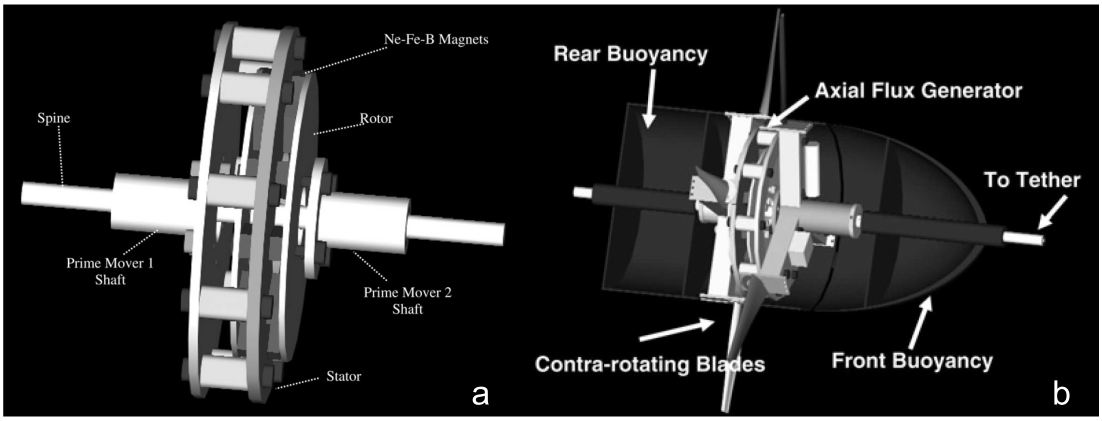

Figure 2.7 (a) CAD design of contra-rotating axial-flux PMSG. (b) Contra-rotating generator prototype [46]**.**

Another non-conventional design of PMSG for tidal current applications is the one described in [47]. The commercial application of this design is utilised by OpenHydro [48] and is based on turbines that are open at the centre and the conversion is achieved by PMSG that is mounted on the rim and is directly driven by the turbine. In Figure 2.8a the OpenHydro turbine is presented and in Figure 2.8b the PMSG design is depicted. Authors in [47] develop a 3D Finite element model (FEM) in order to assess and validate the concept.

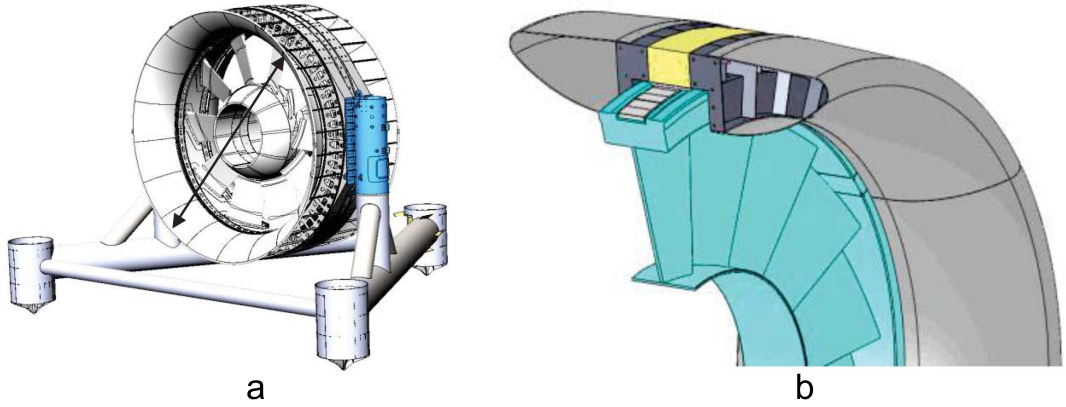

Figure 2.8 (a) OpenHydro tidal current turbine. (b) PMSG arrangement on OpenHydro tidal current turbine [47]**.**

All the above mentioned designs use the horizontal-axis turbine to convert the kinetic energy of the tidal currents to electricity. Vertical-axis PMSG for tidal current devices are examined in [49], [50]. In [49], a PMSG is designed, modelled and validated for a fixed pitch vertical-axis turbine with variable speed operation. Simulated and experimental results present good correlation but the tidal speeds under which the device was tested are up to 2.5m/s which limit the application of the device. The modelling, the dynamics and overall system operation of a vertical-axis tidal current turbine with a PMSG are examined in [50]. A permanent magnet brushless generator is used in this system with a passive three-phase (3Φ) rectifier to convert voltage to DC and a resistor bank to represent the load on the DC link. The electrical configuration of the system designed in [50] is shown in Figure 2.9a and the overall implementation of the system is given in Figure 2.9b. The overall application included the mechanical conversion from the vertical-axis turbine through the gearbox to the generator and the electrical part which includes the generator, the passive rectifier and DC link with the dump load. The authors concluded that three areas of the system require further attention. These include the torque ripples during operation which generate current oscillations at the load, the start-up process which requires significant tidal current speed due to the gearbox and the uncontrollable PMSG and the overall efficiency of the system which is below 20%.

A novel modular air-cored PMSG design for renewable energy applications is the C-GEN generator as described in [51] developed at the University of Edinburgh. Authors model the structure, the electromagnetics and thermal response of the generator and validate their design using a 15kW prototype (Figure 2.10a). The floating device of *Scotrenewables Tidal Power* is used as an example of how the C-GEN generator can be used in a direct drive (DD) application. The advantages of using a directly driven C-GEN generator is the reduced mass compared to conventional DD PMSG, the fault tolerant capabilities of the generator due to the modular design and the high efficiencies due to the elimination of the gearbox. A similar approach is taken in order to integrate the C-GEN generator in the *SeaGen* tidal current turbine (currently an Atlantis Company) [52]. Analytical structural, thermal and electromagnetic results are presented and a specific design of a 600kW DD C-GEN generator is proposed, Figure 2.10b, with 8 parallel axial-flux machines as seen in Figure 2.10c.

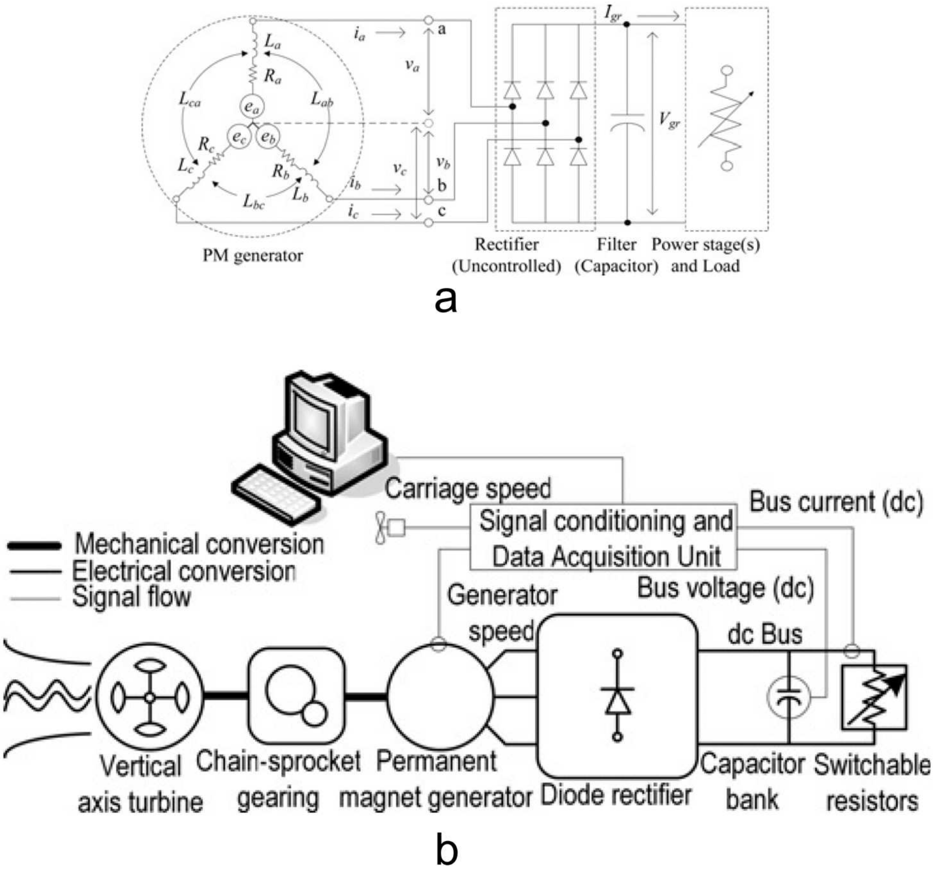

Figure 2.9 (a) Electrical configuration of the vertical-axis system. (b) Data acquisition and overall system presented in [50]**.**

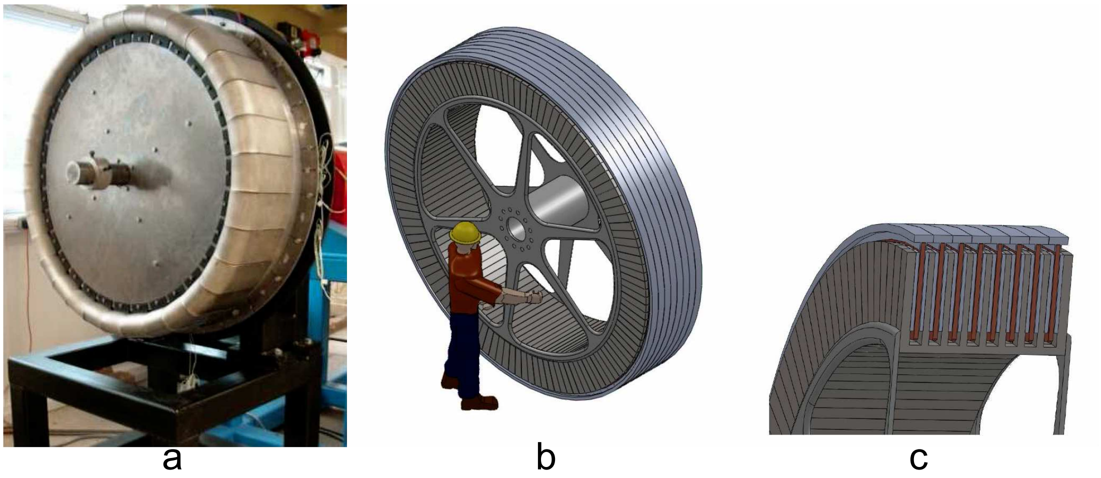

Figure 2.10 (a) 15kW C-GEN prototype [51]**. (b) DD axial-flux C-GEN generator proposed for SeaGen** [52]**. (c) Cross-section of the 8 parallel axial-flux C-GEN generators** [52]**.**

The modularity of the C-GEN generator allows the separate control of each parallel machine. A fault to one of the windings would not require all of the parallel machines to be shut down but only the faulted one. A study has been carried out in [53] to identify and isolate faults in a C-GEN generator. In this study, authors modelled the C-GEN generator and used separate passive rectifiers for each parallel machine so that they can be controller separately. Common short circuit and open-circuit faults were modelled and identification processes were explored to detect these faults. The ability of the C-GEN generator to operate after a fault was simulated, detected and isolated was also depicted in [53]. This ability is defined as fault tolerance and fault tolerant control (FTC) can be a very useful application in tidal current systems, where the generator is difficult to access, so that the operation of the system does not stop but operate at reduced power output until maintenance. Fault tolerant generators in tidal current systems have been explored by other researchers as well in [54], [55]. In [54] authors compare conventional 3-phase PMSG with a 5-phase PMSG with fault-tolerant capabilities. Variable speed models with both types of generators are developed with fault detection using an adaptive reference fault current. The 5-phase PMSG demonstrated smooth torque output during a fault compared to the torque ripples in the 3-phase PMSG. In addition, copper losses were lower and efficiency higher in the fault tolerant 5-phase PMSG. A similar approach was taken in [55] where authors change the control strategy to maximum torque per ampere (MTPA) for a 5-

phase PMSG. They demonstrate that the MTPA strategy can be used during healthy and faulted operation with modifications.

The underwater operation of the TCCS requires increased reliability and efficiency of the generator. In this section, a number of different designs of PMSG were presented that can be used in tidal current systems. PMSG can achieve higher efficiencies in a wider range of speeds compared to SCIG which are preferred by the industry. In addition, the non-conventional designs of PMSG can utilise the kinetic energy of tidal currents with higher efficiency and FTC can increase the reliability of the inaccessible generator.

2.3.3 Mechanical considerations

The continuous underwater operation of the tidal turbine creates additional strain on the turbine-generator system. The tidal turbine is exposed to higher torque and thrust loads compared to wind turbines in addition to the harsh marine environment, with corrosion and aquatic life interacting with the turbines. Prevention or early detection of mechanical failures is of crucial importance in a tidal current system. In [56] authors use large datasets from the operation of HS1000 (AHH) in order to detect anomalies which may indicate a possible fault in the system. They used envelope and curve-fitting techniques to map the normal operation patterns between generator speed and output power. Generator vibrations and rotor speeds were also trended using Kernel density estimation whereas Gaussian mixture modelling was not so effective. The above mentioned techniques can be used with real time data in order to detect patterns that indicate deterioration of the components in a tidal current turbine.

Other researchers have focused on the bearing wear in tidal current devices that use SCIG [57] and on the issues associated with the submerged generator windings for tidal current applications [58].

2.3.4 Generator comparative studies

Comparing the types of generators in tidal current applications is performed in two separate studies under different conditions [59], [60]. In [59] authors compare all the types of generators that can be used in a tidal current system and summarise the advantages and disadvantages of each generator technology. The summary of their results can be seen in Table 2.1. The authors concluded that the DD PMSG is the most advantageous design due to the low maintenance and higher efficiency over a wider range of speeds. Due to these capabilities of the PMSG, the energy generated from a system with DD PMSG is higher compared to the other designs which also leads to higher revenues. However, DD PMSG are still not a proven technology compared to the SCIG and the cost to install such generators is higher. In addition, authors explored the possibility of using DFIG generators due to their popularity with wind energy systems and the lower capital cost of the overall system because of the lower rated power converters (usually 25% of the full rating). However, the disadvantages of DFIG, which are mainly the high maintenance requirements, makes the use of such a generator in an inaccessible underwater system a less attractive option. The discussion of the authors and the results presented in [59] are comprehensive but there is no reference in the research paper about the effect of the generator type in the power transmission system of the TCCS.

Table 2.1 Advantages and disadvantages for different generator types. Table adapted from [59]**.**

Type of Generator	Advantages	Disadvantages
SCIG	☑ Full speed range ☑ No brushes ☑ Control of reactive and active power ☑ Proven technology	☒ Fully rated BTB power converters ☒ Gearbox required
SG	☑ Full speed range ☑ Control of reactive and active power ☑ Eliminate gearbox (DD concept only)	☒ Fully rated BTB power converters ☒ Additional converter for field ☒ Large and heavy generator (DD concept only)
PMSG	☑ Full speed range ☑ Control of reactive and active power ☑ Eliminate gearbox (DD concept only) ☑ Brushless (low maintenance) ☑ No power converter for field compared to SG	☒ Fully rated BTB power converters ☒ Large and heavy generator (DD concept only) ☒ Permanent magnets needed
DFIG	☑ Limited speed range ±30% around synchronous speed ☑ Control of reactive and active power ☑ Reduced rating for power converters	☒ Requires slip rings (high maintenance) ☒ Gearbox required

In [60] researchers compare SCIG and PMSG in a TCCS with direct connection to shore using onshore power converters. Authors create a dynamic model of a TCCS in MATLAB/Simulink and set three criteria to compare the two designs. First, they look at cost and maintenance of each system, then they study the generator efficiency at different operating speeds and finally transmission power losses are compared in order to work out the total system efficiency and total energy generation for each design. Regarding the cost and maintenance the PMSG generator used in this study is using the same gearbox as the SCIG, as seen in Figure 2.11a, and therefore the cost of the PMSG is not significantly higher than the SCIG. In terms of generator efficiency, both designs seem to have high efficiencies near the rated power. However, the PMSG achieved higher efficiencies compared to the SCIG when the TCCS was operating at below rated power. Regarding power transmission losses the TCCS with the PMSG had 0.35% less losses compared to the TCCS with the SCIG. Due to the lower losses, the PMSG system can export an additional 116MWh per year to the grid compared to the SCIG system. The results of energy exported between the two cases can be seen in Figure 2.11b.

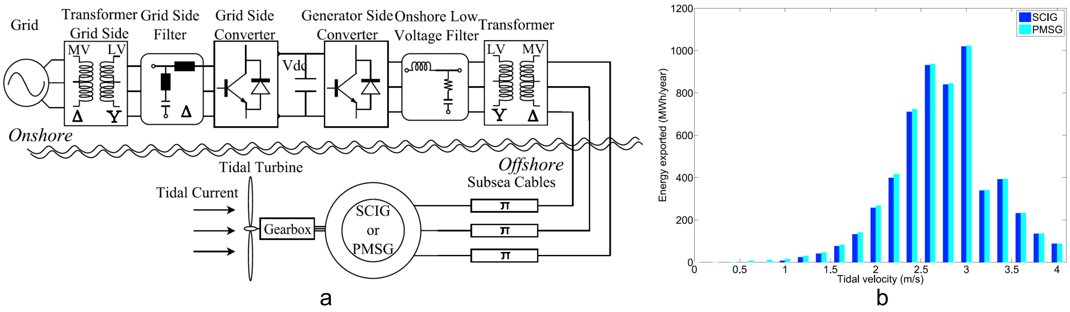

Figure 2.11 (a) Electrical topology of the TCCS designed. (b) Energy exported to grid for the SCIG and the PMSG [60]**.**

2.3.5 Energy storage in tidal current systems

Energy storage in offshore renewables is still at its infancy but there is already research interest in this subject. Authors in [61] study the dynamic stability of an offshore wind farm connected at the same AC bus with a tidal current farm and a flywheel energy-storage system (Figure 2.12). The purpose of adding the flywheel energy-storage system is to smooth the power output fluctuations since the system is connected to the grid. Based on the results from [61] a flywheel energy-storage system rated at 25% of the total renewable energy capacity can significantly mitigate the power fluctuations generated from the unpredictable resource. As proposed in [61] the flywheel energy-storage system can be used in a star cluster system to improve power quality of connected renewable power.

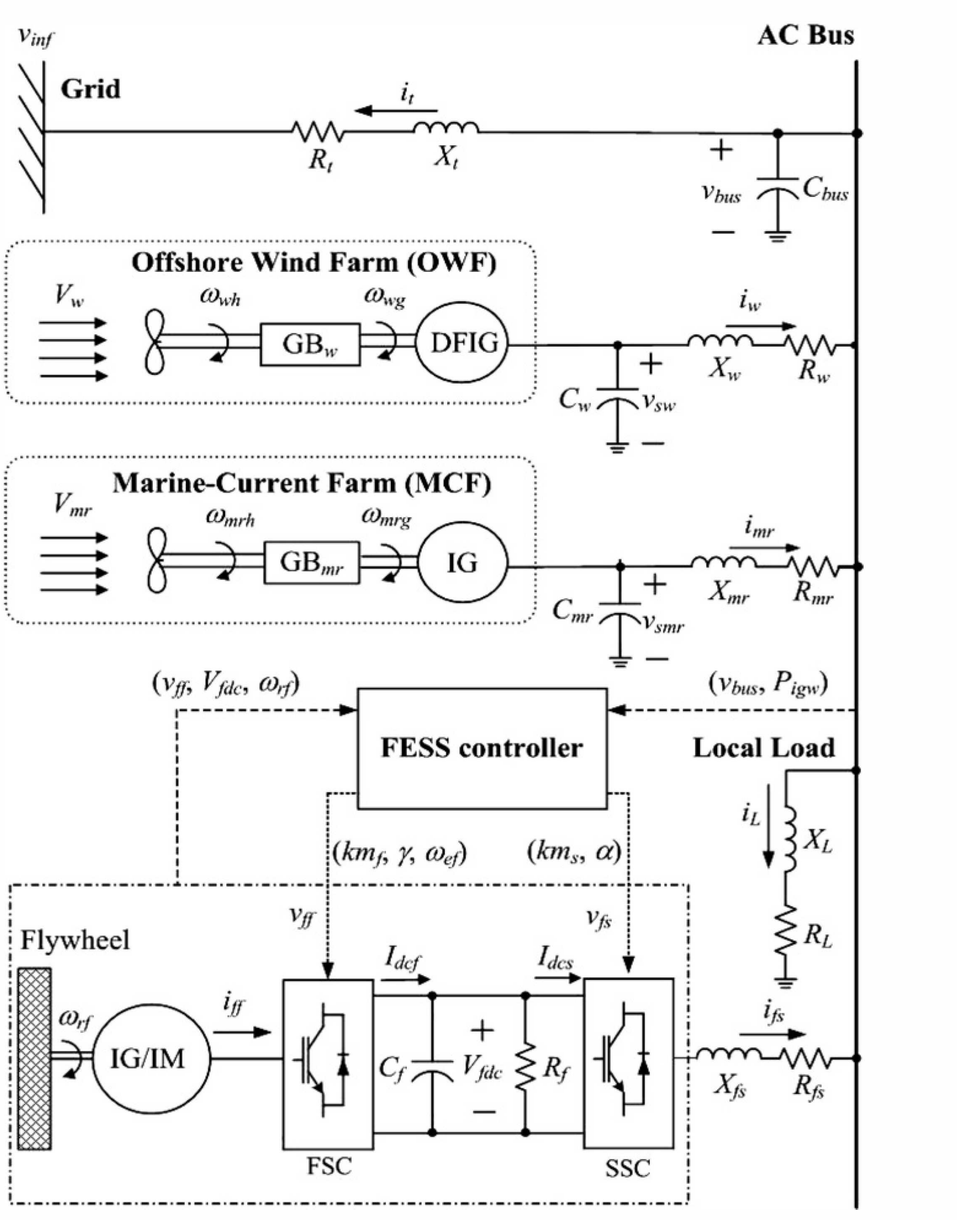

Figure 2.12 Offshore wind farm and tidal current farm with flywheel energy-storage system [61]**.**

In another research paper [62] authors use a DD PMSG tidal current turbine without pitch blades and smooth the power output using a modified maximum power point tracking (MPPT) controller and a super capacitor at the DC link (Figure 2.13a). The modified MPPT algorithm is used in order to compensate for the swell effect, created by the changing sea depth, which can cause vast tidal current speed variations. After designing and testing the modified MPPT authors designed a bi-directional DC/DC converter in order to connect a supercapacitor to the DC link. Power smoothing the swell effect requires a high power rating but not necessarily high energy density and this is the reason why a supercapacitor was chosen by the researchers. Based on simulation results, shown in Figure 2.13b, authors conclude that the use of the modified MPPT and a supercapacitor can effectively mitigate the power fluctuations caused by the swell effect.

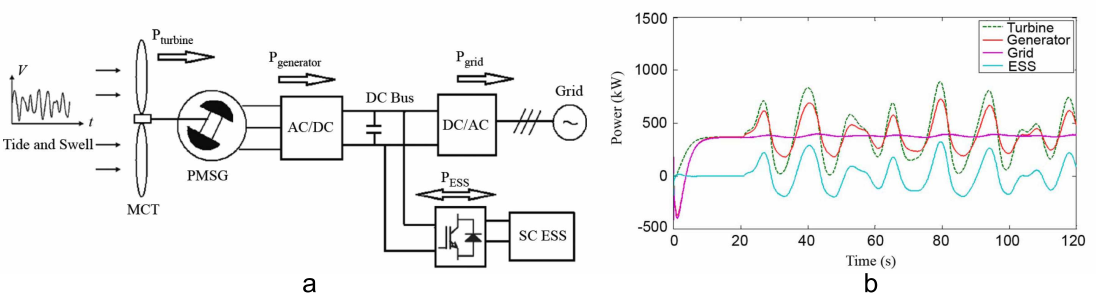

Figure 2.13 (a) Block diagram of the tidal current turbine with supercapacitor storage at the DC link. (b) Power results at different parts of the system with supercapacitor storage [62]**.**

Using the tidal current system shown in Figure 2.13 researchers in [63] proposed the use of a vanadium redox flow battery to manage the daily variations of the load and power generation. Researchers have also focused on the island power management using tidal current turbines and ocean compressed air energy storage in an isolated system [64], [65].

A review paper has also been published [66] regarding energy storage technologies for power smoothing in tidal current systems. Authors separate the phenomena that affect a tidal current system to long period and short period. Long period phenomena require high energy density storage systems with high power rating and discharge time. On the other hand, short-period disturbances require high capacity storage with small discharge time. The choice of the specific energy storage technology is shown in Figure 2.14a and was based on a diagram published in [67] for systems installed until November 2008. A more recent study regarding energy storage technologies is presented in Figure 2.14b and was produced by [68] after reviewing a large number of energy storage technologies and their relevant applications.

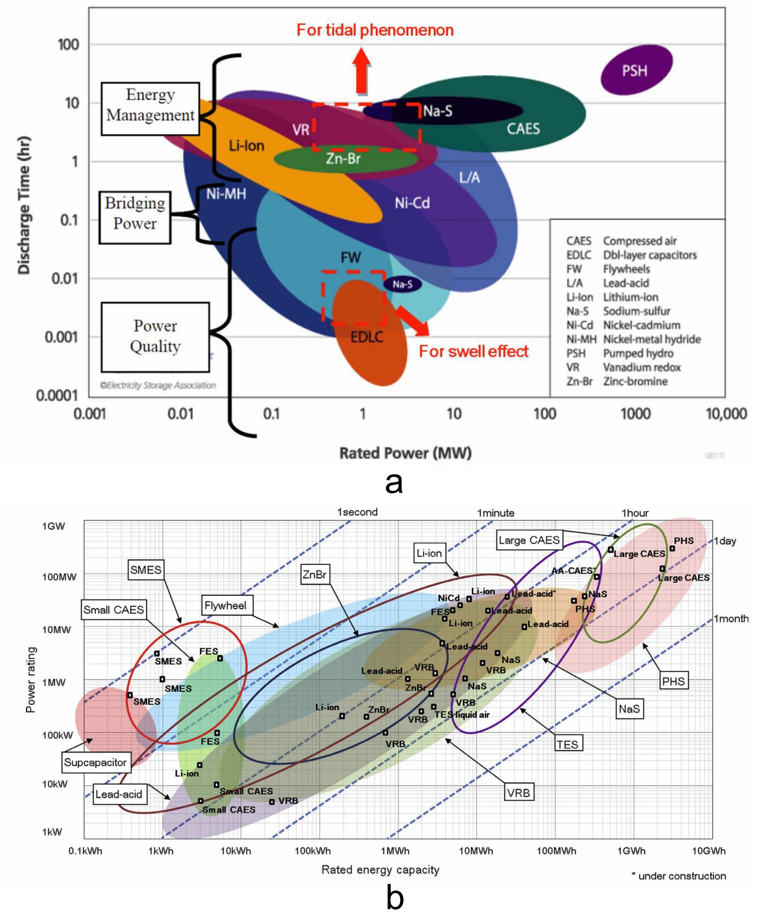

a

b

Figure 2.14 (a) Energy storage technologies as presented in [66]**. (b) An up-to-date energy storage technologies map as presented in** [68]**.**

Researchers in [69] analyse a number of energy storage technologies and their possible application in wind energy systems. Authors in their review paper present data of many characteristics of energy storage technologies including capital cost, energy efficiency and lifetime. Afterwards, authors separate energy storage technologies based on their response time to the different technical challenges associated with the integration and management of wind farms to the grid. Despite focusing on wind energy systems, the technical issues addressed in this review paper can be extended to tidal current energy systems as well.

Energy storage in renewable energy systems is a growing research area and as new storage technologies emerge and become more economically available they will help renewable energy developers export quality power to the weaker and isolated parts of the grid system. In addition, the development of energy storage technologies will help renewables to be integrated in hybrid or off-grid systems in the near future.

2.4 Reliability studies for tidal current turbines

Tidal current turbines are a less mature concept compared to wind turbines for extracting renewable energy and operating data is limited to the prototype devices being tested at present. Consequently, data on the reliability of these devices is not available and therefore reliability prediction can only be based on similar systems such as wind turbines, offshore oil, offshore gas and naval industry. It is already known that tidal current turbines use complex mechanical interfaces, electrical controls and mooring systems and operate under extreme conditions such as high tidal current speeds and wave loads. Using reliability prediction can be a useful tool to minimise the risk of installing tidal arrays and maximise the potential revenue. Two research studies [70], [71] have focused in detail on the reliability of tidal current turbines.

In [70] authors evaluate the reliability of a TCCS with a DFIG. The paper is focused on the failure rates of the power converters during the different operating modes of the DFIG generator. It is concluded that the failure rate of the generator side converter is higher compared to the grid side converter and that it is also highly dependent on the resource input. In addition, authors conclude that during super-synchronous operation, where the DFIG is operating at speeds higher than the synchronous speed with negative slip, the failure rates of the TCCS are much higher compared to the sub-synchronous operation, where the DFIG is operating at speeds lower than the synchronous speed with positive slip, and the idle position where the DFIG rotor is not operating. As it has already been discussed above, the DFIG technology is not a favourable option of tidal current developers despite the extensive use of this type of generator in the wind energy industry. The DFIG needs a gearbox and slip rings, which both require frequent maintenance and are prone to high failure rates. Frequent maintenance and high failure rates are both undesirable in a system with continuous underwater operation.

Researchers in [71] develop four generic reliability models of horizontal-axis TCCS with rated power between 1MW and 2MW. The reliability models are populated with historical reliability data from the wind energy industry, the offshore oil and gas industry and the naval industry. The block diagram of the reliability model created in [71] for a semi-submerged TCCS with tethered mooring can be seen in Figure 2.15.

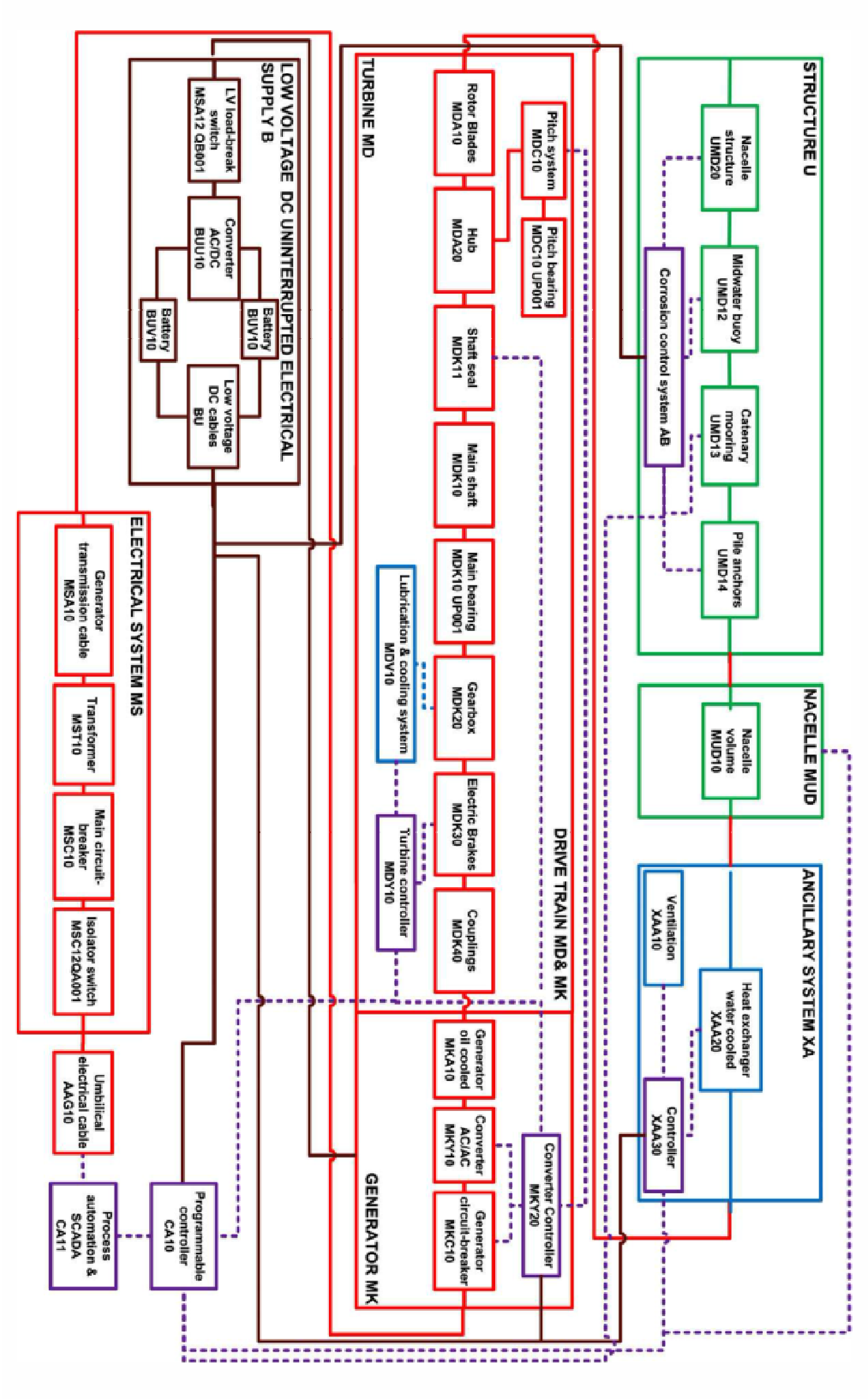

Figure 2.15 Block diagram of a semi-submerged TCCS with tethered mooring [71].

Authors in [71] concluded that a TCCS with seabed bottom-mounted mooring system and single-axis turbine has the lowest failure rates due to the simple technology used. Increasing complexity of a TCCS increases failure rates. As an overall observation authors estimated that the TCCS failure rates are 150% to 200% of the failure rates of a similarly rated wind turbine. Increased failure rates in TCCS is expected as the tidal current technology is at its infancy and authors suggested that the TCCS systems should be easily accessible in order to increase their reliability. The study discussed above has only included the option of having the power electronics in the nacelle and there was no distinction between generator technologies and the possibility to use the DD concept.

In this thesis, the option to use power converters onshore or on an offshore hub is presented which will increase accessibility and improve the operating conditions of the electrical system.

2.5 Electrical architecture studies in AC and DC

Despite the extensive literature regarding AC and DC electrical architectures for offshore wind farms, the research for tidal current arrays is limited. A general study that compares high voltage AC and DC transmission options (HVAC and HVDC) for offshore applications is presented in [72].

Researchers in [72] focus on high power far from land applications and present both technological and economical aspects of the designs. HVDC systems are favourable for applications at least 50km away from the land and have a long list of advantages. These include lower cables losses, lower cable costs and grid stability due to the instantaneous control of power transmitted which makes HVDC systems easier to connect at weaker parts of the grid. Authors separate the HVDC systems based on the two different electrical topologies that exist at the moment: HVDC with line commutated converter (LCC), shown in Figure 2.16a, and HVDC with voltage source converter (VSC), shown in Figure 2.16b. However, for tidal current arrays, which are planned to be installed near the shore, the HVDC option does not look very attractive whereas the HVAC option, with less capital cost and proven technology, is favoured by the developers for power transmission.

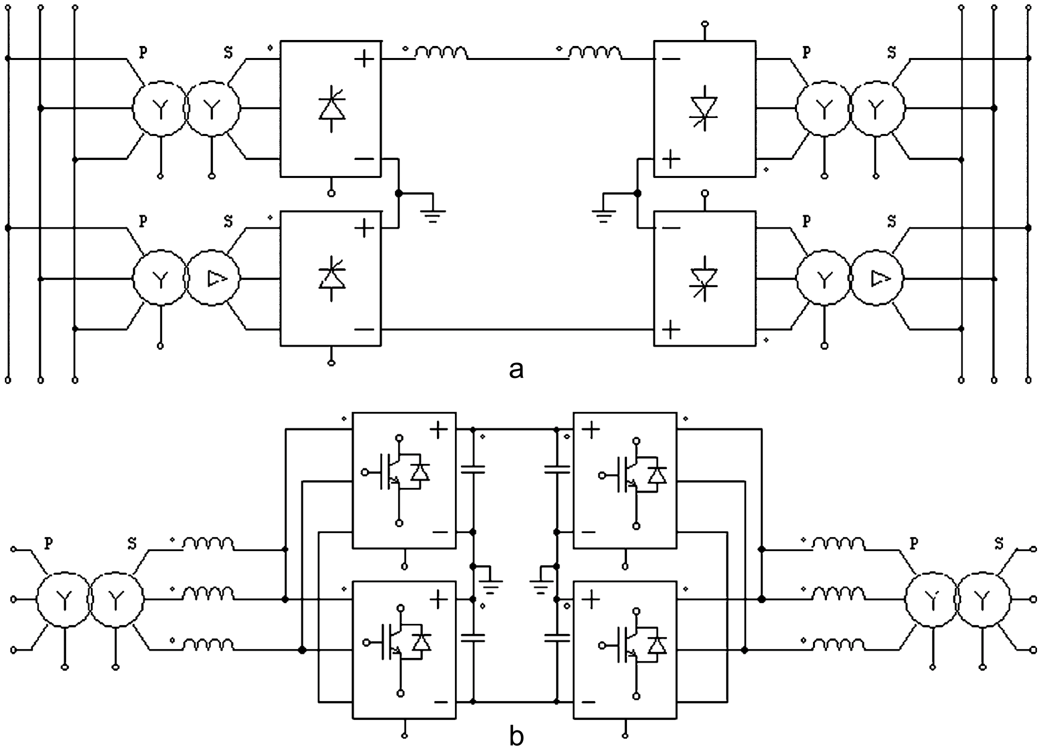

Figure 2.16 (a) Block diagram of a HVDC LCC transmission system. (b) Block diagram of a HVDC VSC transmission system [72]**.**

The previous research reviewed power transmission options; however the main concern for tidal current developers is the offshore collection and aggregation of power. Researchers from ABB presented in [73] a comparative study of different power collection options which were categorised based on the output from the nacelle to: variable frequency AC output (Figure 2.17a), fixed frequency AC output (Figure 2.17b) and DC output (Figure 2.18a). All the power collection options as presented in [73] were compared based on their cost for individual components, cost of installation and the cost for operation and maintenance for three different installed capacities of tidal current arrays, 30MW, 100MW and 200MW. Authors concluded that the collection topology with the least cost is DC-0 and collection topologies VF-0, VF-4, FF-2, DC-1 and DC-3 have comparable losses with DC-0. However, even though the above mentioned collection topologies have low cost when considered on their own, the costs change when studied in a 30MW tidal current array. For a tidal current array, collection topologies with low capital costs are preferred and therefore DC-1 and VF-4 are chosen as preferred options.

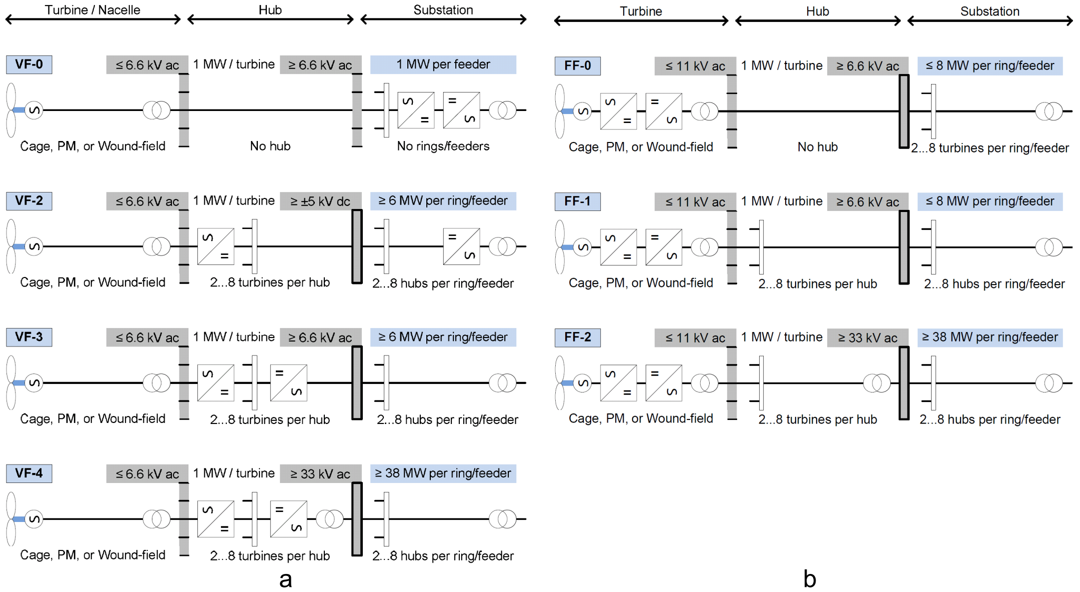

a b

Figure 2.17 (a) Variable frequency from the nacelle collection arrangements. (b) Fixed frequency from the nacelle arrangements [73].

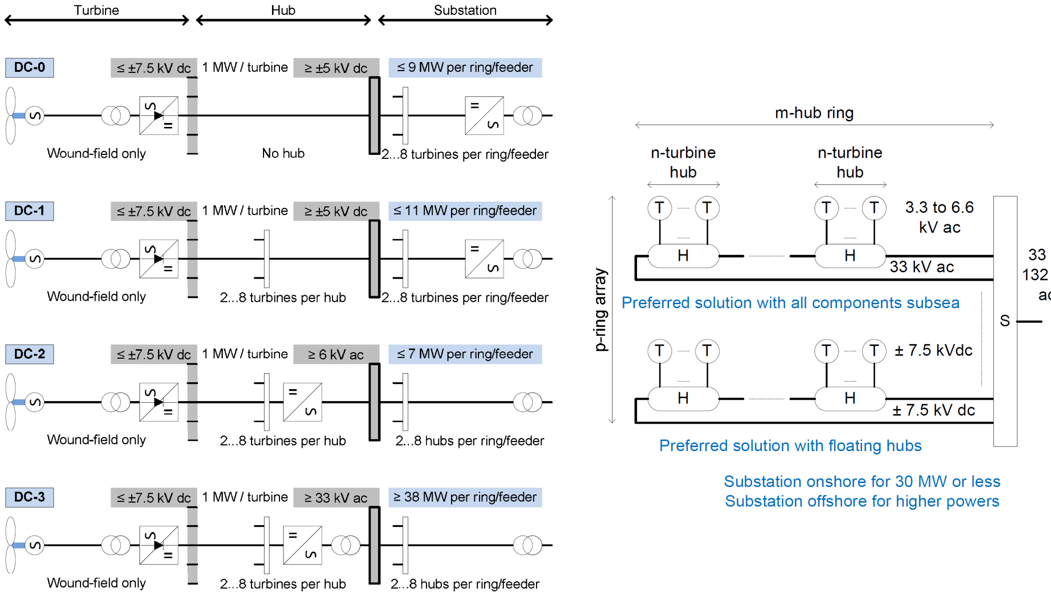

a b

Figure 2.18 (a) DC output from the nacelle arrangements. (b) Preferred power collection solutions for tidal current arrays [73].

Based on DC-1 and VF-4 researchers derived the preferred electrical architecture for tidal current arrays which is presented in Figure 2.18b. Therefore, for authors in [73] the star cluster topology with redundancy is preferred with power being aggregated in an AC 33kV cable or a ±7.5kV DC cable depending on the requirements of the application. In both cases, collection is achieved with cables from the generator to an offshore hub where multiple turbines are connected creating clusters. Authors based their results for the 30MW tidal current arrays and proposed that bigger arrays such as the 100MW and the 200MW arrays should be developed using smaller arrays and aggregating all the power in a substation before power transmission. The above mentioned research paper is a very good guide for estimating the cost of collection topologies that are available at present; however system efficiency is not included in the study. An increase in system efficiency can significantly increase revenue and payback time can be decreased despite initial capital costs. A core part of this thesis is the optimisation of the electrical architectures studied in order to achieve high generator-to-grid efficiencies.

Another research paper [74] focused on the optimisation of power transmission options for offshore marine energy systems based on cost of energy and the reactive power compensation. The paper states that in AC systems the capacitance of the sub-sea cables causes an amount of reactive current to flow, which limits the capacity for real power transmission. In order to mitigate the reactive current flowing in the cables reactive power compensation both onshore and offshore is required. Authors in [74] optimise the reactive power required so that maximum power transmission is achieved and at the same time meeting the UK Grid Code requirements.

Research studies on power transmission in either AC or DC for tidal current systems are limited and no conclusion of a preferred solution can be derived. In the section to follow three reports written by large electrical contractors are presented regarding the electrical infrastructure for tidal current arrays.

2.6 Industrial reports

In November 2013 publicly available reports regarding the electrical infrastructure for commercial scale tidal current arrays were published by three electrical contractors, ABB, GE and Siemens, for Scottish Enterprise [75]–[77]. The aim of these reports was to list and compare technically and economically viable electrical architectures for commercial scale tidal current arrays of 30MW, 100MW and 200MW. A number of requirements were set for these reports so that even though each company produced an individual report the results would be comparable in equivalent terms. These requirements were:

- Include in the designs all the sub-components that require electrical power such as the auxiliary supply, data communications, control systems and instrumentation devices.
- Include in the report mechanical considerations, operation difficulties, maintenance requirements, installation difficulties, retrieval requirements and environmental impact.
- Specific turbine characteristics were defined: 1MW designs with output voltage between 690V and 6600V 3Φ AC, 40kW auxiliary supplies and industry protocols for communications.
- Specific site characteristics: Water depth of up to 80m with flat bed rock, maximum surface tidal current speeds of up to 4.5m/s, 400m across flow and 800m parallel to flow spacing between turbines, up to 10km distance to shore and grid voltages of 33kV for the 30MW array and 132kV for the 100MW and 200MW tidal current arrays.
- Grid compliance for grid connection to shore.
- It was also specified that solutions should be deliverable in the near term, meaning that the technology proposed should be available. If any solution uses technology that it is still in the research phase it should be specified that it is a future option and not a current option.
- Surface piercing platforms were only costed for up to 40m water depth due to technological limitations.

In the following sub-sections, the report from each electrical contractor is explained and the conclusions derived from these reports are presented. The analysis performed in this thesis only focuses on the different ways of collecting, aggregating and transmitting power to shore and does not discuss mechanical aspects and specific components. A summary of the electrical architectures proposed by the electrical contractors is also presented in section 2.6.4.

2.6.1 ABB

ABB produced an extensive report of 121 pages and discusses all the components in a tidal current array [75]. In the beginning, the analysis starts by discussing the options of electrical components such as generators and power electronics topologies. Afterwards the analysis continues with communication systems, auxiliary supplies and safety compliance. In addition, the limitations of operating and installing electrical infrastructure underwater and offshore are discussed including cable installation, environmental impact, the operation of power electronics in the offshore environment, wet-mate connectors, dry-mate connectors and retrieval processes using large crane ships.

ABB distinguishes two options regarding generator and power converter technology that can be used in a tidal current system. *Alternative 1*, as stated in the report, is the preferred option and utilises DC transmission because of the following features:

- Uses conventional synchronous generator with parallel isolated double windings that allow constant voltage operation over a range of frequencies.
- Conventional uncontrolled diode rectifiers are used to convert the AC output of the generator to DC within the nacelle (Figure 2.19).
- With a 5.2kV double winding at the generator, ±7.5kV DC voltage can be achieved after the diode rectifiers, which can be inverted to 11kV 50Hz 3Φ AC voltage.
- The ±7.5kV DC voltage can be fed to a ring topology with a maximum capacity of 15MW (15 turbines of 1MW or 10 turbines of 1.5MW).
- The design is low cost and highly reliable due to the passive components, multiples of the passive components can be included for redundancy, and has reduced requirements for reactive power compensation.

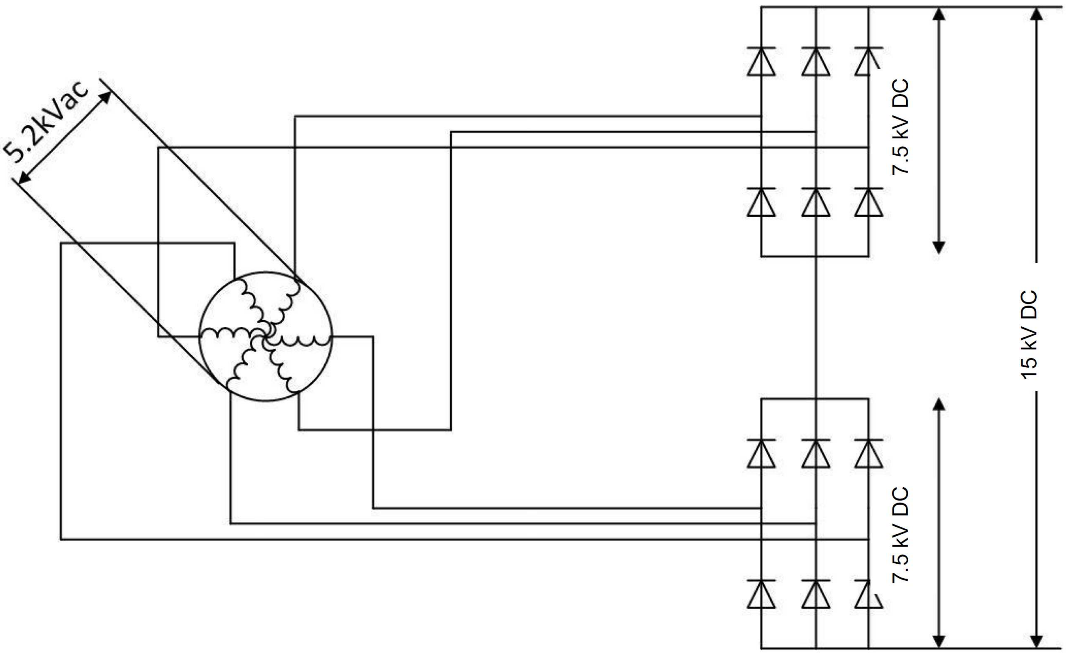

Figure 2.19 Double winding generator with double rectifiers. The proposed generator-converter topology for ABB [75]**.**

Alternative 2, as stated in the report, is based on AC transmission and has the following features:

- Uses SCIG or PMSG at 4.16kV AC 3Φ with operating frequency 0Hz to 60Hz.
- Fully rated BTB power electronics are considered to allow bi-directional power flow.
- Transformer is required to step-up the voltage to 33kV for power transmission or connection to a ring architecture.

Alternative 1 and Alternative 2 as presented in ABB report present the options for the generator and generator side converter. Another distinction in the ABB report is whether an offshore hub is used and if the offshore hub is submerged, floating or surface piercing. This distinction is important for the electrical architecture of the tidal array due to the fact that submerged hubs can only accommodate up to 4 turbines while floating and surface piercing hubs have the capability of connecting up to 16 turbines. The choice of offshore hub depends on many parameters such as environmental concerns, visual pollution, reliability concerns and cost.

Regarding the electrical architecture, the ABB report presents a generic electrical topology based on the two alternatives presented above. This generic topology can be seen in Figure 2.20 and as it can be observed for both cases, a ring topology is preferred with star cluster architecture.

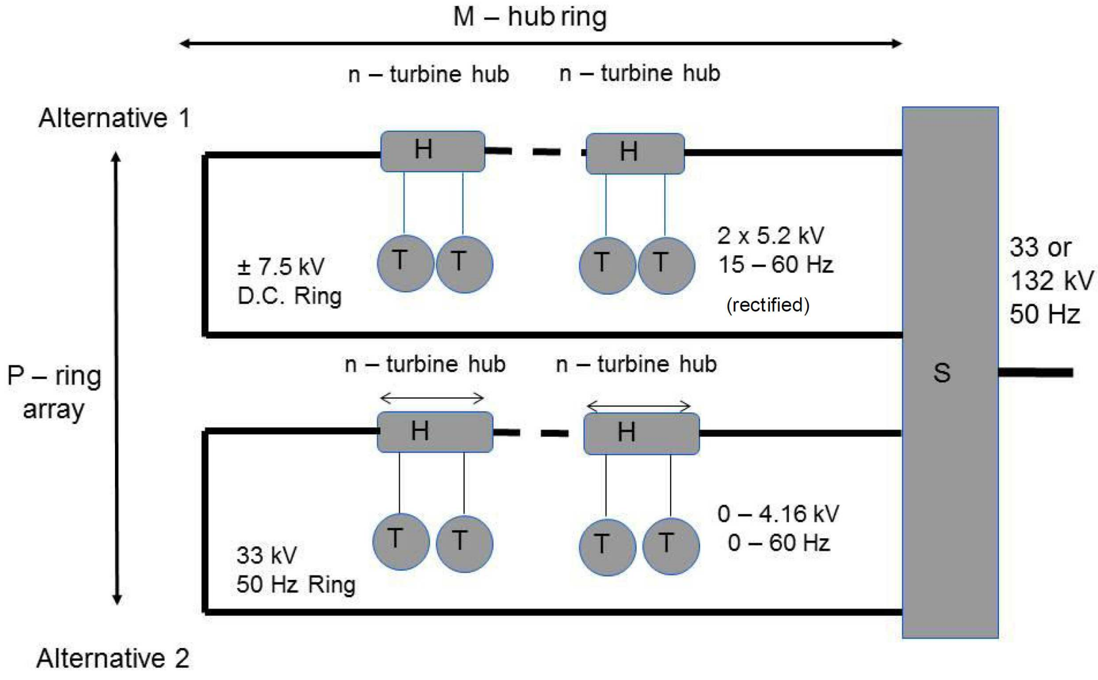

Figure 2.20 Generic ring electrical topologies for the two alternatives proposed by ABB [75]**.**

A number of turbines, *n*, are connected to an offshore hub. The number of turbines that can be connected to the offshore hub, *H*, depends whether it is fully submerged, floating or surface piercing as discussed above. The number of hubs in the ring, *M*, depends on the rated capacity of the cables that create the ring. In the case of *Alternative 1*, the rated capacity is up to 15MW whereas in *Alternative 2* the rated capacity of the ring can be 16MW with floating hubs or 30MW with surface piercing hubs. The number of rings, *P*, in a tidal array depends on the total installed capacity of the tidal array. It is also suggested that the ring topology should be connected to an offshore substation, which will collect power from all the rings and transmit power in HVAC. However, as it will be shown in the preferred ABB topologies the use of an offshore substation may not be required for the smaller scale arrays of 30MW which are close to the shore.

The above analysis describes the solutions that are preferred by ABB regarding the electrical infrastructure of tidal current arrays. However, given the specifics of a 30MW tidal current array, many different ways of connecting the turbines can be derived using the above mentioned preferred solutions. ABB researchers investigated 10 different ways using the generic theory described above and compared the options using estimated peak losses, energy produced per annum, revenue per annum and finally deriving the levelised cost of energy (LCOE). The chosen solution based on the analysis by ABB is given in Figure 2.21a and uses DC transmission whereas the solution that uses AC transmission and has the lowest possible LCOE is shown in Figure 2.21b.

According to the ABB report, the optimum solutions for both AC and DC transmission are achieved by using star cluster architecture with ring topology. In the optimum solutions, star clusters are created with floating hubs that collect and aggregate power from up to 4 turbines. In the case of DC transmission two rings are required due to the fact that the maximum capacity of each ring is up to 15MW. For the AC transmission option, one ring is required because the maximum rated capacity of the cable is 30MW. As it can be observed in both cases presented in Figure 2.21, there is no offshore substation. This is because the distance to shore is deemed close and the power rating of 30MW low to consider an offshore station to aggregate power from the rings and transmit power to the grid.

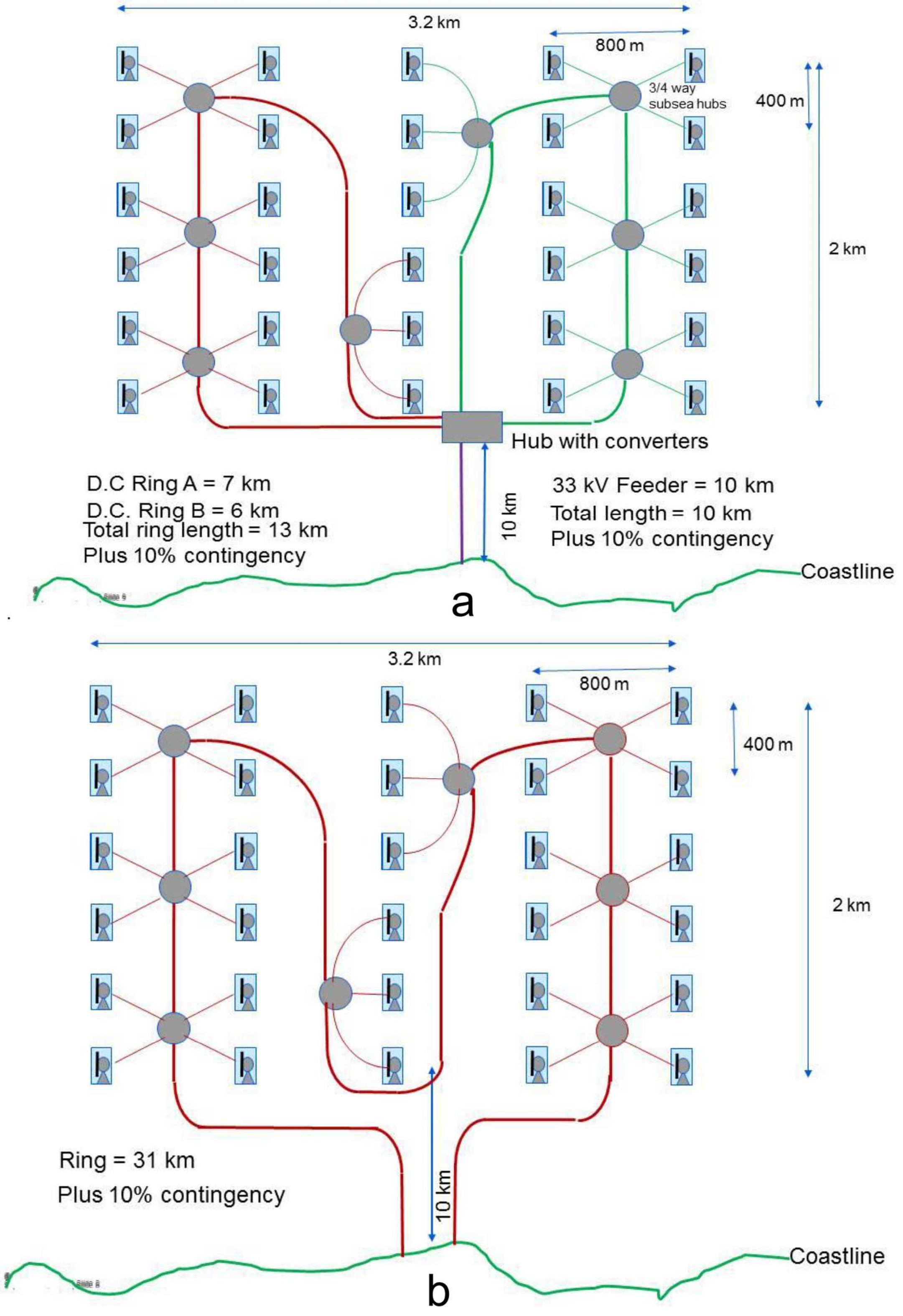

Figure 2.21 (a) ABB preferred solution using DC transmission with floating hubs that include power electronics, switchgear and transformers. (b) The optimum AC solution based on ABB report with floating hubs that include power electronics, switchgears and transformers [75]**.**

The final part of the ABB report discusses the expansion of the 30MW tidal current array to 100MW and then to 200MW. In order to achieve this using DC transmission, multiple 15MW rings, as presented in Figure 2.21a, are connected to an offshore substation. The offshore substation collects and aggregates power from all the DC rings in order to step-up the voltage and transmit power to shore using 132kV HVAC. The above process is similar for AC transmission with the only difference that fewer rings are required. The 200MW tidal current array can be created by developing two 100MW tidal current arrays as proposed by ABB.

2.6.2 Siemens

Siemens produced an 88 page report [76] that discusses in detail every single component in a tidal current array and a product from the Siemens range that can be used for this particular application at present. Special focus is given in the report regarding low voltage (LV) and medium voltage (MV) wet-mate connectors, cables and power converters for sub-sea applications. In addition, Siemens presents a list of all the British, international and other standards that have to be met during the design and installation of a tidal current array. According to the authors of [76] no optimum electrical architecture for tidal current arrays could be identified. Depending on the size of the array and limitations regarding the seabed and visual impact of the array, each solution proposed by Siemens has its advantages and disadvantages. The generic solutions that Siemens looked into can be categorised as:

- Tidal current turbines directly connected to a surface piercing platform with subsequent power transmission to shore.
- Submerged low voltage power converters near the turbine connected to an offshore collection hub.
- Tidal current turbines connected to offshore collection hubs and then to a surface piercing platform.

All the different designs proposed by Siemens are based on one of the three mentioned above. The proposed generic electrical topology for a tidal current array is shown in Figure 2.22. As it is observed, the electrical topology proposed by Siemens is a ring topology with star clusters. Star clusters are created by connecting up to 10 turbines to a single collection hub. The collection hubs are connected with each other using a single cable. Both ends of the cable end to a surface piercing platform or the shore depending on the application.

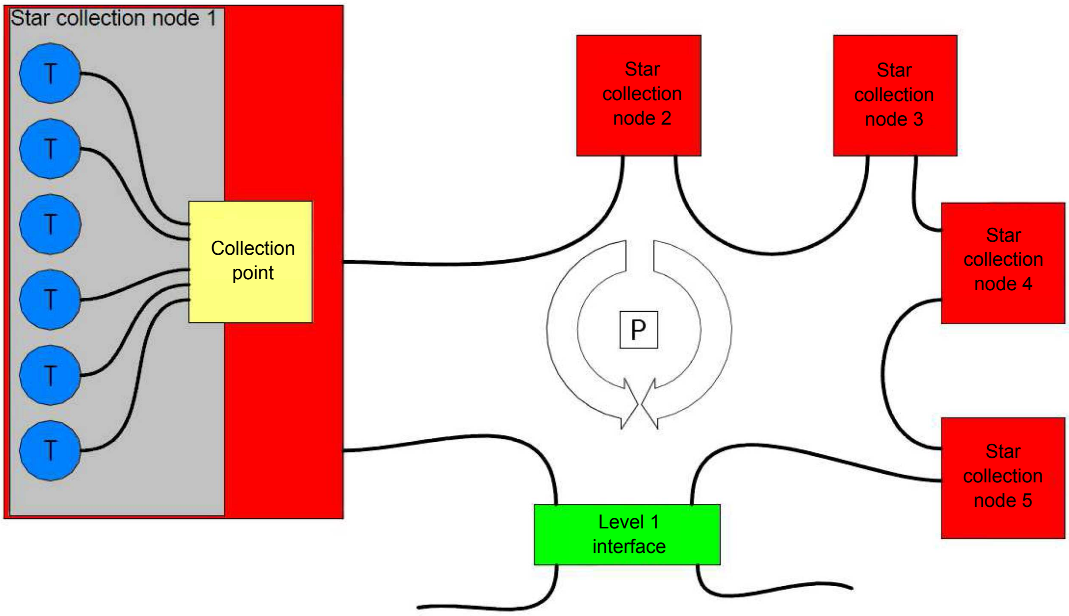

Figure 2.22 Generic electrical topology for tidal current arrays as proposed by Siemens [76]**.**

Based on the generic electrical topology shown in Figure 2.22 authors started exploring the different ways of collecting the power from each individual turbine in order to create the star clusters. Two different ways are proposed by Siemens to collect power from the turbines:

- Low voltage power electronics (690V) installed in the nacelle or close to the turbines and a step-up transformer to 8.6kV to transmit power to the collection point.
- Medium voltage power electronics (3.3kV, 4.15kV or 6.6kV) in the nacelle or close to the turbine and direct transmission to the collection point.

Using medium voltage power electronics has two major limitations. Firstly, Siemens's medium voltage power electronics are rated for above 3MW applications whereas tidal current turbines are rated up to 1.5MW. This raises the already increased cost of the TCCS. Secondly medium voltage power electronics require significant space which is limited in the nacelle. For the above reasons Siemens proposes low voltage power electronics in the nacelle or the close to the turbine. It is known that not all the tidal current turbines have enough space to house power converters, transformers and the necessary electrical equipment in the nacelle. For this reason, Siemens proposes a subsea power converter chamber that will be installed very close to the nacelle of the tidal current turbine and will include all the necessary electrical equipment. This subsea converter chamber is shown in Figure 2.23.

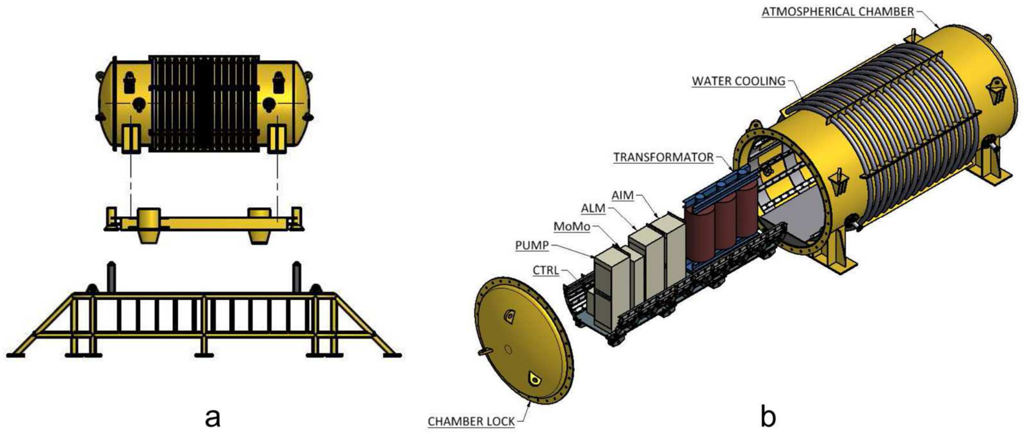

Figure 2.23 (a) Subsea power converter chamber and its foundations. (b) The electrical equipment enclosed in the subsea power converter chamber [76]**.**

As shown in Figure 2.23b the electrical equipment included is:

- A motor module (MoMo) which acts as rectifier.
- DC link.
- An active line module (ALM) which acts as inverter.
- An active interface module (AIM) which includes the filters.
- The transformer to step-up the voltage to 8.6kV.
- All the necessary equipment to keep the conditions of the above mentioned modules within the operating limits.

Apart from the description of the subsea power converter chamber a lot of discussion takes place in the Siemens report regarding the cost and possible cost reductions for this chamber which is estimated in the range of 2.5 to 2.8 million pounds.

After the subsea power converter station in order to collect and aggregate power in star clusters a collection hub is required. The main components for the proposed collection hub by Siemens are:

- Switchgears and circuit breakers to protect and isolate the connections and the equipment in case of faults and unpredicted behaviour.
- A step-up transformer from 8.6kV to 30kV to match the voltage of the ring.
- Wet mate connectors to connect the collection hub to the turbine and the collection hub to the 30kV ring.

A 10MVA collection hub has been designed by Siemens and the schematics are shown in Figure 2.24. For large arrays, larger collection hubs of 20MVA and 30MVA capacity will also be considered.

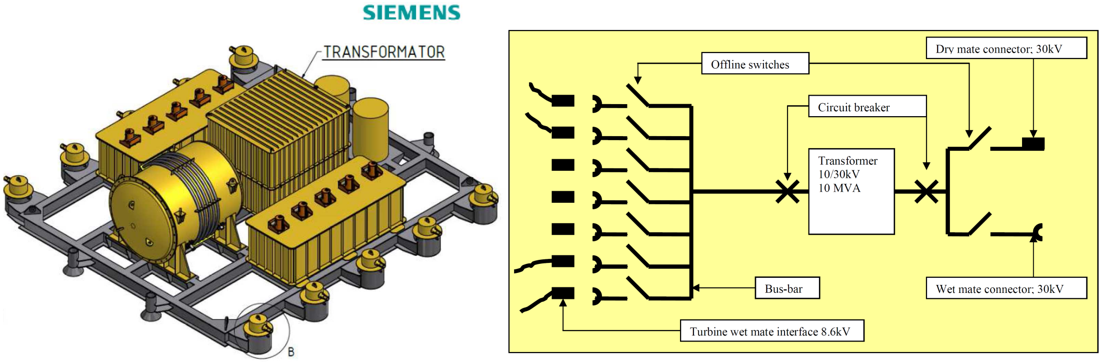

a b

Figure 2.24 (a) Artist impression of the 10MVA collection hub. (b) Schematic diagram of the collection hub [76]**.**

The final part for the design of a tidal current array is the surface piercing platform. In the Siemens report great detail is given regarding the size, the components and the cost of surface piercing platforms for the 30MW, 100MW and the 200MW tidal current array.

In the final part of the report different variations are discussed and compared based on the LCOE. The variations are based on multiples of the collection hubs discussed above. Depending on the size of the tidal current array and the rated power of the collection hubs different variations can be created. A separate variation is the use of medium voltage converters on the surface piercing platforms directly. A summary of the variations and the calculated LCOE for each variation is presented in Table 2.2.

Table 2.2 Summary of the Siemens options for a tidal current array [76]**.**

System	Rated capacity	Power converter module	LCOE
SUBSEA1	10MVA	LV subsea chamber	£150/MWh
SUBSEA2	20MVA	LV subsea chamber	£117/MWh
SUBSEA3	30MVA	LV subsea chamber	£110/MWh
SURFACE1	32MW	MV on surface piercing platform	£78/MWh
HYBRID1	5*SUBSEA2	LV subsea chamber	£133/MWh
HYBRID2	10*SUBSEA2	LV subsea chamber	£130/MWh
HYBRID3	7*SUBSEA3	LV subsea chamber	£120/MWh

As it can be seen from the above table, the least LCOE is achieved with the SURFACE1 option due to the reduced number of components required. However, the study team of Siemens suggests that the options that use a LV subsea chamber should be considered for demonstration arrays.

2.6.3 General Electric

General Electric produced a more focused report of 41 pages [77]. The main points of discussion in the General Electric report are the electrical topology of the tidal arrays, the zero sequence currents in tidal current systems, the auxiliary power for tidal current turbines and a comparative analysis between the proposed options. General Electric separates the electrical topologies for tidal current arrays to four categories:

- *Base case*, also stated as *Option A*, in which each tidal current turbine is connected to shore with individual cables. Power converters are placed onshore close to the grid connection (Figure 2.25). This case is similar to the direct connection case presented in section 1.2.3.
- *Embedded converters* in which power converters are installed in the nacelle and an AC ring at 33kV is created (Figure 2.26 and Figure 2.27).
- *Offshore AC collector* in which an offshore hub is used to collect and aggregate power from nine tidal current turbines and a HVAC ring is created by

connecting the offshore hubs (Figure 2.28). This is similar to a star cluster electrical architecture as presented in section 1.2.3.

- *Offshore DC collector* which is similar to *Offshore AC collector* but the generator side of the power converters is offshore and the grid side of the power converters is onshore or in a surface piercing platform depending on the size of the tidal current array (Figure 2.29).

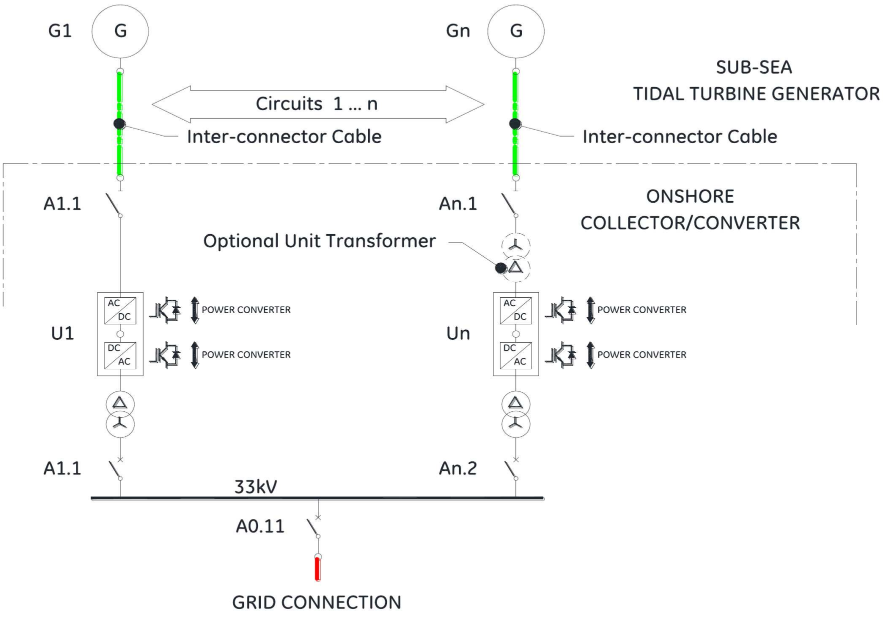

Figure 2.25 Option A of tidal current array electrical architecture as presented in [77]**.**

By locating the power electronics in the nacelle two different configurations can be achieved. The first, *Option B*, shown in Figure 2.26 has individual connections for each turbine and is similar to a radial ring electrical architecture. The second, *Option X*, connects clusters of four turbines to an offshore hub; these hubs are connected in radial ring architecture as shown in Figure 2.27.

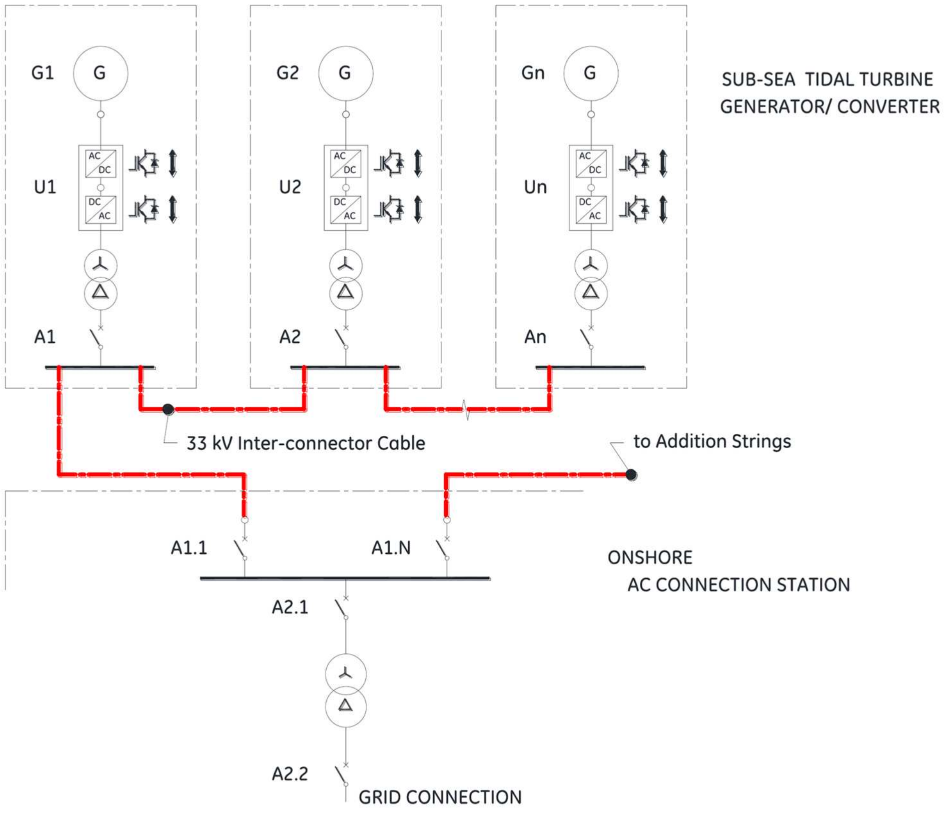

Figure 2.26 Option B with power converters in the nacelle and HVAC ring connection.

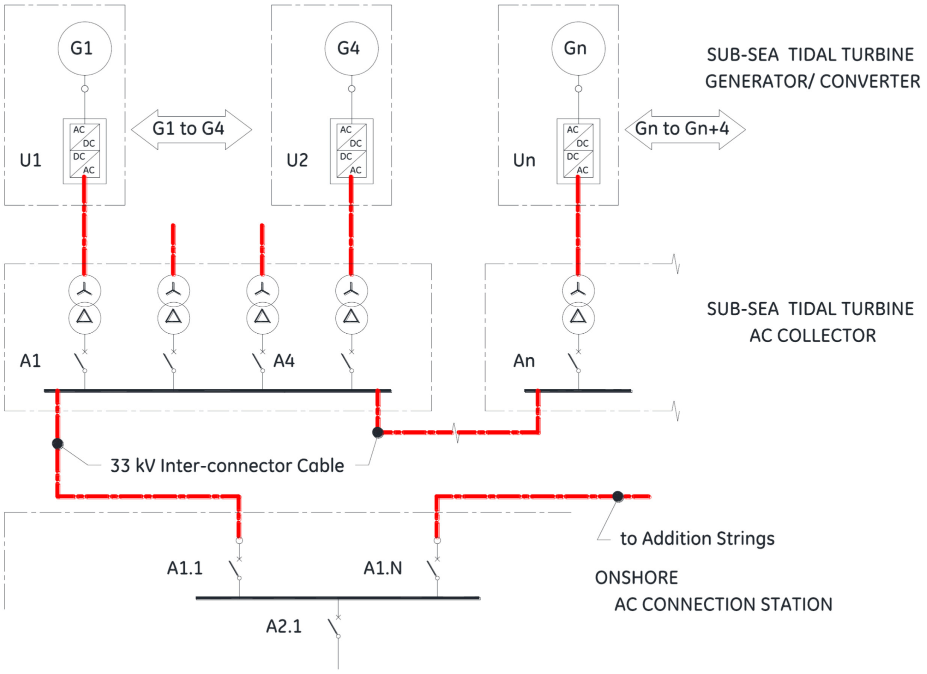

Figure 2.27 Option X with power electronics in the nacelle, aggregation in a subsea hub per four turbines and ring connection of the subsea hubs in HVAC [77]**.**

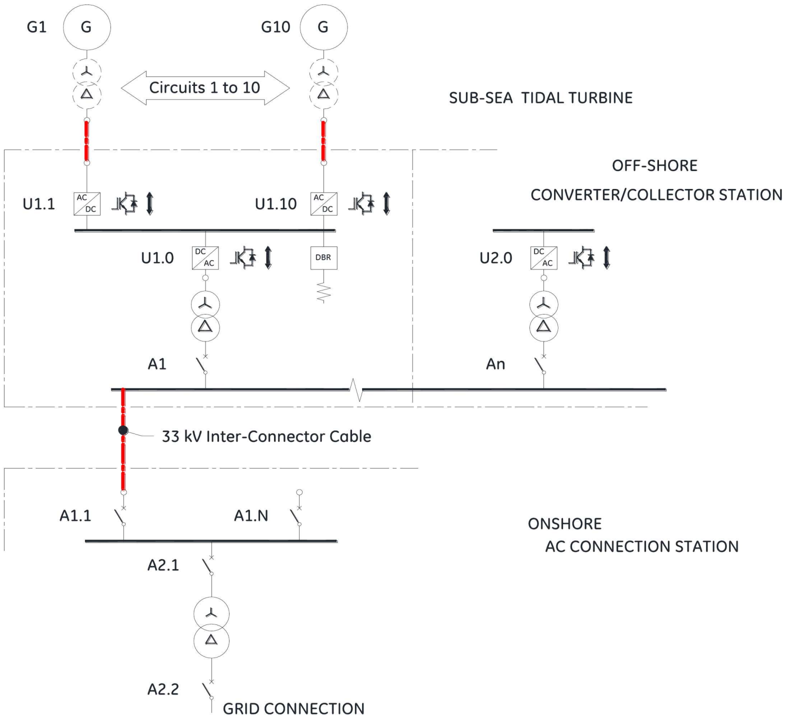

Figure 2.28 Option C with AC offshore collector and HVAC power transmission in star clusters [77]**.**

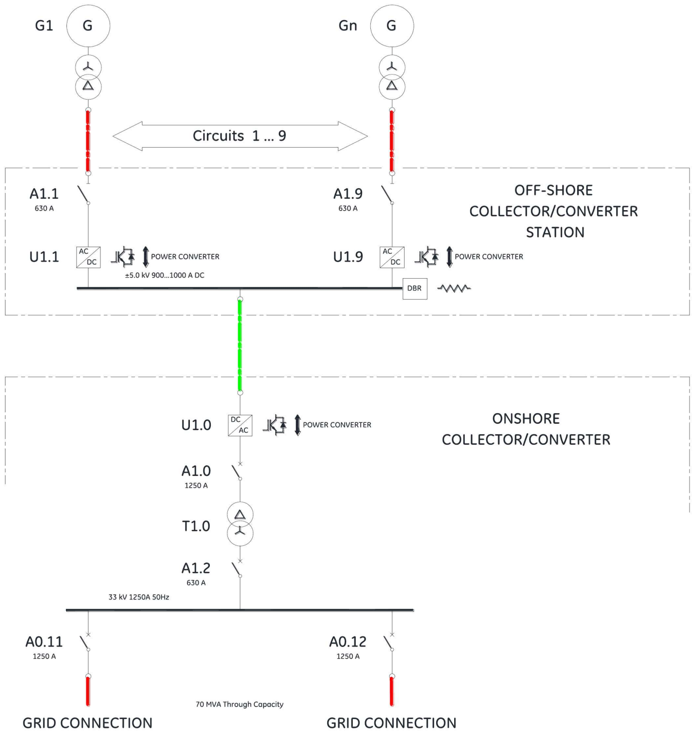

Figure 2.29 Option D with offshore DC collection and power transmission in star clusters [77]**.**

General Electric research team compares all the above mentioned electrical configuration based on capital costs, operational costs, LCOE, availability and reliability. A summary of the data as presented in [77] are given in Table 2.3.

Table 2.3 Summarised relative LCOE, relative system downtime and availability for the electrical architectures presented in [77]**.**

Options	Relative LCOE	Relative system downtime	Availability (%)
Option A	100	100	99
Option B (subsea)	40	569	95
Option X (subsea)	41		
Option C (surface)	27	472	96
Option C (subsea)	39		
Option D (surface)	34	296	97
Option D (subsea)	33		

LCOE and system downtime are calculated on a relative basis, using *Option A* as the base case scenario, where both categories are given a value of 100. Surface option means that a surface piercing platform is considered and costed whereas the subsea options means that a subsea hub is considered. As it can be observed from Table 2.3 *Option C* (surface) has the least LCOE. However, downtime is considerable when compared with *Option D*. Based on the above, authors of [77] prefer the *Option D* with either a surface piercing platform or subsea hub for the optimised tidal current array electrical architecture.

The final part of the General Electric report discusses the suitable configuration for the 30MW, 100MW and 200MW tidal current array.

- For the 30MW tidal current array authors suggest that, using today’s technology, the best option would be *Option D* with surface piercing platform provided that the water depth is less than 40m. For power transmission and grid connection they suggest that two DC cables are enough for the 30MW tidal current array.

- For the 100MW tidal current array authors suggest that three multiples of the 30MW array can be considered. Alternatively, *Option C* can be used depending on the tidal current array location and distance to shore.
- For the 200MW tidal current array it is suggested that two multiples of the 100MW array can be considered either based on *Option D* or *Option C*.

2.6.4 Summarised results from industrial reports

Summarising the industrial reports is a difficult task since each electrical company uses and presents its own technology. In addition, cost calculations are either relative or based on different assumptions and therefore it is difficult to derive a specific list with the cheapest options across all the reports. In [78] authors tried to summarise and compare the results from the industrial reports presenting comparison tables of the components, assumptions and electrical configurations discussed in each report. A summary table was also presented showing the relative costs and the common designs in each industrial report. An adapted version of the comparison table presented in [78] is given in Table 2.4.

Table 2.4 Summary of electrical concepts from the industrial reports [78].

Aggregation	**Electrical concept**	**Industrial Reports**		
		ABB	**Siemens**	**GE**
No aggregation	No power conversion at TCCS Separate cable for each TCCS Dry power converters	12.1.8	SURFACE1	Option A
Daisy-chain	DC conversion in the nacelle Parallel connection of TCCS on MVDC strings or loops	12.1.1		
	BTB converters in the nacelle and AC connection at 11kV or 33kV loops or strings.	12.2.2	SUBSEA 2&3	Option B
Star cluster architecture with hubs on rings	BTB converters in the nacelle TCCS connected to local hub Hubs on AC rings at 33kV	12.1.4	SUBSEA1 HYBRID1	Option X
	No power conversion at TCCS TCCS connected to local hub Hubs on AC rings at 33kV	12.1.5		Option C
	No power conversion at TCCS TCCS connected to local hub Hubs on MVDC rings			Option D
	DC conversion in the nacelle TCCS connected to local hub Hubs on MVDC rings	12.1.2 12.2.1		

The colours in Table 2.4 define the relative LCOE as presented in each report separately. Green defines lowest LCOE, orange defines a medium LCOE and dark red defines high LCOE.

2.7 Tidal current systems with long distance controls

In the above sections, many of different ways to collect, aggregate and transmit power from a tidal current array have been discussed. A viable option in many cases is the installation of the power electronics onshore or on an offshore hub away from the generator of the tidal current turbine. Based on the industrial reports analysed in Section 2.6 a lot of options did not have power conversion in the nacelle of the tidal current turbine and some of these options are with the lowest LCOE such as *Siemens SURFACE1* and *General Electric Option C*.

Depending on the complete electrical architecture, the distance between the generator and the power electronics can vary from a few hundred metres to many kilometres. In the case of direct connection to shore with power electronics installed onshore the distance can be up to 15km depending on the site. In the case of a star cluster architecture, where the tidal current turbines are connected to offshore hubs, the distance between the tidal current turbine and the offshore hub can vary from a few hundred metres to 1km. Controlling a generator from afar requires long distance controls and appropriate analysis of the system so that excessive harmonics, resonance and overvoltages can be mitigated. Excessive harmonics flowing in the cables can cause high power losses in the cables and at the same time cable resonance and overvoltages from the electromagnetic travelling waves can cause faults due to insulation breakdown from voltage spikes. Research literature regarding the mitigation of these effects is significant due to the fact that controlling motors from afar has been used in the offshore oil & gas industry at least 25 years now.

The majority of the research literature studies different types of passive filters in order to mitigate overvoltages from the electromagnetic travelling waves or to suppress resonance from the interaction of the cable parameters with the transformer parameters. In [79] three different types of filters installed at the terminals of an induction motor are designed and compared. Authors in [79] identify two major problems when a machine is controlled through long cables:

- *Damped high frequency ringing* at the machine terminals due to the distributed nature of the cable parameters. The ringing causes overvoltages which can lead to a fault in the motor terminal due to insulation breakdown. Damped high frequency ringing is also referred to as *resonance* in other research papers.
- *Voltage reflection* at the machine terminals. According to the results from [79] authors concluded that if the voltage pulse takes longer than 1/3 of the rise time

> to travel from the converter to the machine then a full reflection will take place and the voltage at the machine terminals will approximately double, thus causing insulation breakdown.

Authors in [79] designed, based on the literature, and proposed a new filter to mitigate the above mentioned effects. However, the use of these filters in a tidal current device is unlikely due to the need to be placed in the nacelle. The space in the nacelle of a tidal current device is limited. Some developers do not have the space to house power electronics or transformers in the nacelle. The same can be said about the use of filters in the nacelle of a tidal current device.

In [80], [81] authors develop and design passive filters at the output of the power converter in order to mitigate the above mentioned effects. For this purpose, a second-order filter is designed that effectively mitigates these effects. Figure 2.30a shows the filter as depicted in [80] and Figure 2.30b shows the filter as shown in [81].

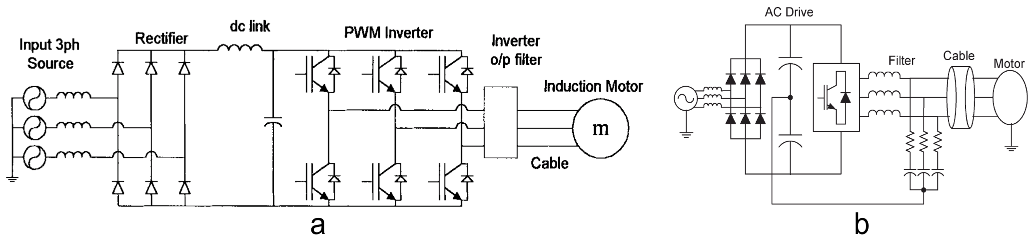

Figure 2.30 (a) Second-order filter at the converter output as presented in [80]**. (b) Second-order filter at the converter output as presented in** [81]**.**

In [82] a passive filter at the machine terminals and the second-order filter at the converter output are compared and tested in a system with a low power induction motor. The passive filter uses a resistor and a capacitor, *RC*, connected in parallel with the machine. The second-order filter is the same as the one proposed in the previous papers, [80], [81], and was defined as *RLC*. Authors compare the two filters based on losses, effectiveness with different cable parameters, DC link current induced and changes in the responsiveness of the controller. Based on the results, it was concluded that *RLC* filter losses increase and voltage regulation achieved is decreased with increasing cable length. However, the *RLC* filter mitigates high-order harmonics more effectively than the *RC* filter and induces less DC current in the DC link. Regarding the controller, using the filters did not seem to have any effect on the response of the controller. A change in overvoltage due to cable parameters changes was also explored. The worst-case scenario is if the cable inductance is reduced and capacitance is increased. In [82] a 50% increase in cable capacitance and a 50% decrease of cable inductance was explored but the results showed that the overvoltage values did not significantly change.

Another comparative study [83] of filters used in long distance controls designed and compared three passive filters at the machine terminals and two filters at the inverter output for a TCCS with a SCIG. Authors proposed a new methodology to calculate the filter parameters in each case by minimising losses they produce and compared their proposed methodology with filters designed using the methodologies available in literature. They concluded that both low losses and effective mitigation of the voltage reflections and resonance can be achieved with proper design of filter parameters. For the filter design process in this thesis, the proposed methodology described in [83] will be extensively used.

Authors in [83] and [84] focus on mitigating the resonance effect. This is due to the fact that in both cases a transformer is placed between the cables and the converter in order to match the transmission voltage to the operating voltage of the converter. The transformer inductance resonates with the distributed cable capacitance creating resonant peaks at lower frequencies which can be destructive for the operation of the system if not mitigated properly. Figure 2.31a shows a generic TCCS with long distance controls and the transformer-cable system while Figure 2.31b shows the effect of connecting long transmission cables to a transformer regarding the resonant frequencies.

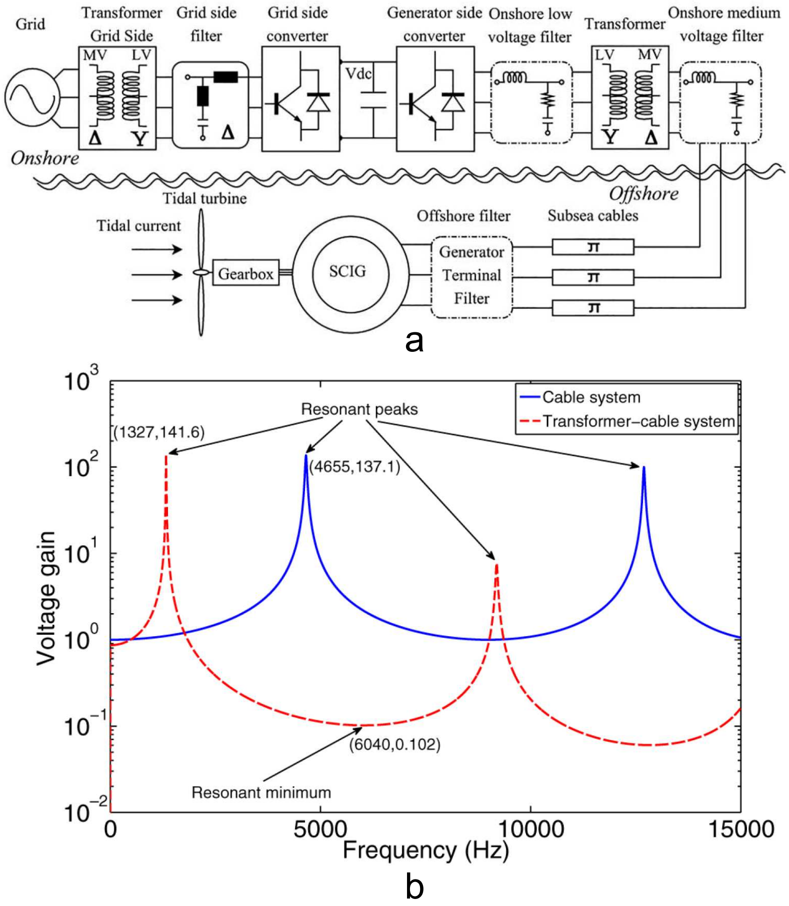

Figure 2.31 (a) Generic block diagram of a TCCS using long distance controls. (b) Example of the resonance in a cable and cable-transformer system [83]**.**

Another research [85] focuses on the effect of *voltage reflections* in a low power tidal current system that uses PMSG and long distance controls. The study states that a low power tidal current system can be used in river systems if the effect of voltage reflection is mitigated using a second-order filter at the output of the converter similar to [80]–[82]. The research describes in great detail the phenomenon behind the reflection of voltage waves in a transmission line and how the relationship of pulse rise time, t_r, and travelling time, t_t, can cause insulation damage at the machine terminals. Figure 2.32 shows in detail the travelling of a voltage pulse from the converter to the terminals of the generator when the pulse rise time is equal to half the travelling time, $t_r = 0.5t_t$.

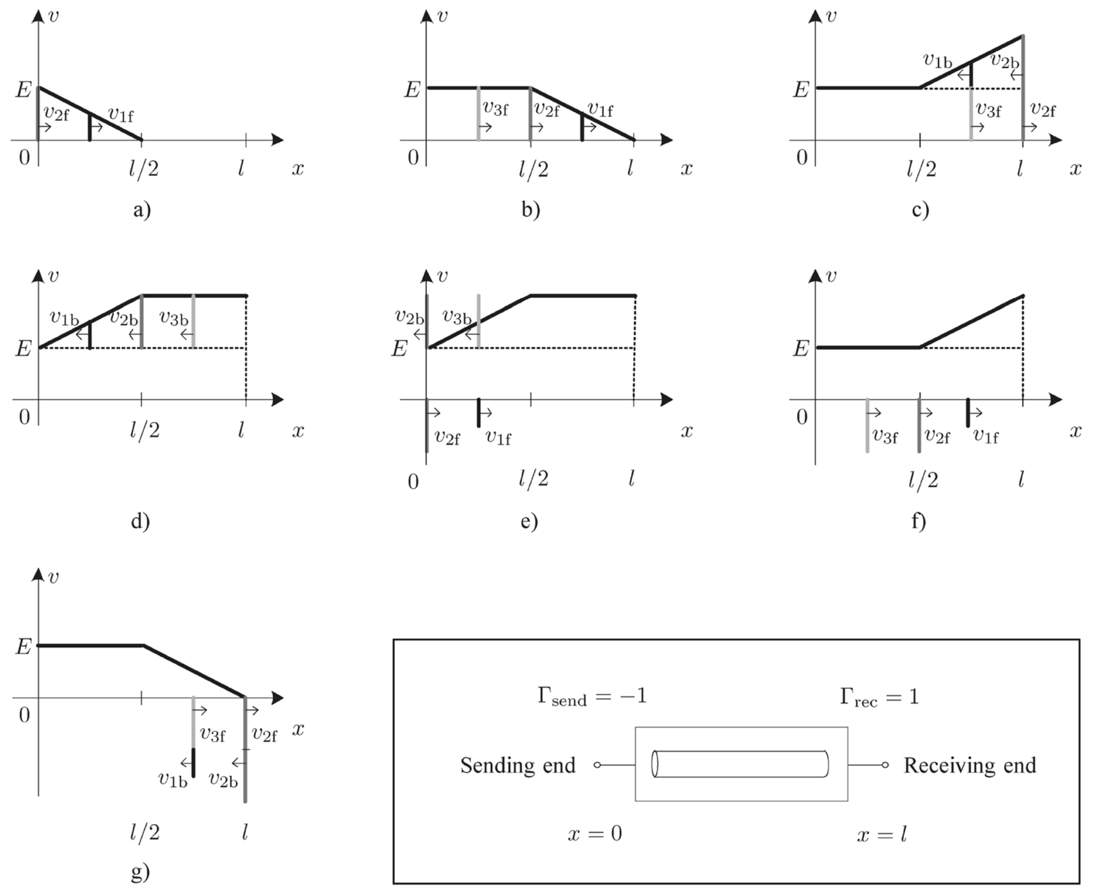

Figure 2.32 Voltage reflection analysis at different timings as presented in [85]**. a) Voltage wave at time 0.5t_t. b) Voltage wave at time 1.0t_t. c) Voltage wave at time 1.5t_t. d) Voltage wave at time 2.0t_t. e) Voltage wave at time 2.5t_t. f) Voltage wave at time 3.0t_t. g) Voltage wave at time 3.5t_t.**

As it can be observed in Figure 2.32c, based on the theory, if the voltage pulse rise time is half the travelling time of the voltage wave in the cables then the voltage at the machine terminals can be approximately doubled, causing irreparable insulation damage and possibly a fault at the machine terminals. Knowing the pulse rise time, the engineer designing the system with long distance controls can calculate the maximum cable length in order to avoid full reflection at the machine terminals. Apart from the design considerations, analytical mathematical expressions can be used to calculate the inductance, resistance and capacitance of a second-order low-pass filter (*LCR*) to be installed at the output of the converter terminals and mitigate the effect of *voltage reflection* [85].

2.8 Summary

In this Chapter, the electrical infrastructure for tidal current arrays was reviewed based on both academic papers and industrial reports. The review focused on the control, power conversions and power transmission for single and arrays of tidal current turbines. Mechanical considerations in the drivetrain of the tidal current device, the potential benefits of using energy storage technologies in tidal current arrays and reliability of a tidal current system were also explored. An extensive review of the industrial reports of ABB, GE and Siemens regarding the power conversion and transmission options for tidal current arrays was undertaken. Even though the industrial reports do not conclude in a specific design, because each electrical company promotes its own technology, the possible configurations of the future tidal current arrays can be distinguished. In the final part of this Chapter particular focus was given in tidal current systems where the power electronics are not in the nacelle. In these systems the electrical generator is controlled from afar through long cables and the power electronics are installed onshore. This is an attractive power transmission concept for tidal current developers who do now want to operate the power electronics underwater due to reliability concerns. However, as it reviewed in this Chapter voltage reflections and resonance are some of the issues that need be addressed in a system that uses long distance controls. In Chapter 4, a thorough study is undertaken in a single tidal current device that uses long distance controls in order to mitigate voltage reflections and resonance.

Chapter 3

Modelling of a single tidal current device

In this chapter all the modelling aspects of a TCCS will be described in detail. The generic resource-to-wire model used in this section is based on the long distance controls concept as described in Section 2.7. The main reason for using a TCCS with long distance controls as a reference model is due to the fact that it is the preferred electrical topology for the prototype and demonstration projects of AHH. In addition, parameters and modelling aspects of the generic resource-to-wire model are based on industrial input from AHH. A secondary reason is that this type of electrical topology includes all the specific components required to be analysed in this thesis. A block diagram of the generic resource-to-wire model can be seen in Figure 3.1. The tidal resource is used as an input to the tidal turbine. Power input from the tidal flow is curtailed using a pitch controller. The tidal turbine shaft is connected to the generator rotor through a gearbox; the modelling of both the SCIG and PMSG is presented in this chapter. The output of the generator is transmitted to shore via long three-phase subsea cables. In order to reduce transmission losses medium voltage generators are preferred for this application. The medium voltage is converted to low voltage using an onshore step-down transformer. Between the generator side voltage source converter (VSC) and the step-down transformer, filters are installed with the aim of mitigating the overvoltage effects described in Section 2.7. In order to enable variable speed operation of the generator, the generator side VSC is controlled by the generator side controller. On the grid side, the low voltage output of the grid side VSC is first filtered and then a step-up transformer is used for grid connection.

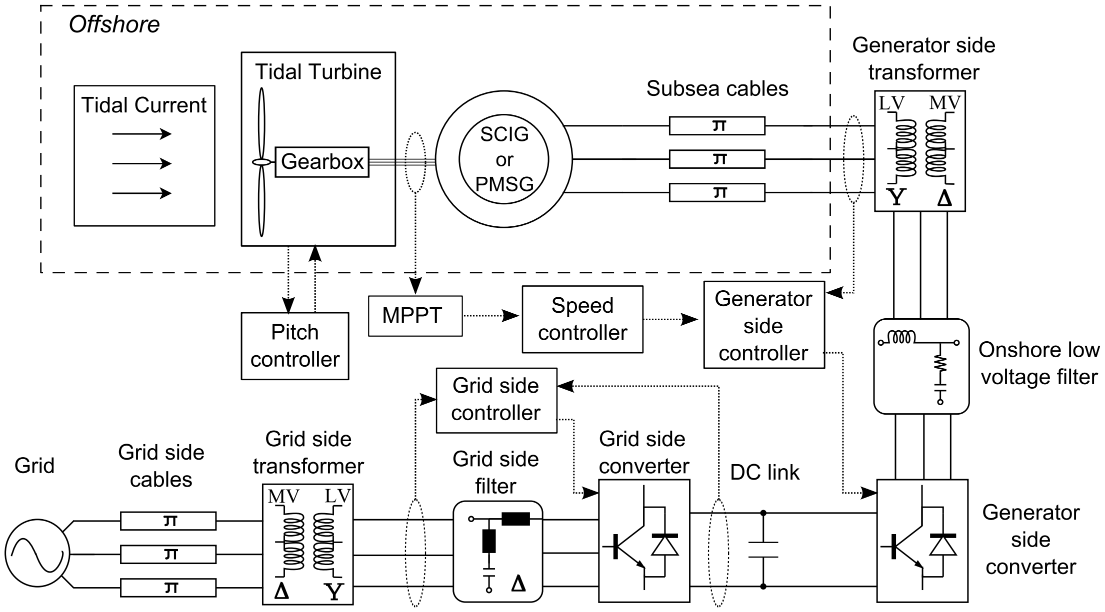

Figure 3.1 Block diagram of the single TCCS with long distance controls.

3.1 The tidal resource

The power potential of tidal currents can be derived by the same formula as for wind energy systems [86].

$$\boldsymbol{P_{tide} = 0.5 \times \rho_{water} \times A \times v^3_{current}} \tag{3-1}$$

Where ρ_{water} is the sea water density in kg/m^3, A is the sweep area in m^2 and $v^3_{current}$ is the fluid speed in m/s. The sea water density is assumed constant at 1025kg/m^3 and the swept area is based on a 10.5m blade. For the purposes of this study the input tidal current speed is chosen to be a half-cycle of a semidiurnal spring tide with high peak flow as it is intended that the model should represent the most complex period of operation of the system. The tidal current speed, $v'(t)$ is constructed by:

- The mean tidal current speed, $\bar{v}$ which is based on actual tidal current measurements at EMEC. The measurements were taken from AHH using an Acoustic Doppler Current Profiler (ADCP). The tidal speed measurements taken from the ADCP were time averaged. The resolution of the data is 2 measurements every 20 seconds. In Figure 3.2a, the complete dataset of tidal current measurements provided by AHH is depicted. In Figure 3.2b the chosen half-cycle of the tidal current is shown.

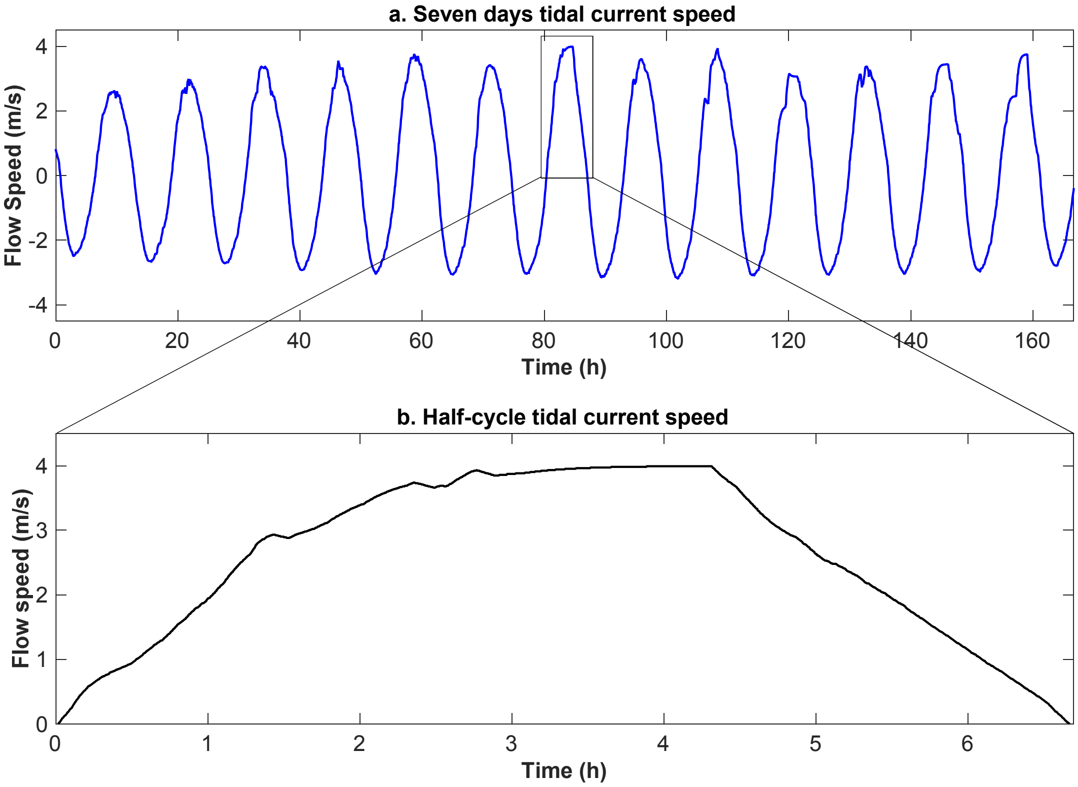

Figure 3.2 Tidal current speed data. a. Seven days available tidal current speed data. b. Tidal current speed data considered in this thesis.

- The predicted turbulence which is modelled by adding band-limited white noise. The added turbulence was chosen to have intensity of 10% from the mean tidal current speed. Turbulence strength is given in equation (3-2) and turbulence intensity (T.I.) in equation (3-3). Figure 3.3a depicts the flow speed with the added turbulence.

$$\boldsymbol{v_{rms}} = \sqrt{\overline{\boldsymbol{v'(t)^2}}} \tag{3-2}$$

$$\boldsymbol{T.I.} = \frac{\boldsymbol{v_{rms}}}{\boldsymbol{\bar{v}}} \tag{3-3}$$

- The swell effect of the tides by using a first-order Stokes model as described in [37] and [62]. The swell effect added is described mathematically in equation (3-4) and shown with the mean tidal current speed and added turbulence in Figure 3.3b.

$$\boldsymbol{v_{swell} = 0.1039 \times \cos(0.42 \times t) + 0.0859 \times \cos(0.63 \times t) + 0.12 \times \cos(1.85 \times t) + 0.05 \times \cos(0.15 \times t)} \quad \textbf{(3-4)}$$

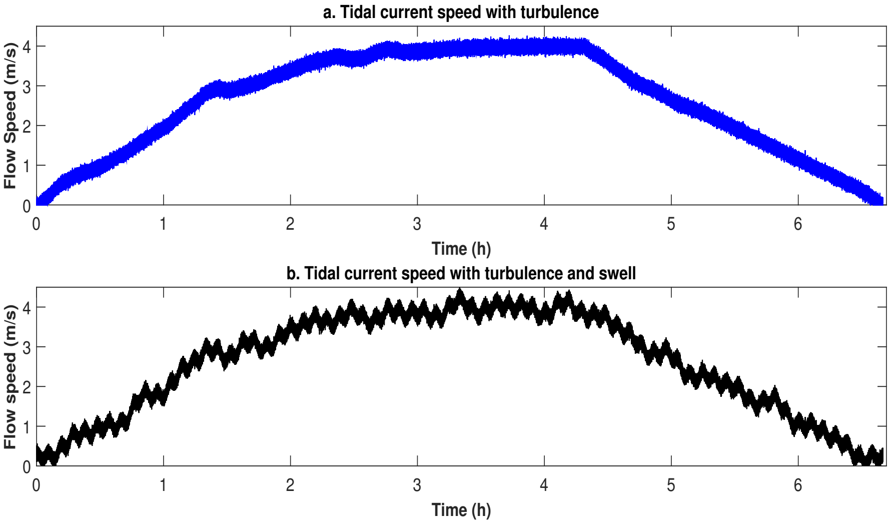

Figure 3.3 Tidal current speed. a. with added turbulence. b. with added turbulence and swell effect.

By comparing Figure 3.2b and Figure 3.3a the effect of the added turbulence, v_{rms}, can be seen. The flow speed profile used as input to the models is the one depicted in Figure 3.3b.

3.2 The tidal turbine

The tidal turbine model converts the power input from the resource model described in Section 3.1 to mechanical power for the generator rotor. The model is based on the AHH HS1000 three-bladed turbine with moment of inertia of 182065kgm^2. The mechanical power output from the tidal turbine is given by equation (3-5).

$$\boldsymbol{P_{mec} = C_p(\lambda, \beta) \times P_{tide}} \quad \textbf{(3-5)}$$

Where P_{mec} is the mechanical output power of the turbine in watts and $C_p(\lambda,\beta)$ is the power coefficient of the blade which is a function of the tip speed ratio (*TSR*), λ, and blade pitch angle or angle of attack, β, in degrees. The TSR is a function of rotor rotational speed, ω_R, in rad/s, rotor radius, R_R, in m and tidal current speed in m/s. TSR can be calculated using equation (3-6).

$$\boldsymbol{\lambda = \frac{\omega_R \times R_R}{v'(t)}} \tag{3-6}$$

The power coefficient, $C_p(\lambda,\beta)$, was approximated using an analytic function described in [87]. This analytic function is given in equations (3-7) and (3-8) and the chosen values for the tidal turbine are shown in Table 3.1.

$$\boldsymbol{C_p(\lambda,\beta) = c_1\left(\frac{c_2}{\lambda_i} - c_3 \times \beta - c_4\right)e^{-\frac{c_5}{\lambda_i}} + c_6 \times \lambda} \tag{3-7}$$

$$\boldsymbol{\frac{1}{\lambda_i} = \frac{1}{\lambda + 0.08 \times \beta} - \frac{0.035}{\beta^3 + 1}} \tag{3-8}$$

Table 3.1 Coefficients chosen for the approximation of the *$C_p(\lambda,\beta)$* curve of the tidal turbine

c_1	c_2	c_3	c_4	c_5	c_6
0.08	145	0.4	4	7	-0.009

In this model a maximum C_p of 0.4596 is assumed and rated power is achieved at 2.5m/s. The values of hydrodynamic coefficient for different values of *TSR* and angle of attack can be seen in Figure 3.4.

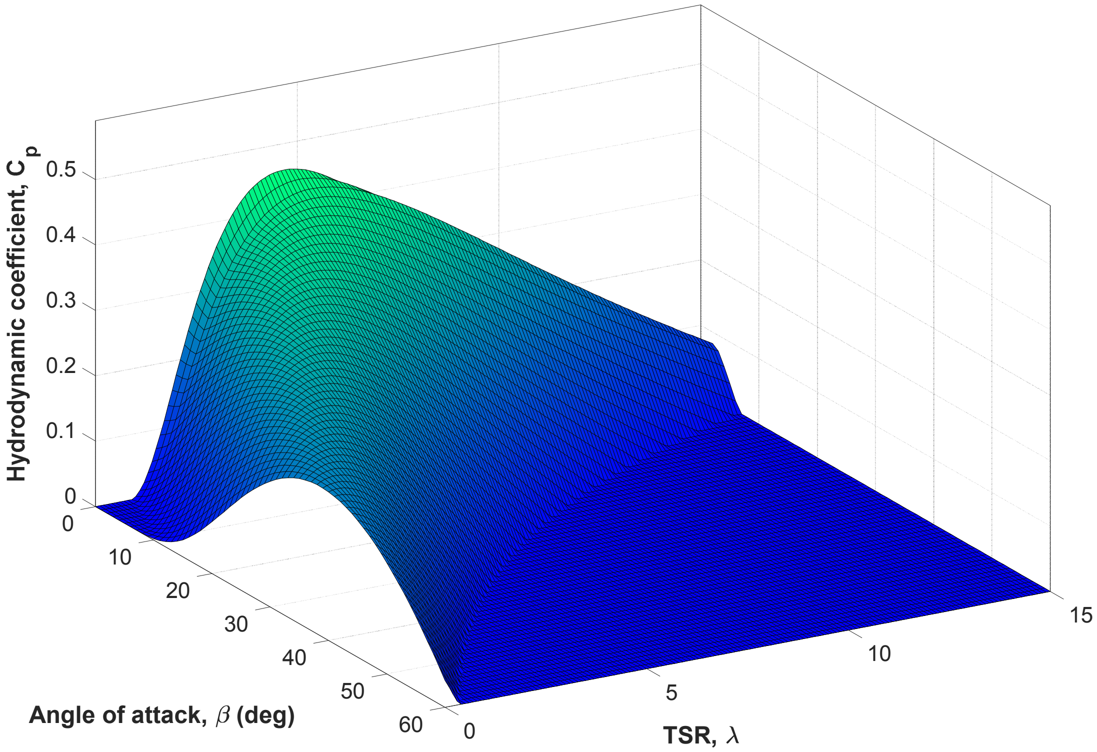

Figure 3.4 Hydrodynamic coefficient of the three-bladed tidal turbine modelled.

Maximum hydrodynamic coefficient is achieved at $TSR = 4.7$ and therefore this is the desired area of operation for the tidal turbine. By increasing the pitch angle, the C_p value drops steeply. As it can be observed in Figure 3.4, in most cases, pitching the blades by 20 degrees drops the C_p near zero. The aim and design of the pitch angle controller is discussed in the following section.

3.2.1 Pitch control

Power limitation in high tidal current speeds is achieved by using pitch angle control. This corresponds to changing the pitch value, β, such that the leading edge of the blade is moved into the flow increasing the angle of attack and thus inducing a blade feathering effect. When tidal current speed is below or at the rated value of the turbine, pitch angle, β, is kept constant. For reference this is chosen to be the 0 degrees. The control structure of the pitching system developed is published in [88] and is shown in Figure 3.5. The pitching mechanism limits the turbine speed to rated speed by reducing C_p in (3-5) and so reducing the mechanical power captured. The way pitch angle, β, changes the value of the power coefficient, C_p, and affects the power output from the tidal turbine can be seen in Figure 3.4.

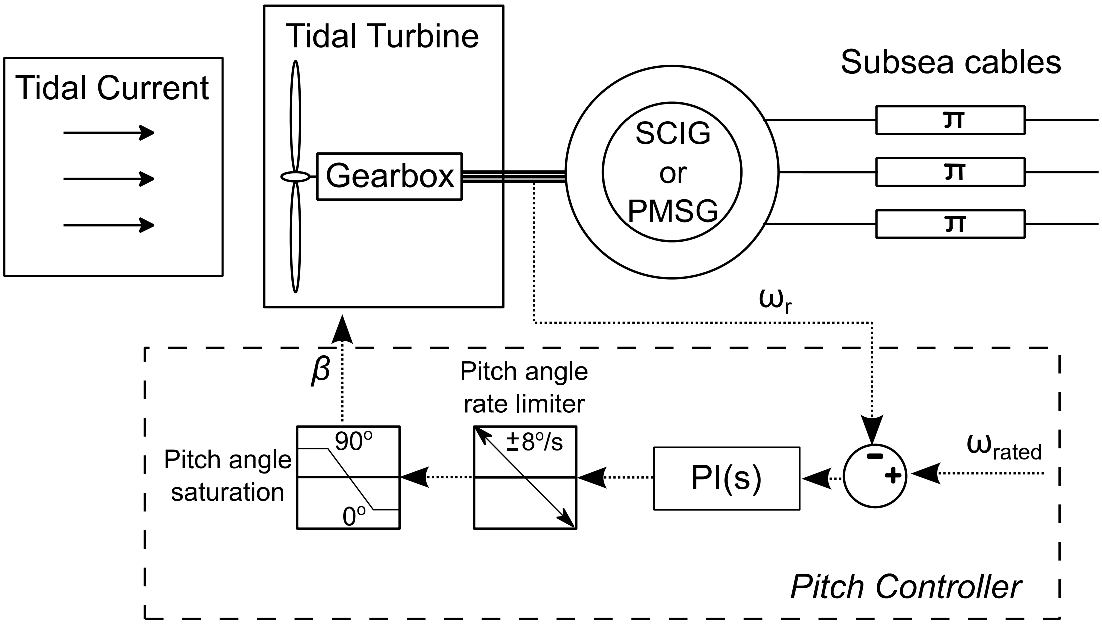

Figure 3.5 Pitch controller block diagram as modelled in MATLAB/Simulink.

3.2.2 Gearbox

The rotor of a large three-bladed tidal turbine usually operates at around 10rpm. This speed is significantly lower compared to the operating speed of 6-pole SCIGs and PMSGs. In order to match the slow moving shaft of the rotor with the high speed shaft of the generator a gearbox is modelled. The gearbox ratio can be calculated using (3-9).

$$\boldsymbol{Gearbox\ ratio} = \frac{\boldsymbol{\omega_R}[\frac{\boldsymbol{rad}}{\boldsymbol{s}}]}{\boldsymbol{\omega_r}[\frac{\boldsymbol{rad}}{\boldsymbol{s}}]} = \frac{\boldsymbol{n_R}[\boldsymbol{rpm}]}{\boldsymbol{n_r}[\boldsymbol{rpm}]} \tag{3-9}$$

Where ω_r is the rotational speed of the generator rotor in rad/s and n_r is the rotational speed of the generator rotor in rpm. In all the models presented in this thesis the gearbox ratio is kept constant at 98.2. As shown in section 3.2 the output from the tidal turbine model is mechanical torque, T_{mec}^{TT}. The gearbox model converts the mechanical torque of the slow speed shaft of the tidal turbine to mechanical torque for the high speed shaft of the generator. The mechanical torque input to the generator, T_{mec}^{G} is modelled using (3-10).

$$\boldsymbol{T_{mec}^{G}} = \frac{\boldsymbol{T_{mec}^{TT}}}{\boldsymbol{Gearbox\ ratio}} \tag{3-10}$$

3.3 The generator

The generator model converts the mechanical torque input from the tidal turbine model to electrical power. Two widely used generator technologies have been considered in this thesis, the SCIG and PMSG.

3.3.1 Squirrel Cage Induction Generator

The SCIG is simple in construction, comparatively inexpensive to PMSG and has been used in industry for many years. The model of the SCIG is described in detail in [89] and is based on the *dq reference frame model*. According to [89] two assumptions are taken into account when developing the model. The first assumption is that the SCIG is symmetrical and three-phase balanced and the second assumption that the magnetic core of the stator and rotor is linear with negligible losses. In order to obtain the *dq-axis* parameters of the machine, the space-vectors have to be decomposed to the *d-axis* and *q-axis* components. As described in [89] space-vector equations can be separated into voltage equations of the rotor and stator in the arbitrary reference frame (3-11), flux linkage equations (3-12) and motion equations (3-13).

$$\begin{cases} \vec{v}_s = R_s\vec{i}_s + \dfrac{d\vec{\varphi}_s}{dt} + j\omega\vec{\varphi}_s \\ \vec{v}_r = R_r\vec{i}_r + \dfrac{d\vec{\varphi}_r}{dt} + j(\omega - \omega_r)\vec{\varphi}_s \end{cases} \qquad \textbf{(3-11)}$$

$$\begin{cases} \vec{\varphi}_s = (L_{ls} + L_m)\vec{i}_s + L_m\vec{i}_r = L_s\vec{i}_s + L_m\vec{i}_r \\ \vec{\varphi}_r = (L_{lr} + L_m)\vec{i}_r + L_m\vec{i}_s = L_r\vec{i}_r + L_m\vec{i}_s \end{cases} \qquad \textbf{(3-12)}$$

$$\begin{cases} J\dfrac{d\omega_m}{dt} = T_e - T_m - F\omega_m \\ T_e = \dfrac{3p}{2}Re(j\vec{\varphi}_s\vec{i}_s^{*}) \\ \omega_m = {}^{\omega_r}/_{p} \end{cases} \qquad \textbf{(3-13)}$$

The specifications for (3-11) to (3-13) are given in Table 3.2.

Table 3.2 SCIG parameters involved in the modelling process.

Symbol	Description	Units
$\vec{v}_s, \vec{v}_r$	Stator and rotor voltage vectors	V
$\vec{i}_s, \vec{i}_r$	Stator and rotor current vectors	A
$\vec{\varphi}_s, \vec{\varphi}_r$	Stator and rotor flux-linkage vectors	Wb
R_s, R_r	Stator and rotor winding resistances	Ω
ω	Rotating speed of the arbitrary reference frame	rad/s
ω_r	Rotor electrical angular speed	rad/s
L_{ls}, L_{lr}	Stator and rotor leakage inductances	H
L_s, L_r	Stator and rotor self-inductances	H
L_m	Magnetising inductance	H
J	Moment of inertia of the rotor	kgm^2
p	Number of pole pairs	-
T_m	Mechanical torque from the generator shaft	Nm
T_e	Electromagnetic torque	Nm
ω_m	Rotor mechanical speed	rad/s
F	Rotor and load viscous friction coefficient	N

Using the above equations the space-vector model of the SCIG in the arbitrary reference frame ω can be created. The *dq reference frame model* can be formulated by using (3-14) for all the rotor and stator vectors described above.

$$\begin{cases} \vec{x}_s = x_{ds} + jx_{qs} \\ \vec{x}_r = x_{dr} + jx_{qr} \end{cases} \tag{3-14}$$

Where $\vec{x}_s$ is the chosen stator vector and $\vec{x}_r$ is the chosen rotor vector. Decomposing all the stator and rotor vectors to their *dq-axis* components as shown in (3-14) a new set of equations are derived from (3-11) to (3-13).

$$\begin{cases} v_{ds} = R_s i_{ds} + \frac{d\varphi_{ds}}{dt} - \omega\varphi_{qs} \\ v_{qs} = R_s i_{qs} + \frac{d\varphi_{qs}}{dt} + \omega\varphi_{ds} \\ v_{dr} = R_r i_{dr} + \frac{d\varphi_{dr}}{dt} - (\omega - \omega_r)\varphi_{qr} \\ v_{qr} = R_r i_{qr} + \frac{d\varphi_{qr}}{dt} + (\omega - \omega_r)\varphi_{dr} \end{cases} \tag{3-15}$$

$$\begin{cases} \varphi_{ds} = L_s i_{ds} + L_m i_{dr} \\ \varphi_{qs} = L_s i_{qs} + L_m i_{qr} \\ \varphi_{dr} = L_r i_{dr} + L_m i_{ds} \\ \varphi_{qr} = L_r i_{qr} + L_m i_{qs} \end{cases} \tag{3-16}$$

$$T_e = \frac{3p}{2}\left(i_{qs}\varphi_{ds} - i_{ds}\varphi_{qs}\right) \tag{3-17}$$

Using (3-15) – (3-17) the *dq-axis* model of the SCIG in the arbitrary reference frame can be developed. For the purposes of this thesis the stationary reference frame was used and therefore the arbitrary rotational speed ω can be set to zero. The equivalent circuit of the SCIG using the stationary reference frame can be seen in Figure 3.6a for the *d-axis*, or *α-axis* as it is usually referred in the stationary reference frame, and in Figure 3.6b for the *q-axis*, or *β-axis* as it is usually referred in the stationary reference frame. The parameters of the SCIG used were provided by AHH and are given in Table 3.3.

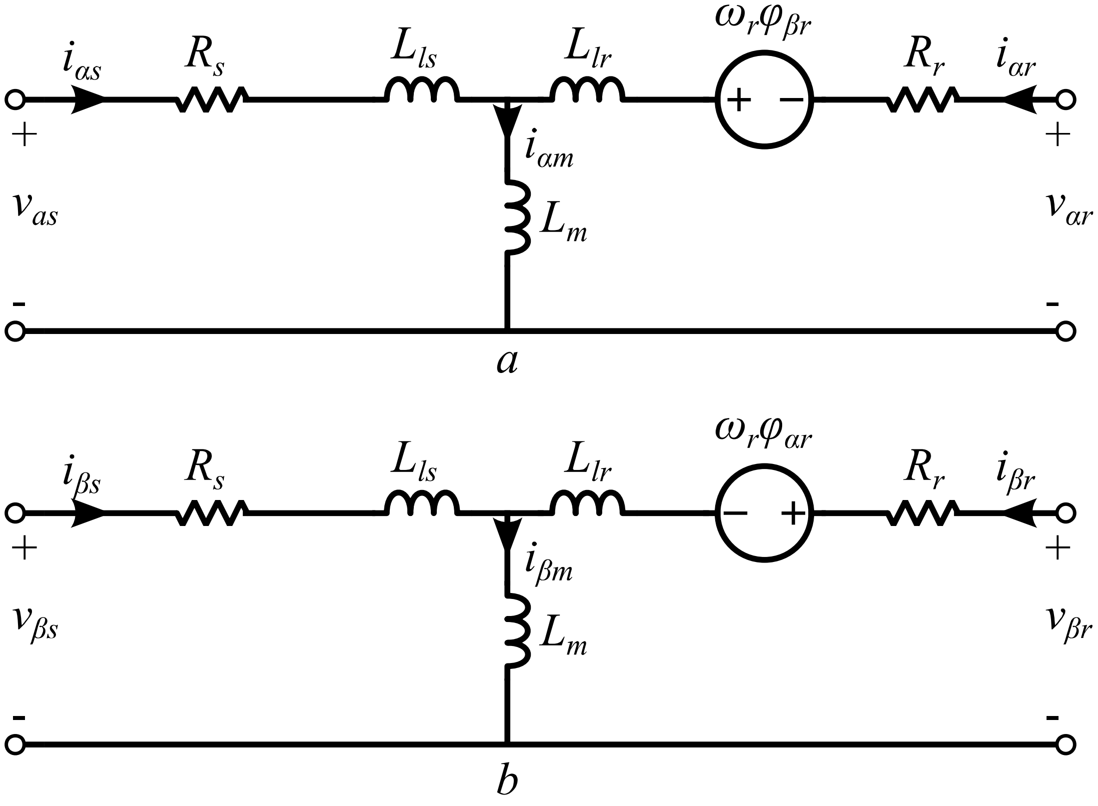

Figure 3.6 SCIG equivalent circuit at the stationary reference frame. a. *α-axis*. b. *β-axis*.

Table 3.3 SCIG parameters.

Parameter	Value	Units
Nominal voltage	6600	V
Apparent power range	1.2 – 1.8	MVA
Frequency	50	Hz
Stator resistance, R_s	0.00548	pu
Stator inductance, L_s	0.08716	pu
Rotor resistance, R_r	0.00399	pu
Rotor inductance, L_r	0.08915	pu
Mutual inductance, L_m	3.99779	pu
Rotor inertia, J	90	kgm^2
Pole pairs, p	3	-
Rotor and load viscous friction coefficient, F	2.3	N

The SCIG model described in (3-15) to (3-17) is controlled by the onshore generator side converter. The control method implemented in the final TCCS model is based on the direct torque control (DTC) theory which is described in Section 3.3.1.1 but with the modification of the space vector modulation and is described in Section 3.3.1.2.

3.3.1.1 Direct Torque Control

The classical DTC has been developed to drive motors [90] using voltage source converters (VSC). However, with slight modifications the control method can be used to enable variable speed operation in TCCS. The principle of DTC is to control the electromagnetic torque T_e of the SCIG which can be expressed as in (3-18). This can be achieved by manipulating the torque angle θ_T while keeping the magnitude of the stator flux φ_s at its rated value. The modelling of the DTC method is described in detail in [91].

$$T_e = \frac{3p}{2}\frac{L_m}{\sigma L_s L_r}\varphi_s\varphi_r \sin(\theta_T) \qquad \textbf{(3-18)}$$

The block diagram of the DTC control method can be seen in Figure 3.7. The DTC presented in this thesis is slightly different from the method presented in [91]. This is due to the fact that voltage and current measurements are taken from the onshore transformer and not at the generator terminals as presented in most cases. This requires a voltage and current estimator as presented in Figure 3.7.

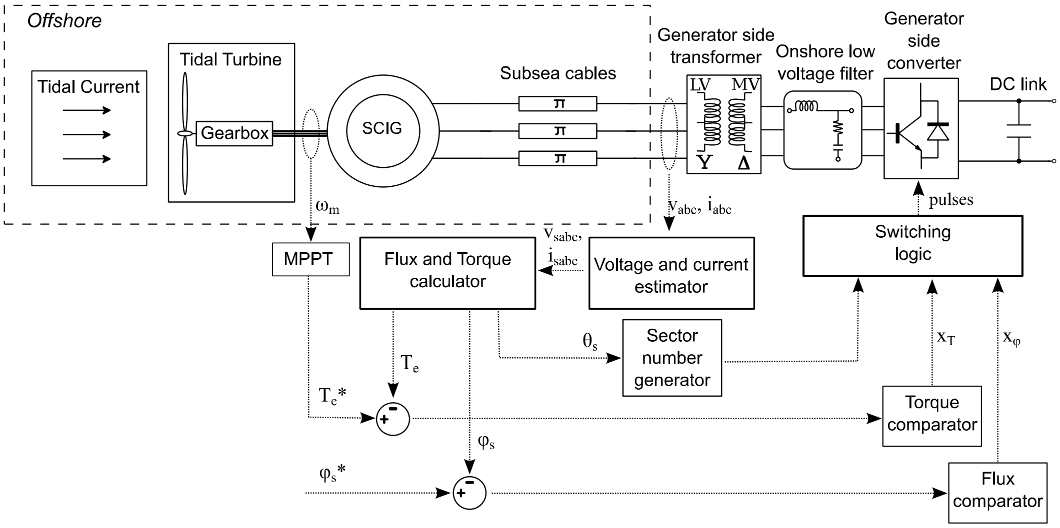

Figure 3.7 Block diagram of the DTC method implemented for the TCCS with long distance controls.

The DTC block diagram of Figure 3.7 is composed of four distinct parts.

- The voltage and current estimator.
- The flux and torque calculator.
- The torque and flux comparators.
- The switching logic.

The flux and torque calculator calculates the actual stator flux and electrical torque of the generator by measuring the generator stator voltage and current. This can be done by using equations (3-19) to (3-21) [91]:

$$\vec{\varphi}_s = \varphi_{\alpha s} + j\varphi_{\beta s} = \int (v_{\alpha s} - R_s i_{\alpha s})dt + j\int (v_{\beta s} - R_s i_{\beta s})dt \tag{3-19}$$

$$\begin{cases} \varphi_s = \sqrt{\varphi_{\alpha s}^2 + \varphi_{\beta s}^2} \\ \theta_s = \tan^{-1}\left(\dfrac{\varphi_{\beta s}}{\varphi_{\alpha s}}\right) \end{cases} \tag{3-20}$$

$$T_e = \frac{3p}{2}\left(\varphi_{\alpha s} i_{\beta s} - \varphi_{\beta s} i_{\alpha s}\right) \tag{3-21}$$

The above equations show that the only generator parameter required in the DTC control method is the stator resistance R_s. This is an advantage of the DTC method compared to other control methods for induction machines such as the Field Oriented Control (FOC). In the FOC scheme most of the generator parameters are needed which can affected the control method in case of miscalculation or generator parameter changes due to environmental factors and ageing. The block diagram of the flux and torque calculator modelled in MATLAB/Simulink as part of this thesis can be seen in Figure 3.8.

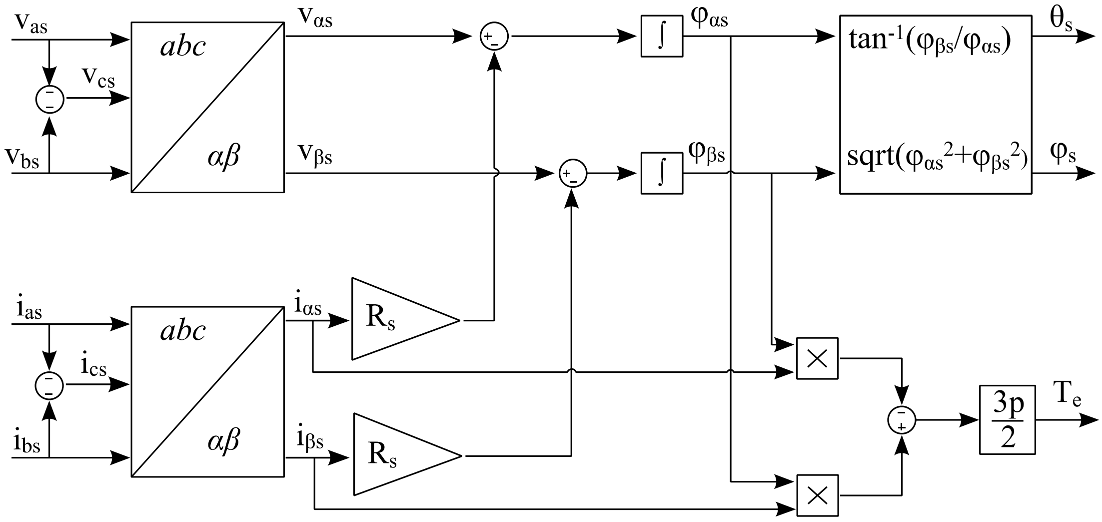

Figure 3.8 The flux and torque calculator as implemented in MATLAB/Simulink.

In many cases it is suggested that the measurements can be taken from an onshore point so that the transfer of information is easier. Therefore, it is possible to measure the voltage and current at the cable end, where the cables are connected to the generator side transformer, and then estimate the stator voltage and current by knowing the cable parameters. This is achieved by the voltage and current estimator shown in Figure 3.7. The disadvantage of this method is that cable parameters change based on the operating frequency of the system and the temperature variations. Therefore, voltage and current estimation of the generator terminals may not be accurate.

If the voltage and current measurements are taken from the generator terminals then the information has to be transmitted to the shore. The time needed to transmit the measured quantities from offshore to onshore has to be less than or equal to the controller computation time. For the purposes of the simulation the controller computation time is equal to 200μs. Assuming a relatively high reduction of 66% of the speed of light in the fibre optics, the light in the fibre optics of the sub-sea cables can travel 0.1km/μs. For the marginal value of 200μs, the maximum cable length in which the information of measured quantities can reach the controller on time is 20km. This means that in all the cases that long distance controls are considered, usually between 1km and 15km, in a TCCS the measurements can be taken from the generator terminals.

In this thesis both measuring cases have been considered in order to identify deviations in results. Both cases produced similar or even identical results and for that reason the results presented in this paper are based on measurements from the onshore point as depicted in Figure 3.7. At this point it should be noted that cable variations where not considered when comparing the two different measuring cases.

As it is shown in Figure 3.7 the switching logic of the classical DTC control method has three inputs, the sector number, the output of the flux comparator and the output of the torque comparator. The torque and flux comparators shown in Figure 3.7 are based on hysteresis. The stator flux reference, φ_s*, is compared with the calculated stator flux, φ_s. The error of the stator flux is sent to the flux comparator. Similarly the electromagnetic torque reference, T_e*, is compared with the calculated electromagnetic torque, T_e. The error of the electromagnetic torque is sent to the torque comparator. The output of the flux comparator, x_φ, is either 1 if there is a need for φ_s to increase or -1 if there is a need for φ_s to decrease. The torque comparators output, x_T, can be 1 if there is a need to increase T_e, -1 if there is a need to decrease T_e or 0 if there is no need to change T_e [91]. The sector number generator divides the *αβ-axis* to six sectors depending on the angle θ_s. The process to choose the appropriate sector number is given in the function below:

```
function Sector = fcn(theta)
Sector = 1;
if (theta > -30) && (theta <= 30)
    Sector = 1;
elseif (theta > 30) && (theta <= 90)
    Sector = 2;
elseif (theta > 90) && (theta <= 150)
    Sector = 3;
elseif (theta > 150) || (theta <= -150)
    Sector = 4;
elseif (theta > -150) && (theta <= -90)
    Sector = 5;
elseif (theta > -90) && (theta <= -30)
    Sector = 6;
end
```

Finally the switching logic is based on Table 3.4. The space vector are shown in Table 3.5 and the 2-level VSC with insulated-gate bipolar transistors (IGBTs) that the space vectors control in Figure 3.9.

Table 3.4 Switching logic for the DTC control method [91]**. The space vectors $\vec{V}_0$ to $\vec{V}_7$control the 2-level VSC.**

Comparator output		**Sector**					
x_φ	x_T	1	2	3	4	5	6
1	1	$\vec{V}_2$	$\vec{V}_3$	$\vec{V}_4$	$\vec{V}_5$	$\vec{V}_6$	$\vec{V}_1$
	0	$\vec{V}_0$	$\vec{V}_7$	$\vec{V}_0$	$\vec{V}_7$	$\vec{V}_0$	$\vec{V}_7$
	-1	$\vec{V}_6$	$\vec{V}_1$	$\vec{V}_2$	$\vec{V}_3$	$\vec{V}_4$	$\vec{V}_5$
-1	1	$\vec{V}_3$	$\vec{V}_4$	$\vec{V}_5$	$\vec{V}_6$	$\vec{V}_1$	$\vec{V}_2$
	0	$\vec{V}_7$	$\vec{V}_0$	$\vec{V}_7$	$\vec{V}_0$	$\vec{V}_7$	$\vec{V}_0$
	-1	$\vec{V}_5$	$\vec{V}_6$	$\vec{V}_1$	$\vec{V}_2$	$\vec{V}_3$	$\vec{V}_4$

Table 3.5 Space vectors for the 2-level VSC of Figure 3.9.

Voltage vector	**Power switch number**					
	Q1	Q2	Q3	Q4	Q5	Q6
$\vec{V}_0$	0	1	0	1	0	1
$\vec{V}_1$	1	0	0	1	0	1
$\vec{V}_2$	1	0	1	0	0	1
$\vec{V}_3$	0	1	1	0	0	1
$\vec{V}_4$	0	1	1	0	1	0
$\vec{V}_5$	0	1	0	1	1	0
$\vec{V}_6$	1	0	0	1	1	0
$\vec{V}_7$	1	0	1	0	1	0

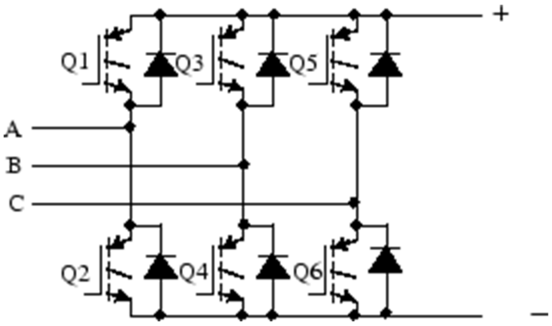

Figure 3.9 The 2-level VSC in MATLAB/Simulink with IGBT-Diodes.

3.3.1.2 Direct Torque Control with Space Vector Modulation

Direct torque control with space vector modulation (DTC SVM) is based on the DTC method described in Section 3.3.1.1 but with a different switching logic and proportional-integral (PI) controllers instead of hysteresis comparators. The main advantage of the DTC SVM control method compared to the DTC method is that it operates at constant switching frequency which results to reduced torque ripple. In addition, constant switching frequency of the generator controller means that the characteristic harmonics will be generated at specific frequencies which can be filtered with single tuned filters. On the other hand, the classical DTC method described in Section 3.3.1.1 generates square-wave pulses. These pulses have harmonic components at a wide range of frequencies which is undesirable for a long distance control system. The importance of having harmonics at known frequencies will become evident in Chapter 4 where the TCCS will be analysed in the frequency domain. Increased harmonics flowing in the cables can cause overvoltages at the generator terminals and can lead to insulation breakdown. In this thesis, for the generator controller, the DTC SVM scheme with closed-loop torque and flux control in stator flux coordinates has been implemented. A version of this DTC SVM scheme is presented in [92]. The control structure of the DTC SVM method modelled in MATLAB/Simulink can be seen in Figure 3.10. The SVM method and the *dq/abc* transformation are presented in [93].

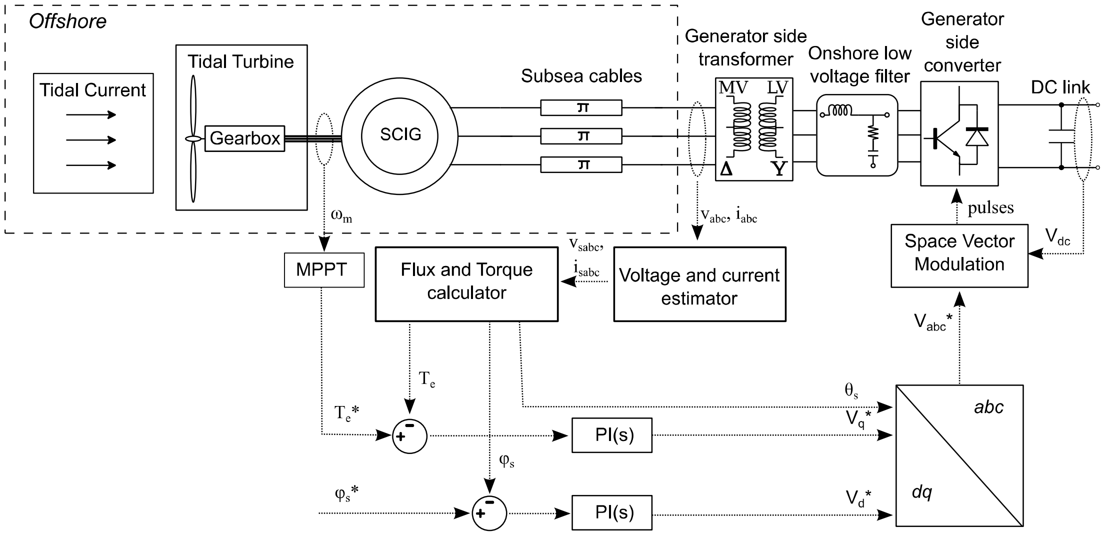

Figure 3.10 Block diagram of the DTC SVM method modelled in MATLAB/Simulink.

The block diagram of the SVM model implemented in MATLAB/Simulink is presented in Figure 3.11.

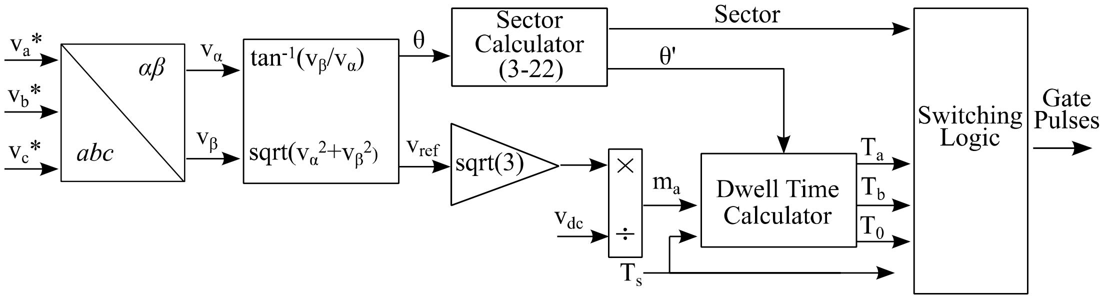

Figure 3.11 Block diagram of the SVM method implemented in MATLAB/Simulink [93].

The sector calculator is based on the space vector diagram for the 2-level VSC and is shown in Figure 3.12. The implementation is similar to the sector calculator presented in Section 3.3.1.1. The modified reference voltage angle θ’ is calculated from equation (3-22) so that it always is between 0 and π/3.

$$\theta' = \theta - (k-1)\pi/3 \tag{3-22}$$

Where k is the sector number.

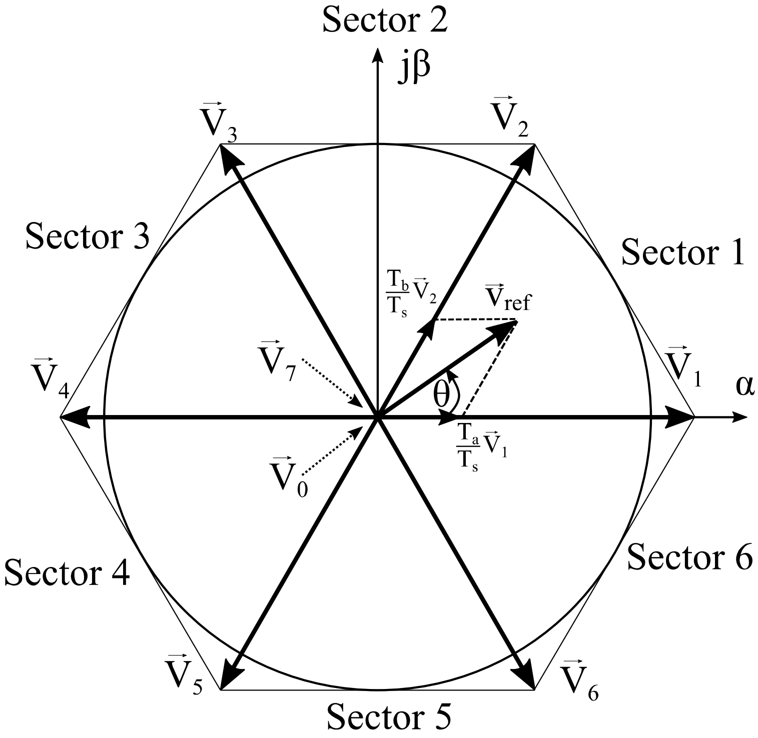

Figure 3.12 Space vector diagram for the 2-level VSC [93]**.**

As it is shown in Figure 3.12 the $\vec{v}_{ref}$ is synthesized by three stationary space vectors with different dwell times for each space vector. For example, for the $\vec{v}_{ref}$ in Figure 3.12 the following applies:

$$\begin{cases} \vec{v}_{ref}T_s = \vec{V}_1T_a + \vec{V}_2T_b + \vec{V}_0T_0 \\ T_s = T_a + T_b + T_0 \end{cases} \quad \textbf{(3-23)}$$

Where T_s is the sampling period which is assumed sufficiently small. Dwell times T_a, T_b and T_0 are calculated based on equation (3-24).

$$\begin{cases} T_a = T_s m_a \sin\left(\frac{\pi}{3} - \theta\right) \\ T_b = T_s m_a \sin\theta \\ T_0 = T_s - T_a - T_b \end{cases} \quad \textbf{(3-24)}$$

The switching logic of the SVM method presented in Figure 3.11 is based on the seven-segment switching sequence presented in [93] and is shown in Table 3.6.

Table 3.6 Seven-segment switching sequence for the switching logic of the SVM method [93].

Sector	**Switching segment**						
	1	2	3	4	5	6	7
	$T_0/4$	$T_a/2$	$T_b/2$	$T_0/2$	$T_b/2$	$T_a/2$	$T_0/4$
1	$\vec{V}_0$	$\vec{V}_1$	$\vec{V}_2$	$\vec{V}_7$	$\vec{V}_2$	$\vec{V}_1$	$\vec{V}_0$
2	$\vec{V}_0$	$\vec{V}_3$	$\vec{V}_2$	$\vec{V}_7$	$\vec{V}_2$	$\vec{V}_3$	$\vec{V}_0$
3	$\vec{V}_0$	$\vec{V}_3$	$\vec{V}_4$	$\vec{V}_7$	$\vec{V}_4$	$\vec{V}_3$	$\vec{V}_0$
4	$\vec{V}_0$	$\vec{V}_5$	$\vec{V}_4$	$\vec{V}_7$	$\vec{V}_4$	$\vec{V}_5$	$\vec{V}_0$
5	$\vec{V}_0$	$\vec{V}_5$	$\vec{V}_6$	$\vec{V}_7$	$\vec{V}_6$	$\vec{V}_5$	$\vec{V}_0$
6	$\vec{V}_0$	$\vec{V}_1$	$\vec{V}_6$	$\vec{V}_7$	$\vec{V}_6$	$\vec{V}_1$	$\vec{V}_0$

3.3.2 Permanent Magnet Synchronous Generator

Permanent magnet synchronous generators have higher efficiencies over a wider range of operating speeds compared to SCIGs. This advantage makes them an attractive option for tidal current developers due to the variability of the tidal current, two high tides and two low tides within 24 hours and 50 minutes in a semidiurnal tide. A secondary advantage of the PMSG is the higher power densities due to the use of permanent magnets on the rotor. Detailed construction, categorisation and modelling of PMSGs is presented in [89]. The dynamic response of the PMSG model in the *dq-axis reference frame* is given in (3-25) and (3-26) [89].

$$\begin{cases} \dfrac{di_{ds}}{dt} = \dfrac{1}{L_d}\left(-v_{ds} - R_s i_{ds} + L_q p\omega_m i_{qs}\right) \\ \dfrac{di_{qs}}{dt} = \dfrac{1}{L_q}\left(-v_{qs} - R_s i_{qs} - L_d p\omega_m i_{ds} + p\omega_m \varphi_r\right) \end{cases} \tag{3-25}$$

$$T_e = \frac{3p}{2}\left[\varphi_r i_{qs} + \left(L_d - L_q\right) i_{ds} i_{qs}\right] \tag{3-26}$$

The motion equations of the PMSG are given in (3-27) [89].

$$\begin{cases} \dfrac{d\boldsymbol{\theta_r}}{dt} = \boldsymbol{\omega_m} \\ \boldsymbol{p}\dfrac{d\boldsymbol{\omega_m}}{dt} = \dfrac{\mathbf{1}}{\boldsymbol{J}}(\boldsymbol{T_e} - \boldsymbol{F}\boldsymbol{\omega_m} - \boldsymbol{T_m}) \end{cases} \tag{3-27}$$

In Table 3.7 a detailed description of the quantities involved in (3-25) to (3-27) is given.

Table 3.7 Description of quantities of the dynamic PMSG model.

Symbol	Description	Units
i_{ds}, i_{qs}	*dq-axis* stator currents	A
v_{ds}, v_{qs}	*dq-axis* stator voltages	V
L_d, L_q	dq-axis inductances	H
R_s	Stator winding resistance	Ω
φ_r	Flux amplitude induced by rotor magnets	Wb
θ_r	Rotor angular position	rad
J	Moment of inertia of the rotor	kgm^2
p	Number of pole pairs	-
T_m	Mechanical torque from the generator shaft	Nm
T_e	Electromagnetic torque	Nm
ω_m	Rotor mechanical speed	rad/s
F	Rotor and load viscous friction coefficient	N

In this thesis a PMSG with round rotor and sinusoidal back electromotive force (EMF) has been chosen. The PMSG model was designed to fit in the nacelle of the current prototype of AHH and this is why a gearbox is necessary. In addition, the nominal voltage and power rating of the PMSG model was designed to match the respective quantities of the SCIG used in AHH HS1000 prototype. The PMSG parameters used in the model are presented in Table 3.8.

Table 3.8 PMSG model parameters.

Parameter	Value	Units
Nominal voltage	6600	V
Apparent power range	1.2 – 1.8	MVA
Frequency	50	Hz
Stator resistance, R_s	0.4149	Ω
dq-axis inductance, $L_d = L_q$	0.0586	H
Flux induced by rotor magnets, φ_r	17.1533	Wb
Rotor inertia, J	22.5	kgm^2
Pole pairs, p	3	-
Rotor and load viscous friction coefficient, F	2.3	N

The PMSG model is controlled from the onshore generator side VSC. The control method used was based on the zero *d-axis* current control (ZDC) method and is presented in the following section.

3.3.2.1 Zero d-axis current control with Space Vector Modulation

The zero *d-axis* current (ZDC) control method is based on the assumption that the *d-axis* stator current of the PMSG can be kept at zero and that the electromagnetic torque of the generator can be controlled by *q-axis* stator current. This possible due to the non-salient rotor of the PMSG used in this thesis. Based on (3-26) and because $L_d = L_q$ the electromagnetic torque of the PMSG generator is transformed to:

$$\boldsymbol{T_e = \frac{3p}{2}(\varphi_r i_{qs})} \qquad \textbf{(3-28)}$$

As shown in (3-28) the relationship between *q-axis* current and electromagnetic torque of the PMSG is linear. The control scheme for the ZDC control method is presented in detail in [94]. In this thesis, a different variation of the control scheme is chosen for the development of the TCCS model compared to the one presented in [94]. The differences lie in the switching logic that generates the pulses for the generator side

VSC and the location of the current measurements. In [94] the control scheme presented is based on pulse-width modulation (PWM) to generate the desired pulses whereas the SVM method is chosen in this thesis. The reason for choosing the SVM method is due to the fact that SVM is also used for the control of the SCIG and therefore results could be comparable. In addition, the SVM method operates at constant switching frequency which results to reduced torque ripple. As described in Section 3.3.1.1 for the control of the SCIG the voltage and current measurements are suggested to be taken from an onshore point so that the transfer of information is easier. This is also the case of the ZDC controller for the PMSG. The block diagram of the ZDC control method developed for the PMSG TCCS model is shown in Figure 3.13 and was published in [60]. The SVM method used to control the PMSG is similar to the one presented in Section 3.3.1.2 for the control of the SCIG.

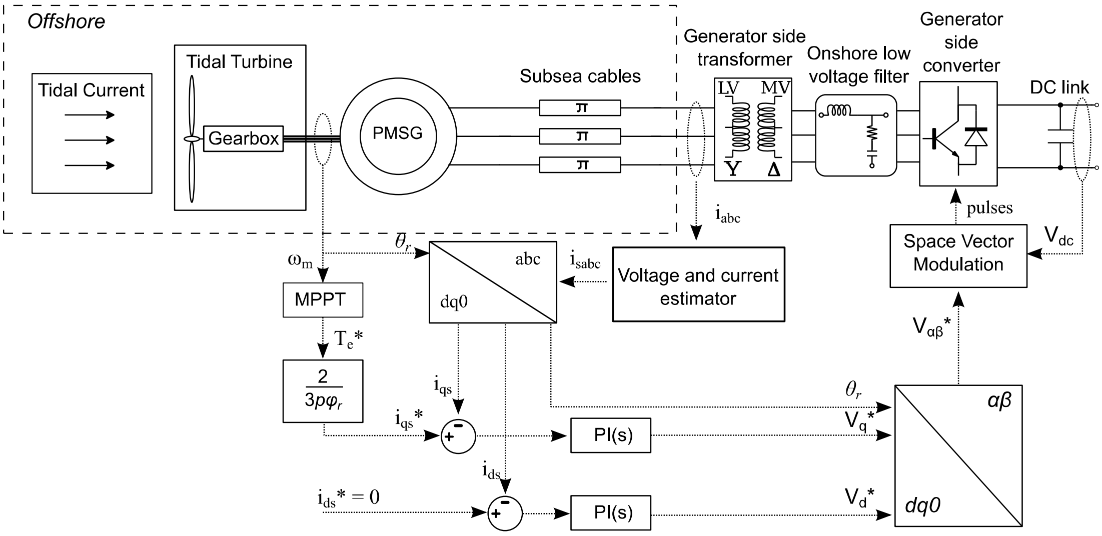

Figure 3.13 Block diagram of the ZDC control method as modelled in MATLAB/Simulink.

3.4 Maximum power point tracking

Maximum power point tracking (MPPT) has one major aim: to control the tidal turbine's speed in order to capture the highest possible power from the tidal currents. However, this is not always possible due to constraints in the operation of the system. Some of these constraints include high system losses at low tidal current speeds, reduced generator efficiency at low generator speeds and maximum electrical power output from the generator. The curtailment of the power output of the generator at above rated output has been discussed in Section 3.2.1 and is achieved by changing the pitch angle of the blades. MPPT is responsible for the efficient operation of the TCCS at tidal current speeds below 2.5m/s, which is the rated tidal current speed. In order to operate efficiently, firstly the operating points where maximum C_p is achieved at different tidal current speeds must be identified. This process is discussed in Section 3.4.1. After identifying the optimum operating points, the speed and torque of the generator have to be controlled based on the optimal operation. This is done by the speed controller which is discussed in Section 3.4.2. The overall MPPT strategy and how it links with the generator controllers is presented in Section 3.4.3.

3.4.1 Maximum power point curve

The maximum power point curve (MPPC) identifies all the operating points with maximum hydrodynamic coefficient, C_p. The maximum power point curve modelled in this thesis is based on (3-29) where k is a constant and is shown in Figure 3.14.

$$\boldsymbol{T_{opt} = k\omega_{opt}^2 \Leftrightarrow \omega_{opt} = \sqrt{\frac{T_{opt}}{k}}} \tag{3-29}$$

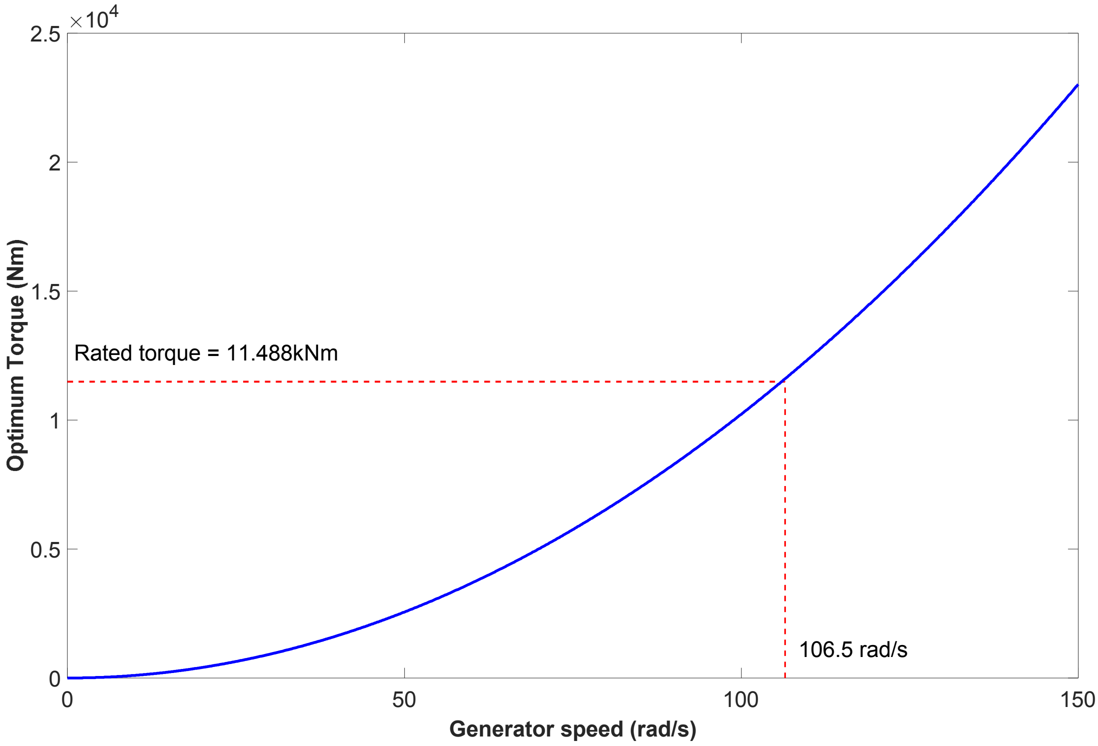

Figure 3.14 Maximum power point curve for the TCCS.

The mechanical torque to the generator shaft is used as an input to the maximum power point curve. Using (3-29) the desired generator speed is calculated based on the mechanical torque input. The desired generator speed is then used as input to the speed controller to calculate the desired electromagnetic torque, T_e*, which is required as input to the generator controllers.

3.4.2 Speed controller

The speed controller is responsible for comparing the optimum generator speed, ω_{opt}, and actual generator speed, ω_m, in order to produce a reference signal for the electromagnetic torque of the generator. A rate limiter is added to ω_{opt} in order to restrict sudden changes of speed from the controller. The reference signal of the electromagnetic torque, T_e*, is used as an input to the generator controllers discussed in Section 3.3.1.2 and 3.3.2.1. The block diagram of the speed controller is shown in Figure 3.15.

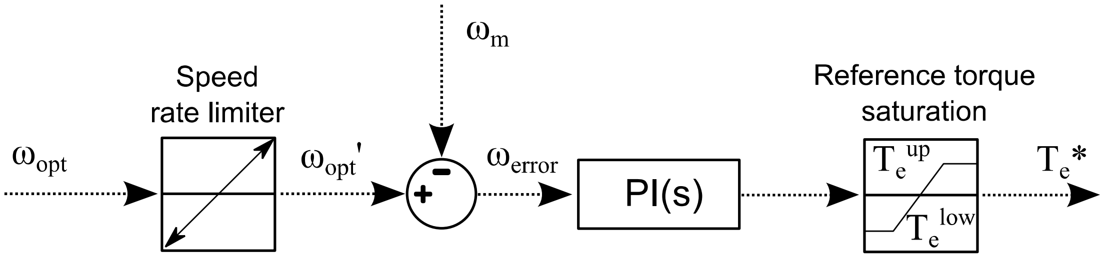

Figure 3.15 Speed controller block diagram as modelled in MATLAB/Simulink.

The way the speed controller, presented in Figure 3.15, operates in order to follow the MPPC discussed in Section 3.4.1 is shown in Figure 3.16 for a step change in tidal current speed and in Figure 3.17 for a ramp increase in tidal current speed. In Figure 3.16 a step change of the tidal current speed occurs from 2.2m/s to 2.5m/s. Figure 3.16a shows the generator speed N_m compared to the optimum speed generated by the MPPC curve, N_{opt}, and the rate limited optimum speed, N_{opt}'. Figure 3.16b shows the power curve diagram of the TCCS and how the speed controller changes the operation of the TCCS in order to follow the MPPC.

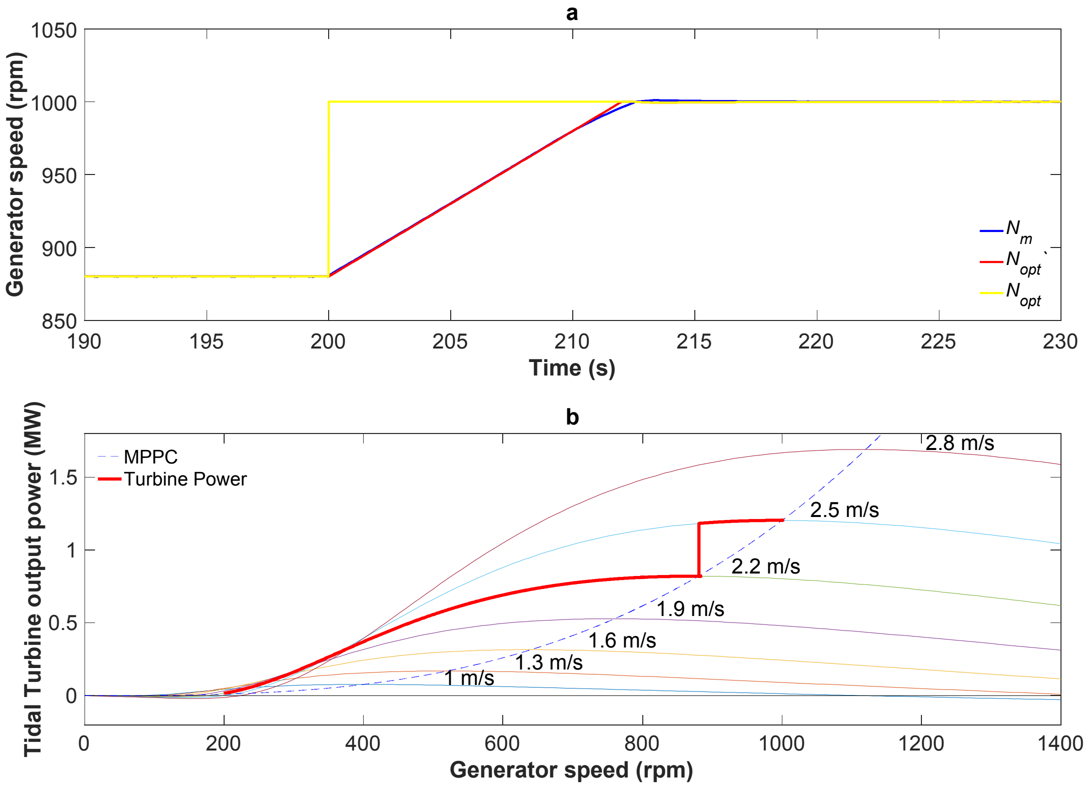

Figure 3.16 Step change response of the speed controller implemented in MATLAB/Simulink. a. Generator speed over time. b. Tidal turbine power depending on the generator speed.

In Figure 3.16a the generator speed over time is observed as the tidal current speed increases from 2.2m/s to 2.5m/s at 200s. Based on equation (3-29) the N_{opt} also increases from 880rpm to 1000rpm as a step change. Due to the restrictions imposed to the speed controller regarding the maximum acceleration of the generator, the N_{opt}' increases to 1000rpm within approximately 12 seconds. The generator speed, N_m, in Figure 3.16a is increasing the same way as N_{opt}' until approximately the 1000rpm are reached. The overshoot of the generator speed is small since the tuning of the speed controller led to only 0.18% overshoot. The speed controller PI was tuned using bode plots to allow a fast and relatively robust response. The speed controller PI gains chosen also achieve good stability (phase margin: 85^o; gain margin: 58dB). The gains of the speed controller have the following values: the proportional gain $K_P^{SC} = 3500$, the integral gain $K_I^{SC} = 20000$.

Figure 3.16b shows the tidal turbine power curves at zero pitch angle for different tidal current speeds, the MPPC which passes from the maximum point of each power curve shown and the tidal turbine power of the simulated TCCS for the step change in tidal current speed. As it can be observed the tidal turbine power output follows the 2.2m/s power curve until it reaches the point that meets the MPPC. For a tidal current speed input of 2.2m/s maximum tidal turbine power output is achieved when the generator is operating at 880rpm. When the step change in tidal current speed occurs, from 2.2m/s to 2.5m/s, the tidal turbine power output increases suddenly but due to the instant increase of the tidal current speed the generator speed is still at 880rpm. For a 2.5m/s tidal current speed input the tidal turbine power output is not optimal when the generator is operating at 880rpm. As it was shown in Figure 3.16a, after the step change the generator speed is increasing until 1000rpm are reached, which is the point that the MPPC crosses the power curve of the 2.5m/s. For any changes in the tidal current speed input the speed controller will try to increase or decrease the generator speed until the point where the MPPC crosses the respective power curve. Figure 3.17 shows an example when the tidal current speed increases relatively slowly.

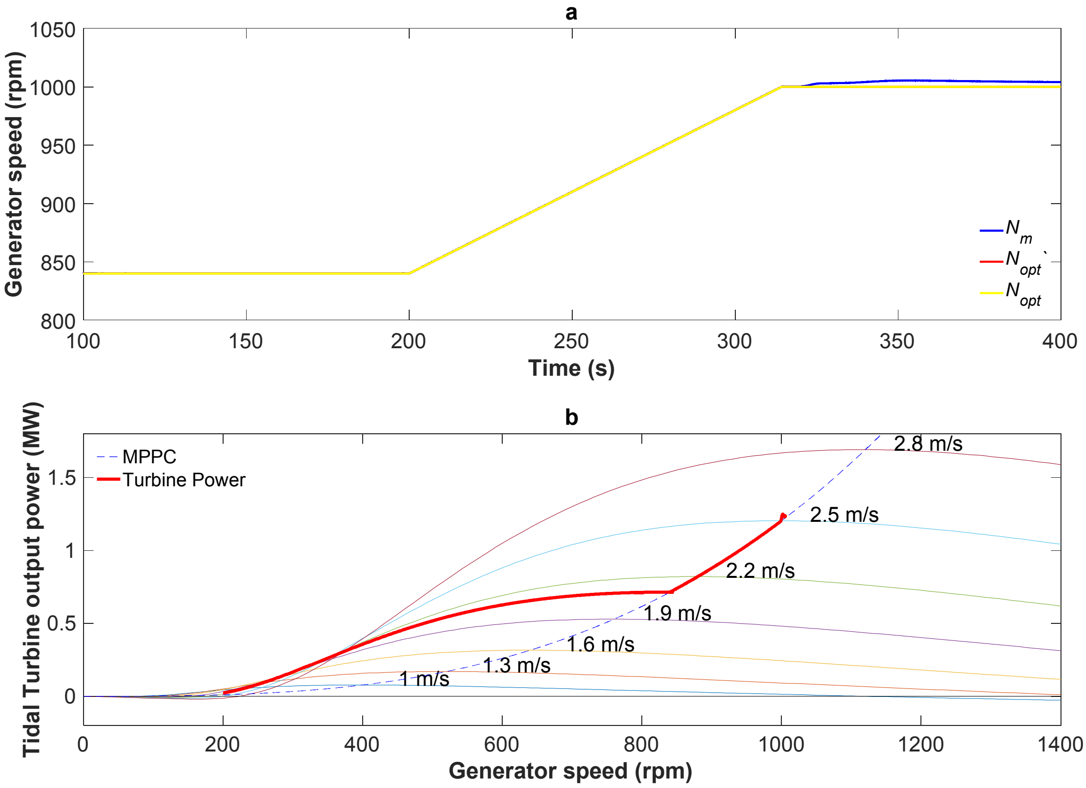

Figure 3.17 Ramp response of the speed controller implemented in MATLAB/Simulink. a. Generator speed over time. b. Tidal turbine power depending on the generator speed.

In Figure 3.17a the generator speed over time for a ramp increase in tidal current speed input is shown. At the first 200s the TCCS is operating at 2.1m/s input until the system reaches steady state. In Figure 3.17b this is shown by the turbine power following the 2.1m/s power curve until it reaches the MPPC. At 200s the tidal current speed increases with a rate of 0.0035m/s per second. In Figure 3.17a N_m follows N_{opt} accurately and no rate limitation is imposed to the optimum speed and therefore N_{opt} is equal to N_{opt}'. At around 315s the tidal current speed input is 2.5m/s which is the rated speed of the turbine. The speed shown in Figure 3.17a after the 315s is limited by the pitch controller discussed in Section 3.2.1. Based on the turbine power results of Figure 3.17b it can be observed that with the operation of the speed controller the MPPC is followed as the tidal current speed is increasing from 2.1m/s to 2.5m/s. This means that tidal turbine is always operating at peak hydrodynamic coefficient harnessing maximum power from the tidal current resource.

The main aim of the reference torque saturation presented in Figure 3.15 is to constrain the electromagnetic torque of the generator at certain values based on the operating region of the generator. The operating regions of the generator are discussed in the following section.

3.4.3 Supervisory control

The supervisory controller's aim is to define the generator operating regions and change the operation of the system by saturating the optimum generator speed, ω_{opt}, and reference electromagnetic torque, T_e*. In order to better understand the operation of the supervisory controller the block diagram of the complete MPPT system is presented in Figure 3.18.

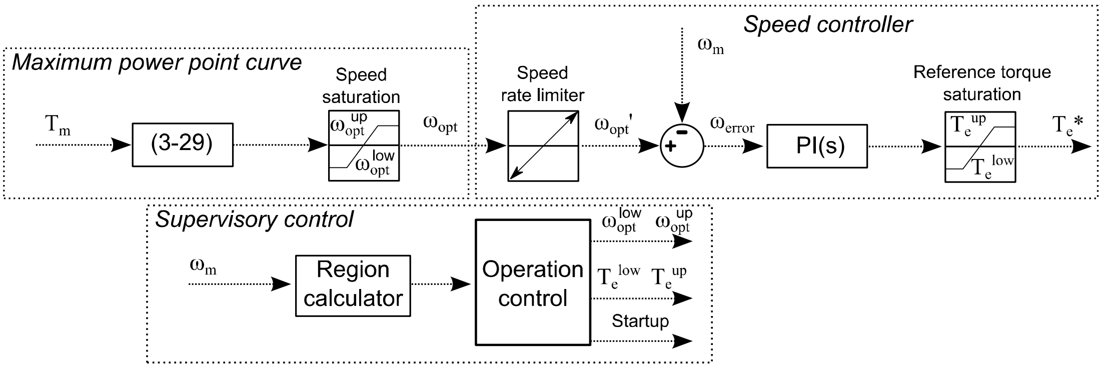

Figure 3.18 Block diagram of the MPPT system.

The way the supervisory controller works changes depending on the application. In this chapter two different supervisory controllers are compared. The first one is based on the prototype of AHH and is published in [56] (*Sup H*). The second one is based on the conventional control of wind turbines (*Sup W*). A summary of the supervisory controllers is presented in Table 3.9.

Table 3.9 Operating principles of *SupH* and *SupW*.

	Sup H		*Sup W*	
Generator	Speed	Torque	Speed	Torque
Region 1	Increasing to 800rpm	Is negative motoring the generator	Increasing from free flow up to 250rpm	No torque production
Region 2	Constant at 800rpm	Increasing as flow increases	Increasing based on (3-23)	Increasing based on (3-23)
Region 3	Increasing based on (3-23) to rated value	Increasing based on (3-23) to rated value	Increasing based on (3-23) to rated value	Increasing based on (3-23) to rated value
Region 4	Constant	Constant	Constant	Constant

The operation of the two different supervisory controllers is shown in Figure 3.19.

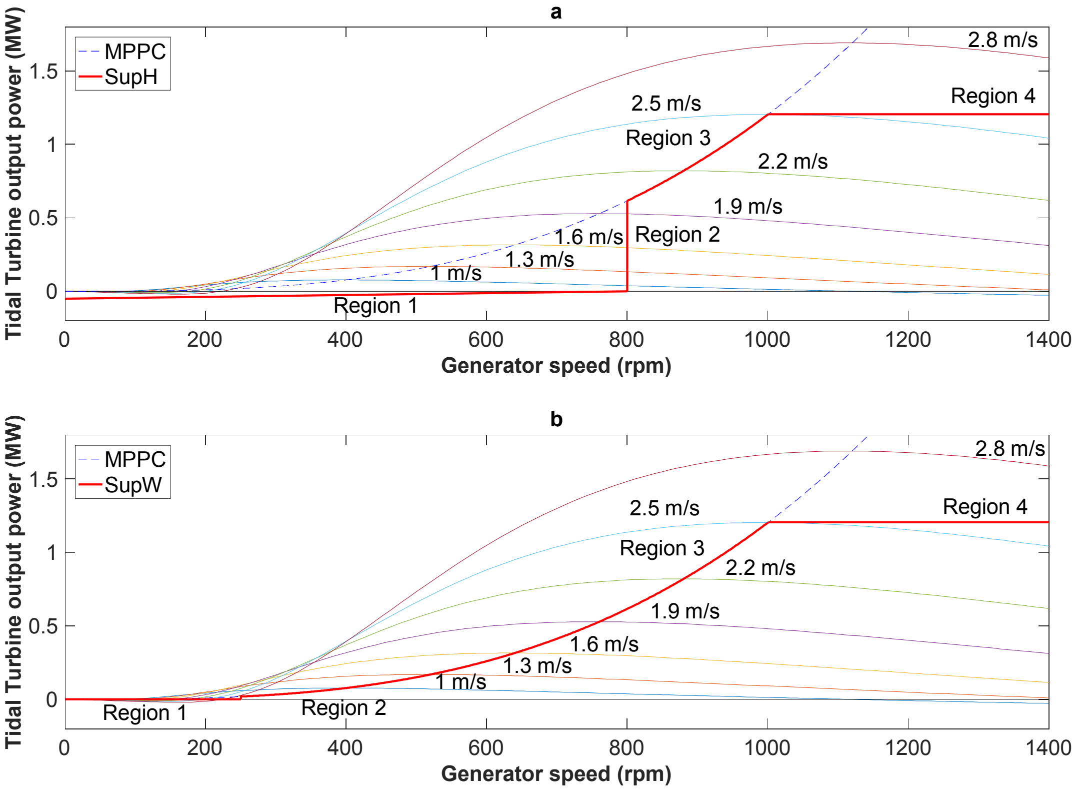

Figure 3.19 a. Power curve of a TCCS with *SupH*. b. Power curve of a TCCS with *SupW*.

3.5 Generator side power transmission

In a system with long distance controls, generator side power transmission will generate the majority of transmission losses. As described above, the generators operate at variable speed which results in variable frequency, current and voltage. The variable frequency output of the generator is transmitted to shore by three-phase cables. A step-down transformer is utilised to convert medium voltage to low voltage for the generator side VSC. Between the generator side VSC and the step-down transformer, filters are installed in order to improve voltage and current quality for the power transmission. These generator side filters have been identified as one of the most important components for a system with long distance controls. By calculating the exact filter parameters, minimum losses and high quality voltage and current in the transmission cables can be achieved. Chapter 4 will focus on the detailed design and effect of the generator side filters. However, in this chapter only the common filters used in the tidal current energy industry will be mentioned since the model described in this chapter is based on the AHH prototype.

3.5.1 Cables

Long subsea cables are modelled with a network of π-sections in order to accurately represent the uniform distribution of the cable resistance R_C, inductance L_C and capacitance C_C. In order to accurately represent the uniform distribution with lumped parameters and therefore to obtain accurate results at the cable terminals for transient analysis, several identical π-sections are connected in series. The number of identical π-sections required to accurately represent frequency transients is given by the following equation [95]:

$$\boldsymbol{N_\pi = \frac{8 \times l_C \times f_{max}}{v_C}} \tag{3-30}$$

Where v_C is the travelling speed of the waves in the cables and is defined in (3-31), l_C is the cable length and f_{max} is the maximum frequency that is required to be accurately represented.

$$\boldsymbol{v_C = \frac{1}{\sqrt{L_C \times C_C}}} \tag{3-31}$$

In this thesis the analysis is based on the particular cases in which AHH is involved. For the above reason the cable model was based on the Pirelli cable used at the tidal site of EMEC and is described in [96]. The Pirelli cable is an 11kV, three core ethylene propylene rubber (EPR) insulated submarine cable constructed for alternating current. It has an optical fibre unit, three 2.5mm^2 copper signal cables and is double wire armoured. Regarding the transient analysis of this system, it lies in the low frequency range and therefore f_{max} is chosen to be 5 kHz. The parameters of the cascaded π-network are given in Table 3.10 and Figure 3.20 shows the π-network modelled for 3.5km cable length.

Table 3.10 Submarine cable network parameters.

Symbol	Quantity	Value
R_C	Cable resistance	0.197 Ω/km
L_C	Cable inductance	0.742 mH/km
C_C	Cable Capacitance	0.310 μF/km
$\lvert Z_C \rvert$	Cable characteristic impedance	55.98 Ω
l_C	Cable length	3.5 km
N_π	Number of π-sections	2.12
N_π`	Number of π-sections chosen	3
f_{max}`	Maximum accurately represented frequency	7000 Hz

Since two π-sections cannot represent the frequency range of 5000Hz, we chose three π-sections that can actually represent f_{max}`.

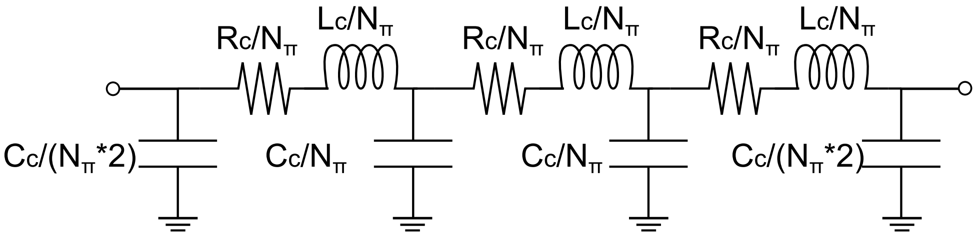

Figure 3.20 Model of the submarine cable with three π-sections.

3.5.2 Filters

Optimisation, detailed design and analysis of filters for long distance control in TCCS will be discussed in Chapter 4. In this section, off-the-shelf filters used by the industry in long distance control applications will be discussed. Based on the industrial input from AHH two common passive filters are used simultaneously for long distance control applications. These two filters are the *first-order damped high-pass filter* (Figure 3.21a) and the *second-order band-pass filter* (Figure 3.21b). In a three-phase system both filters are used in delta-winding connection.

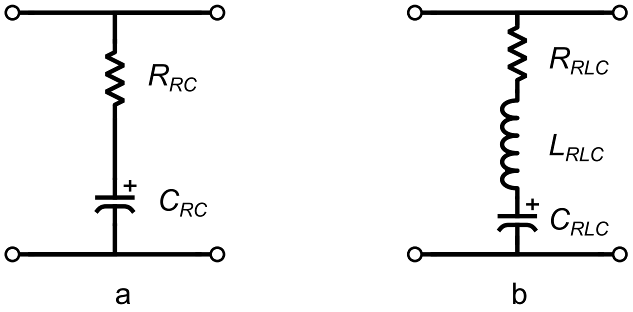

Figure 3.21 Filters modelled for the reference. TCCS a. *RC* filter. b. *RLC* filter.

The *first-order damped high-pass filter*, from now on referred to as the *RC* filter, is composed of a shunt capacitor C_{RC} and a series resistance R_{RC}. The shunt capacitor is used to reduce voltage notching from the rectifier switching and improve the power factor of the generator side system. The series resistance is used to provide damping.

The *second-order band-pass filter*, from now on referred to as the *RLC* filter, comprises a series connection of a capacitor C_{RLC}, an inductor L_{RLC} and a damping resistor R_{RLC}. The aim of the filter is to mitigate a single harmonic component. The harmonic component mitigated is defined by the parameters of the capacitor and the inductor as in (3-32). The damping resistor is usually small and affects the quality factor of the *RLC* filter as shown in (3-33).

$$f_{tuned}^{RLC} = \frac{1}{2\pi\sqrt{L_{RLC}C_{RLC}}} \tag{3-32}$$

$$Q^{RLC} = \frac{1}{R_{RLC}}\sqrt{\frac{L_{RLC}}{C_{RLC}}} \tag{3-33}$$

The parameters used for these two types of filters were provided by AHH and are presented in Table 3.11.

Table 3.11 Parameters used in the TCCS model of the *RC* and *RLC* filters.

Symbol	Description	Value
R_{RC}	*RC* filter damping resistance	0.1 Ω
C_{RC}	*RC* filter capacitance	64 μF
R_{RLC}	*RLC* filter damping resistance	0.1 Ω
L_{RLC}	*RLC* inductance	60 μH
C_{RLC}	*RLC* capacitance	21.5 μC
f_{tuned}^{RLC}	*RLC* filter tuned frequency	2558.4 Hz
Q^{RLC}	*RLC* filter quality factor	9.65

More common type filters are available and the details can be found in [97]. The filters installed on the generator side interact with the generator side choke, which is assumed to be 0.05pu, and the step-down transformer inductances. The details about the step-down transformer are presented in Section 3.5.3.

3.5.3 Step-down Transformer

The transformer at the generator side steps-down the generator voltage of 6600V to 690V which is the voltage that the VSC operates. At the generator side the transformer is delta-connected and at the VSC side the windings are wye-connected. The transformer model is based on three single-phase transformers, one for each phase. Therefore, there are no interactions and mutual inductances between phases. In addition, it is assumed that the transformer always operates at the linear region and never reaches saturation levels. The parameters of the generator side transformer were provided by AHH and are presented Table 3.12.

Table 3.12 Generator side transformer parameters.

Symbol	Quantity	Value
S_{mt}	Apparent power range	1.2 – 1.8 MVA
V_{mt}^{wye}	Wye connection voltage	690 V
V_{mt}^{delta}	Delta connection voltage	6600 V
f_{mt}	Nominal frequency	50 Hz
R_{mt}^{wye}	Wye resistance	0.0016 pu
L_{mt}^{wye}	Wye inductance	0.0639 pu
R_{mt}^{delta}	Delta resistance	0.0072 pu
L_{mt}^{delta}	Delta inductance	0.0479 pu
R_{mt}^{mag}	Magnetisation resistance	618 pu
L_{mt}^{mag}	Magnetisation inductance	418 pu

3.6 The DC link

All the power from the generator that is converted by the generator side VSC passes through the DC link. The DC link voltage is kept constant by converting the input power to the DC link into a constant voltage and frequency on the grid side. This conversion is achieved by the grid side VSC which is controlled by the grid side controller discussed in Section 3.7.1. The DC link model is composed of an ideal capacitor, a discharging resistance and an equivalent series resistance (ESR). The diagram of the DC link model is presented in Figure 3.22 and the dc link parameters are given in Table 3.13.

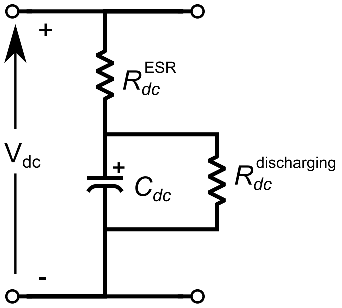

Figure 3.22 Block diagram of the DC link model implemented in MATLAB/Simulink.

Table 3.13 DC link model parameters.

Symbol	Quantity	Value
V_{dc}	DC link voltage	1100 V
C_{dc}	DC link capacitance	11600 μF
$R_{dc}^{discharging}$	Discharging resistance	1 MΩ
R_{dc}^{ESR}	ESR	0.5 mΩ

3.7 The grid side

The power generated by the TCCS is delivered to the grid through a VSC. The grid-tied inverter is connected to the grid through a number of components; a line reactor to reduce line current distortion, a filter that reduces harmonics and a step-up transformer from 690V to 11kV. In some cases, which will be presented in Chapter 5, the grid connection will be at 33kV. The inverter is controlled by a PWM scheme called voltage oriented control (VOC) with decoupled controllers [93] which ensures a constant DC link voltage of 1100V_{dc}, constant frequency output of 50Hz on the AC side and control over the amount of reactive power flowing based on grid requirements.

3.7.1 Grid side controller

As stated above, the grid side controller is based on the VOC scheme with decoupled controllers [93]. The block diagram of the VOC controller implemented for the TCCS is shown in Figure 3.23. The VOC model has three aims:

- To keep the DC link voltage, V_{dc}, constant at 1100 V.
- To synchronise the frequency output on the AC side to 50 Hz.
- To control the amount of reactive power output from the grid side VSC. The amount of reactive power flowing from the grid side VSC to the grid can be controlled by changing Q_g* as shown in Figure 3.23. Depending on power factor requirements of the grid operator at a specific point of the network, Q_g* can vary. For the purposes of this thesis the reactive power flow is set to zero.

The VOC scheme with decoupled controllers is also described in (3-34).

$$\begin{cases} \boldsymbol{V_{di}(t) = -\left[K_P^I(i_{dg}^* - i_{dg}) + K_I^I\int(i_{dg}^* - i_{dg})dt\right] + \omega_g L_g i_{qg} + V_{dg}} \\ \boldsymbol{V_{qi}(t) = -\left[K_P^I(i_{qg}^* - i_{qg}) + K_I^I\int(i_{qg}^* - i_{qg})dt\right] - \omega_g L_g i_{dg} + V_{qg}} \end{cases} \tag{3-34}$$

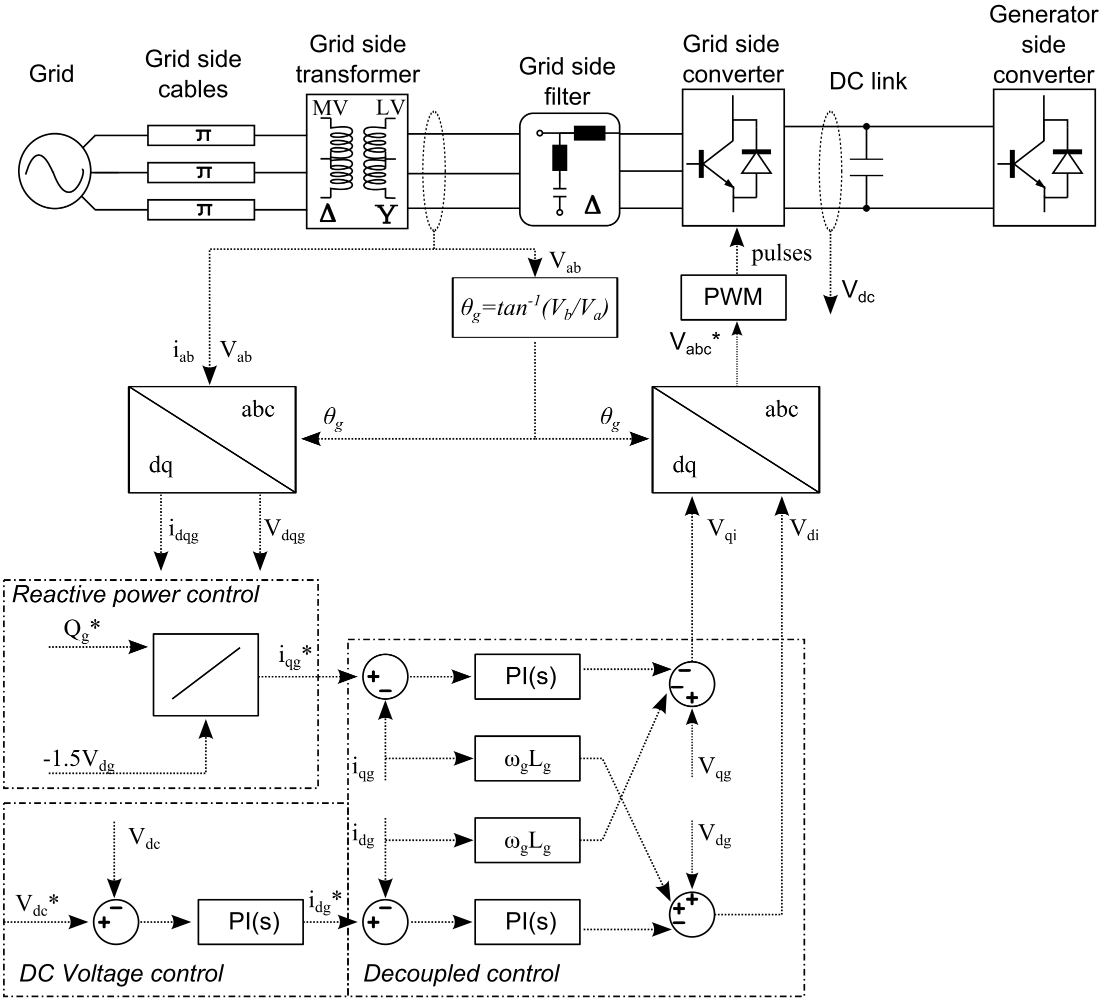

Figure 3.23 Block diagram of the Voltage Oriented Controller implemented in MATLAB/Simulink for the TCCS.

Where L_g is the grid side line reactor inductance, ω_g is the angular frequency of the grid, $V_{dc}*$ is the reference value for the DC link voltage and θ_g is the grid voltage angle. The transfer function of the PI controller is shown in (3-35) where the gains, K_P^I and K_I^I, of the inner current loops can be seen.

$$\boldsymbol{K_P^I + \frac{K_I^I}{s}} \tag{3-35}$$

The VOC controller has two loops. An outer loop in which the DC link voltage is controlled (DC voltage control in Figure 3.23) and the inner current loops. Apart from the DC link voltage regulation, the outer loop of the VOC controller needs to achieve a stable operation. Using bode diagrams for tuning purposes this leads to a high phase margin. For the inner current loops fast response is required which leads to a high bandwidth, at least a decade higher compared to the outer loop. In addition it is desirable that the crossover frequency of the inner current loop to be lower than the switching frequency of the controller in order to avoid harmonic oscillations. The initial tuning of the PI controller gains was implemented based on [98] but the final gains were based on the bode diagram tuning method using the above mentioned controller requirements in MATLAB/Simulink. The PI controller gains for the inner loop are: $K_P^I = 0.3$, $K_I^I = 30$ and for the outer loop: $K_P^V = 1.388$, $K_I^V = 400$.

The operation of the outer loop of the VOC controller can be seen in Figure 3.24 in a step change of the reference DC link voltage from 1100V to 1200V. At this point it has to be noted that the DC link voltage during the operation of the TCCS remains constant at 1100V. Figure 3.24 is presented in order to show the controller response.

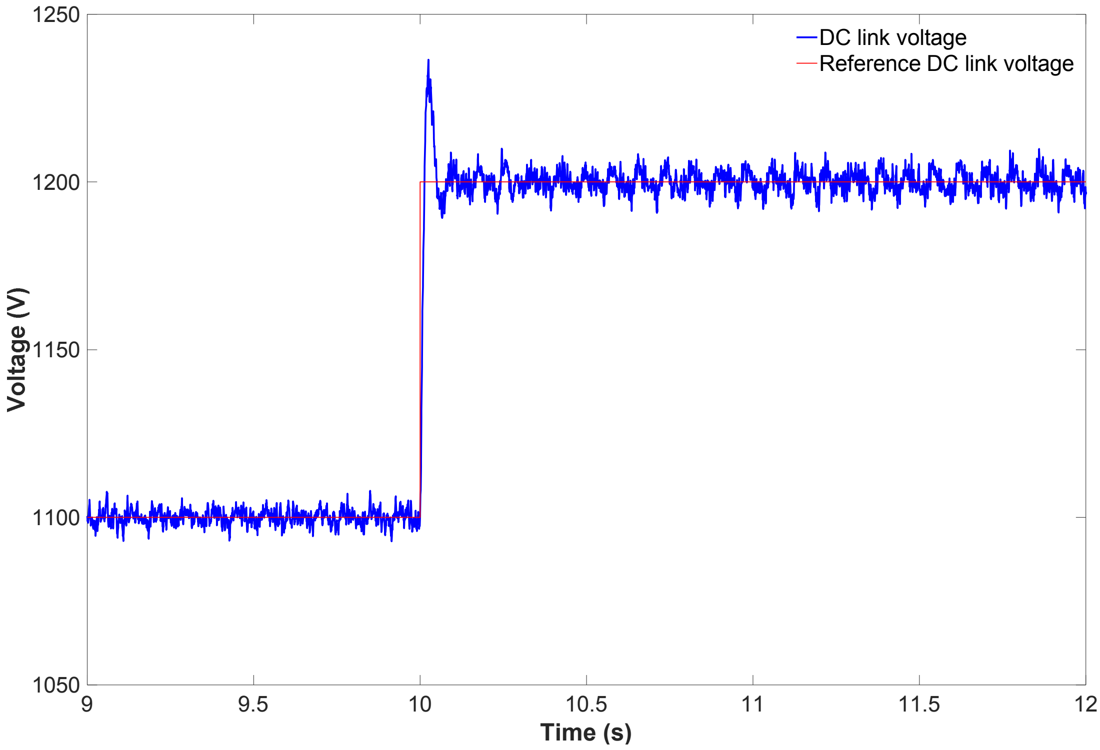

Figure 3.24 Comparison of measured and reference DC link voltage for a step change in the reference DC link voltage from 1100V to 1200V.

Based on the results presented in Figure 3.24 it can be observed that the DC link voltage follow the reference DC link voltage. The overshoot of the DC link voltage is around 3% and the ripple ±0.75%.

The operation of the inner loop of the VOC controller can be seen in Figure 3.25. In Figure 3.25a step change in tidal current speed takes place. Figure 3.25a shows the *d-axis* current response of the VOC controller. Figure 3.25b depicts the *q-axis* current response when the reactive power demand of the grid operator changes from 0pu to 0.2pu.

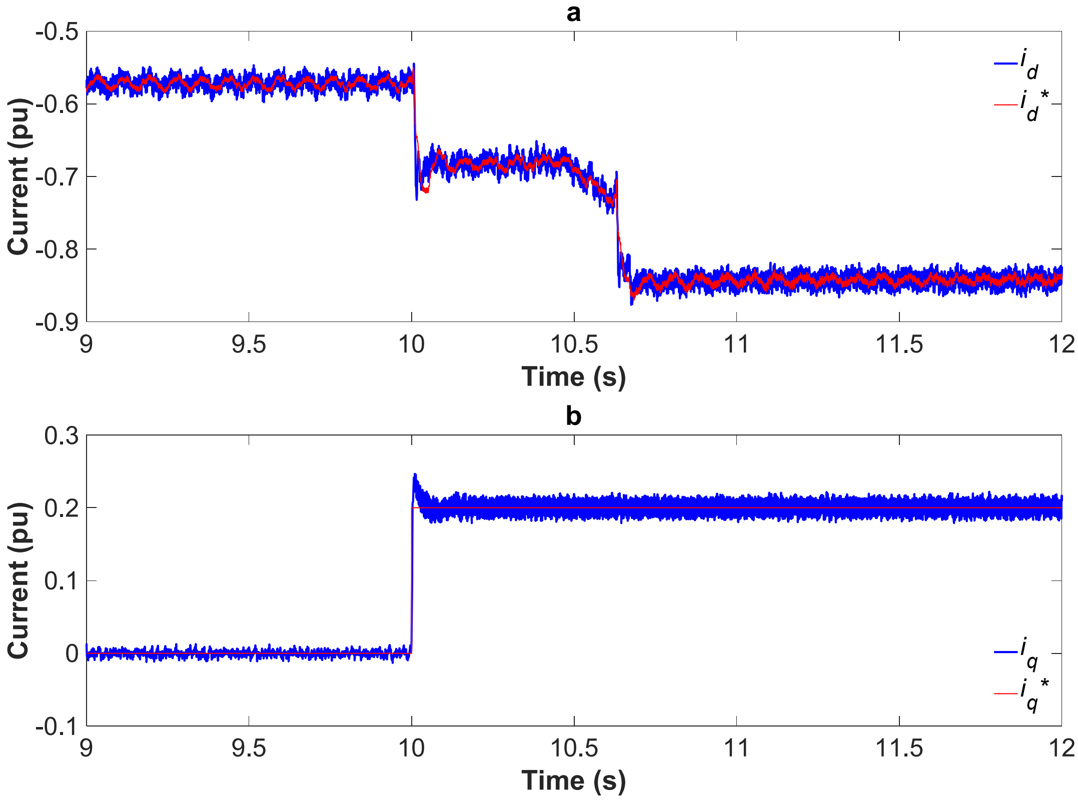

Figure 3.25 VOC inner current controller responses to step changes. a. *d-axis* current for step change in tidal current speed. b. *q-axis* current for a step change in reactive power demand from 0pu to 0.2pu.

Observing Figure 3.25 it can be said that the current loops of the VOC controller follow the reference signals. In both cases the overshoot is very small and the ripple of the currents does not exceed ±10%.

3.7.2 Grid side transformer

The transformer at the grid side steps-up the voltage from the grid side VSC from 690V to 11000V which is the grid voltage. At the VSC side the transformer is wye-connected and at the grid side the windings are delta-connected. The transformer model is based on three single-phase transformers, one for each phase. Therefore, there are no interactions and mutual inductances between phases. In addition, it is assumed that the transformer always operates at the linear region and never reaches saturation levels. The parameters of the grid side transformer were provided by AHH and are presented in Table 3.14.

Table 3.14 Grid side transformer parameters.

Symbol	Quantity	Value
S_{gt}	Apparent power range	1.2 – 1.8 MVA
V_{gt}^{wye}	Wye connection voltage	690 V
V_{gt}^{delta}	Delta connection voltage	6600 V
f_{gt}	Nominal frequency	50 Hz
R_{gt}^{wye}	Wye resistance	0.0009 pu
L_{gt}^{wye}	Wye inductance	0.0812 pu
R_{mt}^{delta}	Delta resistance	0.0038 pu
L_{gt}^{delta}	Delta inductance	0.0651 pu
R_{gt}^{mag}	Magnetisation resistance	520 pu
L_{gt}^{mag}	Magnetisation inductance	430 pu

In the TCCS with long distance controls the grid side transformer is directly connected to the grid. However, in model that will be presented in Chapter 5 the grid side transformer will be connected to grid side cables.

3.7.3 Grid side cables

A TCCS with long distance controls has no need for long grid side cables to connect the TCCS with the grid. Power transmission is achieved by the machine side cables discussed in Section 3.5.1. However, for electrical topologies that will be discussed later in this thesis, grid side cables are considered at different voltages and ratings. Information on cable parameters were drawn from *Nexans Submarine power cables* which is available in Appendix C [99]. The parameters chosen were based on the medium voltage submarine cable, including fibre optic cable. The cable designs range from 10kV to 36kV and conductor cross-sectional areas from 35mm^2 to 630mm^2.

3.7.4 Grid

The grid is modelled as a balanced three-phase voltage source connected in wye. The wye-connection is grounded. The grid model was based on EMEC facilities where tidal and wave energy devices are connected. The fault levels were based on the following:

- For the 11kV connection, the maximum three-phase fault level is defined as 52.1 MVA and the maximum *X/R ratio* is 1.8.
- For the 33kV connection, the maximum three-phase fault level is defined as 45.6 MVA and the maximum *X/R ratio* is 1.024.

3.8 Validation of the tidal current conversion system model

As described at the beginning of this chapter the reference TCCS model is based on the TCCS installed by AHH at EMEC. AHH has provided information about the power generated and losses at the generator side. In order to validate the Simulink model developed in this chapter, the results from the reference TCCS model are compared with the actual data provided by AHH. Based on the available data two comparisons can be made:

- The power generated from the SCIG over a half tidal cycle of a semidiurnal tide.
- The averaged losses at each stage of the generator side as percentage to the power generated.

The power generated from the SCIG over a half tidal cycle of a semidiurnal tide is depicted in Figure 3.26.

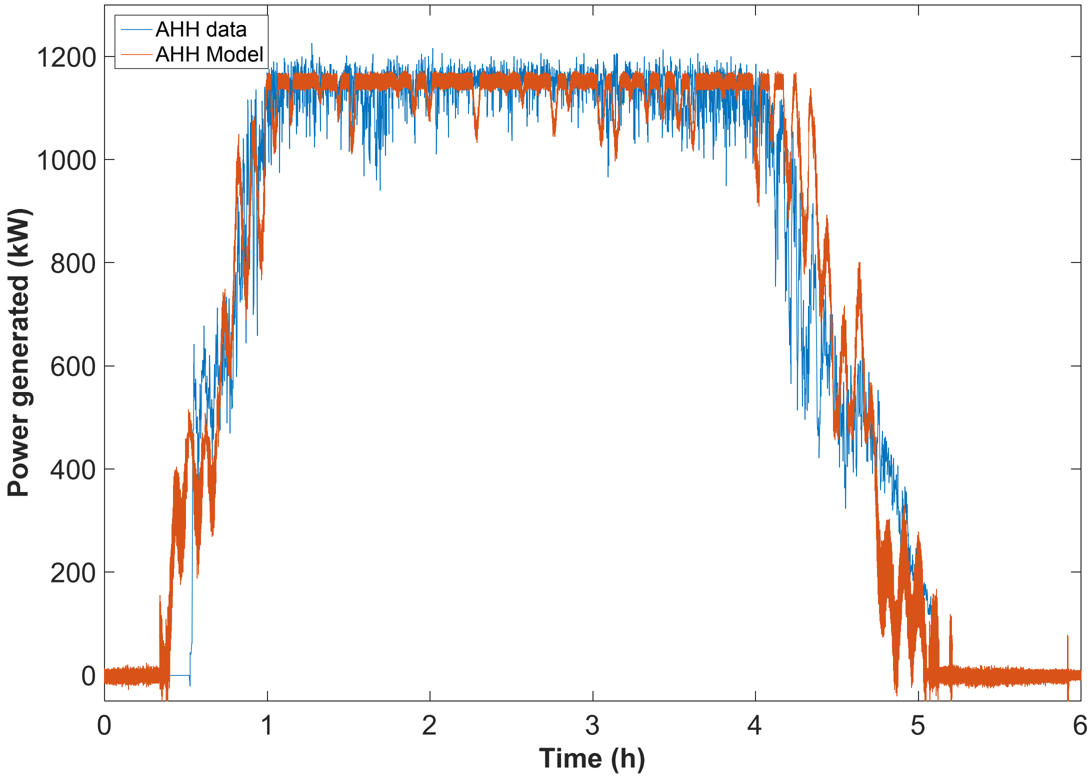

Figure 3.26 Comparison of power generated over time.

As a first observation it can be said that the simulation model matches the AHH data. However, differences at the power output appear at several points. At start-up the power generated from the *AHH Model* increases gradually with high ripples compared to *AHH data* which increases instantly to approximately 600kW. When the generator reaches rated power output the Simulink model produces a more stable power output compared to the AHH data. At rated operation the AHH data reveal power ripples from 950kW to 1200kW. At approximately 4 hours the flow speed is too low for the tidal turbine to maintain rated power and therefore power generated is reducing. During the decreasing period of power generated the model matches the AHH data. In order to quantify the resemblance of model output to AHH data the statistical tools of correlation coefficients, mean values and the residual variance are used. Table 3.15 presents the statistical values that determine the goodness of fit of the *AHH Model* output compared to *AHH data*. More details about the statistical tools used can be found in Appendix B.

Table 3.15 Statistical values for the goodness to fit of power generated between AHH data and TCCS model.

	AHH data	***AHH Model***
Mean	701.2 kW	711.6 kW
%diff of mean value	1.4832	
Correlation coefficients	0.9780	
Residual variance	0.9558	

From the statistical results of Table 3.15 it can be said that the mean values between the two outputs are almost the same. The high value of the correlation coefficient near unity shows a strong linear relationship between AHH data and model output. Finally, the residual variance shows that the *AHH Model* output predicts the 95.58% of the variation of *AHH data*.

Finally the power losses at different stages of the generator side at different operating points are available. The differences between power losses between the *AHH data* and the *AHH Model* developed in Simulink are presented in Table 3.16.

Table 3.16 Power losses of the generator side at different operating points of the TCCS. Comparison between model losses and actual data provided by AHH.

P_{gen} (pu)	Filter losses (*AHH Model*)	Transformer losses (%)		Cable losses (%)	
		AHH data	*AHH Model*	*AHH data*	*AHH Model*
1.00	0.68%	1.92%	1.80%	1.97%	1.99%
0.75	1.21%	2.05%	1.94%	1.50%	1.70%
0.50	8.29%	2.24%	2.55%	1.00%	1.58%

Table 3.16 presents the averaged losses at different stages of the TCCS. When the TCCS operates at rated power (P_{gen} = 1pu) the cable and transformer losses match between the *AHH data* and *AHH Model*. When the TCCS generates 75% or 50% of the rated power, cable losses drop in both cases but at different rates. The cable losses estimated by the *AHH Model* are higher compared to the *AHH data*. This is due to the

fact that the cable resistance used in the cable model, presented in Section 3.5.1, is the resistance when the cables are operating at 90 ^{o}C which is the maximum operating temperature. Therefore whether the TCCS is operating at lower power ratings, which results to reduced temperatures in the cables, the *AHH Model* assumes the worst-case scenario of maximum cable resistance. Regarding the transformer losses, these increase as the power generated is reducing from 1pu to 0.5pu. This is due to the fact that the transformer has a minimum of constant losses. The transformer's constant losses become more significant as less power is generated by the TCCS.

Finally, filter losses generated by the *AHH Model* are presented in Table 3.16. These losses will be compared in the next chapter with the losses produced by a similar type of filter designed using the power loss minimisation algorithm.

3.9 Summary

This Chapter focused on modelling the different parts of the TCCS. The modelling of the TCCS was based on a reference TCCS that uses long distance controls. The parameters of the reference TCCS were provided by AHH. In addition, components for TCCS that have the generator and grid side VSC in the nacelle were analysed. The modelling in this Chapter focused on accurately representing the long three-phase subsea cables and the control of the different types of generators in a long distance control scheme. The speed controller, presented in Section 3.4.2, was also an important aspect of the model because it ensures that the TCCS always captures maximum power from the tidal current speed input. In the final parts of this Chapter, Section 3.8, the reference TCCS was compared with actual power and power loss data supplied by AHH. It is shown, using a number of statistical tools, that the reference TCCS modelled can predict the actual output power of a commercial scale tidal current turbine. In addition, the losses at the different parts of the model and the actual tidal current turbine were compared and showed a perfect match at rated operation and small variations for below rated operation. Finally, the limitation of the TCCS model compared to an actual system were described.

Chapter 4

Tidal current conversion systems with dry converters

Operating a TCCS with dry converters is advantageous in terms of maintenance and cost. This is due to the fact that fewer components are installed underwater. In the case of a fault in the power converter system there is no need for underwater extraction and maintenance. In addition, using dry converters eliminates the need for additional auxiliary systems to maintain normal operating conditions in the nacelle. Dry converters can be placed either on land or on an offshore platform. Both options have been suggested in the reports of the three major electrical companies presented in Section 2.6. In this chapter the issues that arise when a machine is controlled from afar are presented. What is more, ways to mitigate these effects are presented and tested based on literature, using the TCCS model described in Chapter 3. Finally, a novel method of minimising these effects as well as reducing power loss is presented in the last section of this Chapter. It should be noted that the analysis is based on the SCIG model with DTC SVM controller described in Chapter 3.

4.1 Introduction to systems controlled from afar

Literature regarding long distance control has been discussed in Section 2.7. Based on the literature two major problems can be identified when a machine is controlled from afar. The first issue are the voltage reflections in the system between the generator and the VSC and the second problem is resonance due to the interaction of the inductive and capacitive components of the system. Voltage reflection and resonance can cause excessive harmonics to flow in the cables and overvoltages at the generator terminals. These problems will be analysed in the following sections in order to determine the need to mitigate the associated harmonics and overvoltages.

4.1.1 Wave reflection analysis

Voltage pulses, created by the generator side controller, travel from the VSC to the generator through electrical cables. Their behaviour can be analysed the same way as travelling waves in transmission lines [79]. Voltage waves travelling from the VSC to the generator, also called forward-travelling waves, are reflected at the end of the long cables. The reflected voltage waves, also called backward-travelling waves, are mirrored replicas of the forward-travelling waves. This means that the backward-travelling waves are equal to the forward-travelling waves multiplied by the voltage reflection coefficient at the cables end. The voltage reflection coefficient, Γ_n, is determined by the surge impedance ratio at node *n* and is given in (4-1).

$$\boldsymbol{\Gamma_n = \frac{Z_n - Z_C}{Z_n + Z_C}} \tag{4-1}$$

Where Z_n is the impedance at node *n* and Z_C is the cable characteristic impedance at specified frequency ω in rad/s.

$$\boldsymbol{Z_C = \sqrt{\frac{(j\omega L_C + R_C)}{(j\omega C_C)}}} \tag{4-2}$$

The impedance at the VSC terminals is very low because it is dominated by the dc-link capacitor and therefore results in $\Gamma_{VSC} \approx -1$. According to [79], the voltage reflection coefficient of the generator, Γ_{Gen} is close to unity for low power machines but for high power machines this can be less than 0.65 [80].

In this thesis, two cases will be explored regarding the generator surge impedance. Firstly, a worst case scenario is chosen where the travelling waves arriving at the generator terminals are completely reflected resulting in 2 times the voltage magnitude of the travelling waves. Based on (4-1) this leads to $\Gamma_{Gen} \approx 1$. The second scenario assumes a voltage reflection coefficient at the generator terminals equal to $\Gamma_{Gen} = 0.5$ which means that the travelling waves arriving at the generator terminals are reflected by 50% resulting in 1.5 times the voltage magnitude of the travelling wave.

4.1.2 System resonance

Apart from the voltage reflections, additional harmonics can be generated by the interaction of cable capacitance and inductance. This interaction creates frequencies where the system is resonant [80]. If harmonics are generated at the resonant frequencies they can be magnified and lead to overvoltages and increased harmonic distortion at the generator terminals. In addition, when a transformer is installed between the VSC and the cables, the transformer inductance interacts with the cable capacitance creating additional resonant frequencies. In order to quantify the phenomenon of resonance, voltage gain graphs are created for different systems that are controlled from afar as shown in Figure 4.1. The voltage gain graph is created by assuming that the VSC is sending voltage pulses and that the generator terminals are the receiving end of these pulses. Therefore we can compute the state-space model of the system using MATLAB in discrete form:

$$\begin{cases} \boldsymbol{x}(\boldsymbol{kT}+\boldsymbol{T}) = \boldsymbol{Ax}(\boldsymbol{kT}) + \boldsymbol{Bu}(\boldsymbol{kT}) \\ \boldsymbol{y}(\boldsymbol{kT}) = \boldsymbol{Cx}(\boldsymbol{kT}) + \boldsymbol{Du}(\boldsymbol{kT}) \end{cases} \tag{4-3}$$

Where *T* is the sampling interval, *kT* is the time instant, input vector *x* represents inductor currents and capacitor voltages, input vector *u* represent voltage and current sources and output vector *y* represents voltage and current measurements. So, in order to create the voltage gain graph, (4-3) is simplified to:

$$\begin{cases} \boldsymbol{x}(\boldsymbol{kT}+\boldsymbol{T}) = \boldsymbol{Ax}(\boldsymbol{kT}) + \boldsymbol{BV_{VSC}}(\boldsymbol{kT}) \\ \boldsymbol{V_{Gen}}(\boldsymbol{kT}) = \boldsymbol{Cx}(\boldsymbol{kT}) + \boldsymbol{DV_{VSC}}(\boldsymbol{kT}) \end{cases} \tag{4-4}$$

The solution of the discreet time equation (4-4) can be simplified by transforming it to the frequency domain using the unilateral *Z*-transformation [100]. The unilateral *Z*-transformation of a discreet variable *x(kT)* is given in (4-5).

$$\boldsymbol{X}(\boldsymbol{z}) = \sum_{\boldsymbol{kT}=\boldsymbol{0}}^{\infty} \boldsymbol{z}^{-\boldsymbol{kT}} \boldsymbol{x}(\boldsymbol{kT}) \tag{4-5}$$

Applying the Z-transformation on the state-space model of equation (4-4) the model is transformed as shown in (4-6) and can have an algebraic solution as shown in (4-7).

$$\begin{cases} \boldsymbol{zX}(\boldsymbol{z}) - \boldsymbol{zx}(\boldsymbol{0}) = \boldsymbol{AX}(\boldsymbol{z}) + \boldsymbol{BV_{VSC}}(\boldsymbol{z}) \\ \boldsymbol{V_{Gen}}(\boldsymbol{z}) = \boldsymbol{CX}(\boldsymbol{z}) + \boldsymbol{DV_{VSC}}(\boldsymbol{z}) \end{cases} \tag{4-6}$$

$$\begin{cases} \boldsymbol{X(z) = z(zI - A)^{-1}x(0) + (zI - A)^{-1}BV_{VSC}(z)} \\ \boldsymbol{V_{Gen}(z) = zC(zI - A)^{-1}x(0) + [CB(zI - A)^{-1} + D]V_{VSC}(z)} \end{cases} \quad \textbf{(4-7)}$$

From equation (4-7) the voltage gain graph can be computed by assuming zero initial conditions *x(0)*. Equation (4-8) presents the transformed state space model of equation (4-7) for zero initial conditions.

$$\begin{cases} \boldsymbol{X(z) = (zI - A)^{-1}BV_{VSC}(z)} \\ \boldsymbol{V_{Gen}(z) = [CB(zI - A)^{-1} + D]V_{VSC}(z)} \end{cases} \quad \textbf{(4-8)}$$

From equation (4-8) the voltage gain graph in the complex frequency domain can be calculated as shown in equation (4-9).

$$\boldsymbol{V_{GAIN}(z) = \frac{V_{Gen}(z)}{V_{VSC}(z)} = CB(zI - A)^{-1} + D} \quad \textbf{(4-9)}$$

Moreover, the voltage gain graph can be converted to the s-domain shown in equation (4-10) using the Tustin approximation [100] shown in (4-11).

$$\boldsymbol{V_{GAIN}(s) = \frac{V_{Gen}(s)}{V_{VSC}(s)}} \quad \textbf{(4-10)}$$

$$\boldsymbol{z = e^{sT} \approx \frac{1 + sT/2}{1 - sT/2}} \quad \textbf{(4-11)}$$

The magnitude of the voltage gain graph shows how each frequency component of the voltage pulses generated are multiplied to reach the generator. Therefore, if there is a significant harmonic component generated at a frequency where the voltage gain magnitude is above unity, then this harmonic component will be magnified at the generator terminals. On the other hand, if the voltage gain is below unity at a specific frequency range then the harmonic components at these frequencies will be reduced at the generator terminals. The voltage gain magnitude and the positioning of the magnitude peaks are directly related to the cable and transformer parameters. An example of a voltage gain graph can be seen in Figure 4.1. The voltage gain graph y-axis is plotted in logarithmic scale while x-axis is plotted in a linear scale.

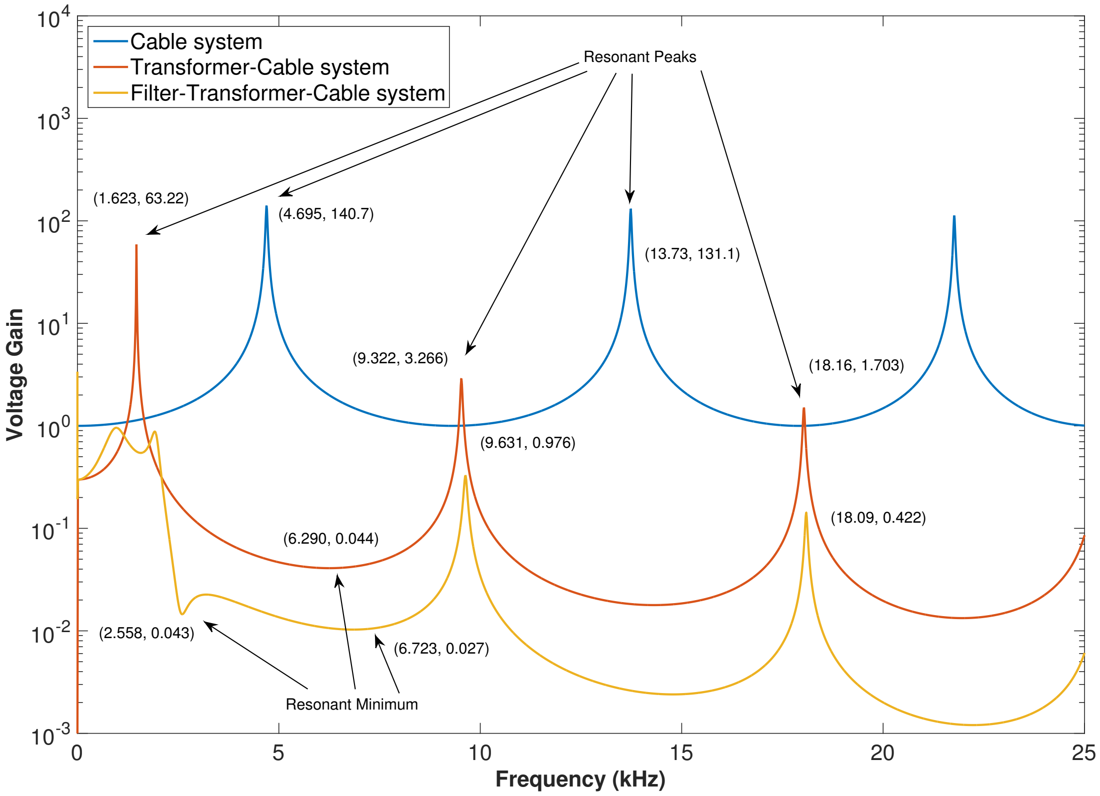

Figure 4.1 Voltage gain graph for a system with cables only and for a system with cables and transformer. There is a significant change in resonant frequencies when the transformer is included in the analysis.

The *Cable system* as shown in Figure 4.1 assumes that the connection between the generator and the VSC is achieved using the generator side cables discussed in Section 3.5.1 without transformer. One can observe in the cable system that three resonant peaks appear at 4695Hz, 13730Hz and 21770Hz. Additional frequency peaks will appear if the frequency range of the study is expanded; however, for the purposes of this study, and since the cable lengths to be analysed are short, the frequency range of 0 to 25 kHz is deemed sufficient. The *Transformer-Cable system (TCS)* is created by using the generator side cables discussed in Section 3.5.1 and the generator side transformer discussed in Section 3.5.3. The *TCS* has resonant peaks at lower frequencies. These appear a lot closer to the switching frequency of the generator controller, 2500Hz, and the operating frequency of the generator, 50Hz. Operating a TCCS with long distance controls with a *Cable system* or a *TCS* without filters would create significant amount of harmonics at the resonant peaks. This will become evident in Section 4.2 where results during the operation of these systems will be presented.

The *Filter-Transformer-Cable system (FTCS)* depicted in Figure 4.1 is based on the reference TCCS model described in Chapter 3. It can be seen that using a filter at the low voltage side reduces significantly the magnitude of the resonant peaks. In addition, due to the *RLC* filter which is tuned at 2558.4Hz a resonant minimum is created. Resonant minimums are defined in this thesis as areas where harmonics are damped and this is shown in Figure 4.1 with low magnitudes of voltage gain. As it will be shown in the next section resonant minimums can be used to improve the operation of the TCCS with long distance controls.

4.2 Switching frequency study

The main aim of this section is to study the effect of resonant peaks and resonant minimums on the operation of the TCCS with long distance controls. The operation of the TCCS is monitored mainly by measuring the voltage at the generator terminals. The voltage at the generator terminals is the quantity most affected by voltage reflections and resonance. Overvoltages appearing at the generator terminals can cause insulation breakdown which in turn can lead to an electrical fault. The study of resonant peaks and resonant minimums will be based on the *Transformer-Cable system* and the *Filter-Transformer-Cable system* presented in Figure 4.1. The *Cable system* is not considered in this study since the reference TCCS modelled in Chapter 3 requires the use of a transformer at the generator side. Each system will be simulated under different controller switching frequencies and the harmonics in each case will be studied. In addition, two different voltage reflection coefficients will be explored; the worst-case scenario where $\Gamma_{Gen} = 1$ and the scenario of $\Gamma_{Gen} = 0.5$, as described in Section 4.1.1.

4.2.1 Transformer-Cable system

The block diagram of a TCCS with long distance controls using a *TCS* is depicted in Figure 4.2. The system is identical to the reference model presented in Chapter 3 with the exception of the absence of generator side filters. The 0.05pu choke at the generator side VSC terminals is still present in this case.

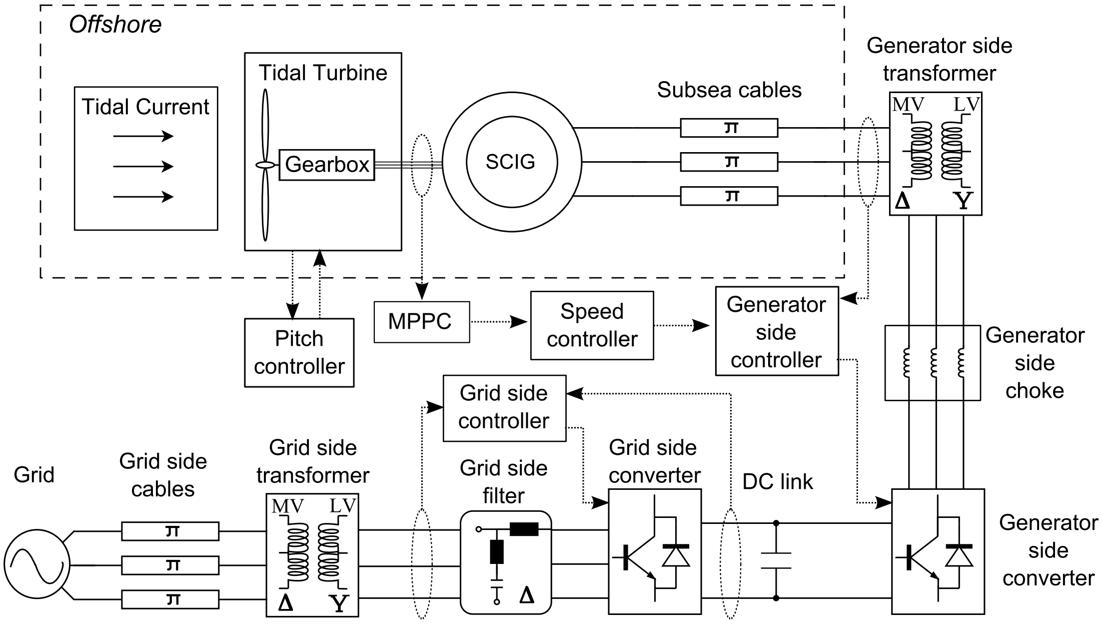

Figure 4.2 Block diagram of the Transformer-Cable system.

The model depicted in Figure 4.2 is simulated at different generator controller switching frequencies, f_{sw}, and results are summarised in Section 4.2.3. An example of the generator voltages at different f_{sw} is depicted in Figure 4.3. In Figure 4.3a and Figure 4.3c the *TCS* is simulated at the reference generator controller switching frequency, f_{sw} = 2500Hz. In Figure 4.3b and Figure 4.3d the *TCS* is simulated at f_{sw} = 6290Hz which is the first resonant minimum frequency as presented in Figure 4.1. The measured generator and transformer voltage in each case is shown in Figure 4.3.

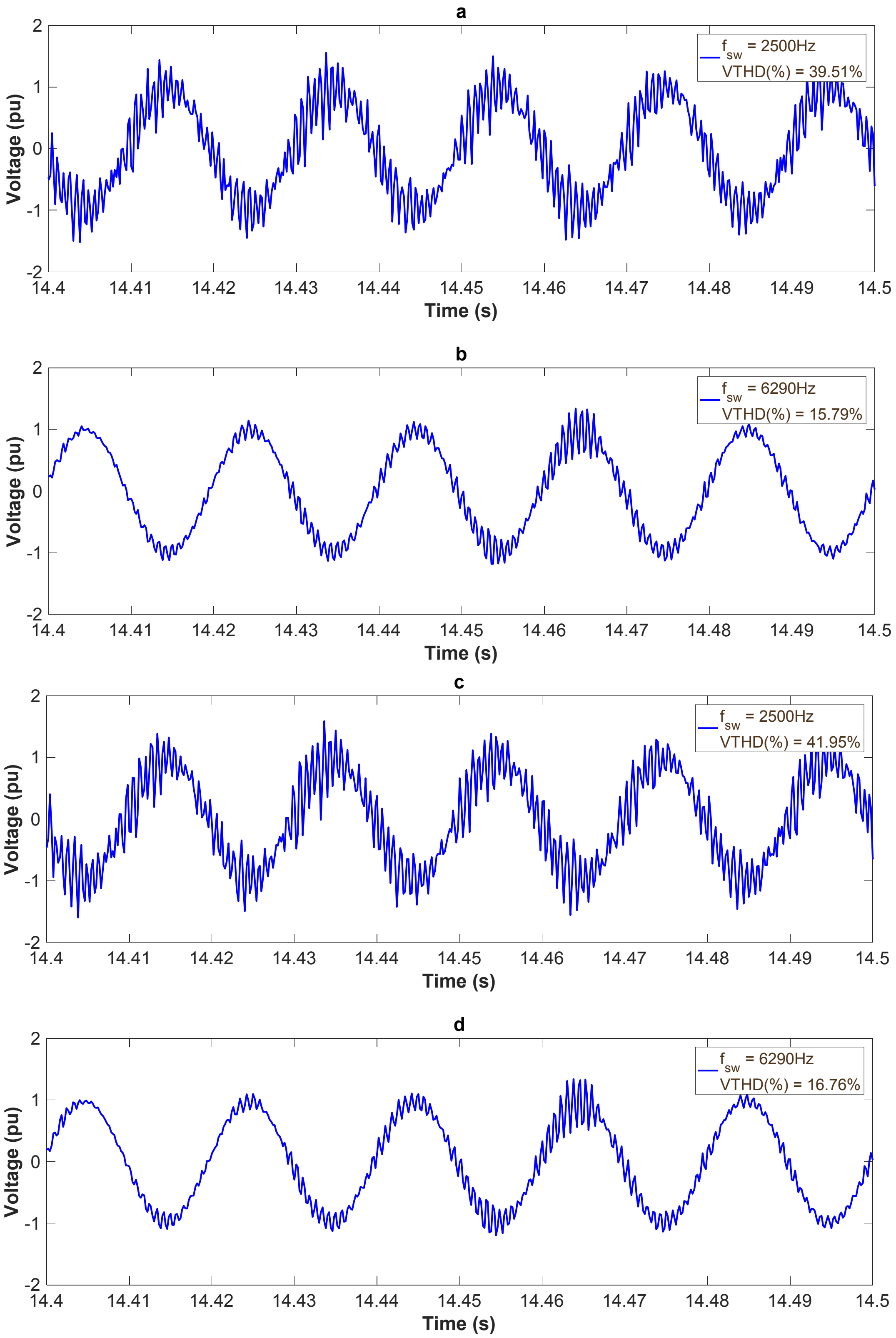

Figure 4.3 Comparison of voltages at different f_{sw} for the *Transformer-Cable system*. a. Generator voltage at f_{sw} = 2500Hz. b. Generator voltage at f_{sw} = 6290Hz. c. Voltage at the MV side of the transformer at f_{sw} = 2500Hz. d. Voltage at the MV side of the transformer at f_{sw} = 6290Hz.

In Figure 4.3a the voltage at the generator terminals for the *TCS* at f_{sw} = 2500Hz is depicted. A very high voltage total harmonic distortion (VTHD) of 39.51% and overvoltage spikes can be observed. Figure 4.3b presents the voltage at the generator terminals at f_{sw} = 6290Hz where the resonant minimum appeared. A significant reduction can be seen in both the overvoltages and the THD of the generator voltage.

Comparing the generator voltage of Figure 4.3a and Figure 4.3b with the transformer voltage at the MV side presented in Figure 4.3c and Figure 4.3d respectively it can be observed that the VTHD is slightly higher at the MV side of the transformer. This can be explained because the distributed nature of the cable parameters can act as a filter for certain harmonics generated by the VSC. On the other hand, cable parameters can magnify the harmonics at the areas where resonant peaks appear as it was demonstrated in the examples of Figure 4.1.

The distribution of the harmonics that constitute the THD are also given in Figure 4.4. In addition, the V_{GAIN} graph for the *TCS* given in Figure 4.1 is plotted in Figure 4.4 in order to show the correlation between the distribution of harmonics and V_{GAIN} magnitude. Figure 4.4c depicts the distribution of harmonics at the MV side of the generator transformer and Figure 4.4d the distribution of harmonics at the VSC terminals.

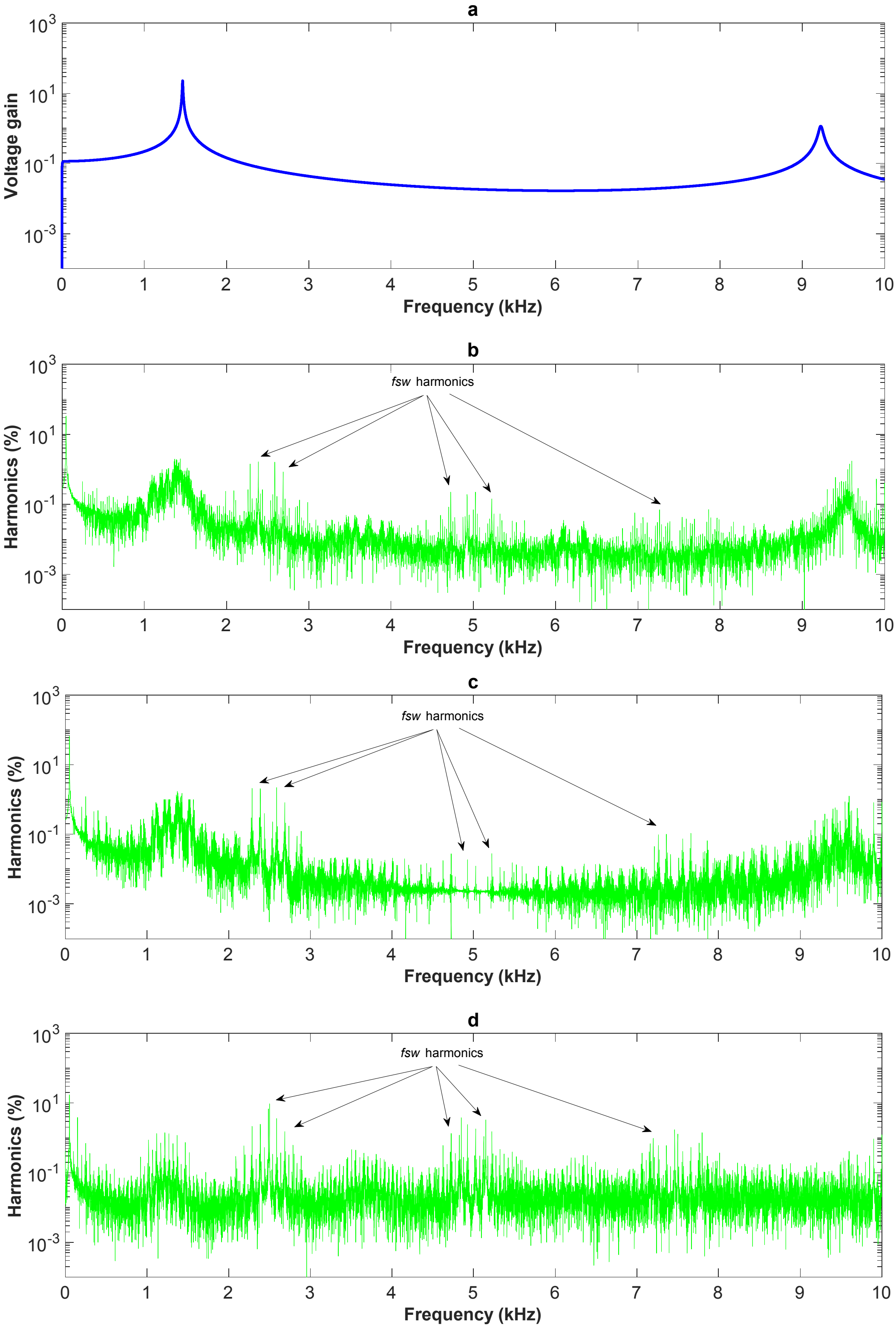

Figure 4.4 Correlation between Voltage Gain graph and distribution of harmonics for the *TCS* at f_{sw} = 2500Hz. a. Voltage gain graph. b. Distribution of harmonics at the generator terminals. c. Distribution of harmonics at the MV side of the transformer. d. Distribution of harmonics at the terminals of the VSC.

In Figure 4.4a the voltage gain graph for the *TCS* is shown and in Figure 4.4b the distribution of harmonics of the generator voltage. The allocation of voltage harmonics at the generator terminals was measured when the system was at rated operation and generator controller frequency, f_{sw} was 2500Hz. In both graphs, the voltage gain graph and the harmonic distribution graph, y-axis is plotted in logarithmic scale while x-axis is plotted in a linear scale. The harmonics distribution graph y-axis shows the magnitude of harmonics as a percentage of the fundamental.

The first observation from Figure 4.4 is that there is a correlation between resonant peaks and appearance of high harmonics. Based on the voltage gain graph in Figure 4.4a, the resonant peaks appear at around 1600Hz and 9300Hz. Observing the harmonics graph it is shown that the percentage of harmonics around these frequencies are significant reaching 8% magnitude of the fundamental. The second observation from Figure 4.4b is the distribution of the characteristic harmonics generated by the generator controller. Based on the theory the characteristic harmonics from the generator controller appear at multiples of the fundamental frequency, 50Hz, around the multiples of the generator controller f_{sw}, 2500Hz. We can observe in Figure 4.4b that around 2500Hz and 5000Hz harmonic spikes appear that reach up to 8%. This creates the need for a filter with a tuned frequency at the generator switching frequency f_{sw} and in addition, an appropriate switching frequency where its multiples are not near a resonant peak at higher frequencies.

Comparing Figures Figure 4.4b, Figure 4.4c and Figure 4.4d the change of distribution of harmonics generated by the VSC as they flow into the system can be observed. In Figure 4.4d the distribution of harmonics generated by the VSC can be observed. It is evident that the characteristic harmonics from the generator controller are dominant and each harmonic spike surpasses the 10% magnitude of the fundamental. These harmonic spikes are slightly reduced in the *TCS* and as it can be seen in Figures Figure 4.4b and Figure 4.4c each spike reaches up to 8% magnitude at the MV side of the transformer or the generator terminals. Apart from the characteristic harmonics generated by the controller switching frequency other harmonics appear to be generated from the VSC. Some harmonic spikes appear between 1000Hz and 1600Hz that have a maximum of 1% magnitude. These harmonic spikes are resonating in the

TCS increasing their magnitude at the generator terminals at around 2%. In addition, it can be observed that the harmonics at the MV side of the transformer, Figure 4.4c, are significantly reduced compared to the harmonics at the VSC, Figure 4.4d. The change is larger for the harmonics that appear between 4000Hz and 6000Hz. At these frequencies there are very low harmonics at the MV side of the transformer. However, these harmonics are increased due to resonance at the generator terminals. It is noteworthy to mention that the harmonic spikes due to the switching frequency of the controller at around 5000Hz are up to 6% at the VSC, very low at the MV side of the transformer and slightly increased at around 0.7% at the terminals of the generator due to resonance. The harmonics at the frequencies between 9000Hz and 10000Hz are very low at the VSC, they increase at the MV side of the transformer and have a significant value of 1.5% at the generator terminals. This is due to the resonant peak that appears between these frequencies as shown in the Voltage gain graph of Figure 4.4a.

4.2.2 Filter-Transformer-Cable system

The block diagram of a TCCS with long distance controls using a *FTCS* is depicted in Figure 4.5. The system is identical to the reference model presented in Chapter 3.

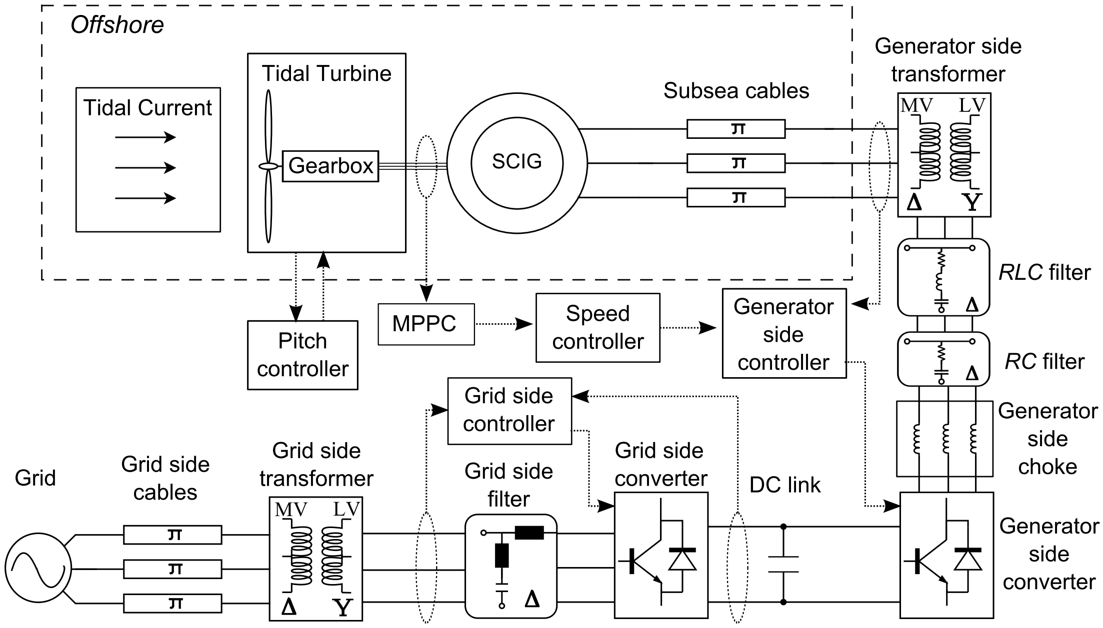

Figure 4.5 Block diagram of the Filter-Transformer-Cable system.

Based on Figure 4.1 the *FTCS* has a resonant minimum at 2558Hz which is the tuned frequency of the *RLC* filter discussed in Section 3.5.2. The model depicted in Figure

4.5 is simulated at the reference generator controller switching frequency, f_{sw} = 2500Hz, which is also near the resonant minimum frequency. In addition, a second resonant minimum appears at 6723Hz according to Figure 4.1. The *FTCS* is also simulated at the second resonant minimum frequency of 6723Hz. The measured voltages at the generator terminals and the MV side of the transformer are shown in Figure 4.6.

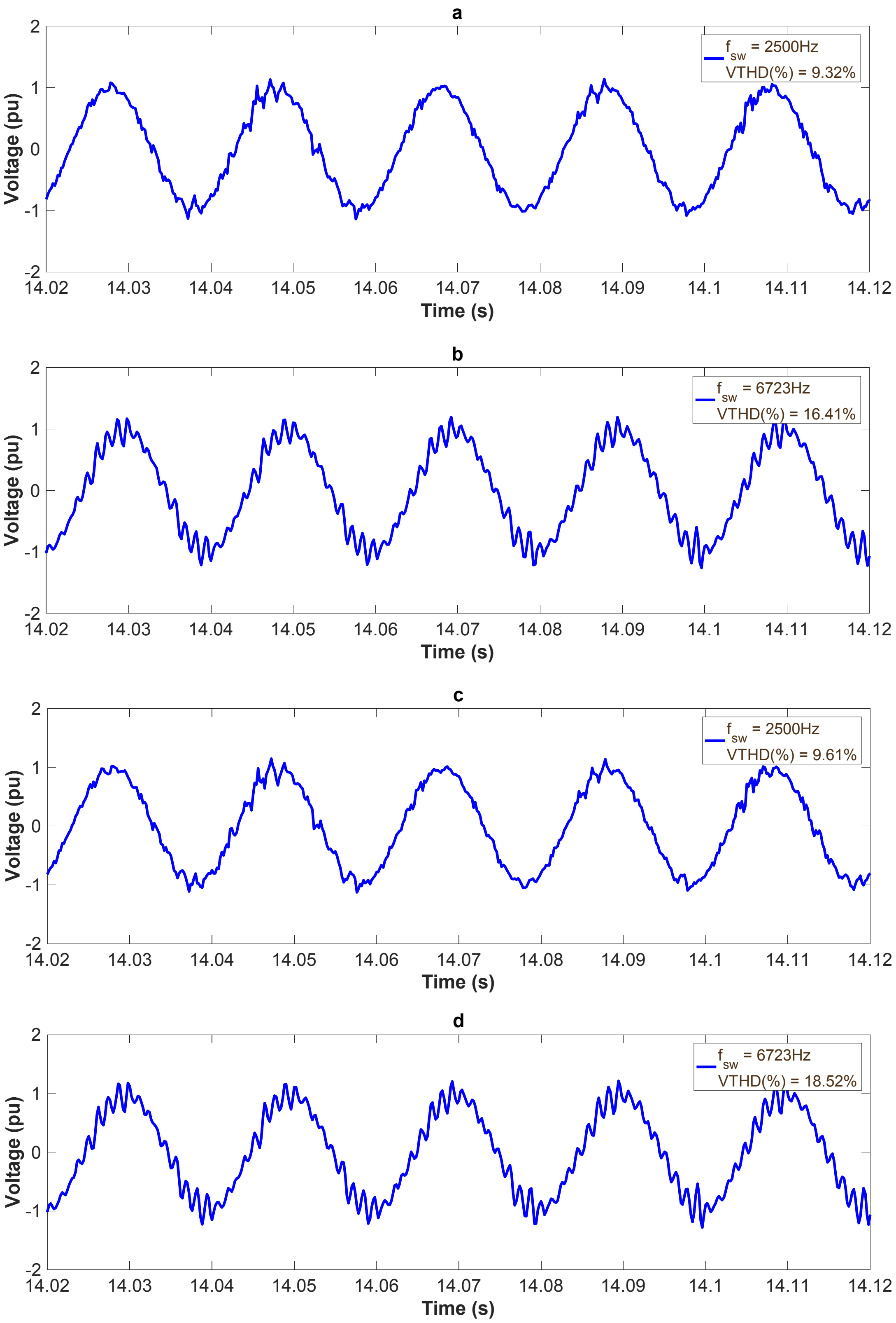

Figure 4.6 Comparison of the voltages at different f_{sw} for the *Filter-Transformer-Cable system*. a. Generator voltage at f_{sw} = 2500Hz. b. Generator voltage at f_{sw} = 6723Hz. c. Transformer voltage at the MV side at f_{sw} = 2500Hz. d. Transformer voltage at the MV side at f_{sw} = 6723Hz.

In Figure 4.6a the voltage at the generator terminals for the *Filter-Transformer-Cables system* at f_{sw} = 2500Hz is depicted. A VTHD of 9.32% and a few overvoltage spikes that do not exceed the 1.2pu limit can be observed. Figure 4.6b presents the voltage at the generator terminals at f_{sw} = 6723Hz where the second resonant minimum appeared. The VTHD at f_{sw} = 6723Hz is higher compared to when f_{sw} = 2500Hz. The main reason of the higher VTHD is that at when the generator controller has f_{sw} = 6723Hz, the harmonics at higher frequencies are excited due to the resonant peak of the *FTCS* at 18090Hz, which is close to the three times the f_{sw}. Similar results are also observed for the voltage at the MV side of the transformer.

Comparing the generator voltage of Figure 4.6a and Figure 4.6b with the transformer voltage at the MV side presented in Figure 4.6c and Figure 4.6d respectively it can be observed that the VTHD is slightly higher at the MV side of the transformer. This can be explained because the distributed nature of the cable parameters can act as a filter for certain harmonics generated by the VSC. On the other hand, cable parameters can magnify the harmonics at the areas where resonant peaks appear as it was demonstrated in the examples of Figure 4.1 and in Section 4.2.1 for the *TCS*.

The distribution of the harmonics that compose the THD of the generator voltage presented in Figure 4.6a are also given in Figure 4.7b in the frequency domain. In addition, the V_{GAIN} graph for the *FTCS* given in Figure 4.1 is plotted in order to show the correlation between the distribution of harmonics in the frequency domain and V_{GAIN} magnitude. Figure 4.7c depicts the distribution of harmonics at the MV side of the generator transformer and Figure 4.7d the distribution of harmonics at the VSC terminals.

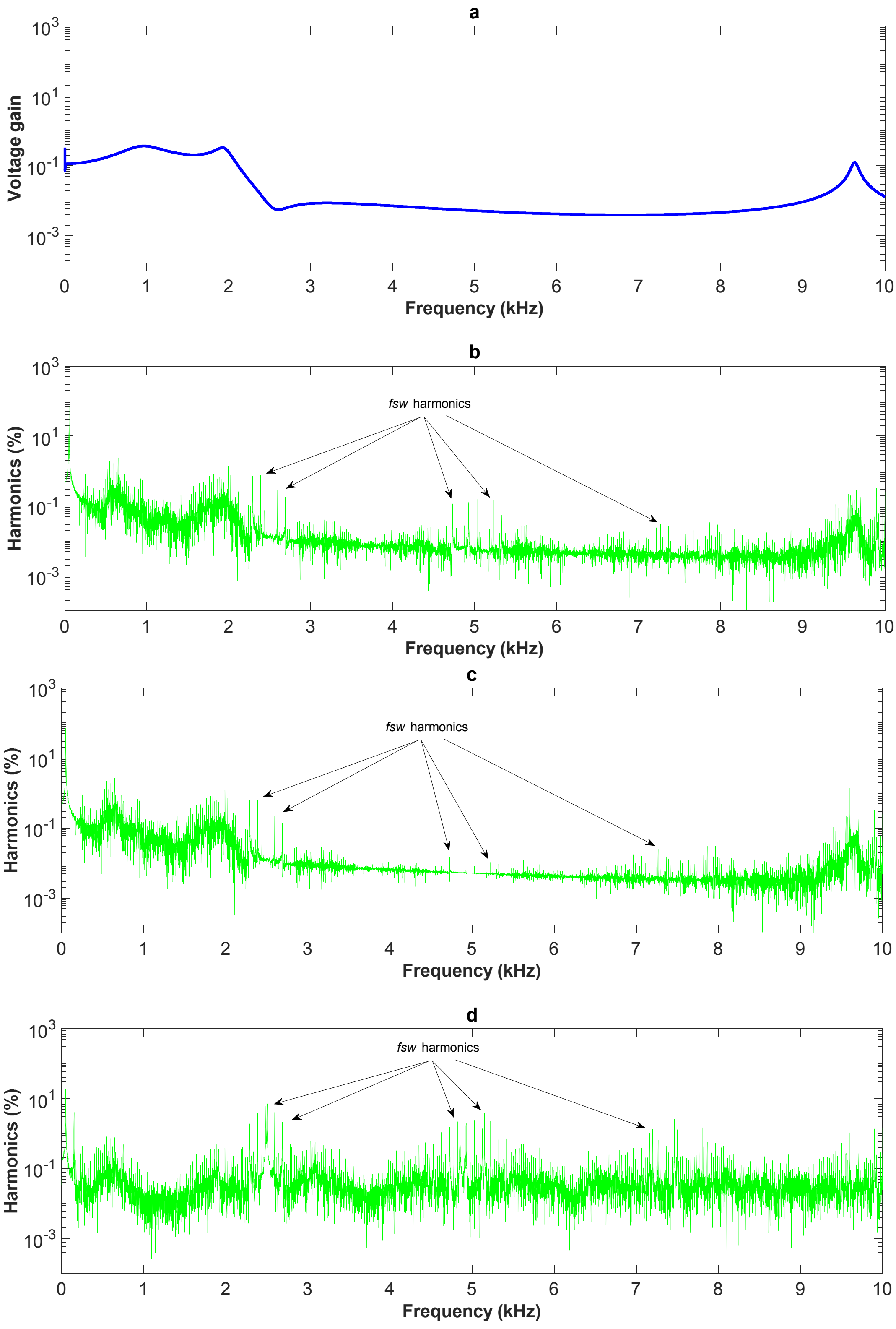

Figure 4.7 Correlation between Voltage Gain graph and distribution of harmonics at different stages for the *FTCS* at f_{sw} = 2500Hz. a. Voltage gain graph for the *FTCS*. b. Distribution of harmonics at the generator terminals. c. Distribution of harmonics at the MV side of the generator transformer. d. Distribution of harmonics at the VSC.

In Figure 4.7 the voltage gain graph for the *FTCS* is shown together with the distribution of harmonics of the generator, transformer and VSC voltage. The allocation of voltage harmonics was measured when the system was at rated operation and generator controller frequency, f_{sw} was 2500Hz. The harmonics distribution graphs, show the magnitude of harmonics in percentage of the fundamental.

The first observation from Figure 4.7 is that there is a correlation between resonant peaks and appearance of high harmonics. Based on the voltage gain graph for the *FTCS*, Figure 4.7a, the resonant peak that appears near 1600Hz in the *TCS* is effectively damped. In addition, the resonant peak near 9600Hz has reduced voltage gain magnitude. Observing the harmonics graph it is shown that the harmonics around 1600Hz and 9600Hz reach 5% magnitude of the fundamental. The second observation from Figure 4.7b is the distribution of the characteristic harmonics generated by the generator controller. Based on theory, the characteristic harmonics from the generator controller appear at multiples of the fundamental frequency, 50Hz, around the multiples of the generator controller f_{sw}, 2500Hz. We can observe in Figure 4.7b that around 2500Hz and 5000Hz harmonic spikes appear that reach up to 3% of the harmonics. Finally, a significant reduction of harmonics can be seen between the *TCS* and the *FTCS*. By comparing Figure 4.4b and Figure 4.7b, the reduction of harmonics in all the frequencies is evident. The expected reduction in harmonics is also depicted in the V_{GAIN} graphs for the two systems given in Figure 4.1. For almost all the frequencies studied *FTCS* has less voltage gain magnitude compared to the *TCS*.

Comparing Figures Figure 4.7b, Figure 4.7c and Figure 4.7d the change of distribution of harmonics generated by the VSC as they flow into the system can be observed. In Figure 4.7d the distribution of harmonics generated by the VSC can be observed. It is evident that the characteristic harmonics from the generator controller are dominant and each harmonic spike reaches up to 10% magnitude of the fundamental. These harmonic spikes are effectively mitigated in the *FTCS* and as it can be seen in Figures Figure 4.7b and Figure 4.7c each spike reaches up to 3% magnitude at the MV side of the transformer or the generator terminals. Apart from the characteristic harmonics generated by the controller switching frequency other harmonics appear to be generated that have less than 1% magnitude. Even though these harmonics may not be significant at the VSC terminals their magnitude is increased due to resonance at the MV side of the transformer and at the generator terminals. For example, the harmonics generated at the VSC between 500Hz and 750Hz have a magnitude less than 1%. This is not the case at the MV side of the transformer and the generator terminals. The harmonics between 500Hz and 750Hz in Figures Figure 4.7b and Figure 4.7c have a magnitude between 2% and 2.5%. In addition, the harmonics generated by the VSC around 9600Hz, where a resonant peak appears in the *FTCS*, have magnitude less than 1%. On the other hand, the harmonics that appear around 9600Hz at the MV side of the transformer and the generator terminals are much more significant due to resonance.

4.2.3 Summary of the switching frequency study

The conclusion from the above observations is that by studying the V_{GAIN} graph the optimum controller f_{sw} for a system with or without filters can be estimated. Minimum harmonics are generated when the generator controller f_{sw} is at the resonant minimum for each case. In addition, the V_{GAIN} graph depicts the resonant peaks. The frequencies associated with resonant peaks must be avoided in order to keep voltage harmonics and overvoltages within limits. Apart from the resonance around the generator controller f_{sw}, resonance around higher frequencies, at multiples of f_{sw}, must be studied before increasing the generator controller switching frequency. Additional simulations were carried out in order to show and understand the effectiveness of voltage gain graphs in predicting and mitigating the harmonics and overvoltages. The simulations were implemented by changing the generator controller f_{sw} and the generator reflection coefficient for the *TCS* and *FTCS*. Some of these results are presented in Table 4.1.

Table 4.1 VTHD results at the generator terminals from the simulation of the modelled TCCS for different filter cases and different controller switching frequencies.

Switching Frequency (Hz)	Generator reflection coefficient	*TCS*	*FTCS*
2000	1	58.96%	27.96%
	0.5	15.11%	10.85%
2400	1	35.27%	9.62%
	0.5	9.24%	5.47%
2500	1	39.51%	9.32%
	0.5	8.21%	5.53%
2600	1	27.71%	9.05%
	0.5	7.55%	4.94%
3000	1	19.86%	9.61%
	0.5	5.81%	5.23%
5000	1	17.15%	13.52%
	0.5	8.53	6.45%
6000	1	29.01%	13.06%
	0.5	9.53%	6.23%

Taking a closer look at the results presented in Table 4.1 it can be said that increasing the f_{sw} of the generator controller does not necessarily mean that the VTHD is also reduced. In addition, in some cases, even though the V_{GAIN} magnitude is lower in one f_{sw} compared to another, VTHD is still higher. For example, in the *TCS* case the 3000Hz and 6000Hz simulation can be compared. At 3000Hz the V_{GAIN} magnitude is higher compared to the 6000Hz. This would mean that the VTHD when the system is simulated with f_{sw} = 6000Hz should be less compared to when the system is simulated with f_{sw} = 3000Hz. However, based on the results in Table 4.1 this is not the case. This is due to the fact that resonant peaks at higher harmonics should also be considered when choosing an f_{sw}. At around 18000Hz the *TCS* has a resonant peak. This is three times the f_{sw} at 6000Hz. Harmonics generated at multiples of the f_{sw} are also magnified if they are at a resonant peak.

Another important outcome from Table 4.1 is that the generator reflection coefficient plays an important role in the amount of voltage harmonics generated and absorbed in a system. Out of all the cases presented in Table 4.1 where the generator reflection coefficient is 1, the equivalent case with a generator reflection coefficient of 0.5 generates less VTHD. This confirms the fact that when $\Gamma_{Gen} = 1$, it is the worst-case scenario under which a TCCS with long distance controls will operate. In reality however, the generator will have a reflection coefficient around 0.5 (for machines around 1.2MVA) and the TCCS system will operate with less harmonics flowing in the cables.

Finally, as it is expected, the *FTCS* operates with less VTHD in all the cases presented in Table 4.1 compared to the *TCS*. In almost all the frequencies presented in Figure 4.1 the *FTCS* has lower V_{GAIN} magnitude compared to the *TCS*.

Even though the above study is important in designing systems with long distance controls, in most cases the choice over the f_{sw} of the generator controller is not possible at this wide scale and therefore the use of filters is needed. The analysis presented here can be useful to avoid resonant peaks, shift operating frequencies closer to resonant minimums and test filter types and parameters so that harmonics and overvoltages are mitigated. In the following section a comprehensive study for the design of filters for systems that use long distance controls is presented without the need to change the f_{sw} of the generator controller.

4.3 Filter design for systems with long distance control

The installation of a filter at the generator side of a tidal energy system with long distance controls must ensure continuous underwater operation, prevent overvoltages and generate the minimum possible losses. In the following sections, filters reported in literature for long distance control are discussed and their parameters are calculated based on the equations provided for the TCCS described previously. After calculating the parameters based on literature, a novel method of calculating filter parameters based on the voltage gain graphs is presented. At the end of this section all filters are compared based on their losses and effectiveness in mitigating overvoltages. In this study cable parameters are maintained, as given in Section 3.5.1. When designing filters in Section 4.3 only the worst-case scenario will be taken into account. Results regarding the two scenarios will be given in Section 4.4.

4.3.1 Filters based on literature

Filters presented in literature for long distance controls can be separated in two different categories. The first category uses filters at the machine terminals in order to change the generator voltage reflection coefficient Γ_{Gen}. As described in Section 4.1.1 the voltage reflection coefficient at the generator terminals can be calculated using (4-1). In a worst case scenario, $\Gamma_{Gen} = 1$; however, the desirable value for the voltage reflection coefficient at the generator terminals is $\Gamma_{Gen} = 0$. Therefore, by terminating the long cables with an impedance equal to the cable characteristic impedance we can achieve the desired value. The process of designing filters by terminating the long cables with an impedance equal to the cable characteristic impedance is presented in Sections 4.3.1.1, 4.3.1.2 and 4.3.1.3. The second category of filters presented in the literature are the filters installed at the generator side VSC terminals. Since the TCCS model presented in this thesis has a transformer between the VSC and the cables, these types of filters can be installed either on the low voltage side or the medium voltage side of the transformer. These filters are presented in Sections 4.3.1.4 and 4.3.1.5. It has to be noted that the cable parameters used in Sections 4.3.1.1 to 4.3.1.5 are based on Table 3.10.

4.3.1.1 Resistor termination

Installing a shunt resistor ($R_{termination}$) at the machine terminals is suggested [79] to provide voltage overshoot damping (Figure 4.8). In order to achieve this, the resistor value must be equal to the cable characteristic impedance (4-12).

$$\boldsymbol{R_{filter} = |Z_C| = 55.98\Omega = Z_{filter}} \tag{4-12}$$

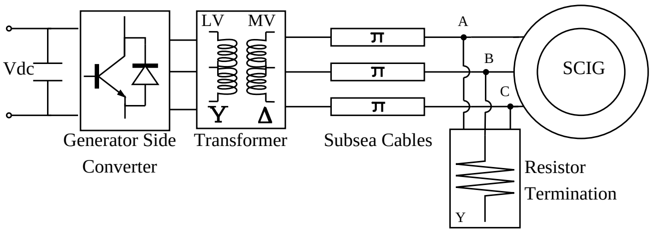

Figure 4.8 Block diagram of the generator side TCCS with resistor termination connected in wye.

4.3.1.2 Capacitor-resistor termination

A *first-order damped high pass capacitor-resistor* (*CR*$_{termination}$) filter at the machine terminals will provide overvoltage mitigation in the same way as *R*$_{termination}$ [79] but with lower losses (Figure 4.9). In order to choose the *CR*$_{termination}$ values we have to consider that initially the capacitor behaves as a short circuit and therefore the filter resistance can be calculated as in (4-13) [82].

$$\boldsymbol{R_{filter}} = \mathbf{real}(\boldsymbol{Z_C}) = \mathbf{52.57\Omega} \tag{4-13}$$

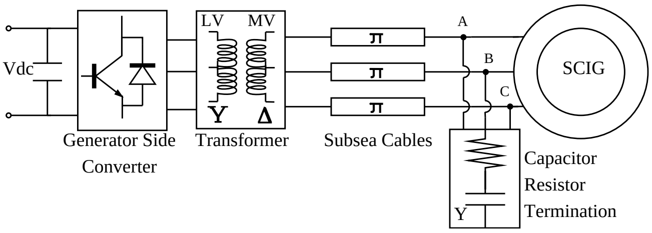

Figure 4.9 Block diagram of the generator side TCCS with CR$_{termination}$ connected in wye.

Filter capacitance is chosen so that there is less than 20% of terminal voltage during steady state operation (4-14) [80].

$$\boldsymbol{C_{filter}} = \frac{(-\mathbf{1}) \cdot \mathbf{3} \cdot \left(\boldsymbol{l_C} \cdot \sqrt{\boldsymbol{L_C} \cdot \boldsymbol{C_C}}\right)}{\mathbf{2} \cdot \boldsymbol{Z_C} \cdot \mathbf{ln}(\mathbf{0.8})} = \mathbf{6.3741\mu F} \tag{4-14}$$

The impedance of the *CR*$_{termination}$ filter is calculated in (4-15):

$$\boldsymbol{Z_{filter}} = \left|\boldsymbol{R_{filter}} + \frac{\mathbf{1}}{\left(\boldsymbol{j} \cdot \mathbf{2} \cdot \boldsymbol{\pi} \cdot \boldsymbol{f} \cdot \boldsymbol{C_{filter}}\right)}\right| = \mathbf{502.15\Omega} \tag{4-15}$$

Where f = 50Hz.

4.3.1.3 Capacitor-resistor-inductor termination

Reference [79] also proposes a *second-order damped high-pass filter* (*CRL*$_{termination}$) to mitigate overvoltages at the machine terminals. The filter is shown in Figure 4.10. The methodology to calculate filter parameters is similar to the *CR*$_{termination}$ filter and is presented in (4-16).

$$\begin{cases} R_{filter} = \mathrm{real}(Z_C) = 52.57\Omega \\ C_{filter} = \dfrac{1}{2 \cdot R_{filter}} \cdot \dfrac{1}{2 \cdot \pi \cdot f_{tuned}} = 6.055\mu\mathrm{F} \\ L_{filter} = \dfrac{1}{C_{filter}} \cdot \left(\dfrac{1}{2 \cdot \pi \cdot f_{tuned}}\right)^2 = 66.9\mathrm{mH} \end{cases} \tag{4-16}$$

The capacitance and inductance of the filter are based on the tuned frequency which can be derived by (4-17):

$$f_{tuned} = \frac{1}{2 \cdot \pi \cdot \sqrt{L_{filter} \cdot C_{filter}}} = 250\mathrm{Hz} \tag{4-17}$$

The *CRL*

The $CRL_{termination}$ impedance can be calculated using (4-18):

$$Z_{filter} = \left| \frac{1}{(j \cdot 2 \cdot \pi \cdot f \cdot C_{filter})} + \frac{R_{filter} \cdot j \cdot 2 \cdot \pi \cdot f \cdot L_{filter}}{R_{filter} + j \cdot 2 \cdot \pi \cdot f \cdot L_{filter}} \right| = 518.21\Omega \tag{4-18}$$

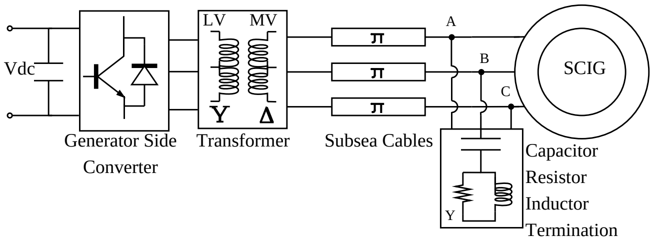

Figure 4.10 Block diagram of the generator side TCCS with $CRL_{termination}$ connected in wye.

4.3.1.4 Medium voltage LCR filter

The filter design method of a *second-order LCR filter* (*LCR_{MV}*) for overvoltage mitigation is described in detail in [85] for a converter-cable-generator system. The methodology to calculate the LCR_{MV} filter parameters is given in (4-19).

$$\begin{cases} R_f = real(Z_C) = 52.57\Omega \\ L_f = R_f \cdot \dfrac{2 \cdot t_{travel} \cdot (\Gamma_{Gen} + 1) \cdot \Gamma_{Gen}}{\Delta V_{max} + 1 + (\Gamma_{Gen} - 1) \cdot (\Gamma_{Gen} + 1)} = 11.3\mathrm{mH} \\ C_f = \dfrac{4 \cdot L_f \cdot \zeta^2}{R_f^2} = 34.31\mu\mathrm{F} \end{cases} \tag{4-19}$$

Where $\zeta = 1.45$ is the damping ratio, $\Gamma_{Gen} = 1$, ΔV_{max} is the maximum allowable overvoltage and t_{travel} is the travelling time of the wave front to the receiving end which is calculated from (4-20).

$$t_{travel} = l_C \cdot \sqrt{L_C \cdot C_C} = 53.08\mu\mathrm{s} \tag{4-20}$$

The application of the above filter to the proposed converter-transformer-cable-generator TCCS is shown in Figure 4.11. To calculate filter impedance only the parallel RC path is considered which is similar to (4-15).

$$\boldsymbol{Z_f = 106.63\Omega} \tag{4-21}$$

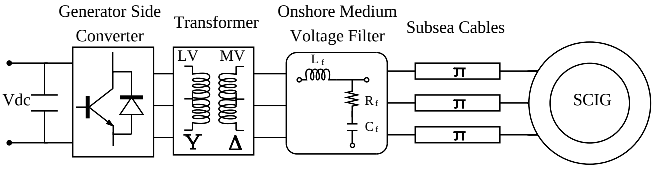

Figure 4.11 Block diagram of the generator side TCCS with $\mathbf{LCR_{MV}}$ filter. The $\mathbf{LCR_{MV}}$ is composed of an inductor connected in series and a resistor-capacitor branch connected in wye in parallel.

4.3.1.5 Low voltage LCR filter

By referring the parameters calculated for the LCR_{MV} filter to the low voltage of the transformer, an LCR filter can be applied to the output of the VSC, as shown in Figure 4.12. Filter parameters are based on (4-19).

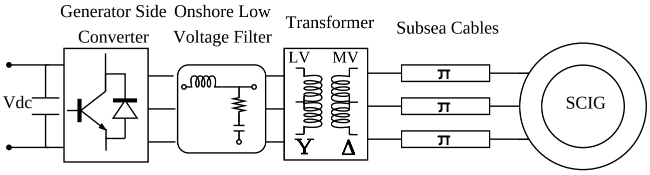

Figure 4.12 Block diagram of the generator side TCCS with $\mathbf{LCR_{LV}}$ filter.

4.3.2 Filter design algorithm based on voltage gain graph

A new method is proposed for choosing filter values based on the voltage gain graph described in Section 4.1.2. The main aims of the algorithm are to choose filter parameters that:

- Reduce resonant peaks that increase the magnitude of specific harmonics.
- Maximize filter impedance in order to reduce losses induced to the system.

The design aim for the majority of the filters described in Section 4.3.1 was to mitigate overvoltages at the motor terminals and increase the reliability of an induction motor. These motors were used in the offshore oil and gas industry as underwater pumps or in the mining industry as underground fans. Reducing filter and system losses in a system that is using long distance drives for the motors described above was a secondary aim. The objectives when using a similar system in the renewable energy industry are different. Minimising losses is a primary objective along with increasing the reliability of the system. Therefore, the filter design process in a long distance controlled TCCS is different compared to the long distance driven motor. The filter design algorithm based on voltage gain graphs goals to design a power harmonic filter that mitigates harmonics and overvoltages but at the same has minimum losses for the system.

Figure 4.13 shows the voltage gain graphs of the TCCS for the filters described in Section 4.3.1. It can be observed that the filters installed at the medium voltage side of the system reduce the resonant peaks to very low values. The LCR filter installed at the low voltage side of the transformer does not reduce the resonant peak effectively.

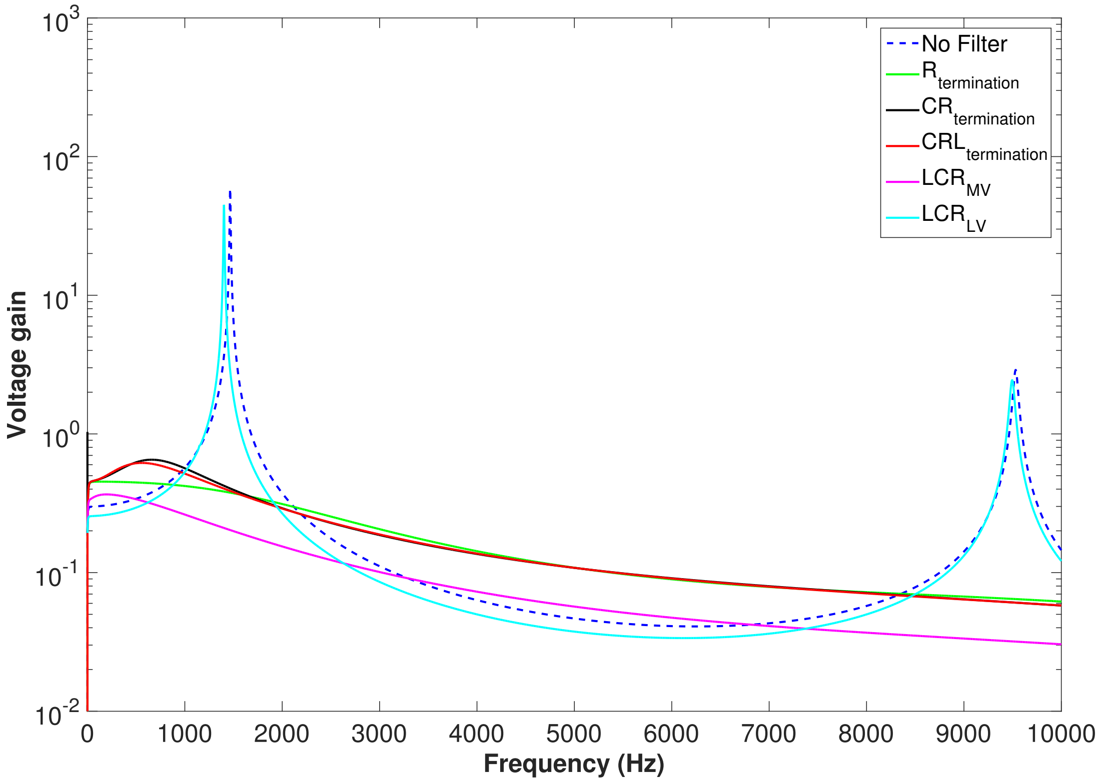

Figure 4.13 Voltage gain graph for the TCCS when different types of filters are installed.

The proposed algorithm for filter design operates in the following way:

1. Reference filter parameters are calculated using filter design equations as described in the literature.
2. A range around the reference parameters is chosen depending on the filter design equations.
3. For a specific set of filter parameters, within the range specified above, the voltage gain graph is computed.
4. The peak value of the voltage gain graph is stored as the worst case overvoltage for that case.
5. Filter impedance is also calculated based on the specific set of parameters chosen in step 3.
6. A new set of filter parameters is chosen and the process is repeated from step 3.

When the algorithm has chosen all the possible sets of filter parameters in step 3, a decision can be made to choose the one that gives the best results. In order to quantify and demonstrate the results, contour plots are created in the following sections. The algorithm chooses which set of filter parameters will have better results compared to reference filter parameters by taking into account:

- Peak voltage gain; higher peak can cause increased overvoltages.
- Filter losses; a filter with higher impedance will have lower losses.
- Voltage gain at 50Hz; the higher the voltage gain at 50Hz, the higher the voltage compensation provided by the filter to the generator terminals.

The flowchart of the algorithm described above is shown in Figure 4.14.

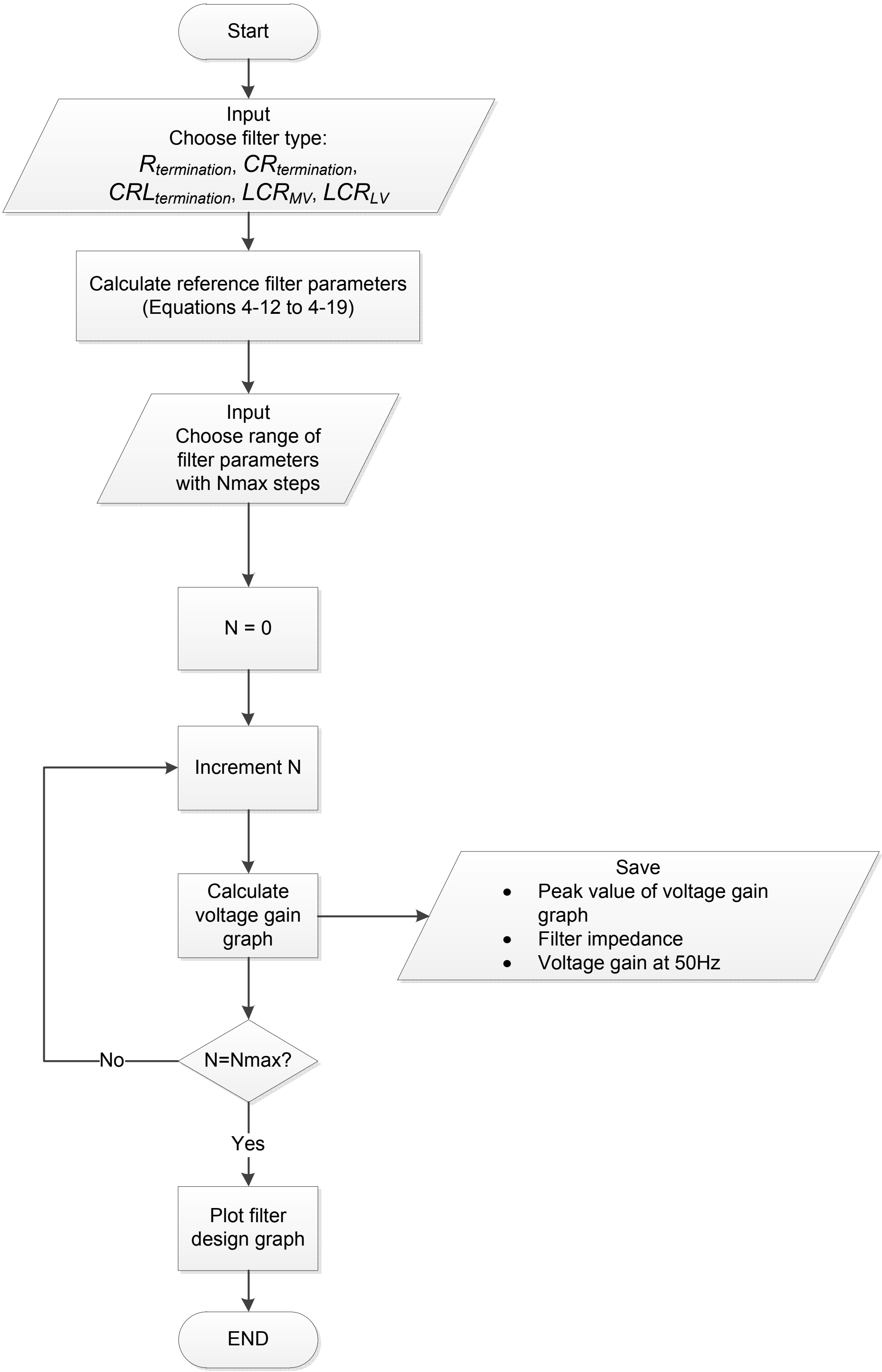

Figure 4.14 Flowchart of the filter design algorithm based on voltage gain graphs.

In the following sections, the process in choosing a set of filter parameters is shown in detail for the $CR_{termination}$ filter. For the other filter types, the process is followed in a similar way but only the final graphs are presented.

4.3.2.1 Capacitor Resistor Termination

The block diagram of the $CR_{termination}$ filter is shown in Figure 4.9. The contour graphs for the maximum voltage gain, filter impedance and voltage gain at 50Hz are given in Figure 4.15.

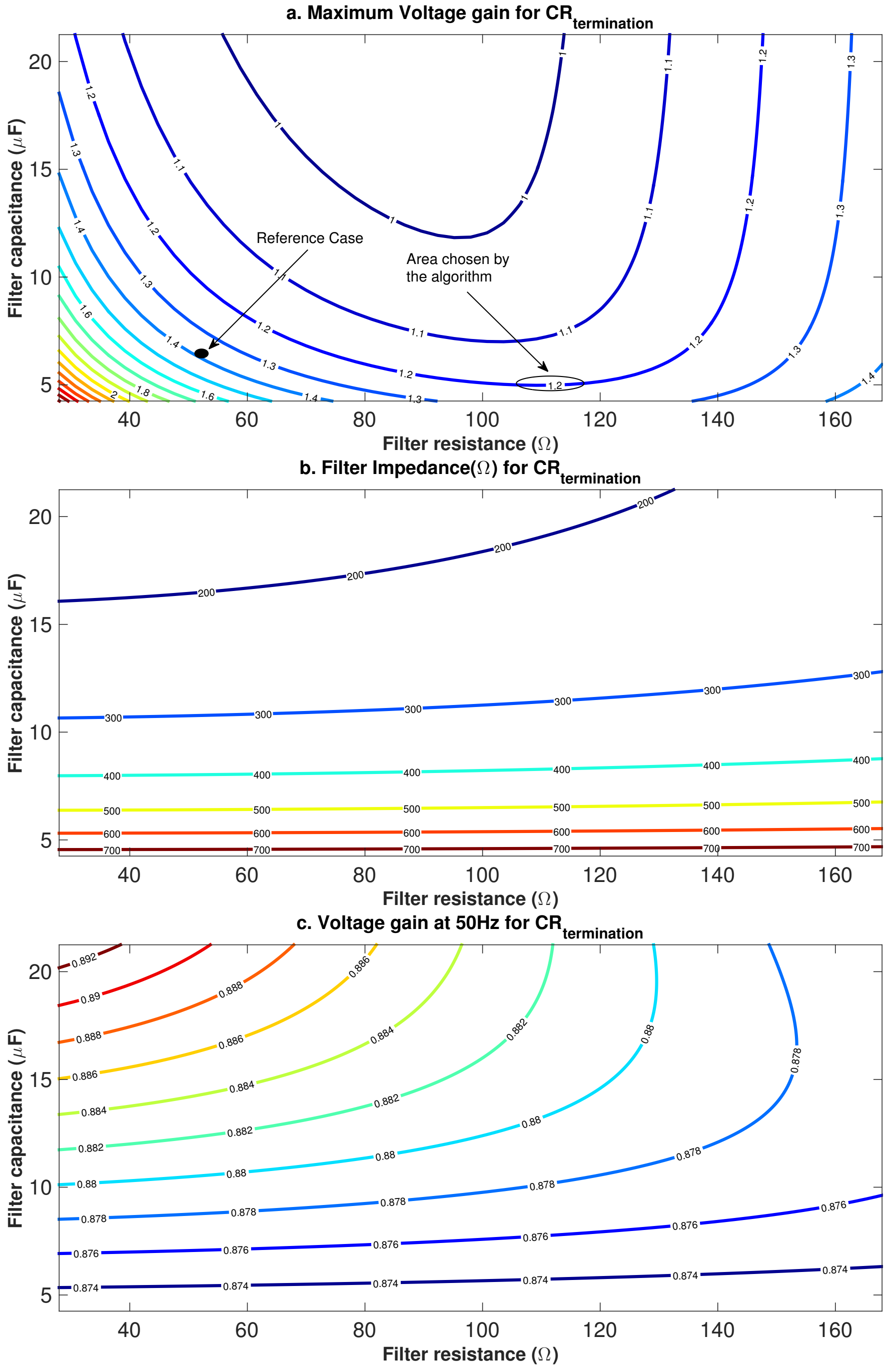

Figure 4.15 Contour plots for the *CR*

Taking a closer look at Figure 4.15a the position of the reference case for this type of filter in the maximum voltage gain map can be noted. The reference case maximum voltage gain is 1.382. The same can be done in Figure 4.15b where the reference case impedance is 502.14Ω. Using the reference case impedance the algorithm can determine a set of filter parameters that is below the ‘502.14’ contour line. Choosing a set of filter parameters which is below the ‘502.14’ contour line will make the filter generate less losses. It is noteworthy to mention that the higher the capacitance the closer to unity is the voltage gain at the operating frequency of the generator. Based on the data presented in Figure 4.15 the algorithm can choose a set of filter values that fulfils the criteria set for overvoltage mitigation and power loss reduction. In order to visualize these results we can create a contour graph with the combination of maximum voltage gain and filter impedance. This contour plot will be referred to as *Filter Design Graph* and, for the $CR_{termination}$ case, this is presented in Figure 4.16.

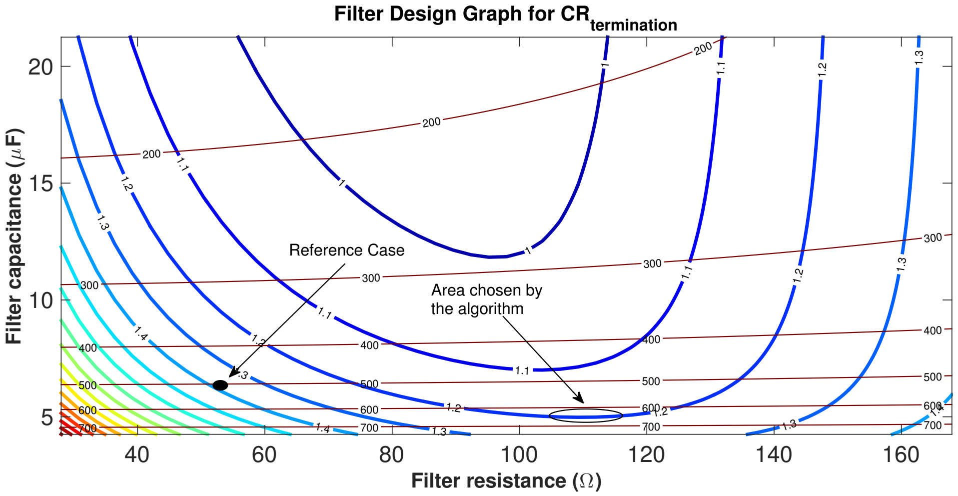

Figure 4.16 Filter design graph for the $CR_{termination}$ filter. The set of parameters the algorithm has chosen are limited by the 1.2 contour line and maximum filter impedance.

The exact values for overvoltage mitigation and power loss minimization of the $CR_{termination}$ filter are given in Table 4.2.

Table 4.2 Filter parameters for the $CR_{termination}$ filter based on the literature and the proposed algorithm.

Method	Filter Parameters	Maximum voltage gain	Filter impedance
Reference case	R_f = 52.57 Ω C_f = 6.37 μF	1.3821	502.14 Ω
Power loss minimization algorithm	R_f = 111.96 Ω C_f = 4.99 μF	1.1995	647.26 Ω

4.3.2.2 Resistor Termination

The block diagram for the $R_{termination}$ filter is given in Figure 4.8. Since resistor termination has only one variable the filter design graph that appears in Figure 4.17 contains the response at each frequency in the y-axis.

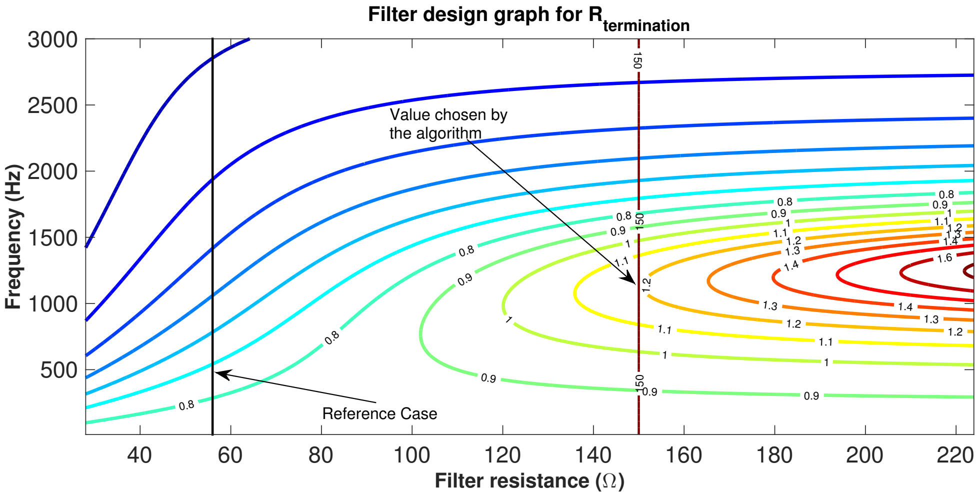

Figure 4.17 Filter design graph for the $R_{termination}$. The set of parameters the algorithm has chosen are limited by the 1.2 contour line and the vertical line of filter impedance that is adjacent to this line.

4.3.2.3 Capacitor Resistor Inductor Termination (CRL)

The block diagram for the $CRL_{termination}$ filter is given in Figure 4.10. Based on (4-16), by changing f_{tuned} we can obtain the capacitor and inductor values needed to design the filter. Figure 4.18 depicts the filter design graph for the $CRL_{termination}$ filter.

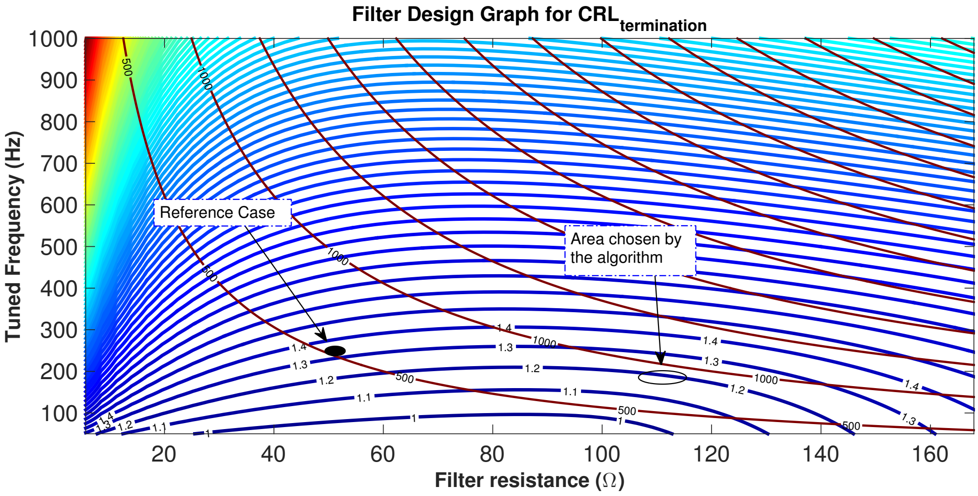

Figure 4.18 Filter design graph for the *CRL$_{termination}$* filter. The set of parameters the algorithm has chosen are limited by the 1.2 contour line and the maximum filter impedance along this line.

4.3.2.4 Medium Voltage LCR Filter

The block diagram for the *LCR$_{MV}$* filter is given in Figure 4.11. The inductor value is kept constant during the analysis at maximum (0.15pu). The maximum value of inductance is limited to 0.15pu because a very large series inductance can reduce the capability of the generator to produce rated torque. The filter design graph for the *LCR$_{MV}$* filter is given in Figure 4.19.

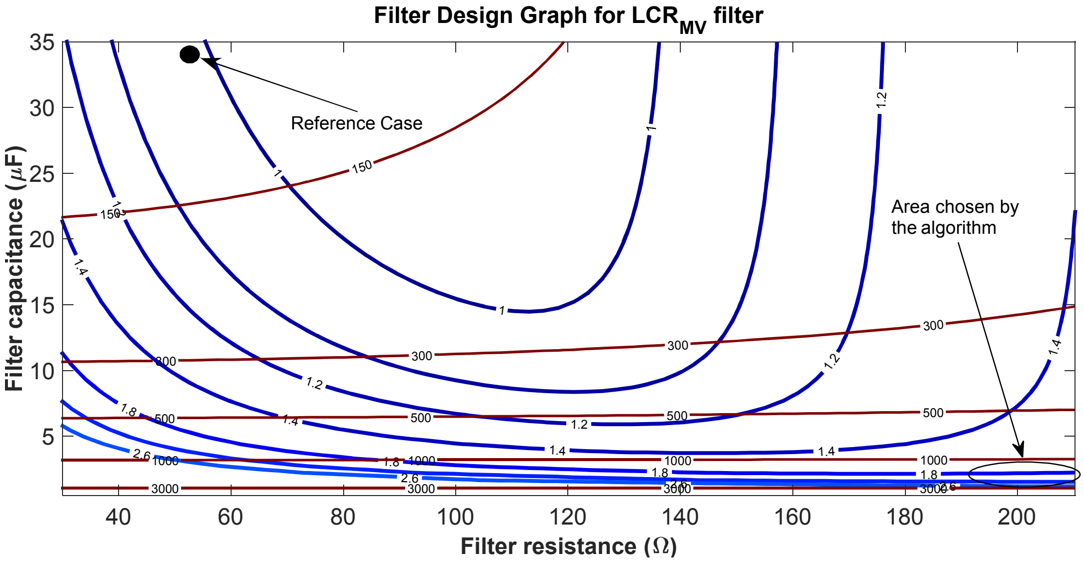

Figure 4.19 Filter design graph for the *LCR$_{MV}$* filter. The set of parameters the algorithm has chosen are limited by the 2.6 contour line and the maximum filter impedance along this line.

4.3.2.5 Low Voltage LCR Filter

The block diagram for the LCR_{LV} filter is given in Figure 4.12. The inductor value is kept constant during the analysis at maximum (0.15pu at the low voltage side of the transformer). The filter design graph for the LCR_{LV} filter is given in Figure 4.20.

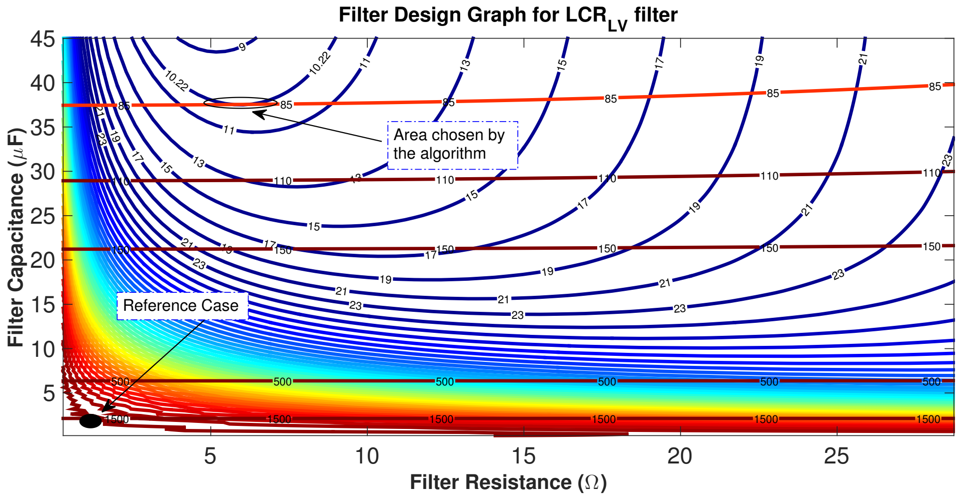

Figure 4.20 Filter design graph for the LCR_{LV} filter. The set of parameters the algorithm has chosen are limited by the 10.22 contour line and the maximum filter impedance along this line.

4.3.2.6 Combination of Filters

An additional advantage of the proposed algorithm is that it can take into account a combination of filters when determining the parameters for overvoltage mitigation. For example, additional harmonics are generated around the switching frequency of the controller. In order to reduce these harmonic components a single tuned filter can be used. The proposed algorithm can take into account the effect of the single tuned filter and calculate the parameters for the filter so that overvoltages are mitigated and losses are at a minimum. The filter design graph for the combination of LCR_{LV} filter and the common RLC filter, discussed in Section 3.5.2, is presented in Figure 4.21.

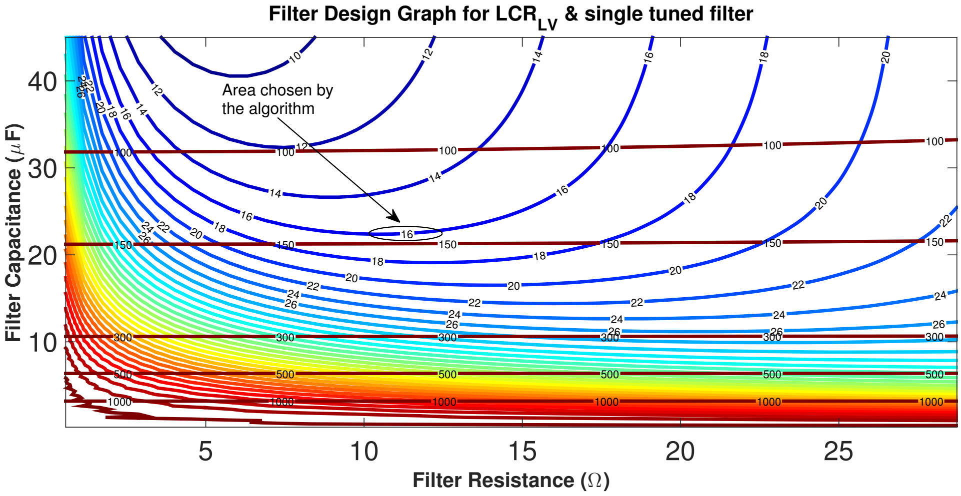

Figure 4.21 Filter design graph for the ***LCR$_{LV}$*** filter with the common ***RLC*** filter.

4.3.3 Summary of filter parameters

Table 4.3 gives a summarized view of the filter parameters, peak voltage gain from the design graph and filter impedance for all the types of filters considered.

Table 4.3 Filter parameters for the reference and proposed filters.

Filter type	Filter design method	Filter Parameters	Peak voltage gain	Filter impedance
$R_{termination}$	Reference	R_f = 55.98 Ω	0.8507	55.98 Ω
	Proposed	R_f = 148.35 Ω	1.1809	148.35 Ω
$CR_{termination}$	Reference	R_f = 52.57 Ω C_f = 6.374 µF	1.3821	502.14 Ω
	Proposed	R_f = 111.96 Ω C_f = 4.991 µF	1.1995	647.26 Ω
$CRL_{termination}$	Reference	R_f = 52.57 Ω L_f = 66.9 mH C_f = 6.055 µF	1.3551	518.21 Ω
	Proposed	R_f = 111.96 Ω L_f = 192.6 mH C_f = 3.842 µF	1.1922	867.79 Ω
LCR_{MV}	Reference	R_f = 52.57 Ω L_f = 11.3 mH C_f = 34.311 µF	1.0151	106.63 Ω
	Proposed	R_f = 210.28 Ω L_f = 11.3 mH C_f = 1.132 µF	2.6716	2820.21 Ω
LCR_{LV}	Reference	R_f = 0.86 Ω L_f = 0.0412 mH C_f = 1.875 µF	1698.0015	1697.71 Ω
	Proposed	R_f = 5.746 Ω L_f = 0.2728 mH C_f = 37.501 µF	10.2242	85.08 Ω
LCR_{LV} & RLC	Proposed	R_f = 10.35 Ω L_f = 0.2728 mH C_f = 22.50 µF	15.9989	141.85 Ω

4.4 Time domain results and discussion

In this section the simulation results are presented for the different filter cases. As it was noted in Section 4.3, two different scenarios will be considered. The first scenario, which is the worst case scenario, will assume that the reflection coefficient at the generator terminals is unity, $\Gamma_{Gen} = 1$. The second scenario assumes that the reflection coefficient at the generator terminals is $\Gamma_{Gen} = 0.5$. Different cases regarding the generator reflection coefficient can also be considered. However, for the purposes of the thesis these two cases are chosen as representatives to show the effect of changing the Γ_{Gen}. In the last part of this chapter the most efficient and effective filter is chosen for a system with long distance controls. Results from the TCCS with the optimised filter are compared with the *AHH Model* presented and analysed in Chapter 3. Power losses at different parts of the tide-to-wire TCCS model are calculated in respect to power generated (P_{el}) using (4-22).

$$\boldsymbol{L^{i}_{part}}(\%) = \left(\frac{\boldsymbol{P^{i}_{input}} - \boldsymbol{P^{i}_{output}}}{\boldsymbol{P_{el}}}\right) \cdot \mathbf{100} \qquad \textbf{(4-22)}$$

Where $L_{part}{}^{i}$ is the percentage losses of *part i* of the TCCS, $P_{input}{}^{i}$ is the power input to *part i* coming from the generator and $P_{output}{}^{i}$ is the power after *part i*.

4.4.1 Worst case scenario: $\Gamma_{Gen} = 1$

The results from simulating the TCCS under all the cases discussed above are given in Table 4.4.

First of all, a comparison is made between the efficiency of the proposed algorithm to derive the filter parameters and reference filter parameters in each case. Based on the results of Table 4.4, we can observe that in all cases the proposed filters have fewer losses from the filters created using reference parameters. In addition, all the proposed filters are able to limit overvoltages at the generator terminals below 1.2pu, the highest overvoltage being 1.1659pu. This is not the case for the reference filters; the LV LCR filter has a peak overvoltage above 1.2pu which can lead to insulation stress or breakdown at the generator terminals [80]. It should be noted that the equations to calculate the reference filter parameters were derived for a *Cable system* whereas the TCCS in this paper also includes a transformer.

Taking a closer look at the losses from the filters we can see that the minimum losses are generated by the proposed LCR_{MV} filter and the LCR_{LV} in combination with the *RLC* filter. In addition to the very low losses, the maximum overvoltage at the generator terminals for these types of filters is close to 1pu which means that voltage reflections and harmonic resonance are mitigated effectively. A possible disadvantage of the proposed LCR_{MV} filter is that the components have to withstand medium voltage and this can increase the capital cost of the filter. The proposed LCR_{LV} filter in combination with a *RLC* filter operates onshore, at low voltage, has the lowest voltage total harmonic distortion (VTHD) and generates minimum losses, making such a combination favourable for a TCCS.

Table 4.4 Comparison of Filter Design Methods for the Worst Case Scenario.

Filter type	Filter Design Method	Peak overvoltage (pu)	Filter Losses (% of P_{el})
$R_{termination}$	Reference	1.0097	56.11
	Proposed	1.1375	21.89
$CR_{termination}$	Reference	1.1877	3.91
	Proposed	1.1659	1.74
$CRL_{termination}$	Reference	1.1709	4.32
	Proposed	1.1303	1.31
LCR_{MV}	Reference	1.0611	14.32
	Proposed	1.0601	0.17
LCR_{LV}	Reference	2.4563	0.35
	Proposed	1.1231	0.23
LCR_{LV} and *RLC*	Proposed	1.0411	0.15

Regarding the offshore filters, it can be observed that $R_{termination}$ generates a very high amount of losses and so this filter type cannot be considered an option. The proposed $CR_{termination}$ and $CRL_{termination}$ filter generate an acceptable amount of losses for TCCS, 1.74% and 1.31% respectively. Generally, offshore filters have to operate underwater and also generate higher losses compared to onshore filters making their use in a TCCS unlikely.

4.4.2 Second scenario: $\Gamma_{Gen} = 0.5$

The results from simulating the proposed TCCS under the second scenario are given in Table 4.5.

Table 4.5 Comparison of filter design methods for the second scenario $\Gamma_{Gen} = 0.5$.

Filter type	Filter Design Method	Peak overvoltage (pu)	Filter Losses (% of P_{el})
$R_{termination}$	Reference	1.0001	56.09
	Proposed	1.0575	21.79
$CR_{termination}$	Reference	1.1471	3.88
	Proposed	1.0935	1.72
$CRL_{termination}$	Reference	1.1012	4.29
	Proposed	1.0678	1.27
LCR_{MV}	Reference	1.0450	14.29
	Proposed	1.0411	0.17
LCR_{LV}	Reference	1.5032	0.34
	Proposed	1.0014	0.21
LCR_{LV} and *RLC*	Proposed	1.0091	0.15

As an overall observation it can be said that filter losses are not significantly affected when Γ_{Gen} changes. In addition, peak overvoltages are lower for both design methods. However, in the reference case of the LCR_{LV} filter we can see that peak overvoltage is above 1.2pu even though it is much lower compared to the worst case scenario. As for the rest of the filters the trends are similar to the worst case scenario. Offshore filters generate very high losses and their use in a TCCS is unlikely. The least possible losses are generated by the proposed LCR_{MV} filter and the combination of $\mathrm{LCR}_{\mathrm{LV}}$ filter with *RLC* filter. The fact that peak overvoltages are much lower is very important since the second scenario is more realistic compared to the worst case scenario. Therefore, using the worst case scenario we can design filters taking into account the limits of the system but in reality the system will operate under more favourable conditions.

4.4.3 Comparison with AHH Model

Based on the results presented in Sections 4.4.1 and 4.4.2 the use of a LCR_{LV} filter in combination with *RLC* filter has the least possible losses and mitigates overvoltages and harmonics effectively. From now on this type of filter which will be designed using the proposed algorithm will be referred as LCR_{opt} and the model using this filter will be referred as *Optimised Power Transmission* (*OPT) Model*. In this section the TCCS which was designed in Chapter 3 to represent the AHH system will be compared with the TCCS with the LCR_{opt} filter. The comparison will be based on the voltage harmonics, system losses and power exported.

Both system use similar types of filters. Both system have the same *RLC* filter tuned at the same frequency 2558Hz. However the *RC* branch and line inductance are different between the two cases. These differences are presented in Table 4.6.

Table 4.6 Filter parameters for the *AHH Model* and *OPT Model*.

Filter type	*RLC*			*RC*		Total line inductance
Filter parameters	R_{RLC} (Ω)	L_{RLC} (mH)	C_{RLC} (μF)	R_{RC} (Ω)	C_{RC} (μF)	L_{line} (mH)
AHH Model	0.1	0.06	21.5	0.10	64	0.2728
OPT Model	0.1	0.06	21.5	10.35	22.5	0.2728

In Table 4.7 the averaged power losses between *AHH Model* and *OPT Model* are compared. The averaged power losses presented in Table 4.7 are presented in percentage relatively to the power generated from the generator. The system parts presented are the cables, the generator side transformer, the generator side filter losses and the grid side losses which includes the DC link losses.

Table 4.7 Averaged power losses between *AHH Model* and *OPT Model*.

P_{el} (pu)	Component	Losses (% of P_{el})		
		AHH Model	*OPT Model*	Difference
1.00	Cables	1.99	2.05	-0.06
	Transformer	1.80	1.81	-0.01
	Filter	0.68	0.14	+0.54
	Grid side	2.66	2.68	-0.02
0.75	Cables	1.70	1.75	-0.05
	Transformer	1.94	1.95	-0.01
	Filter	1.21	0.23	+0.98
	Grid side	2.42	2.45	-0.03
0.50	Cables	1.58	1.56	+0.02
	Transformer	2.55	2.36	+0.19
	Filter	8.29	0.24	+8.05
	Grid side	2.16	2.34	+0.18

Based on the results presented in Table 4.7 a significant reduction of the generator side filter losses can be achieved by using the *OPT method* presented in this Chapter. At rated operation the reduction of losses is estimated to be 0.54% of the power generated. Higher reduction of losses are achieved when the TCCS is operating below rated power. In Table 4.7 the cases of 0.75pu and 0.50pu power generated are presented. The reduced amount of losses of the generator side filter in the *OPT Model* is also reflected in the total system losses. At rated operation the total system losses for the *AHH Model* and the *OPT Model* are 7.13% and 6.68% respectively. Reduced system losses means higher power exported from the TCCS to the grid and increased revenue for tidal current array developers. For a 1.15MW TCCS for which the above simulations were carried out the reduction of losses by 0.35% can increase the power output at rated operation by approximately 4kW. The reduction of losses for the *OPT Model* at the other operating points are higher reaching up to 8.44% for the 0.50pu operation. Detailed comparisons between the *OPT Model* with PMSG and SCIG and the *OPT Model* and a TCCS with BTB converters in the nacelle will be carried out in Chapter 5.

4.5 Summary

This Chapter focused on TCCS that are controlled from a VSC that is far away from the generator. The problems associated with long distance control, voltage reflections and resonance, were established mathematically. In order to quantify the phenomenon of resonance the voltage gain graphs were developed. As the study in this Chapter showed, voltage gain graphs can depict frequencies where harmonics are expected to be increased and frequencies where harmonics are mitigated. Voltage gain graphs for TCCS with different components between the generator and the VSC were studied at different generator controller switching frequencies. This study revealed that changing the switching frequency of the generator controller at a resonant minimum frequency can reduce the harmonics at the generator terminals. However, there are practical limitations on how much the generator controller switching frequency can be increased and in addition the resonant peaks at higher harmonic frequencies have to be avoided as well. In order to eliminate the need to change the generator controller switching frequency drastically, the use of passive power harmonic filters at the generator terminals or the power converter terminals were studied. An extensive review of filters is presented in this Chapter and using equations found in the literature different passive power harmonic filters are designed for the TCCS modelled in Chapter 3. A key novelty presented in Section 4.3.2 is the filter design algorithm based on the voltage gain graphs. Comparison of the power harmonic filters designed by the algorithm and by the equations found in the literature showed that minimum losses and filter effectiveness can be achieved with the optimised filter parameters chosen by the algorithm. In all the cases the filter design algorithm managed to find a set of parameters for the power harmonic filter that mitigates overvoltages at the generator terminals but at the same time keeps filter losses at a minimum.

Chapter 5

Power transmission study for single tidal current devices

5.1 Introduction

This chapter defines the most efficient way of transmitting power from a single tidal current converter to the shore. Firstly, the boundaries of the analysis are set by specifying the TCCS and transmission technology options. Afterwards, the generator technologies for each transmission option are compared in terms of efficiency and total energy generated. A sensitivity analysis is performed in order to investigate the influence of cable parameter uncertainties on the presented results. The final part of this chapter deals with the effect of changing the cable length and its impact on the power transmission options considered.

5.2 Power transmission options considered in the analysis

Four different options are considered in this chapter's analysis:

- SCIG with long distance controls (SCIG LDC).
- PMSG with long distance controls (PMSG LDC).
- SCIG with back-to-back converters in the nacelle (SCIG BTB).
- PMSG with back-to back converters in the nacelle (PMSG BTB).

The DC collection point is excluded from the analysis of the power transmission for single tidal current devices as described in Chapter 1. This is due to the fact that DC collection points for single tidal current devices are not an option for both tidal current developers (see Section 1.2.3) and major electrical companies (see Section 2.6). The block diagrams of the four different electrical topologies are presented in Figure 5.1.

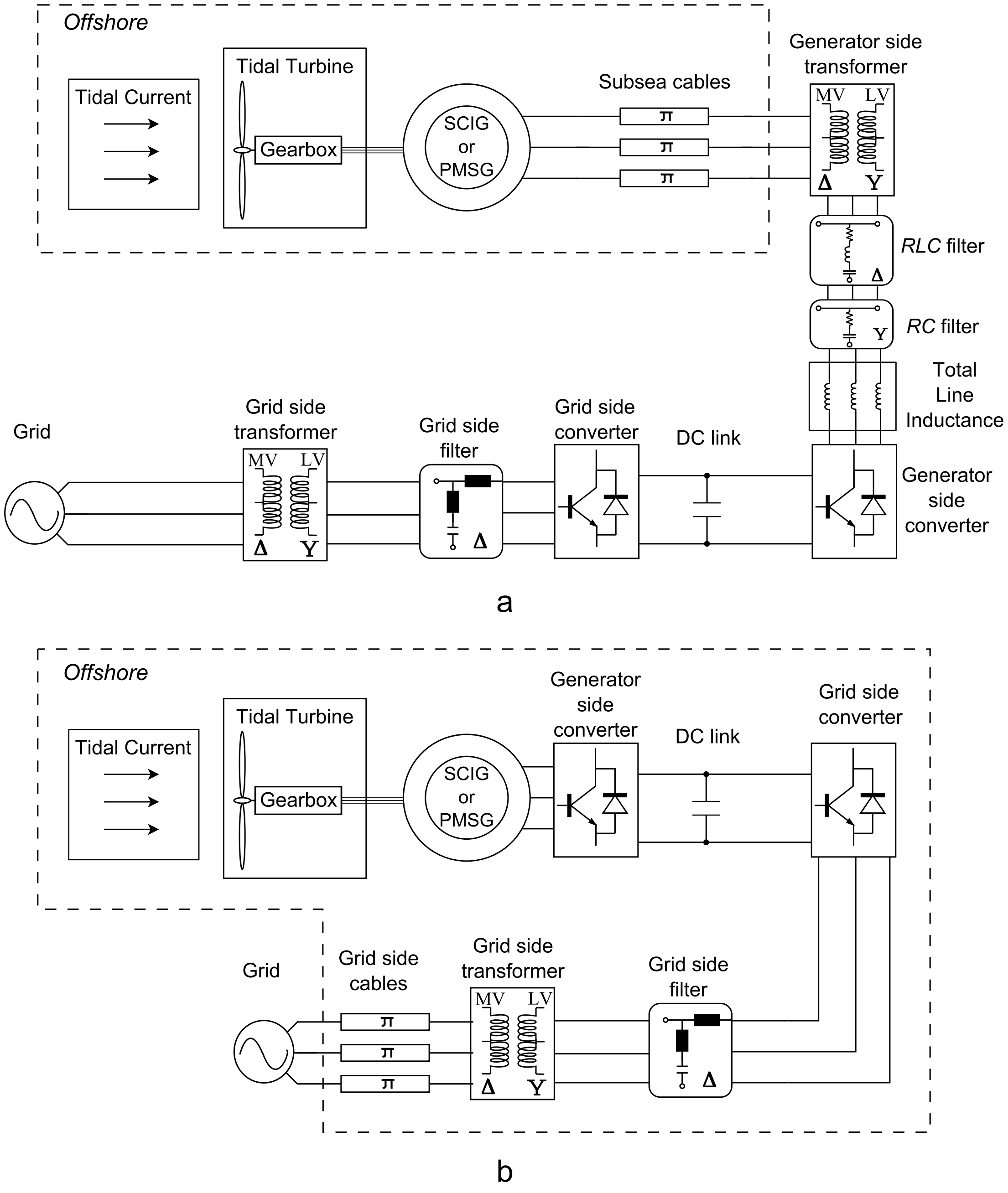

Figure 5.1 Block diagrams of single TCCS. a. SCIG and PMSG options with long distance controls. b. SCIG and PMSG options with back-to-back converters in the nacelle.

5.3 Comparison of the electrical topologies for single tidal current device

In this section different stages of comparison will take place in order to determine the following:

- Whether a PMSG is an efficient alternative for TCCS with long distance controls.
- If using a PMSG in a system with BTB converters yields an advantage in a TCCS.
- Which approach from the four options presented in Figure 5.1 exports more energy to the grid over a half-cycle of a semidiurnal tide.

The comparison will be based on:

- Generator efficiency and energy capture.
- Power losses at different parts of the system.
- System accessibility.

The generator efficiency is calculated using (5-1).

$$\begin{cases} \boldsymbol{P_{mec}(W) = T_{mec} \cdot \omega_{mec}} \\ \boldsymbol{P_{el}(W) = I_a \cdot V_a + I_b \cdot V_b + I_c \cdot V_c} \\ \boldsymbol{\eta(\%) = (P_{el}/P_{mec}) \cdot 100} \end{cases} \tag{5-1}$$

Where P_{mec} is the mechanical input power from the tidal turbine in *Watts*, P_{el} is the electrical power output from the generator in *Watts*, I_{abc} is the three-phase current at the generator terminals, V_{abc} is the three-phase voltage at the generator terminals and η is the generator efficiency.

Power losses at different parts of the tide-to-wire TCCS model are calculated with respect to power generated (P_{el}) using (5-2).

$$\boldsymbol{L_{part\ i}(\%) = \left(\frac{P^i_{input} - P^i_{output}}{P_{el}}\right) \cdot 100} \tag{5-2}$$

Where L_{part}^{i} is the percentage losses of *part i* of the TCCS, P_{input}^{i} is the power input to *part i* coming from the generator and P_{output}^{i} is the power after *part i*.

Finally, system accessibility is assessed based on the number of components that are underwater and the number of components that are installed on land.

The tidal current velocity input in the tidal array is based on Figure 3.3 presented in Section 3.1. Figure 5.2 shows the tidal current velocity used in this Chapter.

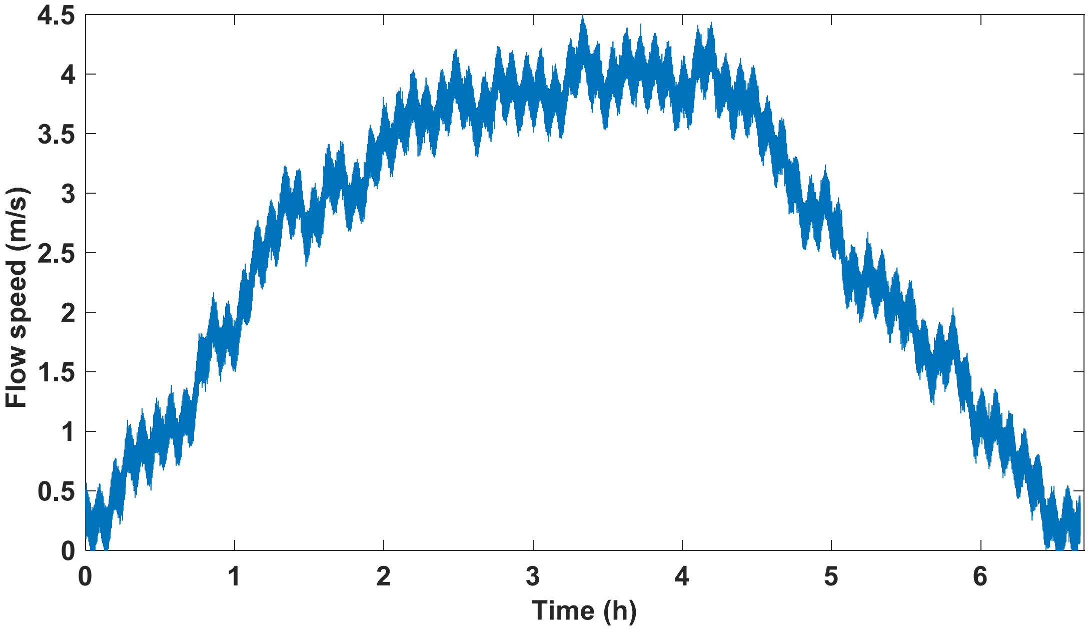

Figure 5.2 Tidal current velocity used as input to the tidal current systems.

5.3.1 Tidal current devices with long distance controls

The block diagram of a TCCS with long distance controls is depicted in Figure 5.1a. At this point it should be noted that TCCSs with long distance controls use the *SupH* supervisory controller discussed in Section 3.4.3 and presented in Figure 3.19a. In addition, the subsea cables connecting the generator to the power converters are based on the cables presented in Section 3.5.1 and the cable parameters presented in Table 3.10. This means that a constant cable length of 3.5km is assumed when comparing both cases. A sensitivity analysis for the cable length is carried out later in Section 5.4.1. The filter is based on the *RLC* filter presented in Section 3.5.2 which was used by AHH, and the *RC* branch is based on the improved *OPT Model* discussed in Section 4.4.3.

Comparison of averaged generator efficiency between the SCIG and the PMSG are depicted in Figure 5.3.

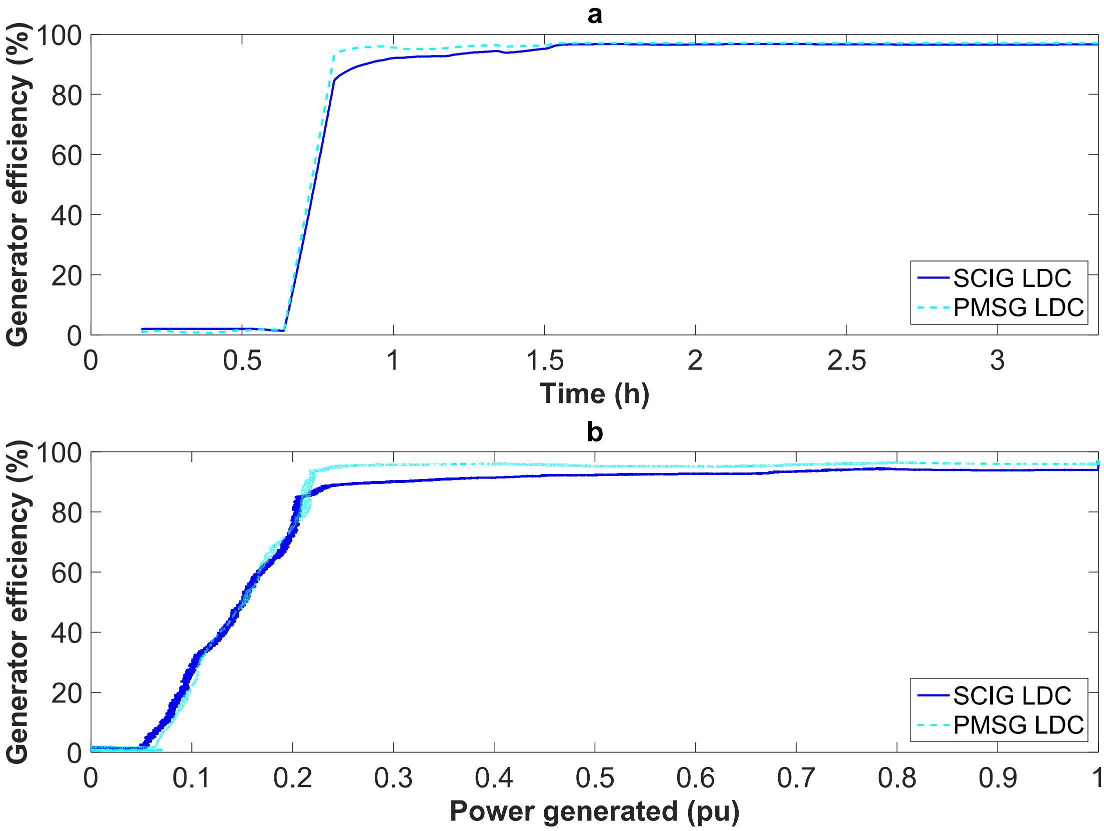

Figure 5.3 Generator efficiency comparison for LDC systems. a. Generator efficiency over time. b. Generator efficiency over power generated.

Observing Figure 5.3 it can be said that the PMSG with LDC achieves and maintains a higher efficiency compared to the SCIG with LDC. For the same tidal flow input and tidal current turbine the PMSG LDC increases its efficiency faster compared to SCIG LDC as the flow speed increases over time (Figure 5.3a). The PMSG LDC achieves a 93.03% generator efficiency when the generator reaches 800rpm whereas generator efficiency for the SCIG LDC is 85.1% (approximately at 0.8h). From 0.8h to 1.6h the TCCS operates based on the MPPC. For the SCIG LDC and the PMSG LDC systems generator efficiency increases from 85.1% to 96.58% and from 93.03% to 97.06% respectively. The generator efficiency achieved at 1.6h is maintained as long as the TCCS operates at rated power. The higher generator efficiency of PMSG LDC can also be observed in Figure 5.3b. For all the operating points of the system the PMSG LDC maintains a higher efficiency compared to SCIG LDC. In addition to generator efficiency system losses at other parts of the system have to be studied during the operation in order to determine the most efficient TCCS.

Studying and comparing the losses between the generator and the onshore converter is of extreme importance for a TCCS that uses long distance controls. These losses also include the transmission losses of the system and can affect significantly the total power exported to the grid. In both TCCS under consideration, three components are connected between the generator and the onshore VSC. These components are the long three phase cables, the transformer and a low voltage filter. Table 5.1 summarises the results regarding the losses under different operating stages of the system. The grid side losses include DC link losses, grid filter losses and grid transformer losses. Observing the two generator cases separately we can note that cable and transformer losses are increasing as the power generated is increasing. This is due to the increased current that is generated as more power is produced. As the current increases, more power is dissipated due to the resistance of the transformer and the cable. On the other hand, filter losses are decreasing as the power generated is increasing. The reason behind this trend is the fact that the filter has significant constant losses and therefore when these losses are calculated as a percentage to power generated, they decrease.

Table 5.1 Comparison of power losses between SCIG LDC and PMSG LDC systems at different stages and operating points.

Power generated (pu)	***Component***	***Losses (% of power generated)***		
		SCIG LDC	***PMSG LDC***	***Difference***
1.00	Cables	2.05	1.95	+0.10
	Transformer	1.81	1.79	+0.02
	Filter	0.24	0.31	-0.07
	Grid side	2.68	2.69	-0.01
0.75	Cables	1.75	1.60	+0.15
	Transformer	1.95	1.93	+0.02
	Filter	0.23	0.29	-0.06
	Grid side	2.45	2.47	-0.02
0.50	Cables	1.56	1.49	+0.07
	Transformer	2.36	2.38	-0.02
	Filter	0.24	0.39	-0.15
	Grid side	2.34	2.36	-0.02

Comparing the losses generated between the SCIG LDC and the PMSG LDC, it can be seen that there is a visible difference in cable and filter losses and a less significant change in transformer and grid side losses. Cable and filter losses are sensitive to cable length, a study which is carried out in Section 5.4.1. In total, the SCIG LDC has approximately 0.07% more losses compared to the PMSG LDC. The difference in losses appears due to the higher harmonics that are present in the SCIG case. As it is depicted in Figure 5.4 generator voltages and currents from both cases are close to 1pu during operation at rated power as it is expected. The voltage total harmonic distortion (VTHD) for the SCIG and PMSG are 4.44% and 3.27% respectively while the current THD is 3.1% and 0.4% respectively. The additional harmonics that are present in the SCIG case generate extra power losses in the TCCS.

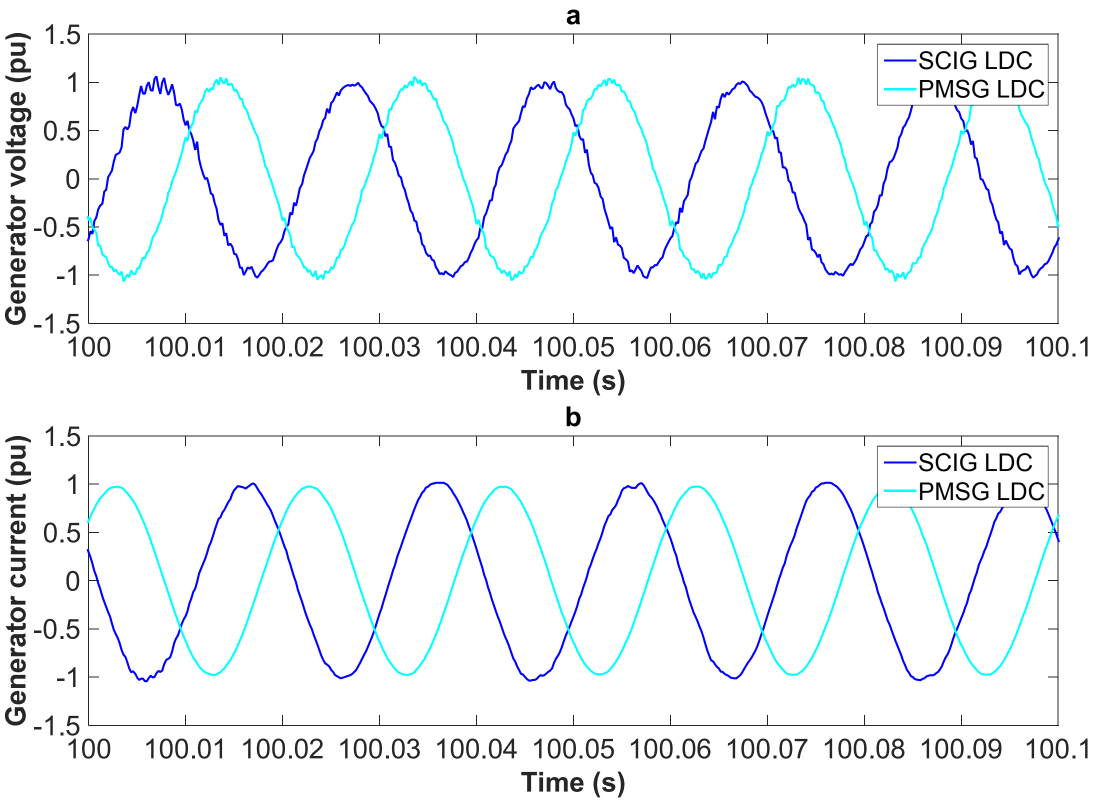

Figure 5.4 Generator output comparison between SCIG LDC and PMSG LDC systems. a. Generator voltage. b. Generator current.

5.3.2 Tidal current devices with converters in the nacelle

The block diagram of a TCCS with converters in the nacelle is depicted in Figure 5.1b. A TCCS with converters in the nacelle has no need to use the *SupH* supervisory controller. Instead the *SupW* supervisory controller can be used which follows the MPPC earlier and therefore tidal flow power is more efficiently converted from the tidal turbine. The *SupW* supervisory controller is discussed in Section 3.4.3 and presented in Figure 3.19b. Another difference in the design of a TCCS with converters in the nacelle compared to a TCCS with long distance controls is the location and type of subsea cables. As shown in Figure 5.1b a transformer is installed offshore at the output of the inverter in order to step-up the low voltage output of the inverter to medium voltage. The medium voltage chosen to transmit power from the single TCCS with BTB converters in the nacelle is 33kV but results from 11kV power transmission will also be shown for comparison purposes. This is significantly higher compared to the 6.6kV transmission voltage in a TCCS with long distance controls. Apart from the transmission voltage the cable type and parameters are also different. A detailed list of cable parameters used for power transmission for the systems with converters in the nacelle are presented in Appendix C. The cable length for this study remains the same at 3.5km in order to have comparable results to Section 5.3.1.

A comparison of generator efficiency over time between the SCIG BTB and the PMSG BTB are depicted in Figure 5.5.

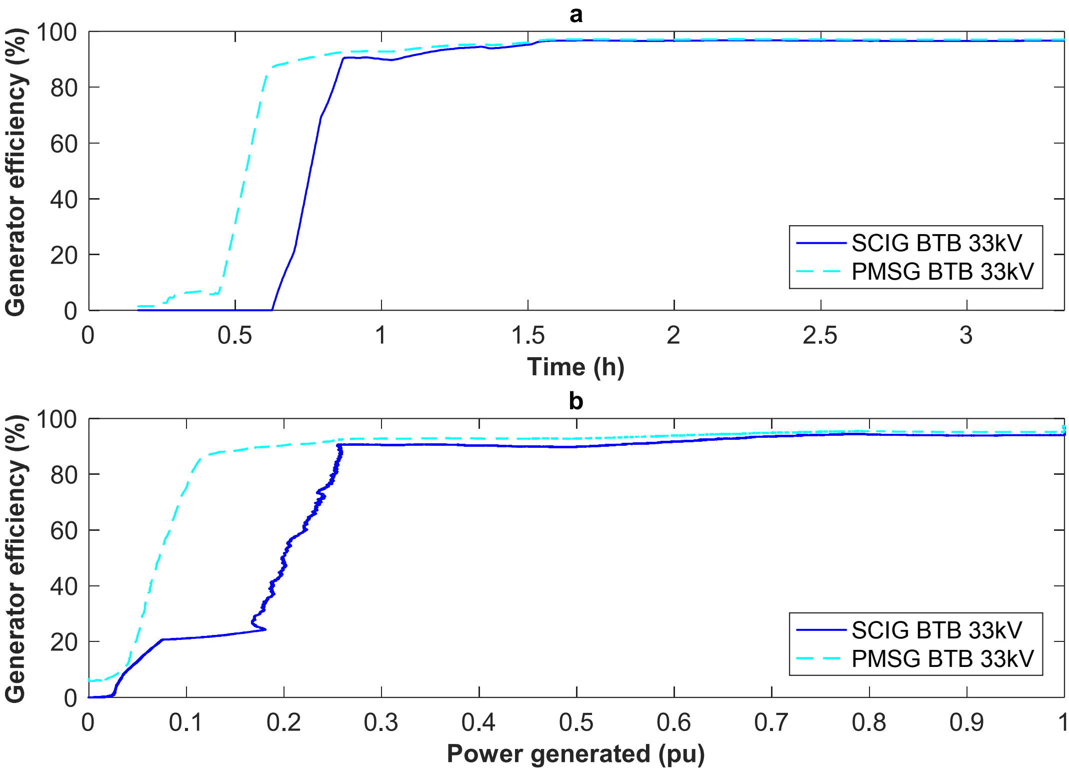

Figure 5.5 Generator efficiency comparison between SCIG BTB and PMSG BTB systems. a. Generator efficiency over time. b. Generator efficiency over power generated.

The PMSG BTB system starts to increase its generator efficiency at around 0.45h which is significantly earlier compared to the SCIG BTB system which starts at 0.63h (Figure 5.5a). After the start-up process the efficiency increase for both systems is steep. For the PMSG BTB system the generator efficiency reaches 87.1% at 0.625h. From 0.625h to 1.57h the PMSG BTB system is increasing its efficiency gradually to 97.03% which is the efficiency at rated power. For the SCIG BTB system the generator reaches 90.52% efficiency at 0.875h and 96.57% at rated power at 1.57h.

In Table 5.2, the averaged system losses are compared at different parts of the SCIG BTB and PMSG BTB systems and also at different operating points. A TCCS with converters in the nacelle is separated into two systems. The *Grid side* which consists of the DC link, grid filter and grid transformer at 33kV and the *Grid side cables* which transmit power from the TCCS to the grid. It should be noted here that the *Grid side* in Section 5.3.1 consists of exactly the same type of components as in this section.

Table 5.2 Comparison of power losses between SCIG BTB and PMSG BTB systems at different stages and operating points.

Power generated (pu)	*Component*	*Losses (% of power generated)*		
		SCIG BTB	*PMSG BTB*	*Difference*
1.00	Grid side	3.99	3.96	+0.03
	Grid side cables	0.17	0.17	+0.00
0.75	Grid side	3.77	3.76	+0.01
	Grid side cables	0.13	0.13	+0.00
0.50	Grid side	3.75	3.77	-0.02
	Grid side cables	0.09	0.09	+0.00

Results presented in Table 5.2 show that SCIG BTB and PMSG BTB systems have similar system losses. A small variation in losses comparing the grid side part is evident but these deviations are negligible.

In Sections 5.3.1 and 5.3.2 results from four different systems were presented. The generator efficiency in each case was studied for a half-cycle of a semi-diurnal tide and the losses at different parts of the system were also presented.

5.3.3 Tidal current conversions system with onshore converters versus with converters in the nacelle

In this section all four systems are compared based on the energy they export to the grid and total energy losses. In Figure 5.6 power generated and power exported to the grid are presented for the four systems for a half-cycle of a semidiurnal tide.

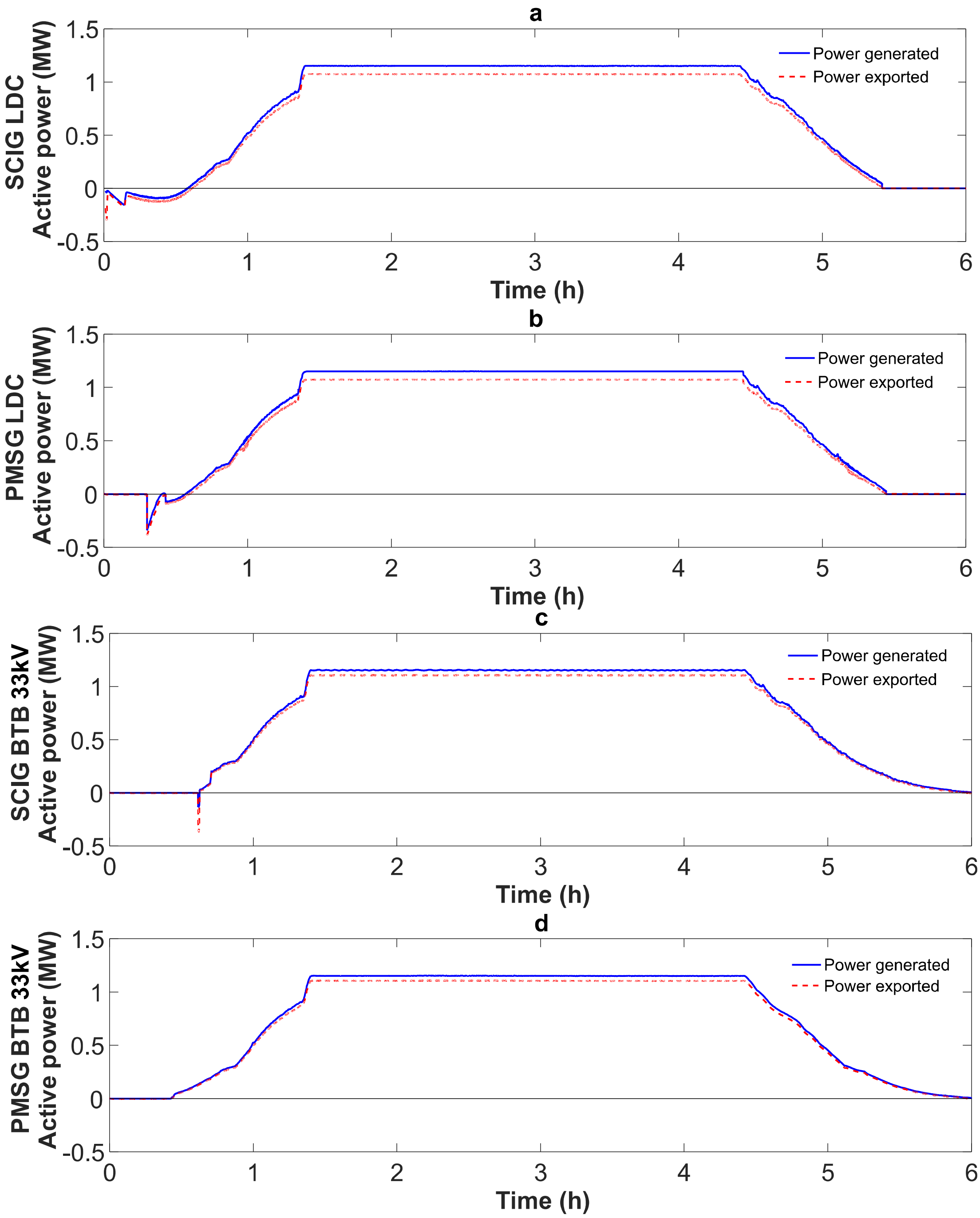

Figure 5.6 Power generated and power exported over a half-cycle of a semi-diurnal tide. a. SCIG LDC. b. PMSG LDC. c. SCIG BTB. d. PMSG BTB.

Observing Figure 5.6 two major differences can be noted between the four systems studied. The first major difference is the fact that the long distance control systems require active power in order to increase the speed of the generator to 800rpm. The SCIG BTB system also requires a small amount of power in order to start-up the induction generator but the total energy is significantly smaller. The PMSG BTB systems does not require any power for the start-up process. Another major difference between systems using long distance controls and systems with converters in the nacelle is the total amount of time the system is generating power. In Figure 5.6a and Figure 5.6b it can be observed that the system stops generating power at around 5.5h. When power exported reaches zero the TCCS is disconnected from the grid and this is the reason why active power after 5.5h is zero. This is not the case for SCIG BTB and PMSG BTB which generate power for the entire 6 hour time period.

Apart from the observations discussed above it is difficult to distinguish which system exports more energy and which has significant energy losses. For that reason the cumulative energy graphs for the exported power for the four systems are presented in Figure 5.7. The cumulative energy graph gives a better insight of the energy each system exports to the grid over the 6 hour time period.

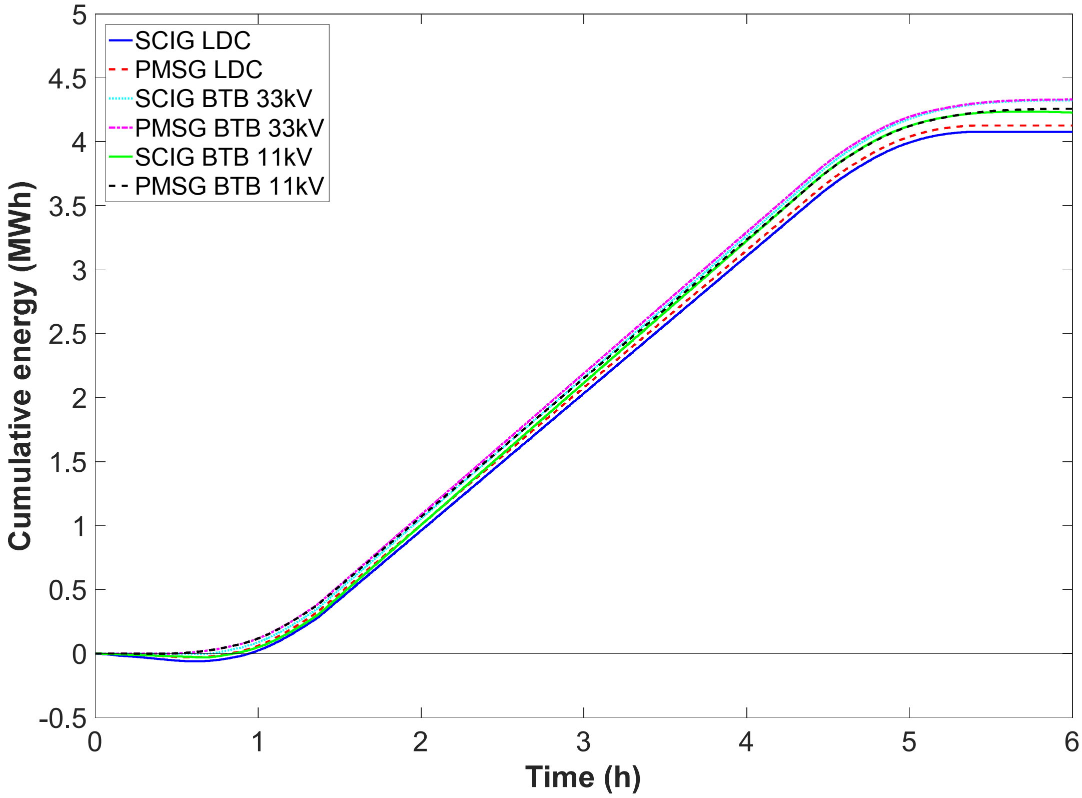

Figure 5.7 Exported cumulative energy over a 6h time period for the four different TCCSs studied and the 11kV variations for the BTB systems.

Based on Figure 5.7 the TCCS with the converters in the nacelle export more energy compared to TCCS with long distance controls. Furthermore, PMSG BTB 33kV, PMSG BTB 11kV and PMSG LDC export more energy compared to SCIG BTB 33kV, SCIG BTB 11kV and SCIG LDC respectively. It has to be noted here that PMSG BTB 11kV and SCIG BTB 11kV refers to a TCCS with converters in the nacelle and transmission voltage of 11kV compared to the 33kV transmission voltage of PMSG BTB 33kV and SCIG BTB 33kV systems. Table 5.3 summarises the quantitative results of Figure 5.7 and in addition presents results for the system efficiency and total energy losses in each case.

Table 5.3 Summarised results for the four TCCS studied under a 6h time period.

TCCS	***Total Losses at 1pu (% of P_{el})***	***Maximum cumulative energy exported (MWh)***	***Total energy losses (MWh)***
SCIG LDC	6.78	4.0789	0.3322
PMSG LDC	6.74	4.1285	0.3257
SCIG BTB 33kV	4.16	4.3249	0.1969
PMSG BTB 33kV	4.13	4.3314	0.1891
SCIG BTB 11kV	5.93	4.2368	0.2737
PMSG BTB 11kV	5.88	4.2586	0.2659

According to results presented in Table 5.3, differences between SCIG and PMSG using the same transmission system are small. PMSG options have maximum cumulative energy exported compared to SCIG options. This is due to the higher total losses of SCIG systems compared to the respective PMSG systems at 1pu operation.

Bigger variations appear between the two different transmission options. TCCS using long distance controls have less maximum cumulative energy exported compared to TCCS with converters in the nacelle. Two reasons are responsible for the lower energy export of the LDC systems:

- LDC systems have more total energy losses. The SCIG LDC option has 0.1353 MWh and 0.0585 MWh more losses compared to SCIG BTB 33kV and SCIG

BTB 11kV options respectively for a 6 hour time period. The same can be said for the PMSG systems. The PMSG LDC has 0.1366 MWh and 0.0598 MWh more losses compared to the PMSG BTB 33kV and PMSG BTB 11kV options respectively for the studied 6 hour period. The main reason for the reduced losses in BTB systems is the higher voltage for power transmission. LDC systems transmit power at 6.6kV while BTB systems transmit power at 33kV or 11kV depending on the case.

- LDC systems generate power for shorter periods compared to BTB systems. This can become evident if the maximum cumulative energy produced is calculated in each system. The PMSG BTB 33kV produces 0.1095 MWh more compared to PMSG LDC and SCIG BTB 33kV produces 0.1107 MWh more compared to SCIG LDC. LDC systems generate for shorter periods because they use the *SupH* supervisory controller as described in Section 3.4.3. The *SupH* supervisory controller forces the generator to operate at 800rpm for tidal current velocities up to 2m/s. Operating the generator at constant speed reduces the hydrodynamic efficiency of the tidal current turbine and therefore decreases power production.

The biggest difference appears between PMSG BTB 33kV and SCIG LDC. Over the 6 hour period, the PMSG BTB 33kV option exports 5.8% more energy compared to the SCIG LDC.

The results presented in Section 5.3 are based on systems with constant cable length and known cable inductance and capacitance. In the following section a sensitivity analysis is performed in order to evaluate how the results presented in this section are affected by the uncertainty of the exact cable length or using inaccurate cable inductance or cable capacitance.

5.4 Sensitivity analysis

In this section sensitivity analysis over the uncertainty of cable length, cable capacitance and cable inductance is carried out and the effect of this uncertainty on voltage regulation is presented. For every sensitivity study one model parameter at a time is considered uncertain.

5.4.1 Cable length uncertainty

Cable length uncertainty is considered a major problem for tidal current developers that use long distance controls. At the initial stages of a tidal current project power transmission cables are estimated based on bathymetry and distance to shore. However, at the installation stage the final cable length might not be the same as the estimated due to several reasons. Seabed morphology, weather conditions at the day of installation, environmental issues and cable connection to the onshore power converter station can affect the final length of the cables. In a system with long distance controls the design of the generator side filter is highly dependent on the cable length. Errors in cable length can lead to ineffective generator side filters. In this section the sensitivity of the generator side filter to cable length uncertainty is examined. The four TCCS studied in Section 5.3 will also be considered for the cable length sensitivity analysis. The cable length sensitivity analysis is carried out in the following way:

- The four TCCS are designed exactly as mentioned in Section 5.3. All four systems are based on 3.5km cable length. The generator side filter for the LDC systems is also designed for 3.5km cable. Its parameters are those presented in Table 4.6 for *OPT Model*.
- The four TCCS are simulated using a different cable lengths. The simulations carried out are based on a percentage difference around 3.5km. The percentage differences studied are: ±5%, ±10%, ±20%.
- Peak overvoltage at the generator terminals and total losses at rated operation are presented and analysed. Systems with converters in the nacelle have no voltage regulation problems at the generator terminals and therefore results for LDC systems are only presented in this case.

Figure 5.8 presents how the peak overvoltage of the LDC systems is changing with uncertainty of the cable length.

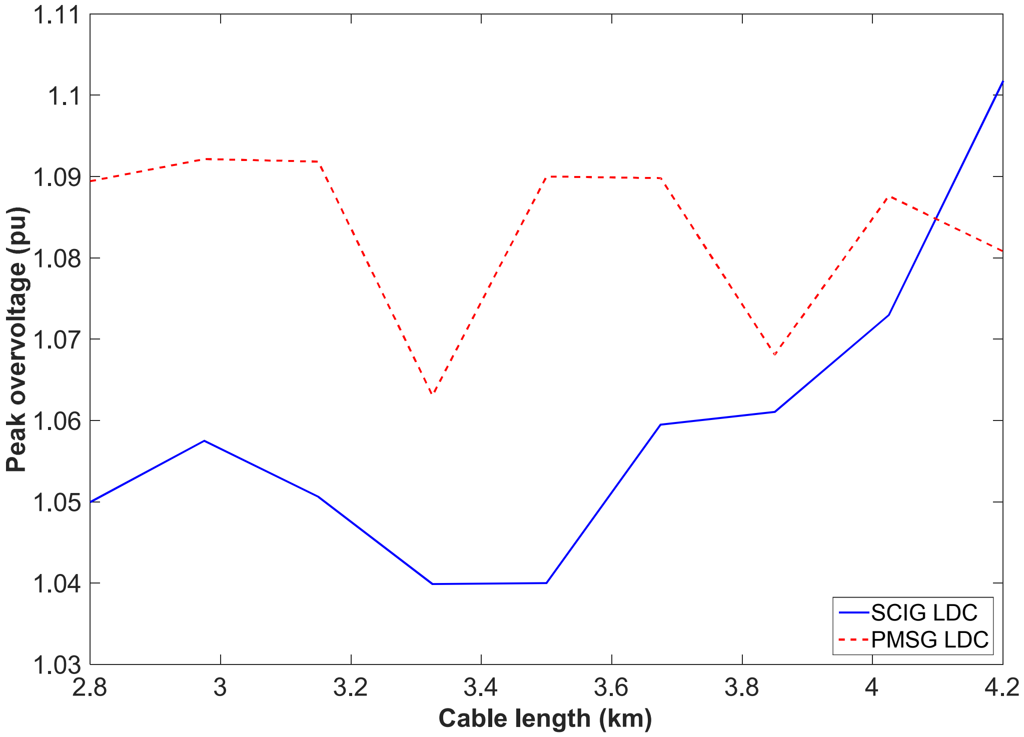

Figure 5.8 Peak overvoltage at the generator terminals over cable length uncertainty.

The results depicted in Figure 5.8 show that for the SCIG LDC peak overvoltage is increasing as uncertainty increases from 5% to 20%. For the PMSG LDC system peak overvoltage remains relatively constant between 1.07pu and 1.10pu. In all cases studied peak overvoltage does not exceed the 1.2pu which is the maximum allowable overvoltage. Table 5.4 shows the change in total losses with uncertainty in cable length.

Table 5.4 Total system losses for the TCCS under study with cable length uncetainty.

Cable Length Uncertainty	***Total losses at 1pu (% of P_{el})***			
	SCIG LDC	PMSG LDC	SCIG BTB 33kV	PMSG BTB 33kV
+5%	7.25	6.78	4.17	4.13
−5%	7.05	6.60	4.16	4.11
+10%	7.35	6.87	4.18	4.14
−10%	6.96	6.51	4.15	4.10
+20%	7.55	7.03	4.20	4.15
−20%	6.76	6.34	4.13	4.09

The general trend from the results presented in Table 5.4 is that the longer the cables the higher the total losses are in each case. However, LDC systems are more affected by cable length uncertainty and even more so the SCIG systems. For example, the SCIG LDC system with +20% uncertainty in cable length generates 0.77% more losses compared to the expected design. This is significantly less in PMSG LDC at 0.29% more losses and even less for the SCIG BTB 33kV and PMSG BTB 33kV at 0.04% and 0.02% more losses respectively.

5.4.2 Cable capacitance or inductance uncertainty

Cable capacitance or inductance uncertainty can greatly affect the voltage regulation of the filter in LDC systems. The same process followed in Section 5.4.1 for cable length uncertainty will also be followed in this section for capacitance and inductance separately.

- The SCIG LDC and PMSG LDC are designed exactly as mentioned in Section 5.3. Both systems are based on 3.5km cable length and the cable parameters as given in Table 3.10. The generator side filter for the LDC systems is also designed based on cable parameters given in Table 3.10. The generator side filter parameters are those presented in Table 4.6 for the *OPT Model*.
- Both systems are simulated using different cable capacitance or cable inductance. The simulations carried out are based on percentage difference around cable capacitance and cable inductance of Table 3.10. The percentage differences studied are: ±20% and ±50%. The limit of ±50% has been chosen based on the study presented in [82].
- Voltage regulation at the generator terminals is presented in Table 5.5.

Table 5.5 Voltage regulation of LDC systems with uncertainty in cable capacitance or cable inductance.

Cable capacitance	Cable inductance	Voltage regulation	
		SCIG LDC	**PMSG LDC**
L_C	C_C	4%	9%
$L_C+20\%$	C_C	8%	8%
$L_C+50\%$	C_C	16%	10%
$L_C-20\%$	C_C	8%	8%
$L_C-50\%$	C_C	7%	9%
L_C	$C_C+20\%$	19%	10%
L_C	$C_C+50\%$	26%	19%
L_C	$C_C-20\%$	7%	10%
L_C	$C_C-50\%$	8%	19%

The SCIG LDC is significantly affected by cable inductance or capacitance uncertainty. Major changes in voltage regulation appear in $C_C+50\%$, $C_C+20\%$ and $L_C+50\%$. However, only in the extreme case of $C_C+50\%$ voltage regulation is outside the limit of 20%. Regarding the PMSG LDC, voltage regulation is affected with cable capacitance uncertainty. In all the other cases voltage regulation varies between 8% and 10%. Table 5.5 presents results only when there is uncertainty in one cable parameter, cable capacitance or cable inductance. In Table 5.6 four extreme cases of voltage regulation are presented with uncertainty on two cable parameters.

Table 5.6 Voltage regulation of LDC systems with uncertainty on both cable capacitance and inductance.

Cable capacitance	Cable inductance	Voltage regulation	
		SCIG LDC	**PMSG LDC**
$L_C+50\%$	$C_C+50\%$	43%	7%
$L_C+50\%$	$C_C-50\%$	8%	19%
$L_C-50\%$	$C_C+50\%$	29%	10%
$L_C-50\%$	$C_C-50\%$	10%	19%

Based on the results presented in Table 5.6 the voltage regulation of the SCIG LDC system is highly affected by the extreme case of cable capacitance increase. In both cases that the cable capacitance is increased by 50% the voltage regulation is outside the limit of 20%. In the cases where cable capacitance is decreased by 50% voltage regulation varies between 8% and 10%. Regarding the PMSG LDC system voltage is regulated in all the extreme cases. However, in the two cases where cable capacitance is decreased by 50% voltage regulation is near the specified limit of 20%.

5.5 Effect of cable length on system losses and energy exported

All the results presented in Section 5.3 and Section 5.4 assumed constant cable length of 3.5km. In this section the effect of increasing or decreasing the cable length on system losses and energy exported is presented. The cable lengths considered are based on [75]–[78] and therefore the study starts from 1km cable length up to 15km cable length with a 0.5km step. For the LDC systems, changing the cable length means different generator side filter parameters. For each different cable length the process followed in Section 4.3.2 and 4.3.2.6 is applied and a different set of filter parameters is calculated. Table 5.7 shows the resistance and capacitance used at the *RC* branch of the generator side filter of the LDC systems for each different cable length.

Table 5.7 *RC* filter parameters for changing cable length.

Cable Length (km)	R_{RC} (Ω)	C_{RC} (μF)
1.0	15.5100	15.00
1.5	11.4900	20.25
2.0	9.7680	26.25
2.5	8.0440	31.50
3.0	7.4700	37.50
3.5	6.8950	44.25
4.0	6.3200	49.50
4.5	3.4480	103.50
5.0	2.0690	186.80
5.5	2.0110	204.80
6.0	1.7240	221.30
6.5	1.7240	239.30
7.0	1.7240	258.00
7.5	1.7240	278.30
8.0	1.4940	294.00
8.5	1.4360	313.10
9.0	1.4360	331.90
9.5	1.0340	506.30
10.0	1.0340	532.50
10.5	1.0340	562.50
11.0	1.0340	592.50
11.5	0.9193	618.80
12.0	0.9193	648.80
12.5	0.6895	1223.00
13.0	0.6895	1268.00
13.5	0.6895	1320.00
14.0	0.5746	1391.00
14.5	0.5746	1455.00
15.0	0.5746	1489.00

Figure 5.9 shows total losses for all six TCCSs studied over cable length.

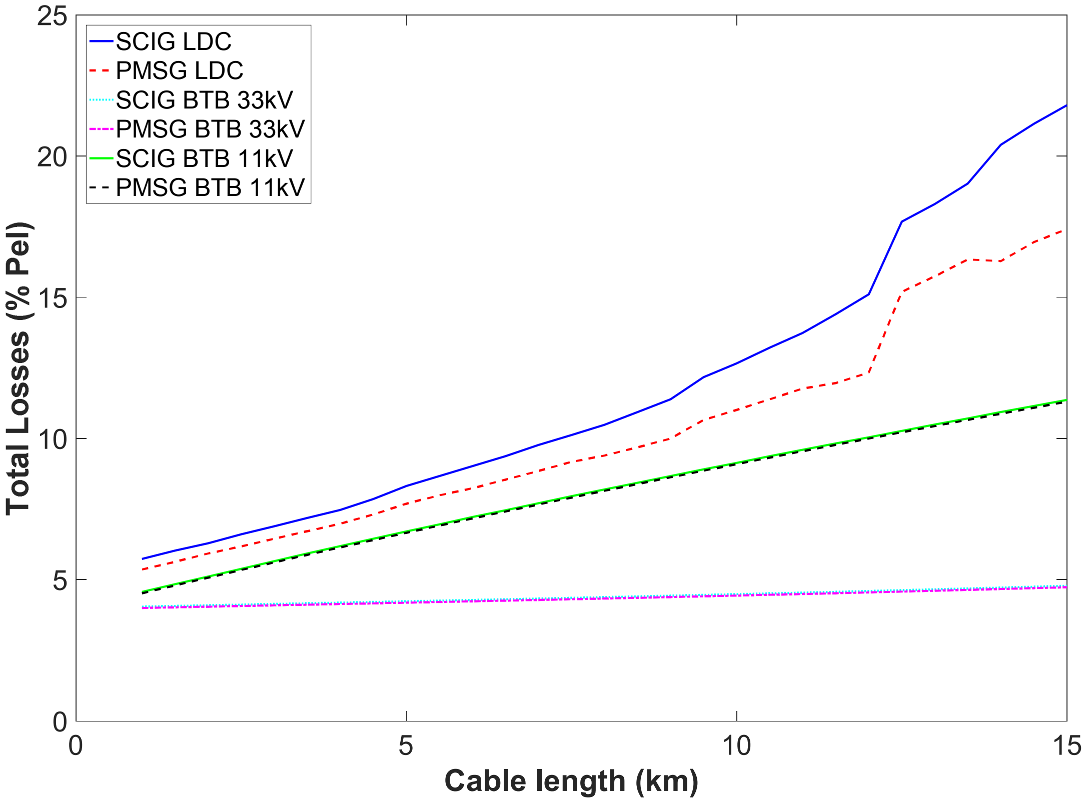

Figure 5.9 Total losses versus cable length for the six TCCS under study.

As it can be observed from Figure 5.9 the total losses in the system widens between LDC and BTB as cable length increases. At 1km cable length the difference in total losses between LDC and BTB is around 1.5% whereas this increases to a 17% difference for the SCIG LDC and 12.5% for the PMSG LDC at 15km cable length. The slope between LDC systems and BTB 11kV systems is similar between 1km and 5km. However, LDC systems have a slightly increased slope between 5km and 10km compared to BTB 11kV systems and an even bigger difference between 10km and 15km. The difference of total losses between SCIG BTB 33kV and PMSG BTB 33kV is very small with 4.789% and 4.738% total losses respectively at 15km cable length. The same can be said for SCIG BTB 11kV and PMSG BTB 11kV. The case is not the same for LDC systems. PMSG LDC has lower total losses compared to SCIG LDC for all the cable lengths studied. The difference in total losses is 0.37% at 1km cable length and widens to 4.39% at 15km. Figure 5.10 presents how the increasing losses affect the cumulative energy exported from a TCCS.

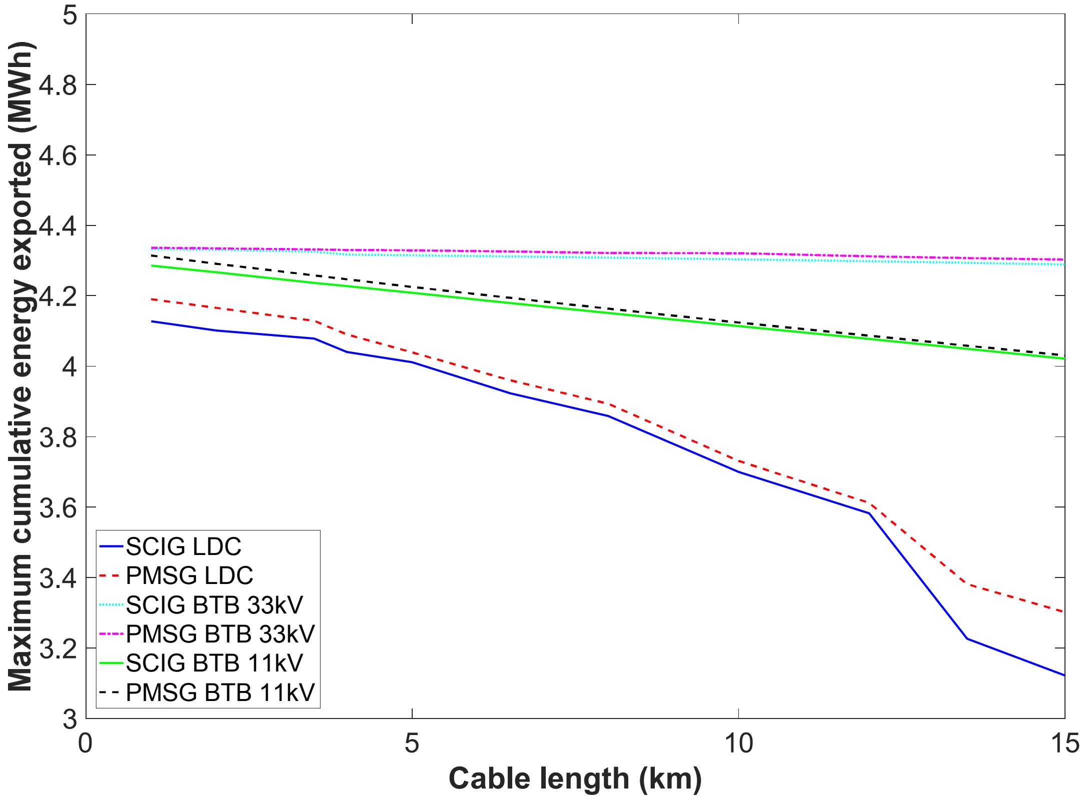

Figure 5.10 Maximum cumulative energy exported over increasing cable length for the four TCCS under study.

Figure 5.10 presents how increasing losses in LDC systems affects the maximum cumulative energy exported from a TCCS. At 1km cable length energy exported is 4.1271MWh and 4.1902MWh for SCIG LDC and PMSG LDC respectively. This value significantly drops to 3.122 MWh and 3.302 MWh respectively at 15km cable length. This is not the case for BTB systems in which the energy loss from 1km to 15km is only 1.01% and 0.77% for the SCIG BTB 33kV and PMSG BTB 33kV systems respectively. Using 11kV for the power transmission in BTB systems significantly changes the energy losses from 1km to 15km. SCIG BTB 11kV and PMSG BTB 11kV TCCSs have 6.18% and 6.57% difference respectively in maximum cumulative energy exported between 1km and 15km cable lengths.

From the results presented in this section it can be concluded that LDC systems are likely to be used at short distances. In addition, the use of PMSG with long distance controls is a favourable option because of the reduced cable losses. Systems with converters in the nacelle have lower losses in all cases. However, the use of underwater converters is not preferred by developers at the present time and therefore their use will be limited to cases where TCCS will be connected individually and the distance to shore is at least 10km. Underwater converters are not preferred by developers because for the deployment of demonstration tidal current arrays the system needs to be as reliable as possible to prove the concept of uninterruptible tidal current power generation. Such an example is the Phase 1Aof the MayGen project in the Inner Sound of the Pentland Firth where developers use long distance controls with individual connections for four tidal current turbines. Regarding the losses in a tidal current system, cable losses are highly dependent on transmission voltage in each system. It has to be noted that LDC systems have a transmission voltage of 6.6kV, because it is limited by the output of the generator, whereas BTB systems can have a transmission voltage of up to 33kV. In the near future the use of 11kV generators will significantly decrease total system losses in LDC systems increasing their applicability in TCCS.

5.6 Summary

In this chapter a comprehensive study of power transmission options for single TCCS has been carried out. SCIG and PMSG were compared using both long distance controls and converters in the nacelle. The results showed that in all the cases studied the PMSG TCCS exported more energy compared to the respective SCIG TCCS. Furthermore, the use of long distance control was analysed and compared to the use of the BTB converters in the nacelle. Uncertainties in cable parameters affect LDC systems more than BTB systems. However, results showed that even in extreme cases of uncertainty, and if the generator side filter of the LDC systems are optimised, the operation of the LDC system is within the acceptable limits. Finally, it becomes evident that using onshore converters with short distances to shore yields the important advantage of accessibility and at the same time additional losses are not significant. However, for distances longer than 10km the difference in energy exported between BTB and LDC systems starts to become significant.

Chapter 6

Power transmission study for small tidal arrays

6.1 Introduction

In this Chapter the power transmission study for single tidal current devices presented in Chapter 5 is expanded to small tidal arrays of up to 16 devices. In Section 1.2.3 an introduction to electrical architecture options for tidal current conversion systems was presented. Based on these electrical architecture options the *Radial* architecture and the *Star Cluster* architecture are studied in this chapter because they require an array formation. The *Direct connection to shore* architecture was presented in Chapter 5. In addition, the *Radial* architecture and the *Star Cluster* architecture are presented with the option of having two connections to shore forming the *Radial Ring* architecture and the *Star Cluster Ring* architecture. In Section 6.2 the positioning of the TCCS in a tidal channel is presented together with the assumptions of the study. Sections 6.3 and 6.4 present the results for the radial and star cluster architectures and finally in section 6.5 the results are summarised.

6.2 Array planning and assumptions

The primary purpose of developing an electrical array architecture is to decrease transmission losses by using high voltage energy transmission. This process will be presented in this chapter. However, an electrical array also requires a parallel electrical network for the auxiliary supplies and communication network. In this thesis the power losses from the auxiliary supplies and the communication network are not considered in the study. The power cables chosen include a fibre optic cable to transmit control signals from the TCCS to the controllers and the monitoring station but the power losses to operate the associated equipment are not included in the total tide-to-grid losses.

At present, there is no clear evidence that supports suggestions for the optimal spacing of tidal current devices. The industrial reports from GE, Siemens and ABB [75]–[77] were based on 400m spacing across the flow and 800m spacing parallel to the flow for 1MW devices. Other reports in marine energy electrical transmission [18] suggest a much smaller spacing of up to 240m for a 20m blade diameter. In this study the spacing is based on the array planning of the industrial reports. In addition, in order to accommodate possible lifting of cables out of the water and possible contingencies due to the strong tidal currents, an additional 100m cable length in each direction is considered. 100m is based on the maximum water depth that tidal current devices can be installed at present. In this chapter, arrays of four (TCCS4), eight (TCCS8) and sixteen (TCCS16) tidal current devices will be studied in a simple tidal current channel. The array topology in each case is presented in Figure 6.1.

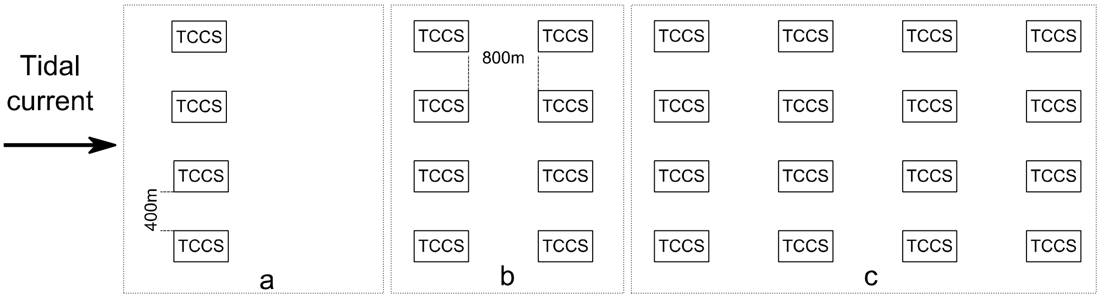

Figure 6.1 Array planning. a. TCCS4. b. TCCS8. c. TCCS16.

Based on results presented in Chapter 5, PMSGs have lower total losses compared to the SCIG options. Therefore the two TCCS topologies that use PMSG, the PMSG LDC and the PMSG BTB, will be analysed in this chapter.

The tidal current velocity input in the tidal array is based on Figure 3.3 presented in Section 3.1. Figure 6.2 shows the tidal current velocity used in this Chapter.

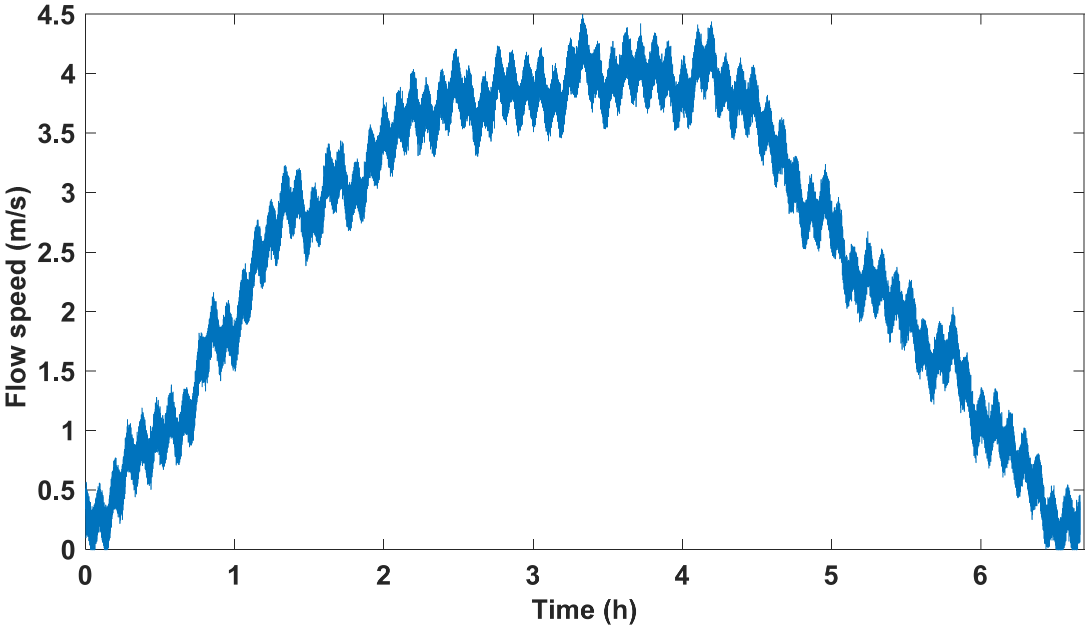

Figure 6.2 Tidal current velocity used as input to the tidal current array.

6.3 Radial architecture

In this section the *Radial* and *Radial Ring* architectures will be presented. Radial networks are common in wind energy systems, however their applicability has some limitations in tidal current energy systems. Some of these limitations are:

- The BTB power converters have to be installed in the nacelle. Not all tidal current turbines have enough space in the nacelle to install the BTB converters.
- At present, tidal current devices have a single power connection. It is not possible to loop the cable in and out of the nacelle in order to connect the TCCS in series [18].
- Three-way connectors can be used (see Figure 1.10) but using them will limit output voltage to 11kV and also limit the number of devices that can be connected to the radial network [18].
- Redundancy in the radial network is limited. A fault in one TCCS can affect the power output of other TCCSs.

Based on the above limitations a possible workaround is to use a *Subsea Transformer System* as suggested in [18] and presented in Figure 6.3.

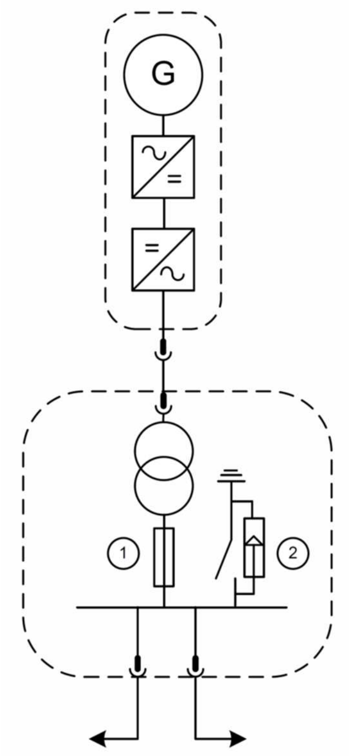

Figure 6.3 Subsea Transformer System. 1. Fuses to isolate the device in case of fault. 2. Earth switch and surge arrester [18]**.**

By using a *Subsea Transformer System*, a higher voltage of 33kV can be used, a potentially faulty TCCS can be isolated from the radial network, and two or more power connections can be used. The disadvantage of a *Subsea Transformer System* is that an additional subsea structure has to be installed for every tidal current converter in the array, potentially increasing total cost. Siemens has already presented designs and feasibility analysis of a similar structure in [76].

Based on requirements of a radial network the *Radial* and *Radial Ring* architectures as developed in MATLAB/Simulink are presented in Figure 6.4 and Figure 6.5 using the PMSG BTB TCCS topology. The lengths shown in Figure 6.4 and Figure 6.5 are the cable lengths and not the distance between the devices.

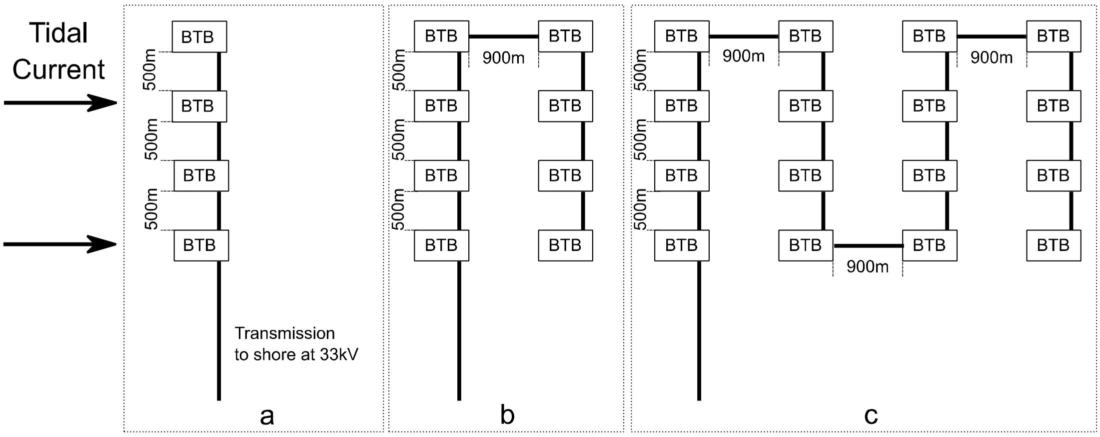

Figure 6.4 The Radial architecture of a tidal current array using PMSG BTB as implemented in Simulink. a. RBTB4. b. RBTB8. c. RBTB16.

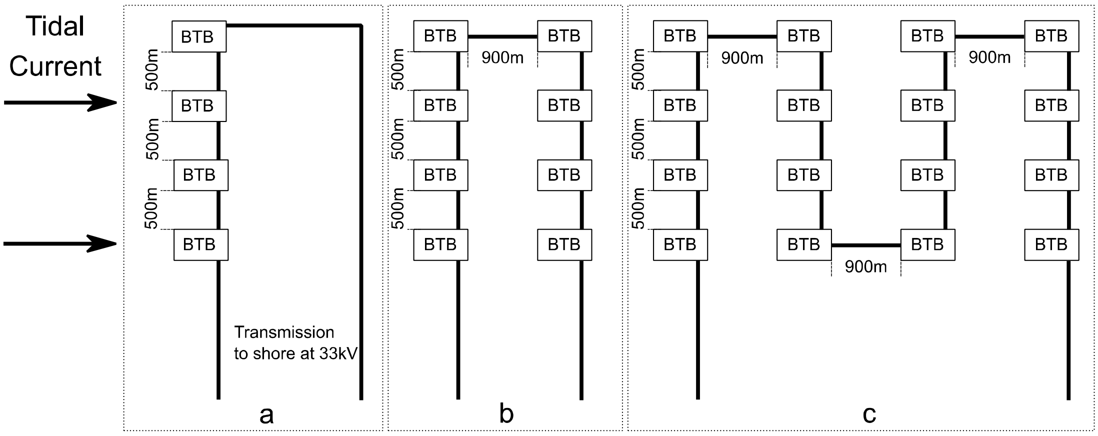

Figure 6.5 The Radial Ring architecture of a tidal current array using PMSG BTB as implemented in Simulink. a. RRBTB4. b. RRBTB8. c. RRBTB16.

The *Radial Ring* architecture offers more redundancy as the whole array does not rely on a single cable connection to shore for power transmission. However, longer subsea cables are required to form a ring connection. For example, in the case of four TCCS devices the total cable length for the ring connection (RRBTB4) is 3km plus two times the distance to shore whereas in RBTB4 the total cable length is 1.5km plus the distance to shore. In addition, in *Radial* and *Radial Ring* architectures all the cables have to be rated at the total power of the array. Cable parameters and ratings used are presented in Appendix C. The architectures presented in Figure 6.4 and Figure 6.5 were simulated for different distances to shore. The total power losses were calculated in each case and are presented in Table 6.1.

Table 6.1 Total electrical losses for the Radial and Radial Ring architectures for changing distance from the shore.

		Total losses at 1pu (% of P_{el})				
Distance to shore (km)		1	3.5	8	12	15
Radial	RBTB4	4.2293	4.6812	5.4867	6.1801	6.6941
	RBTB8	4.5254	5.1515	6.2303	7.1558	7.8287
	RBTB16	4.5357	4.8839	5.5167	6.0771	6.4716
Radial Ring	RRBTB4	4.0705	4.2895	4.7378	5.1128	5.3948
	RRBTB8	4.1815	4.5044	5.0668	5.5651	5.9296
	RRBTB16	4.1392	4.3155	4.6477	4.9179	5.1447

The total losses are calculated based on the total power generated from all the TCCSs in the tidal array at rated power. As it is expected, and based on the results presented in Table 6.1, power transmission losses increase as the distance to shore increases.

In the *Radial* architecture RBTB4 has lower losses compared to RBTB8 which would favour the installation of smaller arrays rather than larger arrays. However, the reason behind the reduced losses in RBTB4 is because of the cable type used. For the RBTB4 system, the C36-214 cables were used; it has a current rating of 214A which can accommodate up to 7 TCCSs based on the parameters used in this study. In the case of the RBTB8 system, the C36-256 cable is used which can accommodate up to 8 TCCS. From the above, it is evident that a tidal array with 4 devices does not use the equipment efficiently. Lower rated cables at 33kV operating voltage were not available from offshore cable manufacturers. The RBTB16 system has lower losses compared to RBTB4 and RBTB8 for distances greater than 12km to shore.

Similar results can be observed between the systems of the *Radial Ring* architecture. The RRBTB8 appears to have higher losses compared to RRBTB4 but this is due to the higher rated cables used to model the RRBTB4. RRBTB16 has lower losses compared to RRBTB4 and RRBTB8 when the distance to shore is greater than 8km. Comparing the *Radial* and *Radial Ring* architectures, it can be said that the *Radial*

Ring architecture has lower losses in all cases of distances and systems. In addition, the *Radial Ring* topology offers system redundancy and no single cable fault can lead to loss of energy from the TCCS array.

6.4 Star cluster architecture

In this section the *Star Cluster* architecture will be analysed. As first presented in Figure 1.11 the *Star Cluster* architecture can be implemented in TCCSs using long distance controls (LDC) or converters in the nacelle (BTB). In addition, the simple *Star Cluster* architecture can be expanded into a ring topology using the clusters as nodes, forming the *Star Cluster Ring* architecture. Based on the reports generated by three major electrical companies [75]–[77] small surface piercing platforms can easily accommodate connections for up to four power converters. According to developers, these surface piercing platforms may be also be available as floating or underwater hubs, minimising their visual impact. Areas for tidal energy arrays are usually close to shore and therefore the visual impact of the projects will have an important role in the actual implementation and consent. Using larger offshore platforms that can accommodate 16 or more devices are possible but are not considered for the above reason.

6.4.1 Long distance controls

Implementing long distance controls in tidal arrays with star clusters is advantageous for the following reasons:

- Power converters are kept dry on a surface piercing platform and therefore maintenance of these components does not require expensive installation or jack-up vessels.
- Distances from the TCCS to the surface piercing platform are short, less than 1km. Additional losses due to the use of long distance controllers are minimised at short distances.

The *Star Cluster* and *Star Cluster Ring* architectures implemented in MATLAB/Simulink based on the PMSG LDC TCCS are presented in Figure 6.6 and Figure 6.7.

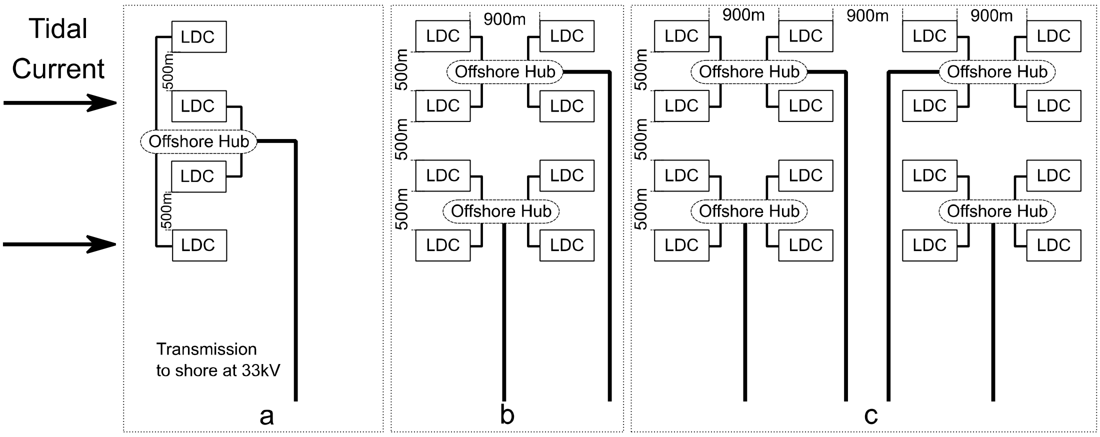

Figure 6.6 The Star Cluster architecture of a tidal array using PMSG LDC as implemented in Simulink. a. SCLDC4. b. SCLDC8. c. SCLDC16.

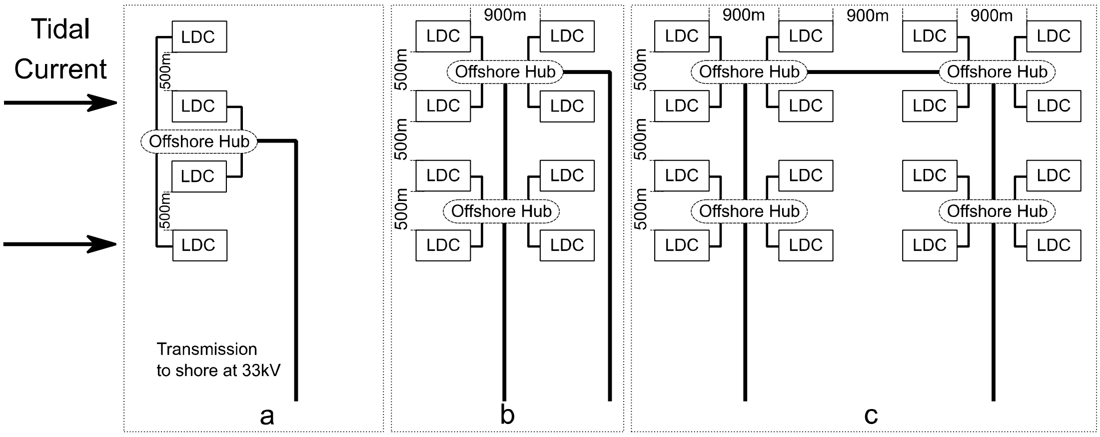

Figure 6.7 The Star Cluster Ring architecture of a tidal array using PMSG LDC as implemented in Simulink. a. SCRLDC4. b. SCRLDC8. c. SCRLDC16.

When four TCCSs are installed (Figure 6.6a and Figure 6.7a) only one cluster is created and therefore a ring topology cannot be created. In the case of eight TCCSs the *Star Cluster Ring* architecture requires an additional 2km cable, rated for eight TCCSs, compared to the *Star Cluster* architecture. Cable length savings for the *Star Cluster Ring* architecture only occur when sixteen TCCSs form the tidal array. Cable parameters and ratings used are presented in Appendix C. The architectures presented in Figure 6.6 and Figure 6.7 were simulated for different distances to shore. The total power losses were calculated in each case and are presented in Table 6.2.

Table 6.2 Total electrical losses for the Star Cluster and Star cluster architectures using PMSG LDC TCCS topology for changing distances to the shore.

		Total losses at 1pu (% of P_{el})				
Distance to shore (km)		1	3.5	8	12	15
Star cluster	SCLDC4	5.4361	5.8665	6.6225	7.2771	7.7626
	SCLDC8	5.4511	5.8826	6.6352	7.2912	7.7745
	SCLDC16	5.2063	5.8824	6.6350	7.2907	7.7745
Star cluster Ring	SCLDC8	5.3463	5.6541	6.1874	6.6556	7.0023
	SCLDC16	5.2524	5.4262	5.7351	6.0069	6.2103

The *Star Cluster Ring* architecture generates less losses in all cases compared to the *Star Cluster* architecture. The longer the distance to shore the higher the benefits of using 16 TCCSs in *Star Cluster Ring* architecture.

Using the *Star Cluster* architecture, with star clusters of 4 TCCS, the losses between an array of 4 devices (SCLDC4), 8 devices (SCLDC8) and 16 devices (SCLDC16) are not very different. This is because the tidal current arrays are formed from multiples of the SCLDC4. Small differences in losses appear due to the different distances to shore for each star cluster, as it can be seen in Figure 6.6.

6.4.2 Converters in the nacelle

In this section the option of using TCCS with BTB converters in the nacelle in a *Star Cluster* architecture and *Star Cluster Ring* architecture is explored. The advantages of using BTB converters in the nacelle compared to long distance controls are the increased transmission voltage from the TCCS to the offshore hub, fixed frequency output which reduces the need for power harmonic filtering, and reduced electrical losses in the cables. Figure 6.8 presents the *Star Cluster* architecture and Figure 6.9 the *Star Cluster Ring* architecture for four, eight and sixteen TCCS using converters in the nacelle.

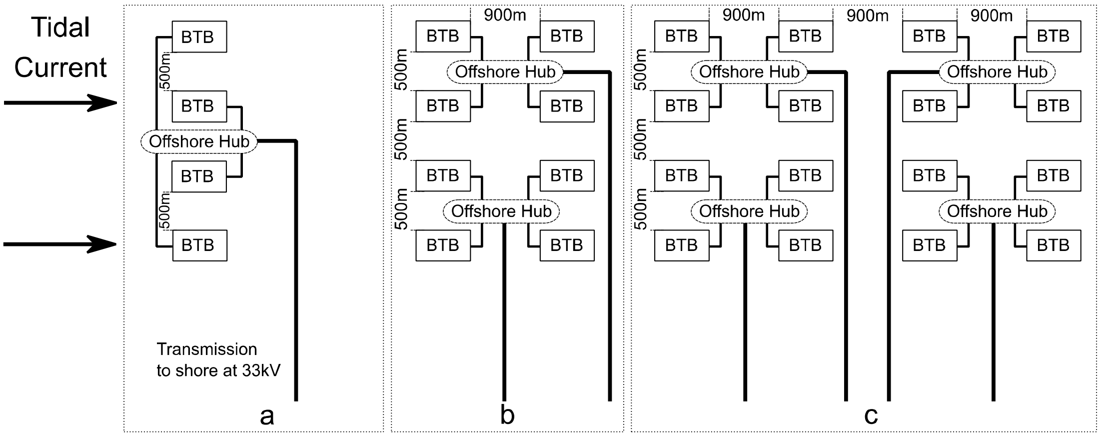

Figure 6.8 The Star Cluster architecture of a tidal array using PMSG BTB as implemented in Simulink. a. SCBTB4. b. SCBTB8. c. SCBTB16.

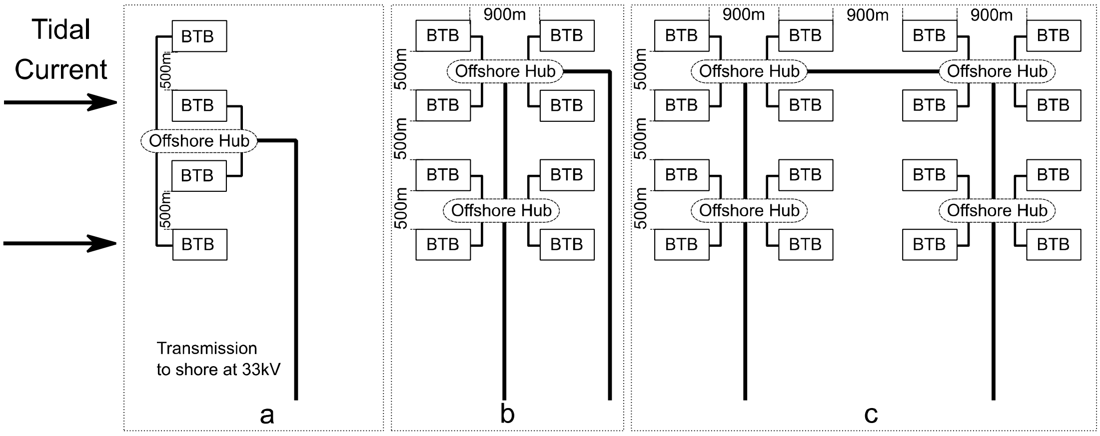

Figure 6.9 The Star Cluster Ring architecture of a tidal array using PMSG BTB as implemented in Simulink. a. SCRBTB4. b. SCRBTB8. c. SCRBTB16.

When four TCCSs are installed (Figure 6.8a and Figure 6.9a) only one cluster is created and therefore a ring topology cannot be created. In the case of eight TCCSs the *Star Cluster Ring* architecture requires an additional 2km cable, rated for eight TCCSs, compared to the *Star Cluster* architecture. Cable length savings only occur when sixteen TCCS form the tidal array. Cable parameters and ratings used are presented in Appendix C. The architectures presented in Figure 6.8 and Figure 6.9 were simulated for different distances to shore. The total power losses were calculated in each case and are presented in Table 6.3.

Table 6.3 Total electrical losses for the Star Cluster and Star cluster architectures using PMSG BTB TCCS topology for changing distances to the shore.

		Total losses at 1pu (% of P_{el})				
Distance to shore (km)		1	3.5	8	12	15
Star Cluster	SCBTB4	4.5642	5.0127	5.8082	6.5006	7.0142
	SCBTB8	4.4294	4.8826	5.6816	6.3789	6.8938
	SCBTB16	4.4391	4.8889	5.6858	6.3827	6.8949
Star Cluster Ring	SCRBTB8	4.3176	4.6447	5.2114	5.7084	6.0778
	SCRBTB16	4.2189	4.4042	4.7311	5.0229	5.2384

The *Star Cluster Ring* architecture generates less losses in all cases compared to the *Star Cluster* architecture. The longer the distance to shore the higher the benefits of using 16 TCCS in *Star Cluster Ring* architecture (SCRBTB16).

Regarding the *Star Cluster* architecture, the three systems compared, SCBTB4, SCBTB8 and SCBTB16 have similar losses for the same distance to shore. This is because SCBTB8 and SCBTB16 are formed from multiples of SCBTB4 with slightly different distances to shore depending on the location of star clusters. This can be seen in Figure 6.8.

6.5 Summarised results

Based on the observations and the results presented above it can be concluded that in all cases ring architectures are advantageous.

For the radial architectures presented in Section 6.3, the ring topology offers reduced transmission losses and redundancy. In the star cluster architectures presented in Section 6.4 the ring topology offers reduced transmission losses and cable installation savings.

An additional observation from the results presented in this chapter is that significant reduction in power losses can be achieved when tidal arrays are formed from 16 TCCS and the distance to shore is at least 1km for the SCRBTB16, 3.5km for the SCRLDC16 and 8km for the RRBTB16. Figure 6.10 presents the total electrical losses for the 16 TCCSs for increasing distance to shore when all the TCCS are operating at rated power.

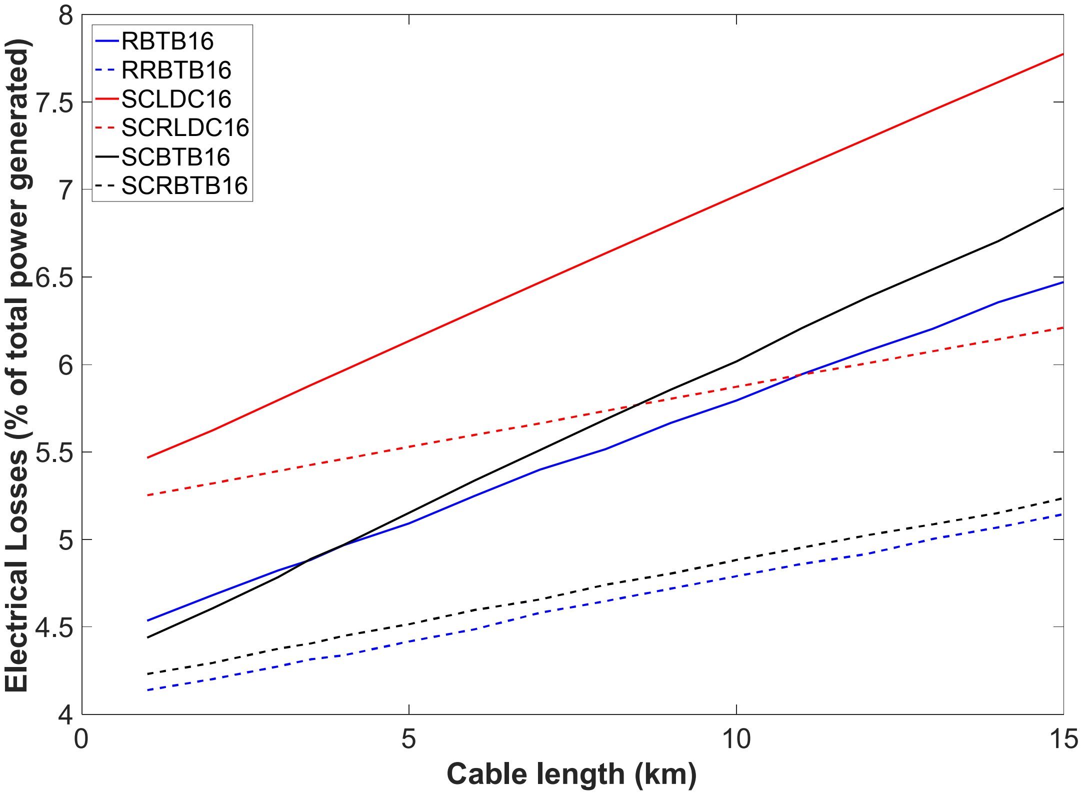

Figure 6.10 Electrical losses of the 16 TCCS systems presented in Chapter 6 with increasing distance to shore.

The ring architectures (dashed lines) always have lower losses compared to their respective non-ring architectures. In addition, the slope with which electrical losses are increasing for the changing cable length is significantly less steep in the ring topologies. The SCLDC16 system has lower losses compared to SCBTB16 for distances above 8km and lower losses compared to RBTB16 for distances above 12km and at the same time it uses long distance controls allowing easier maintenance of power electronics. The RRBTB16 system has the least electrical losses in all cases. However, as stated in the beginning of Section 6.3 radial networks have a number of limitations in their applicability in a tidal array. All the suggested solutions for these limitations require additional underwater components such as the *Subsea Transformer System* (Figure 6.3). These extra components will increase both the cost and the complexity of the system. The SCRBTB16 system has on average around 0.8% additional losses compared to RRBTB16 system. This makes SCRBTB16 the system with the second lowest amount of electrical losses and is most likely to be implemented in a future tidal current array. The disadvantages of using such as system would be the use of underwater power electronics and possible limitations for tidal current developers who currently cannot accommodate power electronics in the nacelle. These disadvantages can be surpassed by implementing the SCRLDC16 system. The disadvantage of using a SCRLDC16 system would be the additional 1% electrical losses which comes from the use of long distance controls between the nacelle and the offshore hub.

Chapter 7

Concluding Remarks

7.1 Discussion

This thesis presents different ways to transmit power from the TCCS to the grid. In Chapter 1 the main aim of the thesis was defined:

> *"The main aim of this thesis is to explore and evaluate the alternative ways of connecting a tidal current turbine to the grid. The purpose of exploring and evaluating the electrical architecture options is to reduce losses to a minimum but at the same time keep the system components as accessible as possible for maintenance."*

Tidal current conversion systems are still at their infancy with a number of prototypes being tested and a few demonstration projects currently being developed. Currently, tidal current turbine developers have not yet decided on the optimal tidal current conversion system and therefore a number of different designs exist. While most of the designs are bottom mounted with low solidity blades and horizontal axis rotors, the approaches differ in generator technology. Dominant choices are direct drive generators or geared permanent magnet synchronous generators and squirrel cage induction generators. Moreover, some tidal current turbine developers have designed systems that do not have enough space in the nacelle to accommodate filters, power electronics and the step-up transformer required.

Considering all the above aspects of tidal current turbine technology, the resource-to-grid tidal current conversion model was developed as part of this thesis. The model was used to achieve the aim of exploring and evaluating alternative ways of connecting a tidal current turbine to the grid. The input to the model from AHH was crucial in order to represent a realistic system and validate its operation. In addition, from this model a number of variations were developed; using SCIG or PMSG and using BTB converters in the nacelle or LDC.

Exploring different generator technologies was part of the process of exploring different electrical architecture options. Using SCIG or PMSG in a system with long distance controls could have an impact on the overall performance of the system. As it was shown in Chapter 5, systems with PMSG have benefits over systems with SCIG. The benefits are even larger the longer the cables are between the generator and the power electronics. Implementing long distance controls in a tidal current conversion system allows easier installation, maintenance and repair of the power electronics.

Long distance controls are a key focus aspect of this thesis. Keeping as many components as possible accessible for easy maintenance is a major requirement set by the tidal current developers. The use of long distance controls allows the power electronics, the transformer and the filters to be kept onshore or dry on an offshore platform. In Section 2.7 of the literature review it became evident that a number of different filter designs can be used but the exact parameters of the filters can be calculated using several approaches. In addition, in most cases a low voltage generator was connected to the power electronics through cables without the need for a transformer in between. However, this was not the case for a tidal current conversion system which requires higher voltages for energy transmission. In Chapter 4 the generic algorithm developed can estimate the filter parameters of a low-pass filter which will reduce the harmonics in a long distance control system to a minimum and at the same time minimise losses. The TCCS using a generator side filter designed by the algorithm was compared to measured data provided by AHH. Results showed the potential benefits of using the generic algorithm for designing filters for systems using long distance controls instead of using off-the-shelf filters.

In the final part of this thesis different options of tidal current arrays were compared. At present, no tidal arrays have been developed except for a number of tidal current devices individually connected. The study in Chapter 6 showed that in order to keep power electronics maintainable a star cluster architecture is required. Implementing the star cluster architecture in ring topology also reduces cable costs and electrical losses for energy transmission. It is very likely that such configurations will be implemented in future tidal arrays. Configurations with the power electronics in the nacelle using the star cluster ring architecture induced slightly less electrical losses in total but require to the operation and maintenance of underwater BTB power electronics, step-up transformers and power harmonic filters. Such a task is expensive and difficult. Similar observations were made regarding the use of radial architectures for a tidal current array. In order to loop a cable and create a radial network it would require, in most cases, an additional underwater structure to house cable looping, transformer, switchgear and filters. Operating and maintaining such a structure for every tidal turbine in an array could be a challenge that developers might want to avoid.

7.2 Contribution to Knowledge

This thesis progresses knowledge in the following ways:

- It provides the renewable energy community with a detailed and validated dynamic resource-to-wire model of a TCCS using actual data.
- An in-depth focus is given to generation systems that use long distance controls. A generic algorithm that calculates filter parameters is proposed in order to minimise losses and increase reliability of systems that use long distance controls.
- A comparative study of a single TCCS is presented based on currently available technology.
- The comparative study of the single TCCS is expanded to arrays of up to 16 TCCS. Different array configurations are explored and advantages and disadvantages of each are stated.

The main tool to answer the research question of this thesis was the dynamic resource-to-wire model of the TCCS. This model, which is presented in Chapter 3, shows in detail all the electrical components of a TCCS as well as some mechanical parts. The electrical and mechanical parameters used were based on input from AHH. In addition, the power output of the model was compared with the measured power output of the AHH prototype installed at EMEC. The resource-to-wire tidal current model developed in this thesis can be easily used to predict the operation of a tidal current conversion system. What is more, this thesis provides extensive details so that the model can be replicated and modified to represent a different tidal current conversion system. This can be a useful tool for tidal current developers or research institutes that focus on tidal current systems. In addition, the model presented in this thesis can be used as a reference for future research in electrical or mechanical parts of the tidal current conversion systems.

A key novelty of this thesis is the detailed presentation of the systems that use long distance controls and the development of a generic algorithm to minimise losses in such systems. The use of long distance controls is crucial in offshore renewable energy systems as it can increase the reliability of the system by having the power electronics dry, either on an offshore hub or onshore. Furthermore, the availability of the TCCS can increase by using long distance controls through minimising onsite visits and nacelle extraction for the power electronics repairs. Tidal current devices are planned to be installed at locations with strong tidal currents. At these locations, the windows of opportunity for onsite visits are relatively short, which means that major operations need to be extremely quick or be able to continue in high flow speeds. Expensive marine vessels are being used for nacelle extraction which greatly increase the operation and maintenance cost of tidal current conversion systems. Using long distance controls the need to use jack-up vessels for the maintenance or repair of the power electronics is eliminated.

However, the use of long, three-phase cables between the generator and the power electronics comes with the disadvantage of higher losses, higher harmonics and risk of overvoltages due to voltage reflections in the cables. A major contribution presented in this thesis is the development of a generic algorithm that calculates the parameters of the low-pass filter installed at the VSC terminals which:

- Minimises losses between the generator and the power electronics.
- Reduces the high order harmonics induced by the resonance of the long subsea cable parameters and the interaction of the cable parameters with the transformer or other components.

- Can be used in conjunction with a single tuned filter tuned at the generator controller switching frequency to further reduce harmonics between the power electronics and the generator.
- Is generic and can be used for any system that has cables or other electrical components such as transformer and loads between the machine and the power electronics.
- Sensitivity analysis of the designed filter can test the filters performance in case of unknown system parameters.

Despite designing an optimum filter to minimise losses in systems with long distance controls, these systems still have higher total electrical losses compared to systems with converters in the nacelle that transmit power at 33kV. The main reason for the higher losses is the reduced output voltage of the generator, which can go up to 6.6kV with current technology. This is significantly lower than 33kV which a TCCS can ideally have as an output if the power electronics are installed in the nacelle together with a step-up transformer. On the other hand, as the comparative study showed in Chapter 5, the difference in electrical losses between LDC and BTB systems is significantly reduced when the output from the BTB system is 11kV. Several prototypes from tidal current developers, such as Oceade, used power electronics in the nacelle with a transformer to step-up the voltage to 11kV. When comparing a single TCCS with LDC at 6.6kV with a single TCCS with BTB converters at 11kV the difference in electrical losses at distances up to 10km is constant at around 0.85%.

An additional contribution of this thesis is the expansion of the single TCCS to small array formations. From the comparative study presented in Chapter 6 it became evident that ring topologies are advantageous for their redundancy and reduced electrical losses. In addition, in the case of star cluster architectures the ring topology offers reduced cable installations. From the star cluster architectures the use of long distance controls offers dry operation of the power electronics on an offshore hub with an additional 1% electrical losses at rated power compared with a system that has power electronics in the nacelle.

Overall, the research work presented in this thesis provides a clearer understanding of the options to transmit power from an underwater tidal current turbine to the grid. In addition, the work sheds light on the applicability of long distance controls in TCCSs as a viable energy transmission option of single tidal devices or in array formations. The research work also contributed to a number of publications which are listed in Appendix D.

The conference paper entitled "Modelling and control of tidal energy conversion systems with long distance converters" [88] discusses the resource-to-grid modelling of a single TCCS that uses SCIG with long distance controls which is presented in Chapter 3. In addition, initial results regarding the resonance and voltage reflections in the cables of a system that uses long distance controls are presented. Passive power harmonic filters are implemented in order to mitigate resonance as it is shown in Chapter 4.

The conference paper entitled "Comparison of permanent magnet synchronous and induction generator for a tidal current conversion system with onshore converters" [60] compares the SCIG and the PMSG options for a resource-to-grid TCCS with long distance controls. The modelling and control of the generators are presented in Chapter 3 and the results from this study are linked to Chapter 5.

The journal paper entitled "Filter Design for Cable Overvoltage and Power Loss Minimization in a Tidal Energy System With Onshore Converters" [83] focuses on the filter design algorithm presented in Chapter 4. The study is undertaken in a resource-to-grid TCCS with SCIG and long distance controls.

The journal paper entitled "Modelling, control and frequency domain analysis of a tidal current conversion system with onshore converters" [35] is an expansion of the conference paper [88]. Research expands on the voltage gain graphs and the generator controller switching frequency study which was presented in Chapter 4.

7.3 Future Work

The work undertaken can be extended in many different ways.

From a modelling aspect, the dynamic resource-to-wire model developed can be extended in a number of ways. From the generator point of view, a realistic model of an 11kV SCIG and PMSG can be designed in order to compare and evaluate their performance in a system with long distance controls. Both AHH and ARL currently install tidal current devices for the Phase 1 of the MeyGen project use generators with an output voltage of up to 6.6kV and long distance controls. Significant gains could be achieved in the electrical losses of the cables if the transmission voltage to shore was higher at 11kV. The development of specific power electronics for long distance controls could be another advancement of the resource-to-wire model of this thesis. Higher level power electronic topologies and their associated control methods could be tested for systems with long distance controls. The higher voltage ratings and reduced harmonics from higher level power electronics could prove useful with the operation of a system using cables between the generator and the power electronics. In addition, the control bandwidth oscillation of the TCCS controllers can be studied. The harmonics flowing to the generator terminals can be related with possible harmonics from the flow speed input or the operation of a control system in the TCCS.

From the mechanical side of the modelling work the resource-to-wire model could greatly benefit from a more detailed tidal turbine model. Mechanical stress, fatigue loads, thrust forces and realistic torque input to the generator could be simulated with a multi-body model of an actual tidal current turbine. What is more, the effect of the long distance control in the mechanical parts of the tidal turbine could be evaluated and compared to the use of power electronics in the nacelle. Low frequency resonance of mechanical components such as torsional vibrations and the effects in a TCCS with long distance controls can be studied.

The research undertaken for this thesis could also be extended through laboratory based work on filter design. In Chapter 4, a novel filter design method for systems using long distance controls is proposed. This method offers generic usage, minimised losses, reduced harmonics flowing in the cables and damped overvoltages. Laboratory based experiments could prove the concept of this filter design method. The challenges of undertaking such a task lies with the provision of long cables and the power rating of the generator. Setting up an experiment that requires kilometres of three-phase power cables in the limited space of the laboratory could prove to be a difficult task. In addition, the interaction of cable parameters and transformer parameters has to be experimentally tested, thereby increasing the number of different components required and filters designed.

Appendix A

Software

MATLAB and Simulink are the two software packages used in this thesis to develop and simulate the models as well as analyse and visualise the results generated.

A.1 MATLAB

MATLAB is a multi-paradigm numerical computing environment and fourth-generation programming language. A proprietary programming language developed by MathWorks, MATLAB allows matrix manipulations, plotting of functions and data, implementation of algorithms, creation of user interfaces, and interfacing with programs written in other languages, including C and C++ [101]. MATLAB software was used throughout the research study in the following way:

- Scripts using MATLAB programming language were created to control, simulate and save results from the Simulink models of tidal current turbines.
- In addition, scripts were developed in order to present the simulated results and compare simulated results with experimental data provided by AHH.
- The fourth-generation programming language of MATLAB was used to develop parts of the tidal current turbines such as the tidal resource (Section 3.1) and the supervisory controller (Section 3.4.3).
- Finally, MATLAB programming language was used to analyse system resonance (presented in Section 4.1.2) and generate the filter design graphs presented in Chapter 4.

A.2 Simulink

Simulink is also developed by MathWorks and is a graphical programming environment for modelling, simulating and analysing multidomain dynamic systems. It offers tight integration with the rest of the MATLAB environment and during the PhD study Simulink software was programmed through MATLAB.

Simulating a dynamic system is a two-step process.

- First, a user creates a block diagram, using the Simulink model editor, which graphically depicts time-dependent mathematical relationships among the system's inputs, states, and outputs (Figure A.1). The user then commands the Simulink software to simulate the system represented by the model from a specified start time to a specified stop time.

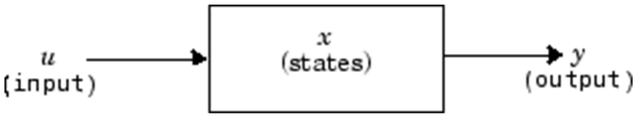

Figure A.1 A simple example of a dynamic system in Simulink.

In order to simulate electrical components in Simulink the Simscape Power Systems (formerly SimPowerSystems) toolbox was used. Simscape Power Systems was developed in collaboration with Hydro-Québec of Montreal and provides component libraries and analysis tools for modelling and simulating electrical power systems. It includes models of electrical power components, including three-phase machines, power harmonic filters and electric drives. In addition, Simscape Power Systems toolbox helps you develop control systems and test system-level performance. Simulink models can be parameterised using MATLAB variables and expressions, and design control systems in Simulink [95].

Simscape Power Systems toolbox works in the following way:

- Once you have built your circuit with the blocks of *powerlib*, you can start the simulation just like any other Simulink model. Each time you start the simulation, a special initialization mechanism is called.

- This initialization process computes the state-space model of your electric circuit and builds the equivalent system that can be simulated by Simulink. The *power_analyze* command is part of that process. It obtains the state-space model and builds the Simulink model of your circuit.
- Sorts all SimPowerSystems blocks, gets the block parameters and evaluates the network topology. The blocks are separated into linear and nonlinear blocks, and each electrical node is automatically given a node number.
- Once the network topology has been obtained, the state-space model (A, B, C, D matrices) of the linear part of the circuit is computed by the *power_statespace* command. All steady-state calculations and initializations are performed at this stage. All the Simulink models in this thesis were created in discrete time. The discrete state-space model is computed from the continuous state-space model, using the Tustin method.
- Builds the Simulink model of your circuit and stores it inside one of the measurement blocks. This means that you need at least one measurement block (*Current Measurement* block, *Voltage Measurement* block, *Three-Phase V-I Measurement* block, or *Multimeter* block) in your model. The connections between the equivalent circuit and measurements blocks are performed by invisible links using the *Goto* and *From* blocks.
- Once *power_analyze* has completed the initialization process, Simulink starts the simulation. You can observe waveforms on scopes connected at the outputs of your measurement blocks. Through the *Powergui*, you can access the *LTI viewer* and obtain transfer functions of your system between any pair of input and output. The *Powergui* also allows you to perform a FFT analysis of recorded signals in order to obtain their frequency spectrum.

A block diagram of the way Simulink models using Simscape Power Systems are simulated is given in Figure A.2. The interconnection between linear and non-linear models is given in Figure A.3.

Simulink and Simscape Power Systems were chosen as the primary modelling and simulation software for this research because of:

- The dynamic simulation capabilities of electrical components.

- The ability to easily work on the frequency domain after the time domain simulation. Frequency domain results are crucial in understanding cable and transformer-cable interaction and resonance.
- The ability to parameterise the models using MATLAB variables and expressions. This feature was important in order to improve the models studied in an analytic way.
- The control design capabilities and the available control and electrical components.
- The fast simulation mode for discretised models.
- The compatibility of Simulink and Simscape Power Systems with the software of the industrial partner, AHH.

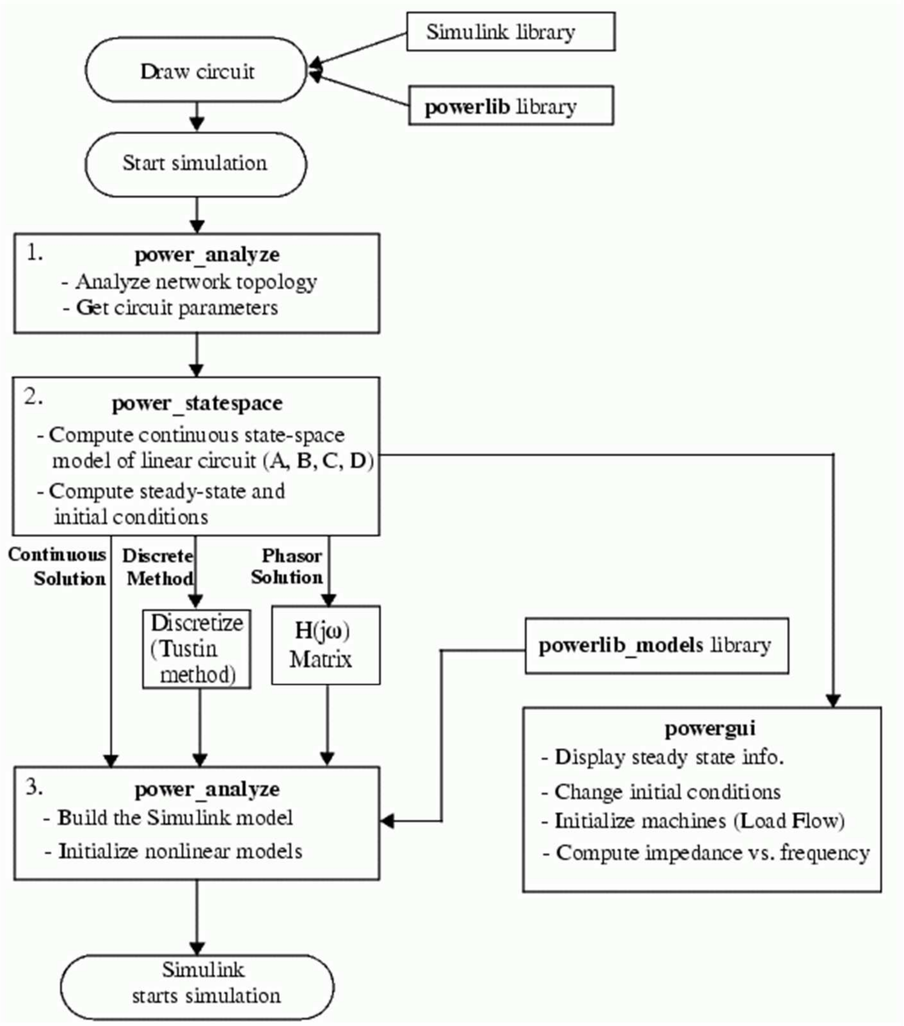

Figure A.2 Flowchart of the simulation when Simscape Power Systems toolbox is used [95].

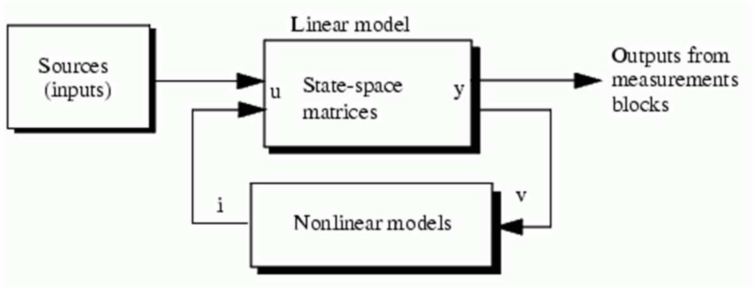

Figure A.3 Interconnection of linear and non-linear models in a Simscape Power Systems simulation [95]**.**

Appendix B

Statistical Tools

Three statistical tool were used:

- Mean value.
- Correlation coefficients between two variables.
- Residual variance

B.1 Average or mean value

The first way to compare data is to find the average value over a specific time scale. In this thesis, for each case we assume that the whole dataset is the time scale for the mean or averaged value. The mean value is defined by the following equation:

$$\boldsymbol{\mu = \frac{1}{N}\sum_{i=1}^{N} P_i} \qquad \textbf{(B-1)}$$

Where $\boldsymbol{\mu}$ is the averaged value, ***N*** is the number of data values and ***P*** is the power data.

Using the mean value the percentage difference can be calculated using the following equation:

$$\boldsymbol{Diff = \frac{\mu_{measured} - \mu_{model}}{\mu_{measured}} * 100}\ (\%) \qquad \textbf{(B-2)}$$

B.2 Correlation Coefficient

The Pearson correlation coefficients are a common way of measuring the linear relationship between two variables. The Pearson correlation coefficients are calculated using either of the following equations:

$$\boldsymbol{\rho(A,B) = \frac{1}{N-1}\sum_{i=1}^{N}\left(\frac{A_i - \mu_A}{\sigma_A}\right)\left(\frac{B_i - \mu_B}{\sigma_B}\right)} \tag{B-3}$$

$$\boldsymbol{\rho(A,B) = \frac{cov(A,B)}{\sigma_A \sigma_B}} \tag{B-4}$$

Where ***A*** and ***B*** are the data to be correlated, $\boldsymbol{\sigma_A}$ is the standard deviation of A and ***cov(A,B)*** is the covariance of ***A*** and ***B***.

The Pearson correlation coefficients, from now on coefficients, are calculated on the scale between -1 and 1. Where -1 (minus one) means that the relationship between variables ***A*** and ***B*** is the opposite of linear, 1 (one) shows that the relationship between variables ***A*** and ***B*** is purely linear and 0 (zero) shows that the relationship between variables ***A*** and ***B*** is random.

B.3 Coefficient of determination

Coefficient of determination (or R-square or square of the multiple correlation coefficient) is a statistical tool that measures how successful the modelled data explains the variation of the measured data. Coefficient of determination (r^2) is defined as the ratio of the sum of squares of the regression (*SSR*) and the total sum of squares (*SST*).

$$\boldsymbol{r^2 = \frac{SSR}{SST}} \tag{B-5}$$

$$\boldsymbol{SSR = \sum_{i=1}^{N}(\hat{y}_i - \mu_{model})^2} \tag{B-6}$$

$$\boldsymbol{SST = \sum_{i=1}^{N}(y_i - \mu_{model})^2} \tag{B-7}$$

Where y is the measured data and $\hat{y}$ is model data.

Alternatively the coefficient of determination can be calculated using the summed square of residuals (SSE).

$$\boldsymbol{SSE = \sum_{i=1}^{N}(y_i - \hat{y}_i)} \quad \textbf{(B-8)}$$

$$\boldsymbol{r^2 = 1 - \frac{SSE}{SST}} \quad \textbf{(B-9)}$$

The residuals from a fitted model are defined as the differences between the response data and the fit to the response data at each predictor value.

$$\boldsymbol{r = y - \hat{y}} \quad \textbf{(B-10)}$$

Assuming the model you fit to the data is correct, the residuals approximate the random errors. Therefore, if the residuals appear to behave randomly, it suggests that the model fits the data well. However, if the residuals display a systematic pattern, it is a clear sign that the model fits the data poorly. The coefficient of determination can take any value between 0 and 1. A value closer to 1 indicating that a greater proportion of variance is accounted for by the model.

Appendix C

Cable Parameters

C.1 Long distance control cables

The long distance control cables are placed between the generator and the generator side voltage-source converter. The only cable used for long distance control in this thesis is the one currently used at EMEC. The parameters of this cable were given in Table 3.10 and reference [96].

C.2 Power transmission cables

Power transmission cables in this thesis are those connecting the grid side voltage-source converter with the grid. The parameters of these cables are given in Table C.1 and are based on [99]. All the cables presented in Table C.1 are rated for up to 36 kV.

Table C.1 Cable parameters for power transmission cables [99]**.**

Name	Conductor resistance AC at 90 °C (Ω/km)	Capacitance (μF/km)	Inductance (mH/km)	Current rating (A)
C11-179	0.670	0.17	0.45	179
C36-214	0.490	0.15	0.46	214
C36-256	0.340	0.17	0.44	256
C36-499	0.098	0.26	0.36	499

Appendix D

List of Publications

- M. C. Sousounis, J. K. H. Shek and M. A. Mueller, "Modelling and control of tidal energy conversion systems with long distance converters," *7th IET International Conference on Power Electronics, Machines and Drives (PEMD 2014),* Manchester, 2014, pp. 1-6. doi: 10.1049/cp.2014.0367.
- M. C. Sousounis, J. K. H. Shek, R. C. Crozier and M. A. Mueller, "Comparison of permanent magnet synchronous and induction generator for a tidal current conversion system with onshore converters," *2015 IEEE International Conference on Industrial Technology (ICIT),* Seville, 2015, pp. 2481-2486. doi: 10.1109/ICIT.2015.7125463.
- M. C. Sousounis, J. K. H. Shek and M. A. Mueller, "Filter Design for Cable Overvoltage and Power Loss Minimization in a Tidal Energy System With Onshore Converters," in *IEEE Transactions on Sustainable Energy*, vol. 7, no. 1, pp. 400-408, Jan. 2016. doi: 10.1109/TSTE.2015.2424258.
- M. C. Sousounis, J. K. H. Shek and M. A. Mueller, "Modelling, control and frequency domain analysis of a tidal current conversion system with onshore converters," in *IET Renewable Power Generation,* vol. 10, no. 2, pp. 158-165, 2 2016. doi: 10.1049/iet-rpg.2014.0331.

References

[1] “UK ENERGY IN BRIEF 2017,” National Statistics, Crown copyright 2017, 2017.

[2] Black & Veatch Consulting Ltd, “UK Tidal Current Resource and Economics Study,” The Carbon Trust, 2011.

[3] D. Krohn, M. Woods, J. Adams, B. Valpy, F. Jones, and P. Gardner, “Wave and Tidal Energy in the UK: Conquering Challenges , Generating Growth,” renewableUK, 2013.

[4] “Spring Neap Tide orientation,” 2004. [Online]. Available: https://www.iupui.edu/. [Accessed: 12-May-2017].

[5] “Atlas of UK Marine Renewable Energy Resources,” *ABPmer*, 2008. [Online]. Available: http://www.renewables-atlas.info/. [Accessed: 15-May-2017].

[6] Black & Veatch Consulting Ltd, “Phase II - UK Tidal Stream Energy Resource Assessment,” The Carbon Trust, 2005.

[7] “EMEC: European Marine Energy Centre - Tidal Energy Devices.” [Online]. Available: http://www.emec.org.uk/marine-energy/tidal-devices/. [Accessed: 12-May-2017].

[8] “AQUARET Delivering knowledge and understanding.” [Online]. Available: http://www.aquaret.com/. [Accessed: 15-May-2017].

[9] “ANDRITZ HYDRO Hammerfest.” [Online]. Available: http://www.andritzhydrohammerfest.co.uk/. [Accessed: 12-May-2017].

[10] “Atlantis Resources.” [Online]. Available: https://www.atlantisresourcesltd.com/services/turbines/. [Accessed: 15-May-2017].

[11] “Scotrenewables,” 2017. [Online]. Available: http://www.scotrenewables.com/. [Accessed: 12-May-2017].

[12] “GE Tidal Energy: Paving the Way for Tidal Power Solutions,” 2017. [Online]. Available: https://www.gerenewableenergy.com/. [Accessed: 12-May-2017].

[13] "TidalEnergyToday," 2017. [Online]. Available: http://tidalenergytoday.com/2017/01/09/ge-drops-oceade-tidal-turbine-sinks-nepthyd-project/. [Accessed: 12-May-2017].

[14] "Nautricity - CoRMaT." [Online]. Available: http://www.nautricity.com/cormat/. [Accessed: 15-May-2017].

[15] "Sustainable Marine Energy ltd," 2017. [Online]. Available: http://sustainablemarine.com/technology. [Accessed: 12-May-2017].

[16] A. Mason, "Marine Energy Electrical Architecture Report 1: Landscape Map and Literature Review," Catapult Offshore Renewable Energy, 2015.

[17] R. Alcorn and D. O'Sullivan, *Electrical Design for Ocean Wave and Tidal Energy Systems*, 1st ed., vol. 44, no. 211014. Institution of Engineering and Technology, 2013.

[18] A. Mason and R. Driver, "Marine Energy Electrical Architecture Report 3: Optimum Electrical Array Architectures," Catapult Offshore Renewable Energy, 2015.

[19] K. Ruud and N. Frank, "Tidal Energy technology brief," IRENA, 2011.

[20] Low Carbon Innovation Coordination Group (LCICG), "Technology Innovation Needs Assessment (TINA) - Marine Energy Summary Report," Low Carbon Innovation Coordination Group, 2012.

[21] I. G. Bryden, S. J. Couch, A. Owen, and G. Melville, "Tidal current resource assessment," *Proc. Inst. Mech. Eng. Part A Power Energy*, vol. 221, pp. 125–135, 2007.

[22] M. Kawase and K. M. Thyng, "Three-dimensional hydrodynamic modelling of inland marine waters of Washington State, United States, for tidal resource and environmental impact assessment," *IET Renew. Power Gener.*, vol. 4, no. 6, pp. 568–578, 2010.

[23] "University of Washington - School of Oceanography - Data Archives for Puget Sound." [Online]. Available: https://www.ocean.washington.edu/data/pugetsound/. [Accessed: 15-May-

2017].

[24] M. Lewis, S. P. Neill, P. E. Robins, and M. R. Hashemi, “Resource assessment for future generations of tidal-stream energy arrays,” *Energy*, vol. 83, pp. 403–415, Apr. 2015.

[25] M. Sánchez, J. A. Fraguela, G. Iglesias, and R. Carballo, “Power peaks against installed capacity in tidal stream energy,” *IET Renew. Power Gener.*, vol. 7, no. 3, pp. 246–253, 2013.

[26] “Delft3D Open Source Community.” [Online]. Available: https://oss.deltares.nl/web/delft3d. [Accessed: 15-May-2017].

[27] R. Malki, I. Masters, A. J. Williams, and T. Nick Croft, “Planning tidal stream turbine array layouts using a coupled blade element momentum – computational fluid dynamics model,” *Renew. Energy*, vol. 63, pp. 46–54, Mar. 2014.

[28] P. Stansby and T. Stallard, “Fast optimisation of tidal stream turbine positions for power generation in small arrays with low blockage based on superposition of self-similar far-wake velocity deficit profiles,” *Renew. Energy*, vol. 92, pp. 366–375, Jul. 2016.

[29] R. Ahmadian and R. A. Falconer, “Assessment of array shape of tidal stream turbines on hydro-environmental impacts and power output,” *Renew. Energy*, vol. 44, pp. 318–327, 2012.

[30] F. Blaabjerg, H. Liu, and P. Loh, “Marine energy generation systems and related monitoring and control,” *IEEE Instrum. Meas. Mag.*, vol. 17, no. 2, pp. 27–32, Apr. 2014.

[31] B. Whitby and C. E. Ugalde-Loo, “Performance of pitch and stall regulated tidal stream turbines,” *IEEE Trans. Sustain. Energy*, vol. 5, no. 1, pp. 64–72, 2014.

[32] M. R. Motley and R. B. Barber, “Passive control of marine hydrokinetic turbine blades,” *Compos. Struct.*, vol. 110, no. 1, pp. 133–139, 2014.

[33] K. Gracie-Orr, T. M. Nevalainen, C. M. Johnstone, R. E. Murray, D. A. Doman, and M. J. Pegg, “Development and initial application of a blade design methodology for overspeed power-regulated tidal turbines,” *Int. J. Mar.*

Energy, vol. 15, pp. 140–155, Sep. 2016.

[34] M. J. Jahromi, A. I. Maswood, and K.-J. Tseng, “Design and Evaluation of a New Converter Control Strategy for Near-Shore Tidal Turbines,” *IEEE Trans. Ind. Electron.*, vol. 60, no. 12, pp. 5648–5659, Dec. 2013.

[35] M. C. Sousounis, J. K. H. Shek, and M. A. Mueller, “Modelling, control and frequency domain analysis of a tidal current conversion system with onshore converters,” *IET Renew. Power Gener.*, vol. 10, no. 2, pp. 158–165, Feb. 2016.

[36] M. L. Rahman, S. Oka, and Y. Shirai, “Hybrid Power Generation System Using Offshore-Wind Turbine and Tidal Turbine for Power Fluctuation Compensation (HOT-PC),” *IEEE Trans. Sustain. Energy*, vol. 1, no. 2, pp. 92–98, Jul. 2010.

[37] S. E. Ben Elghali, M. E. H. Benbouzid, and J.-F. Charpentier, “Modelling and control of a marine current turbine-driven doubly fed induction generator,” *IET Renew. Power Gener.*, vol. 4, no. 1, p. 1, 2010.

[38] S. E. Ben Elghali, M. El Hachemi Benbouzid, T. Ahmed-Ali, and J. F. Charpentier, “High-Order Sliding Mode Control of a Marine Current Turbine Driven Doubly-Fed Induction Generator,” *IEEE J. Ocean. Eng.*, vol. 35, no. 2, pp. 402–411, Apr. 2010.

[39] S. Benelghali, M. E. H. Benbouzid, J. F. Charpentier, T. Ahmed-Ali, and I. Munteanu, “Experimental Validation of a Marine Current Turbine Simulator: Application to a Permanent Magnet Synchronous Generator-Based System Second-Order Sliding Mode Control,” *IEEE Trans. Ind. Electron.*, vol. 58, no. 1, pp. 118–126, Jan. 2011.

[40] N. Odedele, C. Olmi, and J. F. Charpentier, “Power Extraction Strategy of a Robust kW Range Marine Tidal Turbine Based on Permanent Magnet Synchronous Generators and Passive Rectifiers,” in *3rd Renewable Power Generation Conference (RPG 2014),* 2014.

[41] Z. Zhou, F. Scuiller, J. F. Charpentier, M. E. H. Benbouzid, and T. Tang, “Power Control of a Nonpitchable PMSG-Based Marine Current Turbine at Overrated Current Speed With Flux-Weakening Strategy,” *IEEE J. Ocean. Eng.*, vol. 40, no. 3, pp. 536–545, Jul. 2015.

[42] L. Wang and C.-N. Li, “Dynamic Stability Analysis of a Tidal Power Generation System Connected to an Onshore Distribution System,” *IEEE Trans. Energy Convers.*, vol. 26, no. 4, pp. 1191–1197, Dec. 2011.

[43] C. E. Ugalde-Loo, L. A. Amezquita-Brooks, E. Liceaga-Castro, and J. Liceaga-Castro, “Analysis and efficient control design for generator-side converters of PMSG-based wind and tidal stream turbines,” in *2014 Power Systems Computation Conference*, 2014, pp. 1–7.

[44] C. E. Ugalde-Loo, E. Liceaga-Castro, and J. Liceaga-Castro, “2x2 Individual Channel Design MATLAB@ Toolbox,” in *Proceedings of the 44th IEEE Conference on Decision and Control*, 2005, pp. 7603–7608.

[45] L. A. Amezquita-Brooks, J. Liceaga-Castro, E. Liceaga-Castro, and C. E. Ugalde-Loo, “Induction Motor Control: Multivariable Analysis and Effective Decentralized Control of Stator Currents for High-Performance Applications,” *IEEE Trans. Ind. Electron.*, vol. 62, no. 11, pp. 6818–6832, Nov. 2015.

[46] J. Clarke, G. Connor, A. Grant, C. Johnstone, and S. Ordonez-Sanchez, “Analysis of a single point tensioned mooring system for station keeping of a contra-rotating marine current turbine,” *IET Renew. Power Gener.*, vol. 4, no. 6, p. 473, 2010.

[47] N. J. Baker, E. Hodge, S. Cawthorne, and E. Spooner, “Modelling of the generator for OpenHydro’s tidal energy system,” in *7th IET International Conference on Power Electronics, Machines and Drives (PEMD 2014)*, 2014.

[48] “OpenHydro$^{\text{TM}}$,” 2017. [Online]. Available: http://www.openhydro.com/. [Accessed: 12-May-2017].

[49] K. Yuen *et al.*, “Matching a Permanent Magnet Synchronous Generator to a Fixed Pitch Vertical Axis Turbine for Marine Current Energy Conversion,” *IEEE J. Ocean. Eng.*, vol. 34, no. 1, pp. 24–31, Jan. 2009.

[50] M. J. Khan, M. T. Iqbal, and J. E. Quaicoe, “Dynamics of a vertical axis hydrokinetic energy conversion system with a rectifier coupled multi-pole permanent magnet generator,” *IET Renew. Power Gener.*, vol. 4, no. 2, pp. 116–127, 2010.

[51] O. Keysan, M. Mueller, A. McDonald, N. Hodgins, and J. Shek, “Designing the C-GEN lightweight direct drive generator for wave and tidal energy,” *IET Renew. Power Gener.*, vol. 6, no. 3, p. 161, 2012.

[52] O. Keysan, A. S. McDonald, and M. Mueller, “A direct drive permanent magnet generator design for a tidal current turbine(SeaGen),” in *2011 IEEE International Electric Machines & Drives Conference (IEMDC)*, 2011, pp. 224–229.

[53] M. C. Sousounis and M. A. Mueller, “Fault simulation and pattern recognition in a modular generator under two different power converter configurations,” *2013 Int. Electr. Mach. Drives Conf.*, vol. 44, no. 0, pp. 747–754, 2013.

[54] F. Mekri, S. Ben Elghali, and M. E. H. Benbouzid, “Fault-Tolerant Control Performance Comparison of Three- and Five-Phase PMSG for Marine Current Turbine Applications,” *IEEE Trans. Sustain. Energy*, vol. 4, no. 2, pp. 425–433, Apr. 2013.

[55] O. Fall, J. F. Charpentier, N.-K. Nguyen, and P. Letellier, “Maximum torque per ampere control strategy of a 5-phase PM generator in healthy and faulty modes for tidal marine turbine application,” in *2014 International Power Electronics and Application Conference and Exposition*, 2014, no. 2, pp. 468–473.

[56] G. S. Galloway, V. M. Catterson, C. Love, and A. Robb, “Anomaly Detection Techniques for the Condition Monitoring of Tidal Turbines,” in *Proceedings of the Annual Conference of the Prognostics and Health Management Society*, 2014, pp. 1–12.

[57] J. K. H. Shek, D. G. Dorrell, M. Hsieh, D. E. Macpherson, and M. A. Mueller, “Reducing Bearing Wear in Induction Generators for Wave and Tidal Current Energy Devices,” in *IET Conference on Renewable Power Generation (RPG 2011)*, 2011.

[58] J. Fletcher, T. Judendorfer, M. Mueller, N. Hassanain, and M. Muhr, “Electrical issues associated with sea-water immersed windings in electrical generators for wave- and tidal current-driven power generation,” *IET Renew. Power Gener.*,

vol. 3, no. 2, pp. 254–264, 2009.

[59] S. Benelghali, M. E. H. Benbouzid, and J. F. Charpentier, “Generator Systems for Marine Current Turbine Applications: A Comparative Study,” *IEEE J. Ocean. Eng.*, vol. 37, no. 3, pp. 554–563, Jul. 2012.

[60] M. C. Sousounis, J. K. H. Shek, R. C. Crozier, and M. a Mueller, “Comparison of Permanent Magnet Synchronous and Induction Generator for a Tidal Current Conversion System with Onshore Converters,” in *Industrial Technology (ICIT), 2015 IEEE International Conference on*, 2015, pp. 2481–2486.

[61] L. Wang, J.-Y. Yu, and Y.-T. Chen, “Dynamic stability improvement of an integrated offshore wind and marine-current farm using a flywheel energy-storage system,” *IET Renew. Power Gener.*, vol. 5, no. 5, pp. 387–396, May 2011.

[62] Zhibin Zhou, F. Scuiller, J. F. Charpentier, M. El Hachemi Benbouzid, and Tianhao Tang, “Power Smoothing Control in a Grid-Connected Marine Current Turbine System for Compensating Swell Effect,” *IEEE Trans. Sustain. Energy*, vol. 4, no. 3, pp. 816–826, Jul. 2013.

[63] Z. Zhou, F. Seuiller, J. F. Charpentier, M. Benbouzid, and T. Tang, “Application of flow battery in marine current turbine system for daily power management,” in *2014 First International Conference on Green Energy ICGE 2014*, 2014, no. March, pp. 8–13.

[64] L. Sheng, Z. Zhou, J. F. Charpentier, and M. E. H. Benbouzid, “Stand-alone island daily power management using a tidal turbine farm and an ocean compressed air energy storage system,” *Renew. Energy*, vol. 103, no. November, pp. 286–294, 2017.

[65] L. Sheng, Z. Zhou, J. F. Charpentier, and M. Benbouzid, “Island Power Management using a Marine Current Turbine Farm and an Ocean Compressed Air Energy Storage System,” in *Proceedings of the 11th European Wave and Tidal Energy Conference*, 2015, no. September, pp. 1–6.

[66] Z. Zhou, M. Benbouzid, J. F. Charpentier, F. Scuiller, and T. Tang, “Energy storage technologies for smoothing power fluctuations in marine current

turbines," in *2012 IEEE International Symposium on Industrial Electronics*, 2012, pp. 1425–1430.

[67] P. Denholm, E. Ela, B. Kirby, and M. Milligan, "The Role of Energy Storage with Renewable Electricity Generation," National Renewable Energy Laboratory (NREL), 2010.

[68] X. Luo, J. Wang, M. Dooner, and J. Clarke, "Overview of current development in electrical energy storage technologies and the application potential in power system operation," *Appl. Energy*, vol. 137, pp. 511–536, Jan. 2015.

[69] F. Díaz-González, A. Sumper, O. Gomis-Bellmunt, and R. Villafáfila-Robles, "A review of energy storage technologies for wind power applications," *Renew. Sustain. Energy Rev.*, vol. 16, no. 4, pp. 2154–2171, May 2012.

[70] M. Liu, W. Li, C. Wang, R. Billinton, and J. Yu, "Reliability Evaluation of a Tidal Power Generation System Considering Tidal Current Speeds," *IEEE Trans. Power Syst.*, vol. 31, no. 4, pp. 3179–3188, Jul. 2016.

[71] T. M. Delorm, D. Zappala, and P. J. Tavner, "Tidal stream device reliability comparison models," *Proc. Inst. Mech. Eng. Part O J. Risk Reliab.*, vol. 226, no. 1, pp. 6–17, 2012.

[72] I. M. de Alegría, J. L. Martín, I. Kortabarria, J. Andreu, and P. I. Ereño, "Transmission alternatives for offshore electrical power," *Renew. Sustain. Energy Rev.*, vol. 13, no. 5, pp. 1027–1038, Jun. 2009.

[73] S. Bala, Jiuping Pan, G. Barlow, G. Brown, and S. Ebner, "Power conversion systems for tidal power arrays," in *2014 IEEE 5th International Symposium on Power Electronics for Distributed Generation Systems (PEDG)*, 2014, pp. 1–7.

[74] A. J. Nambiar *et al.*, "Optimising power transmission options for marine energy converter farms," *Int. J. Mar. Energy*, vol. 15, pp. 127–139, Sep. 2016.

[75] G. V. Brown, "Proposal for a Commercial Scale Tidal Array Concept Study," ABB, 2013.

[76] M. Petie and N. Platt, "SIEMENS: FINAL REPORT FOR PHASE 2 FOR ELECTRICAL INFRASTRUCTURE OF COMMERCIAL SCALE TIDAL

POWER ARRAY," SIEMENS, 2013.

[77] D. Mumtaz, "ELECTRICAL INFRASTRUCTURE REQUIRED FOR COMMERCIAL SCALE TIDAL POWER ARRAYS: SELECTION OF TURBINE COLLECTION TOPOLOGY," GE Power Conversion, 2013.

[78] R. Driver, "Marine Energy Electrical Architecture Report 2: Review of SSE Contractor Reports," Catapult Offshore Renewable Energy, 2015.

[79] A. von Jouanne, D. A. Rendusara, P. N. Enjeti, and J. W. Gray, "Filtering techniques to minimize the effect of long motor leads on PWM inverter-fed AC motor drive systems," *IEEE Trans. Ind. Appl.*, vol. 32, no. 4, pp. 919–926, 1996.

[80] A. Von Jouanne and P. N. Enjeti, "Design considerations for an inverter output filter to mitigate the effects of long motor leads in ASD applications," *IEEE Trans. Ind. Appl.*, vol. 33, no. 5, pp. 1138–1145, 1997.

[81] R. M. Tallam, G. L. Skibinski, T. A. Shudarek, and R. A. Lukaszewski, "Integrated Differential-Mode and Common-Mode Filter to Mitigate the Effects of Long Motor Leads on AC Drives," *IEEE Trans. Ind. Appl.*, vol. 47, no. 5, pp. 2075–2083, Sep. 2011.

[82] A. K. Abdelsalam, M. I. Masoud, S. J. Finney, and B. W. Williams, "Vector control PWM-VSI induction motor drive with a long motor feeder: performance analysis of line filter networks," *IET Electr. Power Appl.*, vol. 5, no. 5, pp. 443–456, 2011.

[83] M. C. Sousounis, J. K. H. Shek, and M. A. Mueller, "Filter Design for Cable Overvoltage and Power Loss Minimization in a Tidal Energy System With Onshore Converters," *IEEE Trans. Sustain. Energy*, vol. 7, no. 1, pp. 400–408, Jan. 2016.

[84] J. Rodríguez *et al.*, "Resonances and overvoltages in a medium-voltage fan motor drive with long cables in an underground mine," *IEEE Trans. Ind. Appl.*, vol. 42, no. 3, pp. 856–863, 2006.

[85] M. Kuschke and K. Strunz, "Transient cable overvoltage calculation and filter design: Application to onshore converter station for hydrokinetic energy

harvesting,” *IEEE Trans. Power Deliv.*, vol. 28, no. 3, pp. 1322–1329, 2013.

[86] M. O. L. Hansen, *Aerodynamics of Wind Turbines*, 3rd ed. Routledge, 3rd edition, 2015.

[87] S. Heier, “Wind Energy Conversion Systems,” in *Grid Integration of Wind Energy: Onshore and Offshore Conversion Systems*, 3rd ed., vol. 38, John Wiley & Sons, Ltd., 2014, pp. 31–117.

[88] M. C. Sousounis, J. K. H. Shek, and M. A. Mueller, “Modelling and Control of Tidal Energy Conversion Systems with Long Distance Converters,” in *7th IET International Conference on Power Electronics, Machines and Drives (PEMD 2014)*, 2014, p. 4.3.02-4.3.02.

[89] B. Wu, Y. Lang, N. Zargari, and S. Kouro, “Wind Generators and Modeling,” in *Power Conversion and Control of Wind Energy Systems*, 1st ed., Hoboken, New Jersey: John Wiley & Sons, Inc., 2011, pp. 49–85.

[90] I. Takahashi and T. Noguchi, “A New Quick-Response and High-Efficiency Control Strategy of an Induction Motor,” *Ind. Appl. IEEE Trans.*, vol. IA-22, no. 5, pp. 820–827, 1986.

[91] B. Wu, Y. Lang, N. Zargari, and S. Kouro, “Variable-Speed Wind Energy Systems With Squirrel Cage Induction Generators,” in *Power Conversion and Control of Wind Energy Systems*, 1st ed., Hoboken, New Jersey: John Wiley & Sons, Inc., 2011, pp. 191–235.

[92] Y. Xue, X. Xu, T. G. Habetler, and D. M. Divan, “A low cost stator flux oriented voltage source variable speed drive,” in *Conference Record of the 1990 IEEE Industry Applications Society Annual Meeting*, pp. 410–415.

[93] B. Wu, Y. Lang, N. Zargari, and S. Kouro, “Power Converters in Wind Energy Conversion Systems,” in *Power Conversion and Control of Wind Energy Systems*, John Wiley & Sons, Inc., 2011, pp. 87–152.

[94] B. Wu, Y. Lang, N. Zargari, and S. Kouro, “Variable-Speed Wind Energy Systems With Synchronous Generators,” in *Power Conversion and Control of Wind Energy Systems*, 1st ed., Hoboken, New Jersey: John Wiley & Sons, Inc.,

2011, pp. 275–316.

[95] Hydro-Québec, “Simscape^{TM} Power Systems^{TM} User’s Guide (Specialized Technology),” Hydro-Québec and The MathWorks, Inc., 2017.

[96] “EMEC : European Marine Energy Centre Sub-sea cables,” 2017. [Online]. Available: http://www.emec.org.uk/facilities/sub-sea-cables/. [Accessed: 12-May-2017].

[97] E. Fuchs and M. Masoum, *Power Quality in Power Systems and Electrical Machines*. Elsevier Inc., 2008.

[98] C. Bajracharya, M. Molinas, J. A. Suul, and T. M. Undeland, “Understanding of tuning techniques of converter controllers for VSC-HVDC,” in *Nordic Workshop on Power and Industrial Electronics, NORPIE/2008*.

[99] Nexans, “Nexans Global experts in cables and cabling systems - Submarine Power Cables,” Nexans, 2013.

[100] C. H. Houpis and S. N. Sheldon, *Linear Control System Analysis and Design with MATLAB®*, Sixth Edit. Taylor & Francis Group, LLC, 2014.

[101] “MathWorks,” 2017. [Online]. Available: https://uk.mathworks.com/. [Accessed: 12-May-2017].